Fracture modeling in clay materials under hydric shrinkageModélisation de fissure dans les matériaux argileux sous retrait hydrique : numerical models, comparisons with experiments and stochastic aspects

Darith-Anthony Hun

CIVIL & ENVIRONMENTAL ENGINEERING
Duke UNIVERSITY

MSME LABORATOIRE MODÉLISATION ET SIMULATION MULTI ÉCHELLE
Université Gustave Eiffel

Navier
École des Ponts ParisTech

Thèse de Doctorat de l'Université Paris-Est

Discipline : mécanique et génie civil

présentée et soutenue publiquement

le 28 mai 2020

par

Darith Anthony Hun

Fracture modeling in clay materials under hydric shrinkage : numerical models, comparisons with experiments and stochastic aspects

Composition du jury

Rapporteurs :	Jianfu SHAO	Professeur des Universités Université de Lille – Laboratoire LaMcube
	Benoit BARY	Ingénieur de recherche CEA Paris-Saclay
Examinateur :	Karam SAB	Professeur École des Ponts ParisTech – Laboratoire Navier
Directeur de thèse :	Julien YVONNET	Professeur des Universités Université Gustave Eiffel – Laboratoire MSME
Co-directeur de thèse :	Johann GUILLEMINOT	Assistant Professor Duke University – Civil & Environmental Engineering
Co-Encadrant :	Michel BORNERT	Ingénieur en Chef des Ponts, Eaux et Forêts École des Ponts ParisTech – Laboratoire Navier

---

ÉCOLE DOCTORALE UNIVERSITÉ PARIS-EST
Sciences, Ingénierie et Environnement

LABEX MMCD
Multi-Scale Modelling & Experimentation of Materials for Sustainable Construction
INVESTISSEMENTS D'AVENIR

Mis en page avec la classe thesul.

Acknowledgements

Tout d'abord, je souhaite remercier mon directeur de thèse, le professeur Julien Yvonnet pour son encadrement et son investissement durant ma thèse, j'ai apprécié sa pédagogie et son humilité. Il a pu me montrer, au-delà de mon travail de thèse, l'envers du décor de la vie académique au sein du laboratoire Modélisation et Simulation Multi Echelle (MSME) de l'université Gustave Eiffel. De la même manière, il a pu me faire découvrir le processus d'organisation et de préparation de conférences scientifiques nationales et internationales. Ce fut très captivant.

Je remercie mon second directeur, le professeur Johann Guilleminot de Duke University pour sa rigueur scientifique et ses conseils avisés. Il m'a tellement apporté durant cette thèse, que ce soit dans les sciences avec un support massif ou sur le plan personnel. J'ai particulièrement apprécié tous les moments que nous avons partagés aux Etats-Unis. Ce fut juste incroyable.

Mes remerciements vont également au professeur Michel Bornert de l'Ecole des Ponts ParisTech, qui a ajouté le volet expérimental à cette thèse. Le savoir qu'il partage et la justesse de ses analyses m'inspirent le plus grand respect. J'ai particulièrement apprécié l'étude dans l'accélérateur de particules au synchrotron soleil. Ce fut une expérience unique.

Je n'oublie pas le docteur Abdelali Dadda ainsi que le professeur Ahn Minh Tang, pour notre projet d'étude commun entre expérience et modélisation numérique. Cette collaboration a fait émerger des résultats intéressants et tout à fait inédits. Ce fut vraiment enrichissant.

Je tiens à remercier une dernière fois cette équipe de recherche ainsi que le *LabEx MMCD* pour le financement et la conduite de ce formidable projet.

Ensuite, je remercie le jury de thèse et plus particulièrement le professeur Jian FU Shao de l'université de Lille et Benoît Bary du Commissariat à l'Energie Atomique et aux énergies alternatives pour avoir accepté de rapporter ce présent manuscrit, sans oublier le président du jury, le professeur Karam Sab de l'Ecole des Ponts ParisTech pour avoir examiné ce travail. Nous avons longuement discuté lors de cette soutenance, aussi bien sur des aspects très techniques que sur des aspects de fond. Ces éléments témoignent d'un respect à l'égard mes travaux, je leur adresse en retour mon immense respect.

Puis, je remercie bien évidemment la team du bureau 118 : mon copilote Quentin A., ce féroce débatteur, Anthony P. pour sa proximité et tout ce que l'on a partagé, Justin R. pour tous ces mercredis « toundoulis » et fringales en tout genre, Vincent D. mon gym buddy et partenaire d'humour, Jérôme K. pour toutes les longues discussions que l'on a pu avoir, et enfin Brian S. my favorite belge pour sa gentillesse "+" infinie. Je pense que nous avons fondé une sacrée équipe pendant cette thèse, cette dernière s'étant déroulée avec vous de la meilleure des manières. Cette ambiance me manque déjà !

J'adresse une dédicace particulière à Rob, Darwish, Hanane, Tib's et Ludo pour tous ces moments de débat. Je n'oublie pas les autres doctorants du MSME, les responsables administratives pour leur support et leur gentillesse. J'adresse une pensée à mes équipiers fous de volley (APUU), de gym et la coach qui m'a tant appris. Merci pour tous ces moments.

Enfin, je dédie ce travail à ma famille, à mon père, ma chère mère pour leur soutien quotidien, sans oublier mes sœurs, qu'ils voient en ces mots la gratitude pour tout ce qu'ils m'ont apporté et cela depuis le premier jour.

Résumé

La présente thèse traite de la modélisation de la fissuration dans les matériaux aléatoires hétérogènes et de la fissuration par dessiccation lors du séchage des argiles.

Dans un premier temps, une approche stochastique de la propagation de fissures en milieu aléatoire est proposée. La démarche est basée sur l'utilisation de simulation de Monte Carlo, conduites afin d'explorer un ensemble de configurations microstructurales. Cet ensemble est spécifiquement exploité afin de construire et d'identifier un modèle de champ de phase mésoscopique. Dans ce cadre, les coefficients élastiques stochastiques sont associés à des champs de propriétés apparentes, définies par deux types de conditions aux limites bien établies, alors que les paramètres de rupture sont supposés déterministes et sont identifiés au travers d'un problème inverse. L'approche permet de conduire des simulations de propagation de fissure dans un milieu aléatoire sans nécessiter de discrétisation fine à l'échelles des hétérogénéités.

Dans une seconde partie, nous proposons un cadre de modélisation combinant simulations numériques et analyse expérimentale dans le cas du séchage des argiles et de la fissuration induite par dessiccation. Afin de diminuer le caractère aléatoire du processus de fissuration, des inclusions rigides sont introduites de façon contrôlée dans les échantillons d'argile. L'approche par champ de phase est formulée dans le cas de grandes déformations par rétractation, induites par les effets hydriques. Les résultats expérimentaux sont obtenus par corrélation d'images numériques sur un ensemble de configurations intégrant un nombre variable d'inclusions. Les champs locaux de déformations et les trajets de fissuration ainsi obtenus sont analysés et permettent l'identification des paramètres du modèle numérique. Une discussion soulignant les avantages et limitations du cadre établi est enfin proposée.

Abstract

This thesis is focused on the modeling of crack propagation in random heterogeneous materials or induced by desiccation.

A stochastic approach to the modeling of brittle fracture in random media is first proposed. Monte Carlo simulations are specifically conducted to explore microstructural configurations and to subsequently build and identify a mesoscopic phase-field model. In this framework, the stochastic elastic coefficients are defined as fields of apparent properties, obtained under two types of boundary conditions, while the fracture parameters are assumed deterministic and are identified by solving an inverse problem. The methodology allows stochastic simulations of crack propagation to be performed without requiring a fine-grid discretization at the resolution of the heterogeneities.

In a second part, we propose a modeling framework combining numerical simulations and physical experiments for the analysis of crack propagation induced by desiccation. Clay drying is specifically investigated on samples filled with rigid inclusions, with the aim of controlling variability on crack initiation and propagation. A finite-strain phase-field model is formulated for shrinkage deformations induced by hydric effects. The experimental analysis is performed by using a digital image correlation technique on a set of configurations with different numbers of inclusions. The deformation fields and crack paths thus obtained are analyzed and allow for the identification of model parameters. A discussion highlighting the advantages and limitations of the framework is finally proposed.

Summary

Chapter 1

Introduction

Contents

1.1 Background

This thesis is part of a research effort developed within, and funded by, the LabEx MMCD (which is a French acronym for *Multi-scale Modeling and Experimentation of Materials for Sustainable Construction*) at Université Paris-Est, France. The objective of this LabEx is to advance and disseminate fundamental knowledge for the understanding of the physical phenomena that govern the properties of construction materials and geomaterials. In their natural environment, these materials are in permanent contact with humidity causing swelling and hydric shrinkage, inducing many problems in civil engineering, for example during severe drought. In this context, the study of crack propagation in clay materials with humidity is of particular interest. With the goal of better understanding the degradation mecanisms on civil engineering structures, and specifically here the failure and leakage in underground radioactive storage facilities—such as

the structures located in Bure, France (see Fig. 1.1). The design and construction of such structures involve various types of safety specifications, including certified structural integrity with respect to cracking mechanisms driven by aging and humidity. In order to assess the quality of containment and its evolution over time, extensive experimental studies were therefore carried out to characterize the nature and behavior of the geological layers (with Callovo-Oxforian argillaceous rocks being collected on site) [Wang, 2012].

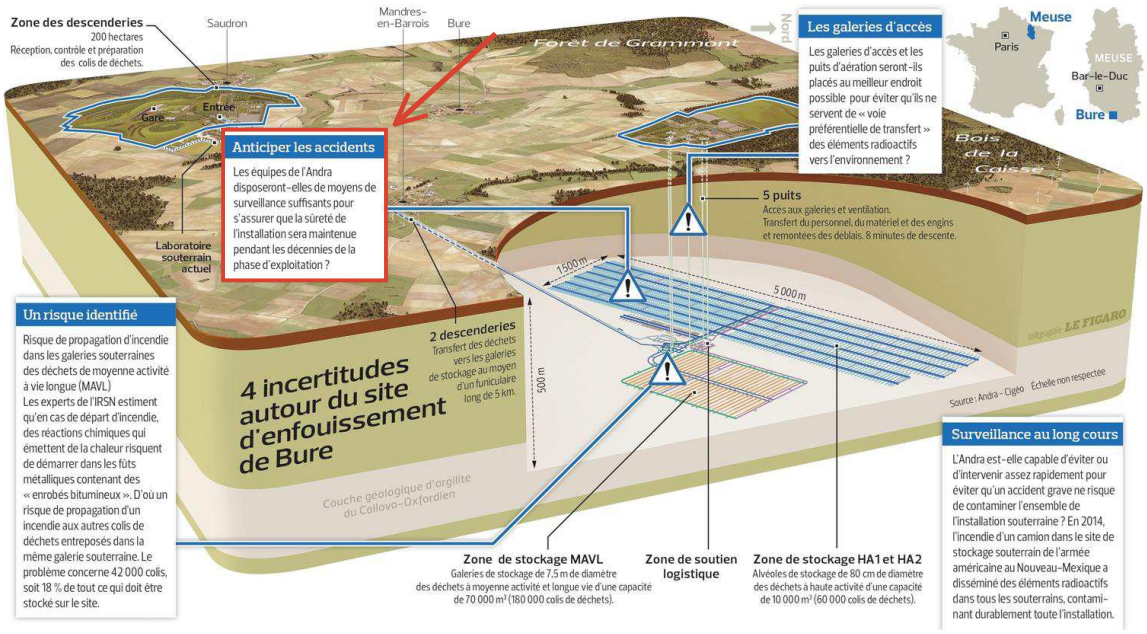

Figure 1.1 – Nuclear waste storage structure in Bure, France (in French) [Vanlerberghe, 2017].

From a simulation standpoint, a deep understanding of the underlying physical phenomena is required to enhance the accuracy and the predictiveness of the computational fracture models. Local mechanisms, in particular, depend on the nature of the constitutive materials (which can be, e.g., cementitious materials and rocks in civil engineering applications), and investigations at fine scales are often crucial to develop predictive material failure models. In this case, the fine scale randomness that is typically exhibited by geological materials can strongly affect simulation outcomes and must thus be integrated in the numerical setting.

Following the above discussion, the overarching goal of this thesis is to develop a modeling framework for micro-cracking in clay materials that combines computational modeling, enhanced by multiscale and stochastic aspects, with experimental characterization.

In the rest of this chapter, we first review the state of the art regarding numerical approaches for modeling crack propagation.

1.2 Research Objectives and Thesis Outline

The thesis is organized as follows. After an extensive review of the cracking models commonly used in the literature, Chapter 2 focuses on the construction of a probabilistic model in the context of random heterogeneous material cracking problems. Then chapters 2, 3 and 4 focus on the aspects of hydric shrinkage of clays with respectively a study on modeling and numerical implementation, followed by an experimental study and a simulation section. The last part

will introduce a discussion to provide a strategic basis for bringing the modelling closer to the complex character of the problem.

- **Chapter 2** presents the construction of a probabilistic model in the case of a heterogeneous environment. The formulation used here aims at identifying the material parameters of a multi-scale cracking problem using the formulation of the phase field method. The identification of the problem is based on Monte-Carlo simulations. The mesocopic material properties are computed on the microstructure through the sliding window approach, and the cracking properties are obtained by an inverse problem based on the mean maximum response between the micro and meso scales.

- **Chapter 3** raises the issue of hydric shrinkage. This part tackles the modelling aspects with the extension in the general framework to large deformations as well as the coupling with a hydric shrinkage model. The problem formulation, the numerical implementation and the benchmarks are described.

- **Chapter 4** exposes the experimental part of the thesis, where wet clay and rigid inclusion samples are followed during the drying process. The setup as well as the experimental conditions are presented. The objective here is to identify and quantify the mechanisms during the drying process. For this purpose, recent image analysis techniques have been used in order to access to the deformation map, providing valuable and precise information on the complex physics of this phenomenon.

- **Chapter 5** aims to reproduce, through numerical simulation, the dynamics observed experimentally. The observation is focused on the crack propagation pattern, as well as on the local deformations of the samples. The comparison of these simulations with the experiments will allow us to analyse the relevance of the model and to identify what has not been taken into account. On the basis of the available information, new strategies will be proposed for future improvements.

1.3 Computational Modeling of Crack Propagation

1.3.1 Discrete models

1.3.1.1 Molecular dynamics (MD)

Molecular Dynamics is a well-known simulation tool (see e.g. [Rapaport, 2004]) to simulate complex phenomena at the atomistic scale. This technique is restricted for scales where all atoms are explicitly described. Non-reversible phenomena, dislocations and other microscopic mechanisms leading to crack activation are easily described, as well as post-fracture frictions, by simply considering the interactions between atoms as nonlinear functions in a Newtonian Dynamics approach (discrete mechanics). The technique consists in solving the dynamic equilibrium (second Newton's law) of atom positions based on a Hamiltonian formulation:

$$M\frac{d^2q(t)}{dt^2} = -\nabla V(q(t)) + f^{ext} \ , \tag{1.1}$$

where M is the mass of each particle and V is a potential (see Fig. 1.2) whose general model is given in the form:

$$V(q) = \sum v_{ij}^{(2)}(q_{ij}) + \sum v_{ijk}^{(3)}(q_{ij}, q_{ik}) + \sum v_{ijk(...)}^{(p)}(q_{ij}, q_{ik}, q_i(...)) \ . \tag{1.2}$$

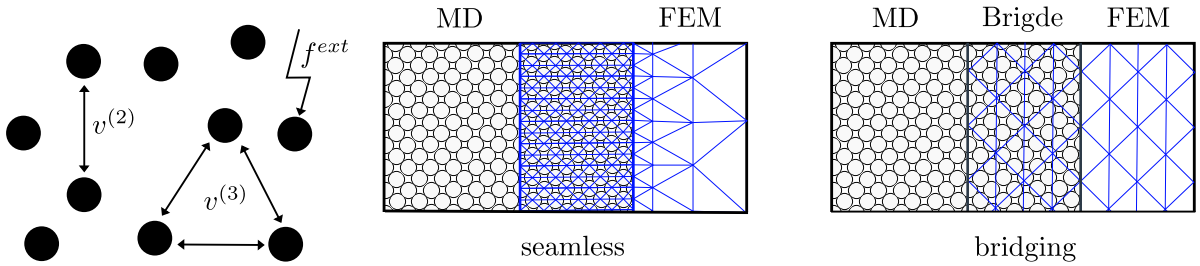

Figure 1.2 – MD particles scheme - MD/FEM coupled.

The empirical potentials are defined as functions of the number of interacting particles p and the nature of the atoms involved. For example, $p = 2$ typically corresponds to axial forces of repulsion or attraction (for, e.g., steric repulsion, Coulomb or dipolar charge attraction/repulsion), while $p = 3$ and $p \geq 3$ can be associated with, e.g., torsional forces and other types of contributions (e.g., metallic bounds), respectively.

The MD does not require complex models and can be easily implemented. For the specific case of cracking, the crack initiation and propagation is naturally taken into account without specific treatment: when atoms are far from each other's, using appropriate potentials the interaction forces decrease and atoms do not have any more interactions (see Fig. 1.3). [Souguir, 2018] works (with LabEX MMCD) on adapted potentials so-called reactive potentials that are relevant over large ranges of interatomic distances. However, the major drawback lies in the drastic restriction of space and time domains for which the simulations are conducted, inducing intractable computational times and memory requirements for engineering scale problems. For example, a volume $V = 1\ \mu m^3$ contains roughly 10^{11} atoms for a silica crystal (10^{11} roughly corresponds to 6.5 Tera-bytes of memory). Another strong limitation lies in the stable time steps related to such small scales, which are of the order of femtoseconds ($\Delta t \propto 10^{-15}$ s). To decrease these limitations, bridging techniques between atomistic and continuum approaches have been developed, where the crack phenomenon is localized in a small discrete (atomistic) area, while the rest of the domain (uncracked) is modeled with continuum approaches. In this context, we can mention the Bridging Domain approach [Xiao and Belytschko, 2004] or the Quasi-continuum approach [Tadmor et al., 1996] (see Fig. 1.2).

In the literature several works concerning cracking at the atomistic scale focus on the phenomena of pre-crack instability [Abraham et al., 1994, Souguir, 2018] and the propagation velocity [Zhou et al., 1996] stress.

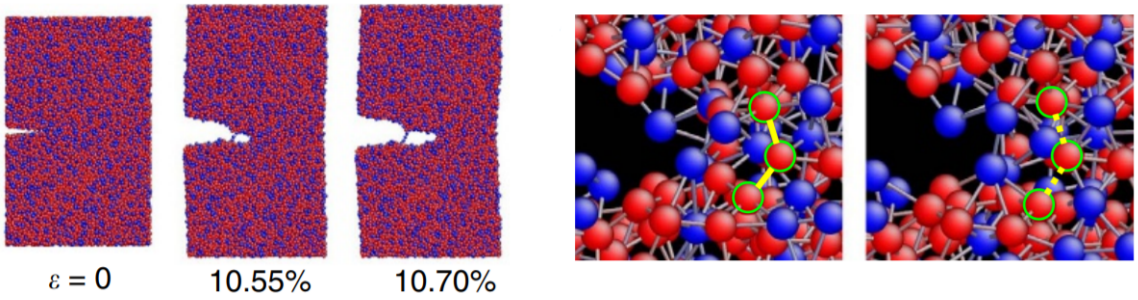

Figure 1.3 – MD snapshots and zoom of brittle fracture for one critical tensile strain step load ε [Wang et al., 2015].

1.3.1.2 Discrete Element Method (DEM)

The Discrete Element method was introduced by [Cundall and Strack, 1979] in rocks mechanics and granular media. Such approach is similar to molecular dynamics, but particles are here considered at a larger scale: they can constitute physical discrete particles such as sand grains, or represent a portion of matter. These particles are modeled by rigid elements interacting through contact and adhesion forces $F_c^{(i)}$, where i is the index of the particle, varying from 1 to N, with N is the number of interacting neighbors (friction, plasticity, adhesion, cohesive contact) having all their own model. The solution to this problem consists in adding to each particle F_c all these contributions and in using an integration method to calculate the next position δu of each particle of the system following the MD scheme (see Fig. 1.4).

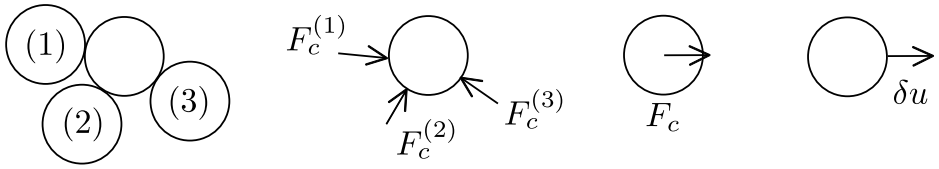

Figure 1.4 – DEM Procedure.

The advantage of this method is to be able to faithfully represent the crack phenomena at the particle scale (see Fig. 1.5). However, when considering continuous media, the definition of particles and interaction models becomes delicate. Indeed, the same scaling rules as in MD prevents to apply the technique to macroscale problems, as a realistic structure might encompass an unaffordable number of particles. As in MD, the method can be coupled with continuum approaches, as e.g. in the "Combined Finite-Discrete Element" (CFDE) method widely used to deal with multi scale problems more efficiently. Such technique has been applied to ceramics, rock, powder, impact and cracking [Munjiza et al., 1999].

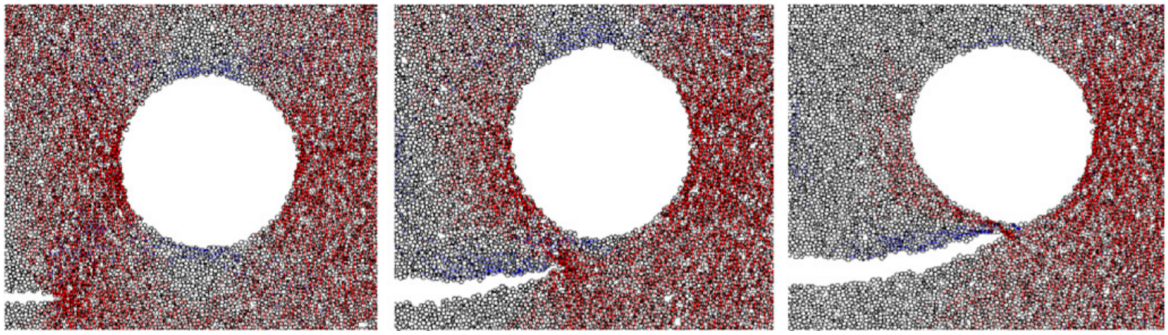

Figure 1.5 – Crack path obtained by DEM in vitreous biopolymer material [Hedjazi et al., 2012].

1.3.1.3 Lattice Spring Model (LSM)

The Lattice Spring model (LSM) is another discrete approach, aiming at modeling continuum matter with discrete approaches, to facilitate the description of crack propagation. This method is inspired by condensed matter physics and is frequently used to simulate deformation and fracture. It has been shown that in the assumption of linear elasticity, LSM can be equivalent to the Finite Element Method (see [Ostoja-Starzewski et al., 1996]). In this approach the nodes are associated with non-volumetric particles connected by springs. The deformation of the spring is

calculated between two particles position $(\boldsymbol{x}_i, \boldsymbol{x}_j)$ as

$$\boldsymbol{\varepsilon}_{(ij)} = \mathscr{E}(\boldsymbol{x}_i, \boldsymbol{x}_j) \ , \tag{1.3}$$

where $\mathscr{E}$ is a deformation function. Under mechanical stress, each node moves and change of position induces a nodal force such as:

$$\boldsymbol{F}_i = \sum_{v=1,\ldots,v_{max}} \mathscr{K}(\boldsymbol{x}_i, \boldsymbol{x}_v) \ , \tag{1.4}$$

where $\mathscr{K}$ is a function associating the spring stiffness between the $i-$th node of interest, the $v-$th neighbor node and theirs positions. In this method, the static equilibrium is invoked

$$\boldsymbol{F}_i + \boldsymbol{F}_{ext} = \boldsymbol{0} \tag{1.5}$$

with $\boldsymbol{F}_{ext}$ is the imposed external force. In the application, when a spring exceeds a critical threshold $\boldsymbol{\varepsilon} > \boldsymbol{\varepsilon}_c$, the crack starts to initiate. The broken springs no longer transmit forces to their neighbors, the system enters an unsteady state, the new rearrangement is done by solving, in each node linked to the broken springs (see Fig. 1.7), the following equation:

$$\boldsymbol{F}_i = \sum_{v=1,\ldots,v_{max-k}} \mathscr{K}(\boldsymbol{x}_i, \boldsymbol{x}_j) = \boldsymbol{0} \ . \tag{1.6}$$

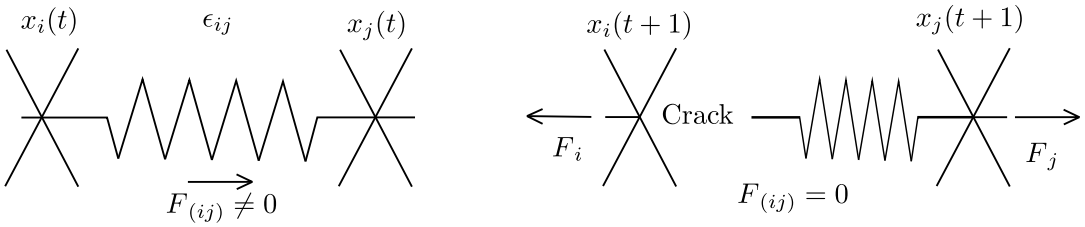

Figure 1.6 – Lattice crack process.

Above, k is the number of broken springs for a node. This can cause a variation of deformation which leads to other ruptures. This chain process, which is solved by the equilibrium of local forces at each node, ends when all induced deformations return below the critical threshold. Numerically this method imposes a structured mesh, which can drastically limit the approach when considering structures with complex geometries.

In the literature [Vogel et al., 2005,Malthe-Sørenssen et al., 1998] have shown the efficiency of these models by comparing its numerical modeling with experiments on homogeneous clay materials under shrinkage conditions. The model shows good crack pattern reproduction, bifurcation angles and model parameters having a physical sense (randomness of heterogeneous friction) on the final state of the sample. However, such approach induces ad-hoc models of interactions and cannot be easily extended to more complex phenomena (plasticity, heterogeneous materials, complex geometries).

1.3.1.4 Peridynamics

This technique originally proposed by [Silling, 2000] is closely related to MD or DEM. It assumes that the material is described by discrete particles which represent the continuous matter. The dynamic equilibrium is solved according to:

$$\rho(x)\ddot{u}(x,t) = \int_R f(u(x',t) - u(x,t), x' - x, x) dV_{x'} + b(x,t) \ , \tag{1.7}$$

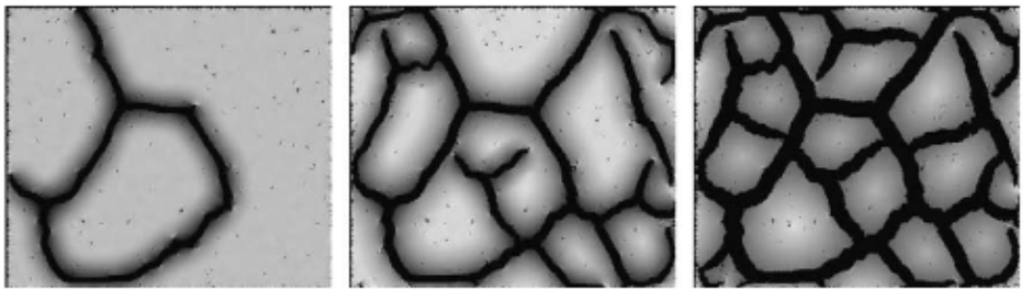

Figure 1.7 – Desiccation crack modelled by LSM [Vogel et al., 2005].

where ρ is the density, u the displacement, f a density force vector function that integrates the displacements and position of its neighbors x'. The right-hand term of this equation is a convolution term, similar to nonlocal elasticity models. Once discretized, it matches the Discrete Element Method above, except that the number of interaction is larger, as one point is related to a large number of surrounding points. Again, in this method, the rupture criterion is based on a threshold elongation $(u(\boldsymbol{x},t) - u(\boldsymbol{x}',t))$ between two particles. When this link breaks up there is no more interaction and the forces are redistributed on the neighborhood links, as in LSM. It then inherits the benefits of DEM and MD to easily model complex cracks patterns (see Fig. 1.8) but has the same drawbacks (ambiguous definition and calibration of interaction models to reproduce general mechanical behavior, spatial convergence issues, etc.)

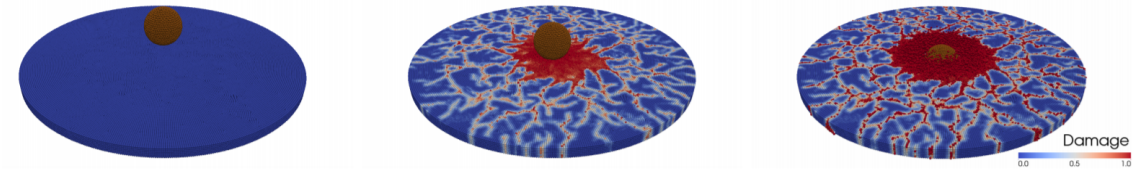

Figure 1.8 – Peridynamic simulation of impact [Littlewood et al., 2015].

1.3.2 Cohesize zone models

1.3.2.1 Cohesive elements

Cohesive models have been introduced in the work of [Dugdale, 1960] and [Barenblatt, 1961] for ductile and brittle materials. In these models, cracks are described by cohesive laws on the lips of the crack (called cohesive zones see Fig. 1.9). The energy of the system with cohesive element can be written as follows :

$$E = \int_{\Omega} \Psi(\boldsymbol{\varepsilon}) d\Omega + \int_{\Gamma} \Psi^I([[\mathbf{u}]]) d\Gamma \ , \tag{1.8}$$

where $[[\delta\mathbf{u}]] = \boldsymbol{u}^+ - \boldsymbol{u}^-$ denotes the displacement jump across Γ. Variation of the energy with respect to the displacement field gives the weak form:

$$\int_{\Omega} \boldsymbol{\sigma}(\boldsymbol{\varepsilon}) : \boldsymbol{\varepsilon}(\boldsymbol{\delta u}) d\Omega + \int_{\Gamma} f([[\mathbf{u}]]) : [[\delta\mathbf{u}]] dS = \int_{\partial\Omega_F} \mathbf{F}^{ext} \cdot \delta\mathbf{u} dS \ . \tag{1.9}$$

In this formulation, $f([[\mathbf{u}]]) = \partial\Psi^I / \partial[[\mathbf{u}]]$ is interpreted as the cohesive force (depending on a chosen cohesive law) between the lips of Γ depending of the value of the displacement jump $[[\mathbf{u}]]$,

defining the local effect of the interface on the global response (see Fig. 1.9). Numerically, the cohesive model is applied between the boundary of elements whose nodes are doubled. It has been shown that this technique has shortcomings, including (i) non-convergence of the energy with mesh refinement; (b) strong mesh-dependency (the cracks are constrained to follow the boundary of the elements) and (iii) additional nonphysical compliance in the material due to the surface spring layer model added into the energy. The reader is referred to [Elices et al., 2002]

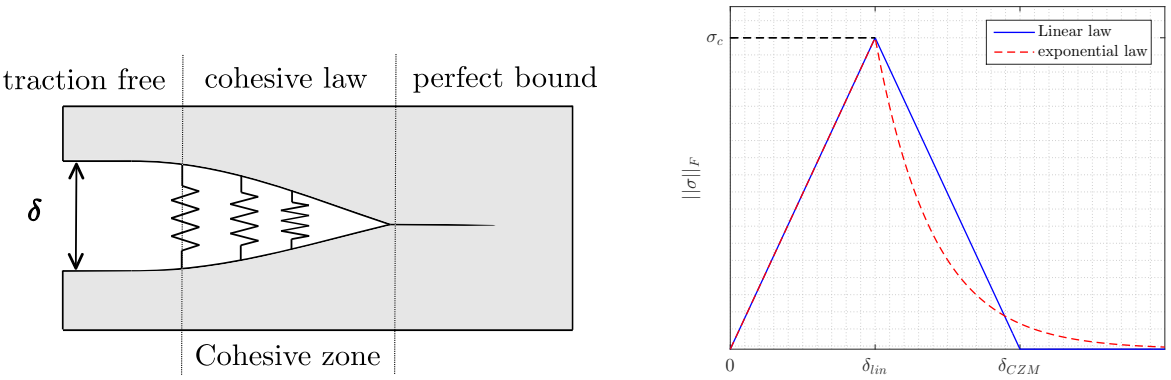

crack zone scheme.

basic material traction force response under different cohesive laws.

Figure 1.9 – Cohesive zone model approach.

for an extensive review on commonly used cohesive zone models. We note that [Vo et al., 2017] used this approach to investigate the desiccation cracking process of clay soils with experimental results.

1.3.2.2 Augmented Finite Element Method (A-FEM)

This method, introduced by [Hansbo and Hansbo, 2004], aims at introducing discontinuity in the model at the level of the numerical discretization. In other words, it does not constitute a crack propagation model but a numerical technique to introduce discontinuities in a convenient manner in regular meshes, even though it can be combined with, e.g., a cohesive model or a crack propagation criterion. The main idea is summarized below. In this technique, a discontinuous enrichment is induced in the FEM displacement approximation by separating an element in several sub-entities called mathematical element (ME) defined on Ω_α as illustrated on Fig. 1.10 $\alpha = \{1, 2\}$. On each ME, the displacement $\boldsymbol{u}(\boldsymbol{x})$ field is interpolated in the FEM sense, using classical nodes $\boldsymbol{u_i}$ and "ghost" nodes $\boldsymbol{u_i'}$ that correspond to split nodes:

$$\forall \boldsymbol{x} \in \Omega_i,\ \boldsymbol{u}'_\alpha(\boldsymbol{x}) = \boldsymbol{N}'_\alpha(\boldsymbol{x}) \cdot \{\boldsymbol{u_{i,\alpha}}\}' \ , \tag{1.10}$$

with $\boldsymbol{u_i'} = (\boldsymbol{u_i}, \boldsymbol{u_i'})^T$. The forms of elementary matrices are provided as

$$\boldsymbol{K}'_\alpha \cdot \{\boldsymbol{u'_{i,\alpha}}\} = \boldsymbol{f}'_{\Gamma_\alpha} + \boldsymbol{f}'_\alpha \ , \tag{1.11}$$

where

$$\boldsymbol{K}'_\alpha = \int_{\Omega_\alpha} \boldsymbol{B}_\alpha^{'T} \boldsymbol{C} \boldsymbol{B}'_\alpha d\Omega; \quad \boldsymbol{f}'_{\Gamma_\alpha} = \int_{\Gamma_\alpha} \boldsymbol{N}_\alpha^{'T} \cdot \boldsymbol{t}_\alpha dS; \quad \boldsymbol{f}'_\alpha = \int_{\partial\Omega_\alpha} \boldsymbol{N}_\alpha^{'T} \cdot \boldsymbol{F}_\alpha dS \ . \tag{1.12}$$

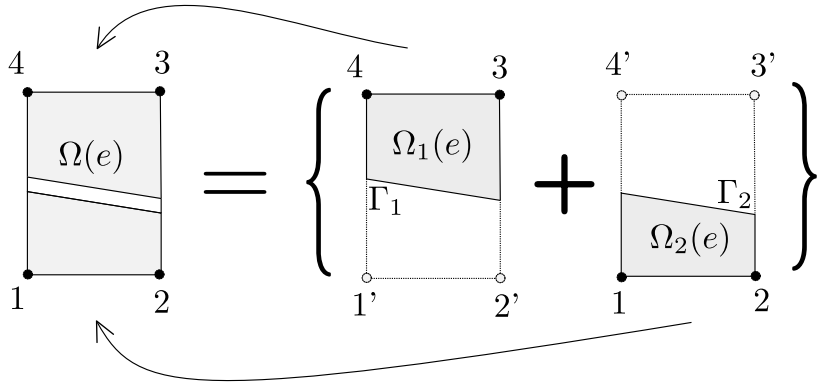

Figure 1.10 – AFEM inter-element superposition.

Above, $\boldsymbol{C}$ denotes the elasticity matrix representation, $\boldsymbol{F}_\alpha$ the surfaces forces, and $\boldsymbol{t}_\alpha$ is the internal force related to the discontinuity where the cohesive law can be used ($\boldsymbol{t}_\alpha = \boldsymbol{t}_\alpha(\delta)$) [Mergheim et al., 2005]. All the interpolation and its derivatives matrix are modified from FEM and explicited in [Ling et al., 2009]. Numerically this method does introduce neither additional degrees of freedom nor remeshing. However, severe issues come with mesh dependency, ill-conditioned matrix systems, and non-convergence with respect to the mesh size. Finally, an extension to the method in 3D is delicate.

1.3.3 Methods based on linear fracture mechanics

The mechanics of linear fracture is based on a macroscopic and energetic description of the cracking process described by the pioneers' work Griffith & Irvin. In its classical theoretical framework the solutions (obtained under restrictive hypotheses) are limited with the increase of the complexity of the problem (geometry, heterogeneities...), involving an increase in mathematical complexity when computed analytically. Combining such approaches with numerical methods like FEM allows defining accurate crack propagation criteria for more complex configurations.

1.3.3.1 FEM remeshing techniques

The classical use of FEM in the context of crack propagation is based on: (i) estimation of the stress state at the crack tip; (ii) defining a propagation condition and (iii) remeshing to update the finite element mesh used to again approximate the stress field.

The estimation of the mechanical state of the material around the crack tip within the framework of the linear fracture mechanics can be quantified either by the stress level or energetically. For the stress approach, the critical criterion is based on an asymptotic solution [Irwin, 1957] at the crack tip under the assumption of a material with linear elastic behavior. For example the stress solution at the crack tip is given in 2D under plane strain conditions by:

$$\begin{cases} \sigma_{rr} \simeq \dfrac{K_I}{4\sqrt{2\pi r}}[5\cos(\theta/2) - \cos(3\theta/2)] + \dfrac{K_{II}}{4\sqrt{2\pi r}}[-5\sin(\theta/2) + 3\sin(3\theta/2)] \ , \\ \sigma_{\theta\theta} \simeq \dfrac{K_I}{4\sqrt{2\pi r}}[5\cos(\theta/2) + \cos(3\theta/2)] + \dfrac{K_{II}}{4\sqrt{2\pi r}}[-3\sin(\theta/2) - 3\sin(3\theta/2)] \ , \\ \sigma_{r\theta} \simeq \dfrac{K_I}{4\sqrt{2\pi r}}[\sin(\theta/2) + \sin(3\theta/2)] + \dfrac{K_{II}}{4\sqrt{2\pi r}}[\cos(\theta/2) + 3\cos(3\theta/2)] \ , \end{cases} \tag{1.13}$$

where (r, θ) is the local coordinate basis defined on the crack tip as illustrated in Fig. 1.11 and (K_I, K_{II}) are stress intensity factors.

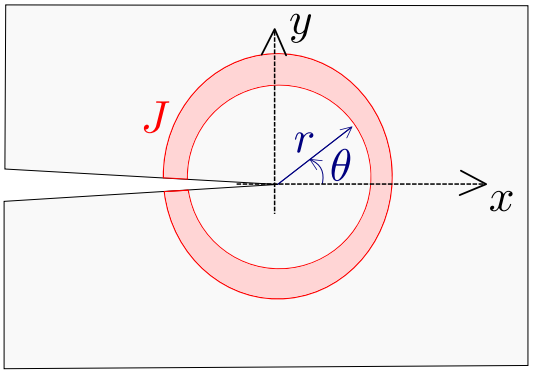

Figure 1.11 – Local crack basis and J-integral domain.

These quantities can be evaluated numerically based on the FEM results in the mesh elements. However, the singularity at the crack tip requires a very fine mesh and a volume average of stress intensity factors may result in a poor accuracy. The G-θ method consists in estimating the rate of energy restitution in the form of a contour path integral (J-integral [Rice, 1968] see Fig. 1.11) closed by the lip of the crack, thus avoiding the numerical issues at the crack tip according to

$$\mathcal{J} = \int_J \left(\frac{\partial \boldsymbol{u}}{\partial x} \cdot (\boldsymbol{\sigma} \cdot \boldsymbol{n}) - \frac{1}{2}(\boldsymbol{\sigma} : \boldsymbol{\varepsilon}) n_x \right) dS \ , \tag{1.14}$$

where the normal $\mathbf{n}$ or partial derivative operators have to be constructed and $\mathcal{J}$ calculated. The direction (angle θ_c) of propagation is found through verifying a given criterion, such as maximum radial stress of minimum energy. After each crack propagation, the mesh must be reconstructed from the crack and boundary, which might be costly and non-robust, especially for 3D geometries or changes of topology of the crack.

1.3.3.2 eXtended Finite Flement Method (X-FEM)

The eXtended Finite Element Method aims at avoiding the remeshing step in the above FEM crack propagation process within Finite Elements and linear fracture mechanics. The main idea is to enrich the FEM discretization to introduce both discontinuities and singularities related to the crack propagation directly within the FEM approximation through additional degrees of freedom at the nodes, which are associated to specific discontinuous and singular shape functions. The method is actually a special case of the Partition of Unity Method [Babuška and Melenk, 1997], which consists in improving a solution of a FEM problem by injecting, into the classical approximation, an additional function involving a basis that is constructed based on an expected solution (enrichment):

$$\boldsymbol{u}(\boldsymbol{x}) = \sum_i N_i(\boldsymbol{x}) \boldsymbol{u_i} + \sum_{i,p} N_i(\boldsymbol{x}) \Phi_{i,p}(\boldsymbol{x}) a_{i,p} \ , \tag{1.15}$$

where $a_{i,p}$ denote additional unknowns associated to the enriched approximation. [Belytschko and Black, 1999] applied this method to crack propagation by defining $\Phi_{i,p}$ as basis functions

describing the asymptotic solution in the vicinity of the crack:

$$\boldsymbol{u}(\boldsymbol{x}) \underset{r\to 0}{=} \left\{ \begin{array}{l} \frac{1}{2\mu}\sqrt{\frac{r}{2\pi}}(K_I \cos(\frac{\theta}{2}))(\mathscr{K} - \cos\theta) + K_{II}\sin(\frac{\theta}{2})(\mathscr{K} + \cos\theta + 2) \ , \\ \frac{1}{2\mu}\sqrt{\frac{r}{2\pi}}(K_I \sin(\frac{\theta}{2}))(\mathscr{K} - \cos\theta) - K_{II}\cos(\frac{\theta}{2})(\mathscr{K} + \cos\theta - 2) \ , \\ \frac{2}{\mu}\sqrt{\frac{r}{2\pi}}(K_{III}\sin(\frac{\theta}{2})) \ , \end{array} \right\} \tag{1.16}$$

where $\mathscr{K}$ is the Kolosov constant is defined for isotropic, plane stress (as $\mathscr{K} := 3-4\nu$) and plane strain (as $\mathscr{K} := (3-\nu)/(1+\nu)$), (r,θ) defines the geometry of the crack by a local coordinate system based on the crack tip, and (K_I, K_{II}, K_{III}) are the stress intensity factors defined for the basic fracture modes from linear elasticity [Irwin, 1957]. [Moës et al., 1999] enriched the basis with another additional discontinuous function H separating the crack lips and alleviating the remeshing step within the FEM procedure:

$$\boldsymbol{u}(\boldsymbol{x}) = \boldsymbol{u}(\boldsymbol{x}) = \left(\sum_i N_i(\boldsymbol{x})\boldsymbol{u_i} + \sum_{i,p} N_i(\boldsymbol{x})\bar{\Phi}_{i,p}(\boldsymbol{x})a_i, p \right) + \sum_i H(\boldsymbol{x_i})\boldsymbol{a_i} \ , \tag{1.17}$$

with the discontinuous function H being defined by:

$$H(\boldsymbol{x}) = \left\{ \begin{array}{l} +1, \text{ if } \phi > 0 \ , \\ -1, \text{ if } \phi < 0 \ , \end{array} \right. \tag{1.18}$$

and ϕ is a local coordinate attached to the crack surface defined by a couple of level set functions (ϕ, ψ) in 3D [Stolarska et al., 2001] (see Fig. 1.12)

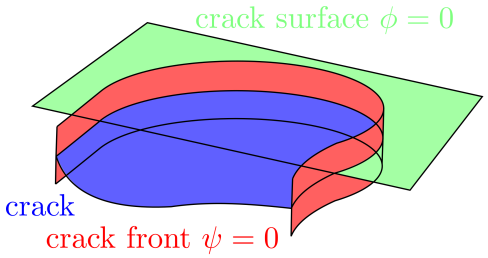

Figure 1.12 – Level set functions (ϕ, ψ) defining a 3D crack.

Even though this method has been very popular in the last decades, its interest has decreased recently because of the following drawbacks: (i) as being based on linear fracture mechanics, it does not include initiation of cracks, then requires an initial crack to start the simulation; (b) it can hardly take into account multiple cracks due to the complexity of handling multiple level-set functions; (c) there is no criterion for crack branching; (d) finally, the technique cannot deal with merging of cracks. In a context where we want to simulate cracks within microstructures, such limitations are penalizing.

1.3.4 Methods based on damage model

1.3.4.1 Continuum Damage Models (CDM)

The introduction of a damage model within a micromechanics framework was first conducted in [Kachanov, 1958]. The model characterizes damage induced by the formation of micro-cracks.

In this context, an isotropic degradation function was introduced and involves a scalar damage parameter d, ranging from 0 to 1. The constitutive equation relating the stress field $\boldsymbol{\sigma}$ and the strain field $\boldsymbol{\varepsilon}$ of an isotropic damage model is written as:

$$\boldsymbol{\sigma} = (1-d)\mathbb{C} : \boldsymbol{\varepsilon} \ , \tag{1.19}$$

where $\mathbb{C}$ is the stiffness tensor of the elastic, healthy material. In the case of anisotropic damage effects, a damage tensor $\mathbb{D}$ must be introduced in lieu of d. In addition, an evolution law is necessary for d. This damage law may be chosen in order to reflect the behavior of the considered material. For example, for quasi-brittle materials, the following model has been adopted in [Peerlings et al., 1998]:

$$d = \begin{cases} 0 & if \quad \kappa < \kappa_0 \ , \\ 1 - \frac{\kappa_0}{\kappa}[(1-\alpha) + \alpha \exp^{-\beta(\kappa-\kappa_0)}] \ . \end{cases} \tag{1.20}$$

In (1.20), the scalar parameter β describes the softening behavior, α is a scalar which controls the residual state in the post peak stage, κ_0 is the threshold for the initiation of damage and κ is a history scalar parameter which takes the largest value of an equivalent strain $\tilde{\varepsilon}$ function of $\boldsymbol{\varepsilon}$ (see below). Damage evolution is governed by the Kuhn-Tucker inequalities as follows:

$$\dot{\kappa} \geq 0 \ , \qquad f(\tilde{\varepsilon}, k) \leq 0 \ , \qquad \dot{d} f(\tilde{\varepsilon}, k) = 0 \ , \tag{1.21}$$

where $f(\tilde{\varepsilon}, k) = \tilde{\varepsilon} - \kappa$ is the loading function driving the evolution of damage. Early developments in the context of numerical methods can be found in [Krajcinovic, 1983, Chaboche, 1988, Lemaitre and Chaboche, 1994]. Various definitions for $\tilde{\varepsilon}$ have been later proposed. For example, according to the [Mazars, 1984] criterion, cracks can only propagate due to tensile strains, according to:

$$\tilde{\varepsilon}(\boldsymbol{\varepsilon}) = \sqrt{\langle \varepsilon_i \rangle : \langle \varepsilon_i \rangle} \ , \tag{1.22}$$

where ε_i are principle strains and $\langle \varepsilon_i \rangle = \frac{|\varepsilon_i| + \varepsilon_i}{2}$. For ductile fracture, the modified von Mises equivalent strain is usually defined as:

$$\tilde{\varepsilon}(\boldsymbol{\varepsilon}) = \frac{k-1}{2k(1-2\nu)} I_1(\boldsymbol{\varepsilon}) + \frac{1}{2k} \sqrt{\frac{(k-1)^2}{(1-2\nu)^2} I_1^2(\boldsymbol{\varepsilon}) + \frac{12k}{(1-\nu)^2} J_2(\boldsymbol{\varepsilon})} \ , \tag{1.23}$$

where k is the tensile/compressive strength ratio which is adapted depending on the material, ν is the Poisson's ratio, I_1 and I_2 are the first two invariants of the strain tensor. Another choice is the so-called smooth Rankine calibration [JiráSek and Bauer, 2012]:

$$\tilde{\varepsilon}(\boldsymbol{\varepsilon}) = \frac{1}{E} \sqrt{\langle \sigma_i \rangle : \langle \sigma_i \rangle} \ , \tag{1.24}$$

where $\langle \sigma_i \rangle$ is the principle stress tensor, and E is the Young's modulus.

Such local models induce numerical issues when implemented using the finite element method. In particular, a non-convergence of the response with respect to mesh density is typically observed (see the left panel in Fig. 1.13), for the strain localizes in an infinitely narrow band of elements as the mesh is refined, and crack trajectories (identified as localization bands of damage) turn out to be highly sensitive to mesh construction (regular or unstructured). To avoid these issues, different regularization techniques were introduced, including the use of:

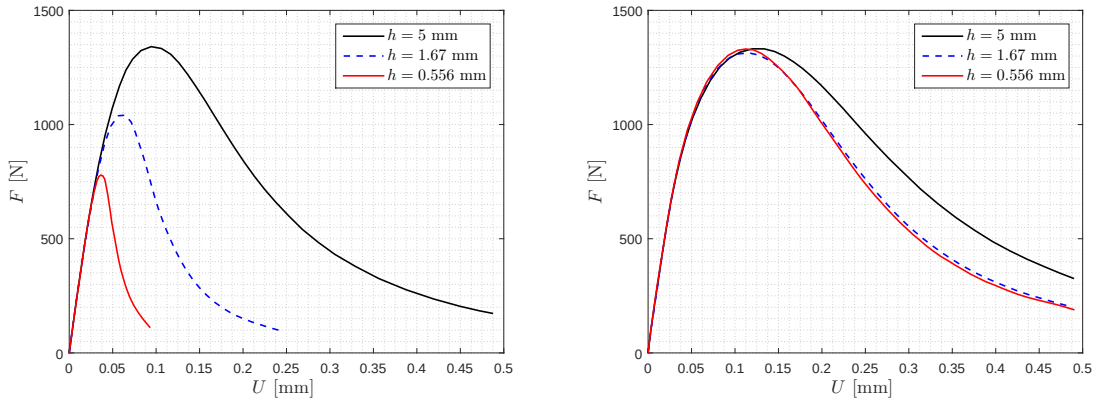

(a) Local damage model.

(b) Regularized damage model.

Figure 1.13 – Local and regularized damage models: response of a concrete three-point bending beam [Jirásek, 2004].

- A Cosserat continuum or a micropolar model (see, e.g., [Lakes et al., 1990, Borst, 1991]) that involves a higher-order continuum model, and an associated internal length scale regularizing the energy of the system across the mesh.
- An artificial viscosity technique [Etse and Willam, 1999].
- Gradient Enhanced Damage (GED) models [Peerlings et al., 1996].
- An integral-type regularization [Bažant and Pijaudier-Cabot, 1988, JiráSek, 2007, Bažant and Oh, 1983] where a convolution operator is used to regularize the strain field.
- Higher-order gradients of deformation [Needleman, 1988, Needleman, 1990, Bourdin et al., 2000, Karma et al., 2001, Miehe et al., 2010a].

An illustration of this regularization of damage model on the mechanical response compared to the classical damage model is depicted in the right panel in Fig. 1.13.

Pros and cons of these methods have been discussed in [Borst et al., 1993]. Among these techniques, the last two are the most used in computational analysis and are called regularization techniques. A very popular method in this context is the so-called phase field method to fracture [Bourdin et al., 2000, Karma et al., 2001, Miehe et al., 2010a], which will be detailed in the sequel and used in this thesis.

1.3.4.2 Phase Field (PF) method

The so-called "phase field method" presented in the following is a non-local damage method which has been initiated by different communities in both physics and mechanics. The name "phase field" comes from the fact that in the physics community, this approach has been developed following the well-known material phase change models with smeared interfaces (see below) to describe the transition between an undamaged phase and a damaged phase in the material, mimicking the transition between one material phase to another one. In the mechanics community, the technique has been developed from the concept of variational approach to fracture, as presented below. Both origins of the method are energetic minimization concepts. In what follows, we present the main ideas and ingredients of the method. Recent and complete reviews on phase field methods can be found e.g. in [Ambati et al., 2015] or [Wu et al., 2018].

Variational approach to fracture

The variational approach to fracture has been originally proposed by [Francfort and Marigo, 1998]. The method has been recast in a regularized form by [Bourdin et al., 2000] and is nowadays called phase field method by most authors [Kuhn and Müller, 2008, Miehe et al., 2010a]. While in its original form the method estimated the energy based on unknown sharp discontinuities, the regularized approach uses a continuous (called damage) field to describe the discontinuities thanks to a Mumford - Shah functional as proposed in [Ambrosio and Tortorelli, 1990], which gratefully simplifies the minimization process with respect to both displacements and damage fields. The regularization process involves a parameter ℓ, which defines an internal length variable. The obtained models are close to gradient-enhanced damage models [Borst and Verhoosel, 2016] but differ regarding the following points: (a) a convergence to the variational principle embedding true discontinuities as the internal length tends to zero; (b) an algorithmic structure where the damage field is obtained by solving a global problem over the structure.

In the following, we describe the equations describing the model of fracture for each homogeneous phase of the fully heterogeneous medium, defined in an open domain $\Omega \subset \mathbb{R}^D$, where D denotes the space dimension. The corresponding boundary of Ω is denoted by $\partial\Omega$, where $\partial\Omega = \partial\Omega_u \cup \Omega_F$, $\partial\Omega_u \cap \Omega_F = \emptyset$, where traction forces $\mathbf{F}^*$ are prescribed over the boundary $\partial\Omega_F$ and displacements $\mathbf{u}^*$ are prescribed over the boundary $\partial\Omega_u$ (see Fig. 1.14).

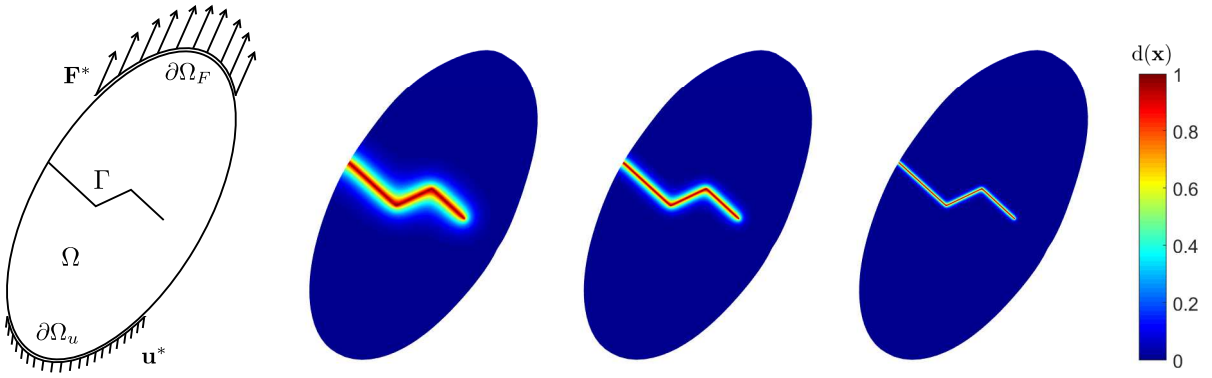

(a) (b): $\ell \sim (1/10)$ L (c): $\ell \sim (1/20)$ L (d): $\ell \sim (1/50)$ L

Figure 1.14 – (a) sharp description of a cracked solid; (b), (c), (d): smeared description within the phase field framework (damage profiles $d \in (0, 1)$ for different regularization lengths ℓ).

The solid may contain cracks denoted collectively as Γ. The total energy of the system is defined, in the absence of body forces, as:

$$E = \int_\Omega \Psi(\boldsymbol{\varepsilon}, \Gamma) d\Omega + g_c \int_\Gamma d\Gamma - \int_{\partial\Omega_F} \mathbf{F}^* \cdot \mathbf{u} d\Gamma \ , \tag{1.25}$$

where $\Psi(\boldsymbol{\varepsilon}, \Gamma)$ is the elastic strain density function and g_c is the critical energy release rate in the sense of Griffith. A regularized form is given by [Bourdin et al., 2000, Miehe et al., 2010a]:

$$E = \int_\Omega \Psi(\boldsymbol{\varepsilon}, d) d\Omega + g_c \int_\Omega \gamma(d, \nabla d) d\Omega - \int_{\partial\Omega_F} \mathbf{F}^* \cdot \mathbf{u} d\Gamma \ , \tag{1.26}$$

where γ denotes the crack density function, $g(d)$ is a degradation function such that $g(0) = 1$, $g(1) = 0$ and $g'(1) = 0$ and Ψ is an elastic strain density function (see examples in the following).

The variational approach to fracture as proposed in Bourdin, Francfort and Marigo [Francfort and Marigo, 1998, Bourdin et al., 2000, Bourdin et al., 2008] and developed in a convenient algorithmic setting by Miehe [Miehe et al., 2010a], and is presented here. The phase field formulation implies: (a) minimization of the total energy with respect to the displacement field $\mathbf{u}$ and (b) minimization of the energy with respect to the scalar field d describing the crack surface in a smooth manner. This second minimization is subjected to an inequality constraint: $\dot{d} \geq 0$. To formulate this minimization problem in a simpler setting, a time-stepping $\mathcal{T} = \{t^0, t^1, ..., t^n, t^{n+1}, ..., t^N\}$ is introduced. At each time step t^{n+1}, the problem is to find the displacement field $\mathbf{u}^{n+1}$ and damage field d^{n+1} such that

$$\mathbf{u}^{n+1}, d^{n+1} = \underset{\substack{\mathbf{u}\in\mathcal{S}_{\boldsymbol{u}} \\ 0\leq d^n \leq d^{n+1}}}{\text{Arg min}} \; E \; , \tag{1.27}$$

where $\mathcal{S}_{\boldsymbol{u}}$ is a set of kinematically admissible fields. One possible algorithm (see further discussion below) to solve this problem is to use sequential solving of the two following minimization problems:

$$D_{\delta\mathbf{u}} \; \mathscr{L} = 0 \; , \tag{1.28}$$

$$D_{\delta d}\mathscr{L} = 0, \quad 0 \leq d^n \leq d^{n+1} \; , \tag{1.29}$$

where $D_{\delta\mathbf{v}} f(\mathbf{u})$ is the Gateaux (directional) derivative, defined by:

$$D_{\delta\mathbf{v}} f(\mathbf{u}) = \left\{ \frac{f}{d\alpha} (\mathbf{u} + \alpha \; \delta\mathbf{v}) \right\}_{\alpha=0} \; . \tag{1.30}$$

The first equation (1.28) defines the mechanical problem, whereas the second one (1.29) defines the so-called phase-field problem.

Link with material phase field

The phase field approach has been derived independently within the Physics community, by considering the damage process as a phase transition between a sound phase and a damaged phase. To develop this idea, [Aranson et al., 2000] introduced the following free energy functional:

$$\Psi = \int_\Omega \left(D_{\delta\xi} |\nabla\xi|^2 + \phi\xi \right) d\Omega \; , \tag{1.31}$$

where $\xi = (1 - d)$, $d \in [0, 1]$ describes the phase in the domain $(d = 0)$ outside of the crack and $(d = 1)$ within the crack, $D_{\cdot}$ denoting the directional derivative and ϕ being a polynomial function. This formulation leads to a time crack evolution problem, defined as:

$$\dot{d} = -D_{\delta\xi}\Delta\phi + \phi(d)[\alpha_1(1 + (tr(\varepsilon) - \alpha_2)\phi - \gamma\dot{u})\nabla\phi] \; , \tag{1.32}$$

where α_i is a model parameter and $\ll . \gg$ is the temporal derivative operator. This formulation of the free energy was enriched in [Karma et al., 2001], by integrating the balance momentum equation, by changing the stress/strain relationship and crack evolution, and by defining the form of the energy functional as

$$\Psi(\boldsymbol{u}, d) = \int_\Omega [g(d)(\psi_0(\nabla(\boldsymbol{u})) - \psi_c) + V(\xi) + \frac{1}{2} D_{\delta\xi} |\nabla\xi|^2] d\Omega \; , \tag{1.33}$$

where g is a function coupling elasticity and damage. Above, V is a double-well potential, ψ_c is a critical strain energy, and ψ_0 the elasticity part subjected to some different model as:

$$\begin{cases} \psi_0 = \boldsymbol{\varepsilon} : \mathbb{C} : \boldsymbol{\varepsilon} \ , \ \text{[Karma, 2001]} \\ \psi_0 = \mathbb{1}(tr\boldsymbol{\varepsilon}^+)\psi_0 + \mathbb{1}(tr\boldsymbol{\varepsilon}^-)(\psi_0 - \frac{1}{2}\alpha k(tr(\boldsymbol{\varepsilon}))^2) \ , \ \text{[Henry and Levine, 2004]} \end{cases} \tag{1.34}$$

where k is the bulk modulus, α a scalar parameter ($\alpha > 1$) guarantying a safe material under compression and $\mathbb{1}(tr\boldsymbol{\varepsilon}^+) = 1$, if $tr(\epsilon) > 0$ (0 otherwise) respectively $\mathbb{1}(tr\boldsymbol{\varepsilon}^-) = 1$, if $tr(\epsilon) < 0$ (0 otherwise). The two models are subject to mode III fracture [Karma, 2001] and mode I & II fracture [Henry and Levine, 2004].

The phase field method has several crucial advantages as compared to other numerical methods for crack modeling. Specifically:

(i) The initiation of cracks from undamaged structures or materials can be handled.

(ii) Branching and merging of cracks are naturally taken into account.

(iii) Arbitrary geometrical configurations of crack networks can be treated (see, e.g., Fig. 1.15).

(iv) The phase field problem defined with the first-order damage gradient can be solved with classical finite elements, without modifying existing codes.

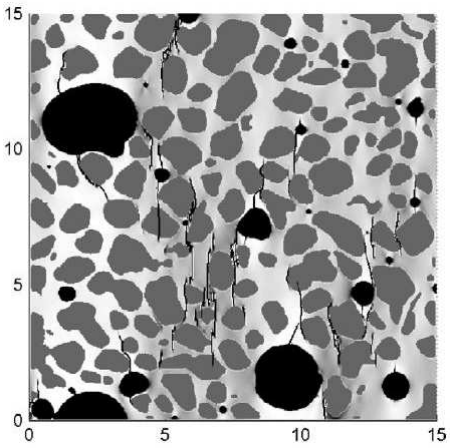

Figure 1.15 – Multiple, complex cracks networks in a model concrete sample simulated by the phase field [Nguyen et al., 2016a]).

One drawback which can be reported is the requirement of a fine mesh along the crack path. The definition of a suitable crack density function, the treatment of self-contact within the crack and the definition of a proper degradation function constitute key ingredients of the phase field formulation. These aspects are reviewed below.

Definition of a crack density function

Many choices are possible regarding the definition of the crack density function γ in (1.26). In [Wu, 2017], a general definition was introduced as:

$$\gamma(d, \nabla d) = \frac{1}{c_0}\left[\frac{2}{\ell}\mathscr{D}(d) + \frac{\ell}{2}|\nabla d|^2\right] \ , \tag{1.35}$$

where c_0 a scaling parameter and $\mathscr{D}$ is a function that characterizes the distribution of the smooth cracks, with $c_0 = 4\int_0^1 (\mathscr{D}(x))^{1/2} dx$. The function $\mathscr{D}$ is expressed as

$$\mathscr{D}(d) = \xi d + (1-\xi)d^2 \ , \tag{1.36}$$

where $\xi \in [0,2]$ is a scalar parameter, and $\mathscr{D}(d) \in [0,1]\ \forall d \in [0,1]$. In this context, the profile of the diffused damaged normal to the crack is defined in 1D according to

$$d(\boldsymbol{x}) = \text{Argmin}\left(\int_{\Omega^*} \gamma(d, \nabla(d)) d\Omega \right) \ , \tag{1.37}$$

where d is define on its domain Ω^*. Several particular cases of this framework can be found in the literature.

- The choice $\mathscr{D}(d) = d^2$ and $\xi = 0$ is widely used in the literature [Bourdin et al., 2000] and leads to
$$\gamma(d, \nabla d) = \frac{1}{2}\left(\frac{1}{\ell} d^2 + \ell \nabla(d) \cdot \nabla(d) \right) \ . \tag{1.38}$$
The corresponding 1D profile is then given by $d(\boldsymbol{x}) = \exp(-|\boldsymbol{x}|/\ell)$.

- The definition $\mathscr{D}(d) = d$ and $\xi = 1$ considered in [Pham et al., 2011] yields
$$\gamma(d, \nabla d) = \frac{8}{3}\left(\frac{1}{\ell} d + \ell |\nabla d|^2 \right) \ . \tag{1.39}$$
This form induces a linear part of the response before failure.The 1D profile is given by $d(\boldsymbol{x}) = (1 - (|\boldsymbol{x}|/2\ell))^2\ \forall \boldsymbol{x} \in \Omega^* = [-2\ell, 2\ell]^3$.

- The case $\mathscr{D}(d) = 2d - d^2$ and $\xi = 2$ was proposed in [Wu, 2017] and gives
$$\gamma(d, \nabla d) = \frac{1}{\pi}\left(\frac{1}{\ell} (2d - d^2) + \ell |\nabla d|^2 \right) \ . \tag{1.40}$$
The 1D profile of the damage is a sinus function $d(\boldsymbol{x}) = 1 - \sin(|x|/\ell)\ \forall \boldsymbol{x} \in \Omega^* = [-\pi\ell/2, \pi\ell/2]^3$.

- An extension involving higher-order gradients was introduced in [Borden et al., 2014] as
$$\gamma(d, \nabla d) = \frac{1}{2}\left(\frac{1}{\ell} d^2 + \frac{\ell}{2} \nabla(d) \cdot \nabla(d) + \frac{\ell^3}{16} \Delta^2(d) \right) \ . \tag{1.41}$$
This form leads to a more regular damage profile given in 1D by $d(\boldsymbol{x}) = \exp(-|\boldsymbol{x}|/2\ell)(1 + |\boldsymbol{x}|/(2\ell))$. The main drawback of this choice is that C^1 continuity is required for the finite element scheme, which may increase the computational complexity, especially in 3D.

These examples of regularization are illustrated in Fig. 1.16 (left). The reader is referred to [Wu et al., 2018] for an extensive list of regularized functions. Note that each model of regularization introduces the regularization parameter ℓ. The value of ℓ depends on the critical stress value and the degradation function affecting the maximal force response (see the right panel in Fig. 1.16, based on [Kuhn et al., 2015]; see also Table 1.3.1.2). A discussion on the choice of ℓ can be found in, e.g., [Nguyen et al., 2016b].

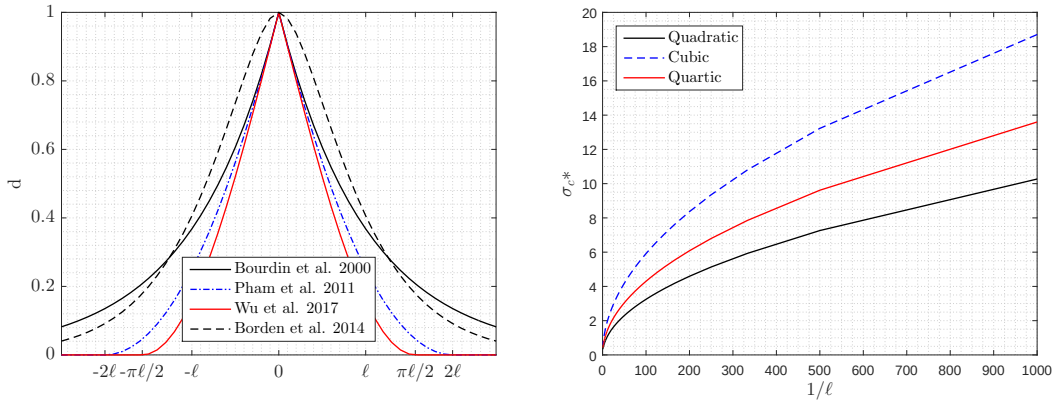

Different crack density functions. Critical stress with respect to ℓ.

Figure 1.16 – Influence of the crack density function and of parameter ℓ.

Treatment of self-contact (strain split)

To describe the difference between compressive and tensile damage and to model self-contact within the crack, the strain density function can be split into two parts as:

$$\Psi = \Psi^+ + \Psi^- \ , \tag{1.42}$$

where Ψ^+ and Ψ^- will be defined momentarily. The idea is then to associate damage with the "positive" part only, according to:

$$\Psi = g(d)\Psi_0^+ + \Psi^- \ , \tag{1.43}$$

where Ψ_0^+ denotes the positive part of the strain density energy for the undamaged material, and g is a degradation function that depends on the damage parameter d. Several choices were proposed for such a decomposition in the case of isotropic damage:

- [Amor et al., 2009] proposed a decomposition based on the spherical and deviatoric parts of the strain tensor (denoted as $\boldsymbol{\varepsilon}_H$ and $\boldsymbol{\varepsilon}_D$ respectively). In this model the damage is generated by a positive spherical and deviatoric strain.

$$\Psi^+(\boldsymbol{\varepsilon}) = \frac{1}{2}k[tr(\boldsymbol{\varepsilon})]^2 + \mu\boldsymbol{\varepsilon}_D : \boldsymbol{\varepsilon}_D \ , \quad \Psi^-(\boldsymbol{\varepsilon}) = \frac{1}{2}k[-tr(\boldsymbol{\varepsilon})]^2 \ , \tag{1.44}$$

  where k and μ are the bulk and shear moduli, and $tr(.)$ is the trace operator. This choice introduces damage for the positive hydrostatic strain ($\boldsymbol{\varepsilon}_H := tr(\boldsymbol{\varepsilon})/n$, n the spatial dimension) only, while the deviatoric part ($\boldsymbol{\varepsilon}_D := \boldsymbol{\varepsilon} - \boldsymbol{\varepsilon}_H$) does not induce damage:

$$\boldsymbol{\sigma} = g(d)\mathbb{1}_{(\boldsymbol{\varepsilon}_H^+)}[k\boldsymbol{\varepsilon}_H + 2\mu\boldsymbol{\varepsilon}_D] + \mathbb{1}_{(\boldsymbol{\varepsilon}_H^-)}[k\boldsymbol{\varepsilon}_H] \ , \tag{1.45}$$

  where $\mathbb{1}(\boldsymbol{\varepsilon}_H^+) = 1$ if $\boldsymbol{\varepsilon}_H^+ > 0$ (0 otherwise) and $\mathbb{1}(\boldsymbol{\varepsilon}_H^-) = 1$ if $\boldsymbol{\varepsilon}_H^+ < 0$ (0 otherwise) and λ and μ denote the elastic Lamé constants.

- [Miehe et al., 2010a] introduced another model, based on the spectral decomposition of the strain tensor:

$$\Psi^{\pm}(\boldsymbol{\varepsilon}) = \frac{\lambda}{2}\left(\langle Tr\,(\boldsymbol{\varepsilon})\rangle^{\pm}\right)^2 + \mu Tr\left\{\left(\boldsymbol{\varepsilon}^{\pm}\right)^2\right\} \ , \tag{1.46}$$

where λ and μ are the Lamé constants. In Eq. (1.46), $\boldsymbol{\varepsilon}^+$ and $\boldsymbol{\varepsilon}^-$ are such that $\boldsymbol{\varepsilon} = \boldsymbol{\varepsilon}^+ + \boldsymbol{\varepsilon}-$ and are defined by

$$\boldsymbol{\varepsilon}^{\pm} = \sum_{i=1}^{m} < \kappa_i >^{\pm} \boldsymbol{\varphi}^{(i)} \otimes \boldsymbol{\varphi}^{(i)} \ , \tag{1.47}$$

in which $\{(\kappa_i, \boldsymbol{\varphi}^{(i)})\}_{i=1}^{m}$ are the pairs of associated eigenvalues and eigenvectors of the strain tensor $\boldsymbol{\varepsilon}$, and $< \cdot >^{\pm}$ is the operator given by

$$< z >^{\pm} = \frac{1}{2}(z \pm |z|) \ , \quad \forall z \in \mathbb{R} \ . \tag{1.48}$$

Within this scheme, the stress tensor is derived according to:

$$\sigma = g(d)\mathbb{1}(tr(\boldsymbol{\varepsilon}^+))[\lambda tr(\boldsymbol{\varepsilon}) + 2\mu\boldsymbol{\varepsilon}^+] + \mathbb{1}(tr(\boldsymbol{\varepsilon}^-))[\lambda tr(\boldsymbol{\varepsilon}) + 2\mu\boldsymbol{\varepsilon}^-] \ . \tag{1.49}$$

- [He and Shao, 2019] new failure model is based on the decomposition of the strain tensor into two complementary parts, which are orthogonal in the sense of an inner product where both fourth-order elastic stiffness and compliance tensors act as metric operators. Let $\mathbb{C}$ be the fourth-order stiffness tensor, the traction (denoted by $(.)^+$) and compression parts (denoted by $(.)^-$) of the strain energy density can be expressed by

$$\psi^{e\pm}(\boldsymbol{\varepsilon}) = \frac{1}{2}\left[\boldsymbol{\varepsilon}^{\pm} : \mathbb{C} : \boldsymbol{\varepsilon}^{\pm}\right] \ . \tag{1.50}$$

This model can be applied to arbitrary initial anisotropic elastic behavior, in contrast to the above other models.

The orthogonality condition for the positive/negative parts $\boldsymbol{\varepsilon}^{\pm}$ can be defined as follows

$$\boldsymbol{\varepsilon}^+ : \left(\mathbb{C} : \boldsymbol{\varepsilon}^-\right) = \left(\mathbb{C} : \boldsymbol{\varepsilon}^+\right) : \boldsymbol{\varepsilon}^- = 0 \ . \tag{1.51}$$

The requirement described in Eq. (1.51) can be ensured through a method based on elastic energy preserving transformation. Within this framework, the square root of the elastic stiffness tensor is introduced

$$\mathbb{C}^{1/2} = \sum_i \Lambda_i^{1/2} \boldsymbol{\omega}_i \otimes \boldsymbol{\omega}_i \quad \text{and} \quad \mathbb{C}^{-1/2} = \sum_i \Lambda_i^{-1/2} \boldsymbol{\omega}_i \otimes \boldsymbol{\omega}_i \ , \tag{1.52}$$

where Λ_i are the eigenvalues of $\mathbb{C}$, and $\boldsymbol{\omega}_i$ are second-order eigentensors associated to Λ_i. Defining $\tilde{\boldsymbol{\varepsilon}}^{\pm}$ as the positive and negative parts of $\mathbb{C}^{1/2} : \boldsymbol{\varepsilon}$, we compute $\boldsymbol{\varepsilon}^{\pm}$ by

$$\boldsymbol{\varepsilon}^{\pm} = \mathbb{C}^{-1/2} : \tilde{\boldsymbol{\varepsilon}}^{\pm} \ . \tag{1.53}$$

The derivatives of $\tilde{\boldsymbol{\varepsilon}}^{\pm}$ with respect to the transformed strain tensor $\tilde{\boldsymbol{\varepsilon}}$ also define two projection tensors $\tilde{\mathbb{P}}^{\pm}(\tilde{\boldsymbol{\varepsilon}}) = \partial_{\tilde{\boldsymbol{\varepsilon}}}[\tilde{\boldsymbol{\varepsilon}}^{\pm}(\tilde{\boldsymbol{\varepsilon}})]$, which can be determined following the approach proposed by Miehe [Miehe, 1998]. This implies the complete formulation for the proposed decomposition scheme as follows

$$\boldsymbol{\varepsilon}^{\pm} = \left[\mathbb{C}^{-1/2} : \left(\tilde{\mathbb{P}}^{\pm} : \ \mathbb{C}^{1/2}\right)\right] : \boldsymbol{\varepsilon} \ . \tag{1.54}$$

Compared to the scheme proposed by Miehe et al. [Miehe et al., 2010a], this model is computationally more efficient due to the very simple and analytical expressions of the different operators, which do not require numerical evaluation of eigenvalues and eigenvectors of the strain tensor.

In this framework, the Cauchy stress $\boldsymbol{\sigma}$ is obtained as

$$\boldsymbol{\sigma}(\boldsymbol{\varepsilon}, d) = g(d)\ \frac{\partial \psi^{e+}(\boldsymbol{\varepsilon})}{\partial \boldsymbol{\varepsilon}} + \frac{\partial \psi^{e-}(\boldsymbol{\varepsilon})}{\partial \boldsymbol{\varepsilon}} = \mathbb{C}(d) : \boldsymbol{\varepsilon}\ . \tag{1.55}$$

From (1.54) and by introducing $\mathbb{P}^{\pm} = \mathbb{C}^{-1/2} : \left(\tilde{\mathbb{P}}^{\pm} :\ \mathbb{C}^{1/2}\right)$, the general form of the elastic tensor accounting for damage is defined by

$$\mathbb{C}(d) = g(d)\ \mathbb{P}^{+} : \mathbb{C} : \mathbb{P}^{+} + \mathbb{P}^{-} : \mathbb{C} : \mathbb{P}^{-}\ . \tag{1.56}$$

An illustrative example for a shear test is presented to demonstrate the impact of the aforementioned modeling choices on both the mechanical response (see Fig. 1.17) and crack propagation (see Fig. 1.18). This three force response tests have been performed until the crack affected the boundary of the domain for the Miehe's model.Concerning the shear tests, the strains (positive and negative) are localized axisymmetrically along the pre-crack axis. As the first damage model [Bourdin et al., 2000] affected all the strain energy (positive and negative), the crack propagates symmetrically and diagonally. For the [Amor et al., 2009] damage model, the crack only propagates on the positive hydrostatic and deviatoric strain energy. It has been noted that this model generated side effects. For the last model [Miehe et al., 2010a] example, the damage is activated only by positive (traction) part of strain energy and explain why as the previous model the crack propagate diagonally.

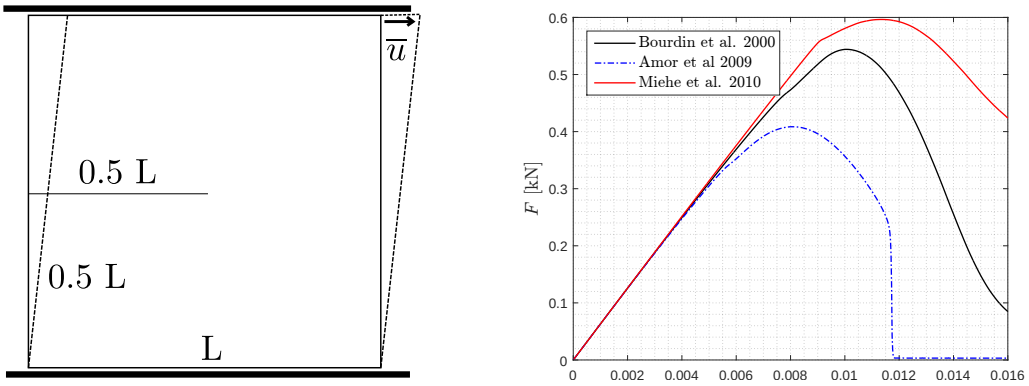

Shear test. Mechanical response.

Figure 1.17 – Shear test setting (left) and mechanical response of the concrete material parameter (right).

Definition of the degradation function

Several choices can also be made for the degradation function g. The latter is required to satisfy the following conditions:

- $g(0) = 1$ and $g(1) = 0$ must hold to ensure that the material is initially undamaged and ultimately, fully damaged, respectively.

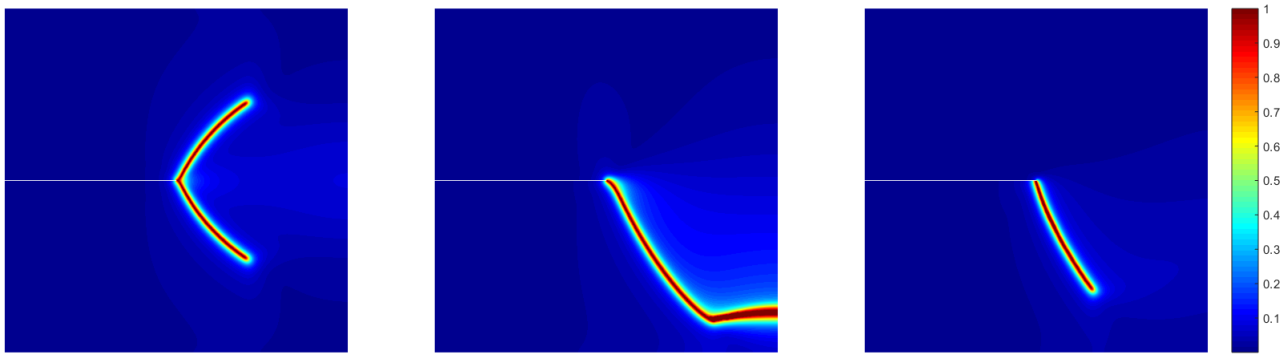

[Bourdin et al., 2000] [Amor et al., 2009] [Miehe et al., 2010a]

Figure 1.18 – Damage fields associated with the shear test, obtained with three different formulations.

- $g'(1) = 0$ must hold to ensure a finite value of the stress at the crack tip.

- g must be monotonically decreasing to ensure damage decrease away from the crack.

Many degradation functions satisfying these conditions have been proposed in the literature. [Bourdin et al., 2000] have used a quadratic polynomial function borrowed from [Ambrosio and Tortorelli, 1990]. Higher-order (quadratic, cubic, and quartic) polynomial degradation functions were studied in [Kuhn et al., 2015], and the impact on the mechanical response is illustrated in Fig. 1.19. Note that plastic softening can be taken into account in the formulation proposed

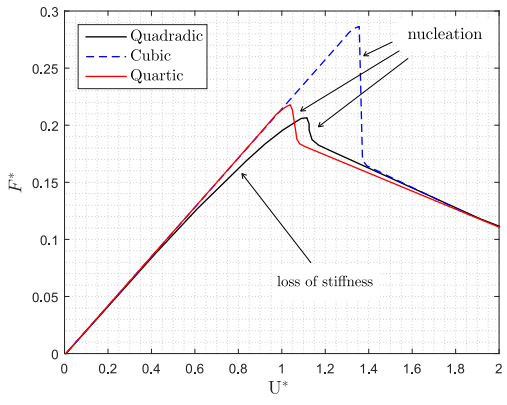

Figure 1.19 – Influence of the degradation function g on the material response $U^* \mapsto F^*(U^*)$, where F^* is the adimensional force response and U^* denotes displacement.

in [Borden et al., 2016]. Some examples of degradation functions are listed below.

Degradation function	Reference
$g(d) = (1-d)^2$	[Bourdin et al., 2000]
$g(d) = (3-s)(1-d)^2 - (2-s)(1-d)^3$	[Borden et al., 2016]
$g(d) = (1-d)^2$ (quadratic)	[Kuhn et al., 2015]
$g(d) = 3(1-d)^2 - 2(1-d)^3$ (cubic)	[Kuhn et al., 2015]
$g(d) = 4(1-d)^3 - 3(1-d)^4$ (quartic)	[Kuhn et al., 2015]
$g(d) = \frac{1-d}{1-d+md}$ (quasi-linear, $m \geq 1$)	[Geelen et al., 2019]
$g(d) = \frac{(1-d)^2}{(1-d)^2+md(1+pd)}$ (quasi-quadratic $p \geq 1$)	[Lorentz, 2017]

Table 1.1 – Degradation function examples.

Note that the degradation function may include a small regularizing parameter $0 < \eta \ll 1$, introduced to ensure the well-posedness of the boundary value problem. In this case, a modified function g^* such that $g^*(d) = g(d) + \eta$ is considered ([Miehe et al., 2010b] shows the impact of the η parameter on the post-rupture mechanical response). Other solutions can be found for that purpose, such as in [Lorentz, 2017] and [Geelen et al., 2019].

Chapter 2

Stochastic Multiscale Modeling of Crack Propagation in Random Media

Contents

2.1 Introduction

Since microstructural randomness strongly impacts the macroscopic response of (quasi-)brittle materials in various ways, ranging from size effects [Bazant and Planas, 1997, Bažant and Novák, 2000, van Vliet and van Mier, 2000, Genet et al., 2014] to high stochasticity in failure patterns and ultimate properties [Tregger et al., 2006, Daphalapurkar et al., 2011, Rahman and Chakraborty,

2011], the development of approaches incorporating multiscale and probabilistic ingredients all together is a natural path to extend the predictive capabilities in fracture simulations.

In this chapter, presented in [Hun et al., 2018, Hun et al., 2019a] and adapted from the published paper [Hun et al., 2019c], we propose a stochastic, multiscale-informed phase-field approach to model crack propagation in random quasi-brittle materials. The objective is to construct a "simplified" mesoscopic model which does not require an explicit description of fine scales heterogeneities, while retaining the stochastic features that allow reproducing the crack paths and response of the related structures. In the proposed framework, the parameters involved in the elasticity-phase-field formulation are specifically defined through multiscale analysis with non-separated scales. This particular setting ensures consistency with critical subscale information, and allows for the propagation of stochasticity at the macroscopic level. Similar ideas were pursed in the very recent work [Acton et al., 2018], with a few noticeable differences though. First, the approach developed in the above reference is concerned with dynamical fracture, solved using an asynchronous space-time discontinuous Galerkin method, and it is focused on fracture strength random fields. A phase-field approach to brittle fracture modeling is alternatively considered and extended here, in which validation is further assessed on a macroscopic quantity of interest. Second, and while both contributions invoke information theory as a rationale to define probability measures, stochastic modeling aspects and related methodological issues are addressed more extensively hereinafter. Note also that crack paths are simulated in the sequel by propagating a pre-existing crack, whereas crack nucleation sites are identified, for each sample of the microstructure, as the weakest material points in [Acton et al., 2018].

This chapter is organized as follows. The computational approach enabling the description of crack propagation at the microscopic scale is first detailed in Section 2.2. The phase field formulation with mesoscopic descriptors (elasticity and damage) is then introduced, and some results comparing the mechanical response and the crack paths at micro and meso-scale are presented in Section 2.3. Stochastic methodologies to represent and subsequently identify the mesoscopic descriptors are introduced and applied to the aforementioned microstructure. The relevance of the framework is finally assessed by comparing macroscopic predictions based on either the reference microscopic model or the proposed mesoscopic stochastic modeling.

2.2 Microscopic Crack Propagation

In this section, we define the random heterogeneous microstructures studied in this work and describe the Monte Carlo approach used to generate realizations of crack paths at the microscale. Governing equations for the crack propagation problem are introduced within the phase field method, in the continuity of Section 1.3.4.2. These realizations will be used, in Section 2.4.1, to identify a mesoscale stochastic model constructed in Section 2.3.2.1.

2.2.1 Generation of heterogeneous random microstructures

In order to illustrate the methodology, a prototypical stationary, isotropic random microstructure made up of a homogeneous matrix and monodisperse spheres is selected hereinafter ($N_p \in \{1, 2\}$ is defined as a phase index). A two-dimensional square domain $\Omega =]0, L[^2$ is considered, with $L = 1$ mm, and the radius of the inclusions is set to $R = 0.04 \times L$. Plane strain conditions are assumed. A set of $\theta^{obs} = 1000$ realizations was generated by using the molecular-dynamics-type algorithm (based on event-driven molecular dynamics [Donev et al., 2005]) used in [Skoge et al., 2006] for hard-sphere packings (under periodic boundary conditions). Each periodized

sample contains $N_{inc} = 50$ non-overlapping heterogeneities. Four independent realizations of this microstructure are shown in Fig. 2.1.

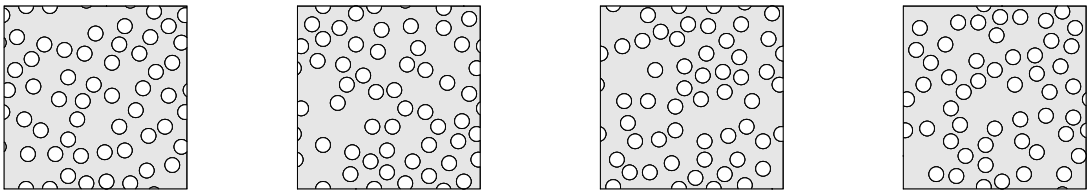

Figure 2.1 – Independent realizations of the periodized random microstructure.

2.2.2 Phase-field formulation

Using the phase-field framework to simulate crack propagation, variation of (1.26) with respect to $\mathbf{u}$ and d leads to the coupled equations:

$$\begin{cases} \dfrac{g_c}{\ell}(d - \ell^2 \Delta d) - 2(1-d)\mathscr{H}(\boldsymbol{\varepsilon}) = 0 \ , \\ \boldsymbol{\nabla} \cdot \boldsymbol{\sigma}(\boldsymbol{u}, d) = \mathbf{0} \ , \end{cases} \tag{2.1}$$

Where $\nabla \cdot (.)$ is the divergence operator. It should be noted that the elastic energy density Ψ uses the model (1.46), the crack description follows the model (1.38) and a displacement boundary problem is only considered ($\boldsymbol{F}^* = \mathbf{0}$). $\mathscr{H}$ is a strain density history function, used to prescribe damage irreversibility [Miehe et al., 2010a]:

$$\mathscr{H}(\mathbf{x}, t) = \max_{\tau \in [0,t]} \left\{ \Psi^+ (\boldsymbol{x}, \tau) \right\} \ . \tag{2.2}$$

For an isotropic medium, the stress tensor for the damaged material reads as

$$\boldsymbol{\sigma}(\boldsymbol{u}, d) = \frac{\partial \Psi}{\partial \boldsymbol{\varepsilon}} = g(d)\mathbb{1}(tr(\boldsymbol{\varepsilon}^+))[\lambda Tr(\boldsymbol{\varepsilon}) + 2\mu\boldsymbol{\varepsilon}^+] + \mathbb{1}(tr(\boldsymbol{\varepsilon}^-))[\lambda Tr(\boldsymbol{\varepsilon}) + 2\mu\boldsymbol{\varepsilon}^-] \ .$$

The system of equations (2.1) is complemented by the following boundary conditions

$$\begin{cases} \boldsymbol{u} = \boldsymbol{u}_D \text{ on } \partial\Omega_u \ , \\ \boldsymbol{\sigma}\boldsymbol{n} = \boldsymbol{F}^* \text{ on } \partial\Omega_F \ , \\ \boldsymbol{\nabla} d \cdot \mathbf{n} = 0 \text{ on } \partial\Omega \ , \end{cases} \tag{2.3}$$

where $\nabla(.)$ is the gradient operator, $\boldsymbol{u}_D$ and $\boldsymbol{t}_N$ are prescribed vector fields of displacements and tractions, and $\boldsymbol{n}$ is the outward-pointing normal vector on $\partial\Omega$ (see Fig. 1.14 (a)).

The classical weak form associated with Eq. (2.1) is given by

$$\begin{cases} \displaystyle\int_\Omega \left\{ \left(2\mathscr{H} + \frac{g_c}{\ell} \right) d\delta d + g_c \ell \nabla d \cdot \nabla(\delta d) \right\} d\Omega = \int_\Omega 2\mathscr{H}\delta d d\Omega \ , \\ \displaystyle\int_\Omega \boldsymbol{\sigma}(\boldsymbol{u}, d) : \boldsymbol{\varepsilon}(\delta \boldsymbol{u}) d\Omega = \int_{\partial\Omega_t} \boldsymbol{t}_N \cdot \delta \boldsymbol{u} dS \ , \end{cases} \tag{2.4}$$

where $(\delta d, \delta \boldsymbol{u})$ are test functions belonging to appropriate functional spaces. It should be noticed that in the phase field method, crack propagation is described through the evolution of the

damage field $\boldsymbol{x} \mapsto d(\boldsymbol{x})$, which is updated at each load step by solving the coupled equations (2.1) (under Eq. (2.3)). Algorithmic details on the method can be found in, e.g., [Miehe et al., 2010a, Nguyen et al., 2016b].

Notice that the definition of $\Psi^{\pm}$ in the phase field formulation (see (1.46)) encapsulates the stochastic aspect of the propagation, since the elasticity field corresponds (at microscale) to a realization of the elasticity tensor random field $\{\mathbb{C}(\boldsymbol{x}), \boldsymbol{x} \in \Omega\}$ given by

$$\mathbb{C}(\boldsymbol{x}) = \sum_{i=1}^{N_p} \mathbb{1}_{\Omega_p}(\boldsymbol{x}) \mathbb{C}^p \left(\lambda^p, \mu^p\right) \ , \tag{2.5}$$

where $\{\mathbb{1}_{\Omega_p}(\boldsymbol{x}), \boldsymbol{x} \in \Omega\}$ and $\mathbb{C}^i$ are the indicator function and elasticity tensor of phase p (assumed to be isotropic here), occupying the domain Ω_p. The couple of Lamé coefficients (λ_p, μ_p) is constant in each phase and follows the random spatial distribution of inclusions. Respectively we define the toughness random field as:

$$g_c(\boldsymbol{x}) = \sum_{i=1}^{N_p} \mathbb{1}_{\Omega_p}(\boldsymbol{x}) g_{c,p} \ . \tag{2.6}$$

For random microstructures, the indicator functions are, indeed, non-Gaussian random fields: in practice, it is thus required to proceed to Monte Carlo simulations of these fields, and to solve the coupled elasticity-phase-field problem for each realization of Ω. This strategy allows the variability in crack paths (and consequently, in the nonlinear part of the macroscopic response) to be simulated at microscale, as illustrated in the next section.

2.2.3 Statistical analysis of crack trajectories at microscale

In the simulations presented throughout this chapter, the constitutive materials are assumed isotropic, and the bulk and shear moduli are denoted as (k_m, μ_m) and (k_i, μ_i) for the matrix phase ($Np = 2$) and inclusions ($Np = 1$), respectively. Accordingly, $g_{c,m}$ and $g_{c,i}$ denote the toughness of the matrix and inclusions. These properties are chosen such that the mechanical contrast α satisfies $\alpha = k_i/k_m = \mu_i/\mu_m = g_{c,i}/g_{c,m}$, where the properties of the matrix are taken as $k_m = 175$ [GPa], $\mu_m = 81$ [GPa] and $g_{c,m} = 2.7 \times 10^{-3}$ [kN.mm^{-1}]. Dirichlet boundary conditions are applied in the form $\boldsymbol{u}_D(x_1, 0) = \boldsymbol{0}$ and $\boldsymbol{u}_D(x_1, L) = u_D \boldsymbol{e}^{(1)}$, for $0 \leqslant x_1 \leqslant L$, in which $\boldsymbol{e}^{(1)} = (1, 0)$ is the first vector of the canonical basis in $\mathbb{R}^2$ (note that $\partial\Omega_N = \emptyset$) and $u_D \in [0, \overline{u}_D]$ (the final displacement is taken for $\overline{u}_D = 2 \times 10^{-2}$[mm]); see Fig. 2.2. The incremental displacement value $\Delta u_D = 2 \times 10^{-5}$ [mm] is selected, and an initial crack is positioned as described in Fig. 2.2. These boundary conditions correspond to a pure shear loading (see Fig. 2.2), and the evolution of the damage field and displacement-force curve (associated with the microstructural sample shown in Fig. 2.2) can be seen in Figs. 2.3 and 2.4, for $\ell = 0.0075$ [mm] (in the two phases) and $\alpha = 10$. The finite element mesh adapted to this value of ℓ contains about $150,000$ (linear triangular) elements, with a mesh size comprised between 3×10^{-4} and 1.5×10^{-2} [mm]. As expected given the selected contrast in toughness, the crack exclusively propagates within the matrix phase.

Since the crack path Γ is, by definition, identified as the collection of points $\boldsymbol{x}^{\Gamma}$ for which $d \approx 1$, and upon restricting the analysis to configurations containing a single crack, the variability in the crack propagation generated by the underlying microstructural randomness can be observed by considering the stochastic process $\{x_1^{\Gamma}(x_2), x_2 \in \mathbb{X}_2\}$, in which $\mathbb{X}_2 \subseteq [0, 0.5]$. Likewise,

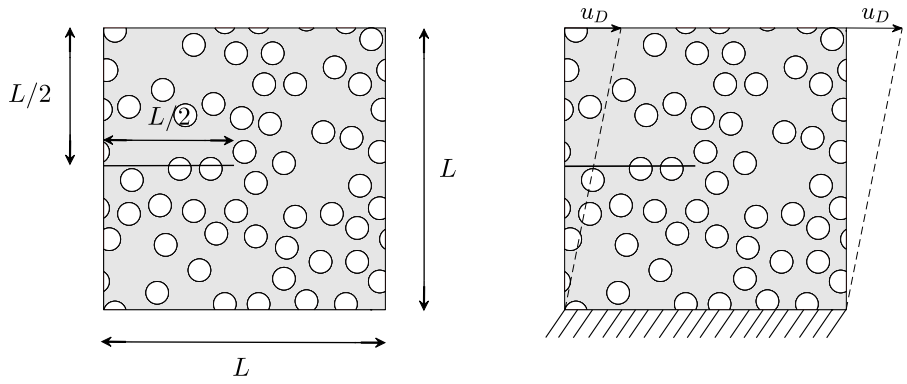

Figure 2.2 – Boundary conditions applied to the domain and initial crack.

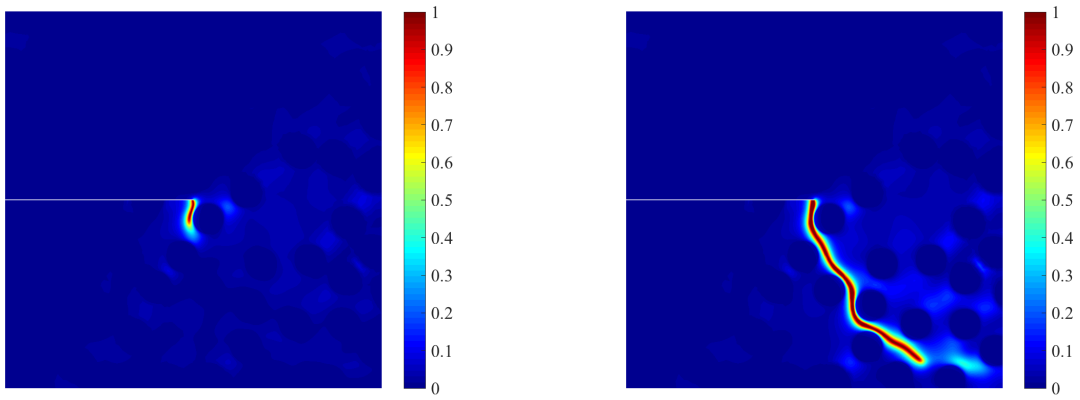

Figure 2.3 – Evolution of the damage field $\boldsymbol{x} \mapsto d(\boldsymbol{x})$ for the microstructure shown in Fig. 2.2.

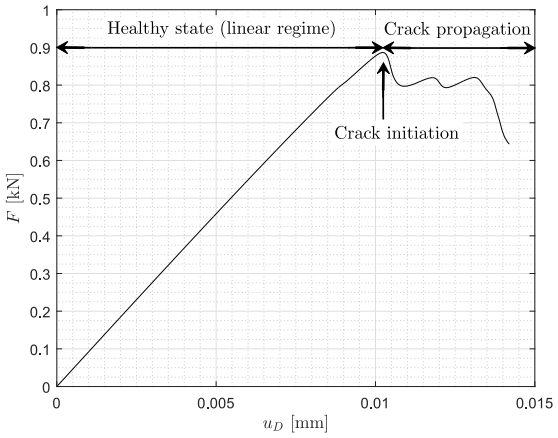

Figure 2.4 – Simulated displacement-force response for the microstructure shown in the left panel in Fig. 2.2.

the stochasticity induced on the macroscopic response can be characterized by computing the horizontal force on the top edge ($x_2 = L$) of the samples, denoted by F. The mean and standard deviations for these quantities of interest, together with sample-based envelopes are shown in Fig. 2.5.

In these figures, $u_D \mapsto \underline{F}(u_D) = E\{F(u_D)\}$ and $u_D \mapsto \sigma_F(u_D) = \sqrt{E\{F(u_D)^2\} - E\{F(u_D)\}^2}$ represent the mean and variance functions for the macroscopic force, and the statistical estimators and envelopes are obtained using 100 independent realizations of the microstructure. Similar notations are used for studying the second-order properties of the process $\{x_1^\Gamma(x_2), x_2 \in \mathbb{X}_2\}$.

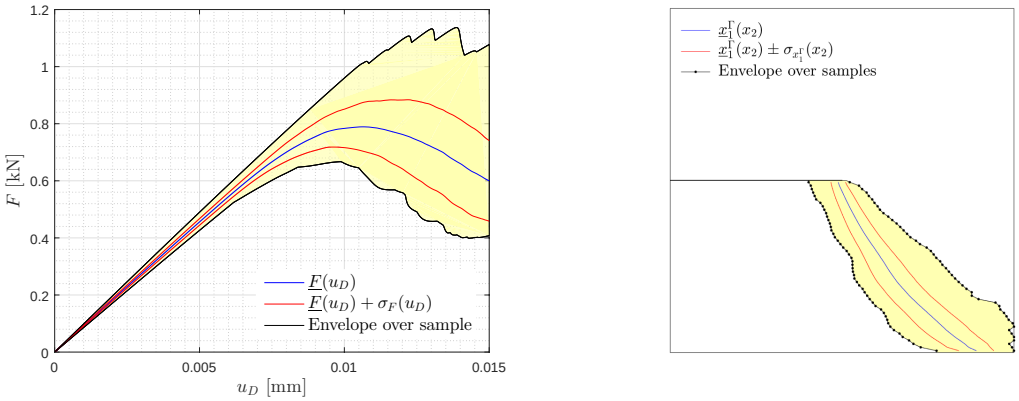

Figure 2.5 – Envelope, mean and standard deviation for the displacement-force curve (left) and the crack path (right).

2.3 Mesoscopic Modeling of Crack Propagation

In this section, we propose a "simplified" model of crack propagation at a mesoscopic scale where the piecewise constant fields of elastic properties defining the detailed microstructure are replaced by smooth approximations.

2.3.1 Phase-field formulation

In order to characterize crack propagation using coarse descriptors, we specifically introduce an *upscaled* version of the elasticity-phase-field problem as follows:

$$\begin{cases} \boldsymbol{\nabla} \cdot \boldsymbol{\sigma}(\boldsymbol{u}, \boldsymbol{d}) = \mathbf{0} \ , \\ \dfrac{\widetilde{g}_c}{\widetilde{\ell}}(d - \widetilde{\ell}^2 \Delta d) - 2(1-d)\widetilde{\Psi}^+(\boldsymbol{\varepsilon}) = 0 \ , \end{cases} \tag{2.7}$$

It should be noted that the choice to use the same formulation as in micro scale has been made. Only the parameters of the problem change. This study is part of an empirical, exploratory approach which aims to become an operational tool (insofar as there is no homogenization theory in fracture).

where the stress tensor

$$\boldsymbol{\sigma}(\boldsymbol{u}, \boldsymbol{d}) = g(d)\frac{\partial \widetilde{\Psi}^+(\boldsymbol{\varepsilon}(\boldsymbol{u}))}{\partial \boldsymbol{\varepsilon}(\boldsymbol{u})} + \frac{\partial \widetilde{\Psi}^-(\boldsymbol{\varepsilon}(\boldsymbol{u}))}{\partial \boldsymbol{\varepsilon}(\boldsymbol{u})} \tag{2.8}$$

is here expressed as a function of a new, mesoscopic stored energy function

$$\widetilde{\Psi}^\pm(\boldsymbol{\varepsilon}) = \boldsymbol{\varepsilon}^\pm : \widetilde{\mathbb{C}} : \boldsymbol{\varepsilon}^\pm \ , \tag{2.9}$$

in which $\boldsymbol{x} \mapsto \widetilde{\mathbb{C}}(\boldsymbol{x})$ is a mesoscopic elasticity tensor field, here chosen as isotropic (so that the negative/positive decomposition of Miehe can be used), $\widetilde{g}_c$ represents an equivalent toughness for the mesoscale medium and $\widetilde{\ell}$ is the characteristic length associated with the regularized description at the mesoscale. Note that the restriction related to isotropy could be alleviated by using the recent framework proposed in [He and Shao, 2019] (see Section 1.3.4.2): this decomposition was not explored hereafter, due to time constraints and to the fact that the assumption of isotropy is, indeed, reasonably accurate for the system under investigation (see Section 2.3.2.3).

Note that (i) this mesoscale model differs from a fully homogenized one, as it maintains some statistical fluctuations raised by microstructural randomness; (ii) the formulation remains predictive to study crack propagation, in contrast with an approach that would describe cracks through first-order, averaged characteristics (such as crack density).

In what follows, the definition of the mesoscopic elasticity and equivalent toughness is investigated through a two-step methodology:

- First, the definition of the elasticity field $\boldsymbol{x} \mapsto \widetilde{\mathbb{C}}(\boldsymbol{x})$ is achieved using a moving-window upscaling approach under different types of boundary conditions. This point is discussed in Section 2.3.2.1.
- Second, the definition of the toughness $\widetilde{g}_c$ is addressed in Section 2.3.3, where a statistical inverse problem involving the peak force at the macroscopic scale is introduced.

The results from the first step will be used, in Section 2.4.1, to construct a stochastic surrogate for the elasticity field. This model will enable us to draw additional samples of the mesoscopic elasticity field without having recourse to the homogenization solver.

2.3.2 Construction of mesoscopic elasticity

In this section, we define the technique used to construct a (smooth) mesoscopic definition of the heterogeneous elastic medium from fully detailed realizations of microstructures. Such an approach has been extensively discussed over the past two decades. Within a multiscale setting, this can be achieved by using a local homogenization (see [Ostoja-Starzewski, 2008] for a survey) or a filtering approach [Yvonnet and Bonnet, 2014, Bignonnet et al., 2014, Tran et al., 2016]. For averaging-type upscaling, kinematic and static uniform boundary conditions (which are denoted by KUBC and SUBC hereinafter) can be considered [Ostoja-Starzewski, 1998] and provide bounds for the field of apparent tensors [Huet, 1990, Hazanov and Huet, 1994]. Alternatively, periodic boundary conditions (PBC) can be invoked, especially when a fast convergence toward the effective properties is sought; PBC were employed in the so-called moving-window approach [Graham et al., 2003], for instance. In the sequel, kinematic uniform boundary conditions (KUBC) and static uniform boundary conditions (SUBC) are selected. While square-shaped domains are typically used in the literature of homogenization, a circular moving window is considered to prevent the generation of spurious anisotropic features at the mesoscale created by the corners of a square window (see, e.g., [Bignonnet et al., 2014]), see also [Salmi et al., 2012] for the consideration of, and comparison with, alternative boundary conditions based on Voronoi cells. A method for obtaining a smoothed, equivalent field with fluctuations is described in the following.

2.3.2.1 Methodology

Let $\widetilde{\Omega}_{\boldsymbol{x}}$ be a circular domain of radius $\widetilde{R}$, centered at $\boldsymbol{x} \in \Omega$, with boundary $\partial\widetilde{\Omega}_{\boldsymbol{x}}$. For one realization of the microstructure, $\{\widetilde{\mathbb{C}}(\boldsymbol{x}), \boldsymbol{x} \in \Omega\}$ is obtained by performing a homogenization

locally in $\widetilde{\Omega}_{\boldsymbol{x}}$, for both KUBC and SUBC (see Fig. 2.6). As $\boldsymbol{x}$ moves within Ω, we obtain a smooth, equivalent medium characterized by wavelengths associated with the radius $\widetilde{R}$ (see the illustration of this process in Fig. 2.7 for different radii $\widetilde{R}$). We recall that KUBC correspond to the following boundary conditions:

$$\boldsymbol{u}_D^{(ij)}(\boldsymbol{z}) = [E^{(ij)}]\boldsymbol{z} \ , \quad \forall \boldsymbol{z} \in \partial\widetilde{\Omega}_{\boldsymbol{x}} \ , \tag{2.10}$$

where in the present 2D plane strain context, the indices i and j run over $\{1,2\}$, leading to:

$$[E^{(11)}] = \begin{bmatrix} 1 & 0 \\ 0 & 0 \end{bmatrix} \ , \quad [E^{(22)}] = \begin{bmatrix} 0 & 0 \\ 0 & 1 \end{bmatrix} \ , \quad [E^{(12)}] = \frac{1}{2}\begin{bmatrix} 0 & 1 \\ 1 & 0 \end{bmatrix} \ . \tag{2.11}$$

The strategy is schematically depicted in Fig. 2.6. For SUBC, traction vectors are applied in the

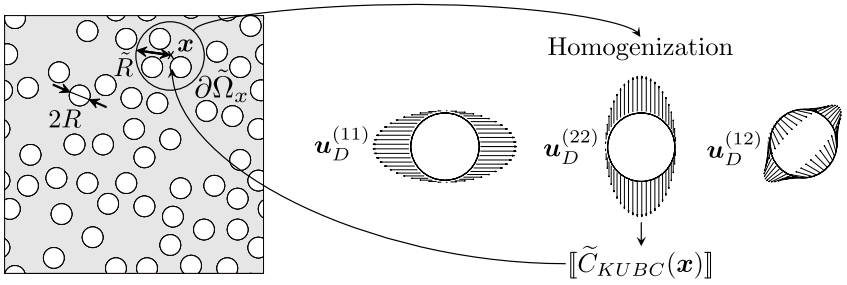

Figure 2.6 – Defining mesoscale fields of stiffness through homogenization (case of KUBC).

form

$$\boldsymbol{t}_N(\boldsymbol{z}) = [\Sigma^{(ij)}]\,\boldsymbol{n}(\boldsymbol{z}) \ , \quad \forall \boldsymbol{z} \in \partial\widetilde{\Omega}_{\boldsymbol{x}} \ , \tag{2.12}$$

where $\boldsymbol{n}(\boldsymbol{z})$ is the outward-pointing normal vector at point $\boldsymbol{z} \in \partial\widetilde{\Omega}_{\boldsymbol{x}}$. Combinations of indices similar to those introduced for KUBC are considered, with

$$[\Sigma^{(11)}] = \begin{bmatrix} 1 & 0 \\ 0 & 0 \end{bmatrix} \ , \quad [\Sigma^{(22)}] = \begin{bmatrix} 0 & 0 \\ 0 & 1 \end{bmatrix} \ , \quad [\Sigma^{(12)}] = \frac{1}{2}\begin{bmatrix} 0 & 1 \\ 1 & 0 \end{bmatrix} \ . \tag{2.13}$$

Let $\{\widetilde{\mathbb{C}}_{KUBC}(\boldsymbol{x}), \boldsymbol{x} \in \Omega\}$ and $\{\widetilde{\mathbb{C}}_{SUBC}(\boldsymbol{x}), \boldsymbol{x} \in \Omega\}$ be the random fields of mesoscopic elasticity tensors defined under the aforementioned boundary conditions. Note that when $\boldsymbol{x}$ approaches the boundary $\partial\Omega$, the realization of the microstructure is virtually replicated, by periodicity, and the mesoscopic tensor is still well defined.

Denoting by R the radius of the inclusions, the ratio $\widetilde{R}/R$ plays an important role in defining a continuous transition from the microscale ($\widetilde{R}/R \to 0^+$) to the macroscale ($\widetilde{R}/R \to +\infty$). Additionally, it specifies the level of anisotropy exhibited by the local apparent elasticity tensor, ranging from microscopic isotropy to mesoscopic anisotropy, and then to macroscopic isotropy (in the present case). This aspect turns out to be critical for the phase-field approach, since the constitutive model used for the damaged material is based on the isotropy of the background media (see Eq. 2.9). In particular, the local isotropy of the underlying mesostructure is implicitly assumed in the presented formulation. The definition of the isotropic approximation for the mesoscale elasticity tensor field is addressed in the following.

2.3.2.2 Construction of the mesoscopic isotropic approximations

Let $\{\widetilde{\mathbb{C}}^{iso}_{BC}(\boldsymbol{x}), \boldsymbol{x} \in \Omega\}$ denote the isotropic approximation of the field $\{\widetilde{\mathbb{C}}_{BC}(\boldsymbol{x}), \boldsymbol{x} \in \Omega\}$, where the subscript BC refers to the type of boundary conditions under consideration (KUBC or SUBC). In two-dimensional elasticity, and assuming plane strain conditions, the Voigt-type matrix representation $\{[\widetilde{\mathbb{C}}^{iso}_{BC}(\boldsymbol{x})], \boldsymbol{x} \in \Omega\}$ of the aforementioned field is given by

$$[\widetilde{\mathbb{C}}^{iso}_{BC}(\boldsymbol{x})] = \begin{bmatrix} \widetilde{k}_{BC}(\boldsymbol{x}) + \frac{4}{3}\widetilde{\mu}_{BC}(\boldsymbol{x}) & \widetilde{k}_{BC}(\boldsymbol{x}) - \frac{2}{3}\widetilde{\mu}_{BC}(\boldsymbol{x}) & 0 \\ \widetilde{k}_{BC}(\boldsymbol{x}) - \frac{2}{3}\widetilde{\mu}_{BC}(\boldsymbol{x}) & \widetilde{k}_{BC}(\boldsymbol{x}) + \frac{4}{3}\widetilde{\mu}_{BC}(\boldsymbol{x}) & 0 \\ 0 & 0 & \widetilde{\mu}_{BC}(\boldsymbol{x}) \end{bmatrix} , \quad \forall \boldsymbol{x} \in \Omega , \tag{2.14}$$

where $\{\widetilde{k}_{BC}(\boldsymbol{x}), \boldsymbol{x} \in \Omega\}$ and $\{\widetilde{\mu}_{BC}(\boldsymbol{x}), \boldsymbol{x} \in \Omega\}$ are the random fields of *three-dimensional* bulk and shear moduli defining the isotropic approximation, in plane strain elasticity, of the actual (anisotropic) elastic tensor $[\widetilde{\mathbb{C}}_{BC}(\boldsymbol{x})]$. To obtain these coefficients, we minimize the distance (in the sense of the metric defined below) between $[\widetilde{\mathbb{C}}_{BC}(\boldsymbol{x})]$ and $[\widetilde{\mathbb{C}}^{iso}_{BC}(\boldsymbol{x})]$ (see [Guilleminot and Soize, 2012b, Tran et al., 2016] and the references therein):

$$(\widetilde{k}_{BC}(\boldsymbol{x}), \widetilde{\mu}_{BC}(\boldsymbol{x})) = \underset{k>0,\, \mu>0}{\operatorname{argmin}} \, \|[\widetilde{\mathbb{C}}_{BC}(\boldsymbol{x})] - [\widetilde{\mathbb{C}}^{iso}_{BC}(\boldsymbol{x})]\|_F^2 , \tag{2.15}$$

in which

$$[\widetilde{\mathbb{C}}_{BC}] = \begin{pmatrix} \widetilde{C}_{11} & \widetilde{C}_{12} & \widetilde{C}_{13} \\ \widetilde{C}_{12} & \widetilde{C}_{22} & \widetilde{C}_{23} \\ \widetilde{C}_{13} & \widetilde{C}_{23} & \widetilde{C}_{33} \end{pmatrix} , \tag{2.16}$$

where the Voigt's notation has been used for the different components of the tensor and $\|\cdot\|_F$ is the Frobenius norm.

The optimization problem defined by Eq. (2.15) can be solved by a direct differentiation of the cost function, and the mesoscopic moduli of the isotropic approximation are found as

$$\widetilde{k}(\boldsymbol{x}) = \frac{1}{60}(11\widetilde{C}_{11}(\boldsymbol{x}) + 11\widetilde{C}_{22}(\boldsymbol{x}) - 4\widetilde{C}_{33}(\boldsymbol{x}) + 38\widetilde{C}_{12}(\boldsymbol{x})) \tag{2.17}$$

and

$$\widetilde{\mu}(\boldsymbol{x}) = \frac{1}{5}(\widetilde{C}_{11}(\boldsymbol{x}) + \widetilde{C}_{22}(\boldsymbol{x}) + \widetilde{C}_{33}(\boldsymbol{x}) - 2\widetilde{C}_{12}(\boldsymbol{x})) , \tag{2.18}$$

where the subscript BC has been dropped for notational convenience (this convention will be used in the sequel when no confusion is possible).

2.3.2.3 Identification of mesoscale elastic properties

In this section, we first analyze the error generated by the isotropic approximation at mesoscale. A few fundamental properties of the field thus constructed are then investigated.

Isotropic mesoscopic approximation

The effect of the mesoscopic resolution on the isotropic approximation (for KUBC) is qualitatively shown on a single realization in Fig. 2.7. As expected, the field becomes more homogeneous as the ratio $\widetilde{R}/R$ increases. In order to further assess the relevance of the isotropic approximation,

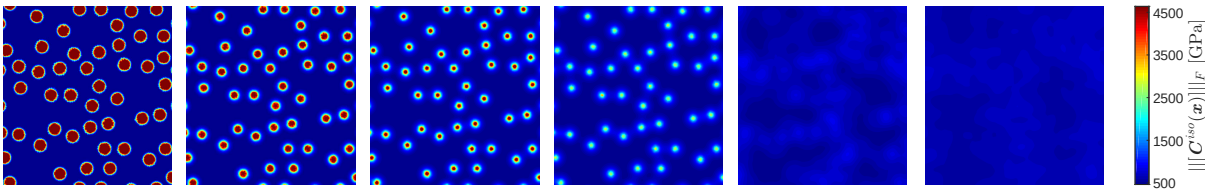

Figure 2.7 – One realization of the random field $\{\|[\widetilde{\mathbb{C}}^{iso}_{KUBC}(\boldsymbol{x})]\|_F, \boldsymbol{x} \in \Omega\}$ for $\widetilde{R}/R \in \{0.2, 0.6, 0.8, 1, 2, 4\}$ (from left to right).

the following random field $\{\mathscr{A}_{BC}(\boldsymbol{x}), \boldsymbol{x} \in \Omega\}$ is introduced [Guilleminot and Soize, 2012b, Tran et al., 2016]:

$$\mathscr{A}_{BC}(\boldsymbol{x}) = \frac{\|[\widetilde{\mathbb{C}}_{BC}(\boldsymbol{x})] - [\widetilde{\mathbb{C}}^{iso}_{BC}(\boldsymbol{x})]\|_{\mathrm{F}}}{\|[\widetilde{\mathbb{C}}_{BC}(\boldsymbol{x})]\|_{\mathrm{F}}} \ , \quad \forall\, \boldsymbol{x} \in \Omega \tag{2.19}$$

The graphs of the fields of mean and standard deviation evaluated for a coarse mesoscopic grid (with 20 points along each direction) are shown in Figs. 2.8 and 2.9, for both KUBC and SUBC and for $\widetilde{R}/R = 3$. It is seen that the error between the homogenization-based random fields

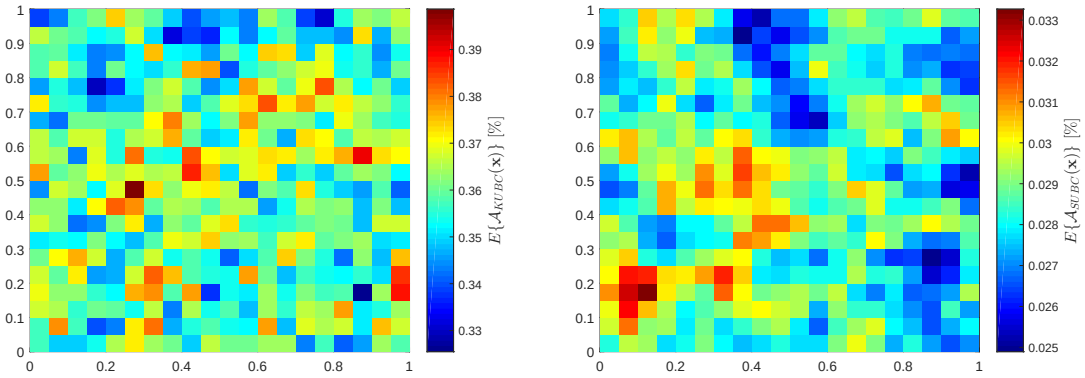

Figure 2.8 – Graphs of the mean functions for the random fields $\{\mathscr{A}_{KUBC}(\boldsymbol{x}), \boldsymbol{x} \in \Omega\}$ (left) and $\{\mathscr{A}_{SUBC}(\boldsymbol{x}), \boldsymbol{x} \in \Omega\}$ (right) for $\widetilde{R}/R = 3$.

and their isotropic approximations remain small in mean and variance, and that the error is larger in the case of KUBC. The approximation in the set of isotropic tensors is satisfactory and allows the phase-field approach to be applied with an isotropic background medium. In this rest of this chapter, we will consider the characterization and simulation of the non-Gaussian fields $\{\widetilde{k}_{BC}(\boldsymbol{x}), \boldsymbol{x} \in \Omega\}$ and $\{\widetilde{\mu}_{BC}(\boldsymbol{x}), \boldsymbol{x} \in \Omega\}$ for $\widetilde{R}/R = 3$.

Statistical analysis on mesoscopic elasticity

The graphs of the first-order marginal probability density functions for the bulk and shear moduli are shown in Fig. 2.10. The well-known ordering with respect to boundary conditions is observed almost surely (that is, $\widetilde{k}_{SUBC} \leqslant \widetilde{k}_{KUBC}$ and $\widetilde{\mu}_{SUBC} \leqslant \widetilde{\mu}_{KUBC}$ for each microstructural sample), and it is seen that the level of statistical fluctuations associated with KUBC is larger than for SUBC.

The estimated normalized correlation functions along $\boldsymbol{e}^{(1)}$ and $\boldsymbol{e}^{(2)}$ for the fields of bulk and shear moduli (for SUBC) are shown in Fig. 2.11. In these figures, the notation $\tau_i \mapsto R^{data}_{\widetilde{k}}(\tau_i)$

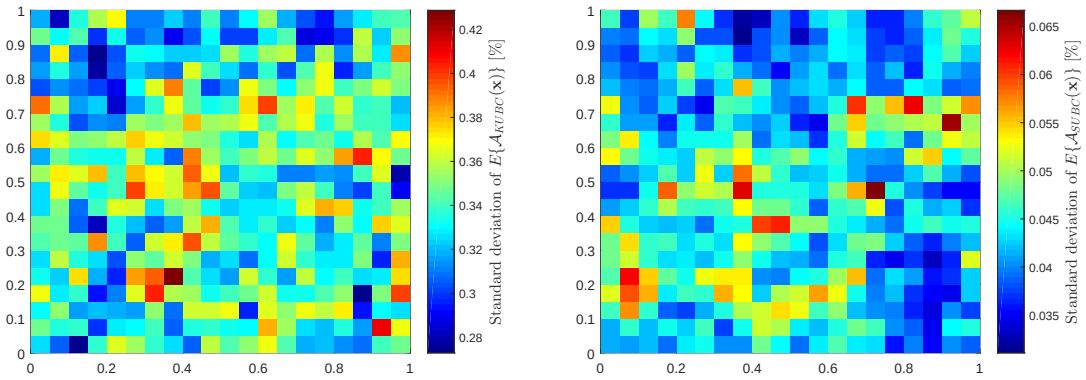

Figure 2.9 – Graphs of the fields of standard deviation for the random fields $\{\mathscr{A}_{KUBC}(\boldsymbol{x}), \boldsymbol{x} \in \Omega\}$ (left) and $\{\mathscr{A}_{SUBC}(\boldsymbol{x}), \boldsymbol{x} \in \Omega\}$ (right) for $\widetilde{R}/R = 3$.

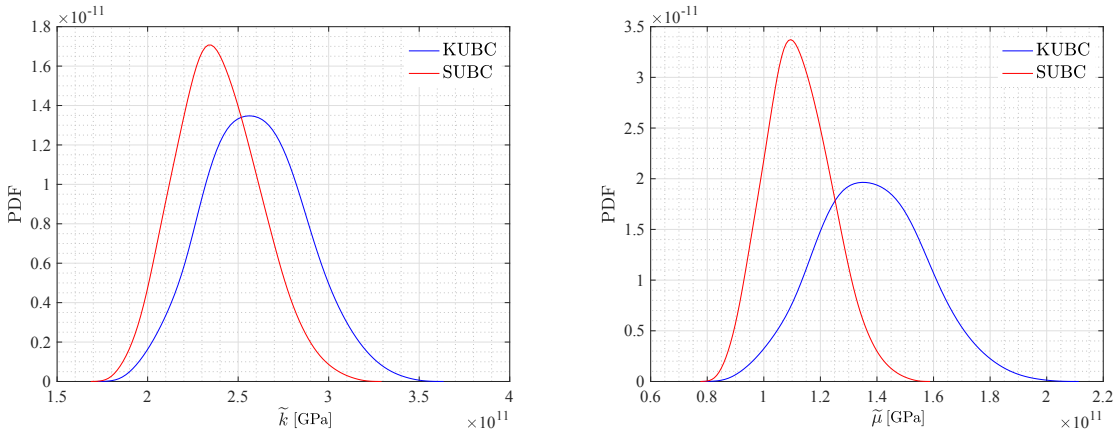

Figure 2.10 – Graphs of the first-order marginal probability density functions for the bulk (left) and shear (right) moduli.

indicates that the correlation function of the bulk modulus random field is evaluated along the unit vector $\boldsymbol{e}^{(i)}$ (a similar notation is used for the shear modulus). It is seen that the differences between the correlation functions for the two random fields are almost indistinguishable, due to the very strong cross-correlation between the two properties. Moreover, it can be observed that the correlation first decreases over the range $[0, L/2]$ (with $L = 1$) and then starts increasing on $[L/2, L]$, in accordance with the periodicity of the underlying background medium. This information will be used to select an appropriate form of the correlation functions for the random field models, constructed in Section 2.4.1.1.

2.3.3 Mesoscopic Toughness

This part is concerned with the identification to the mesoscopic toughness, solving an inverse problem. A validation study involving both the mechanical response (under some given, macroscopic loading) and crack path variability is then undertaken.

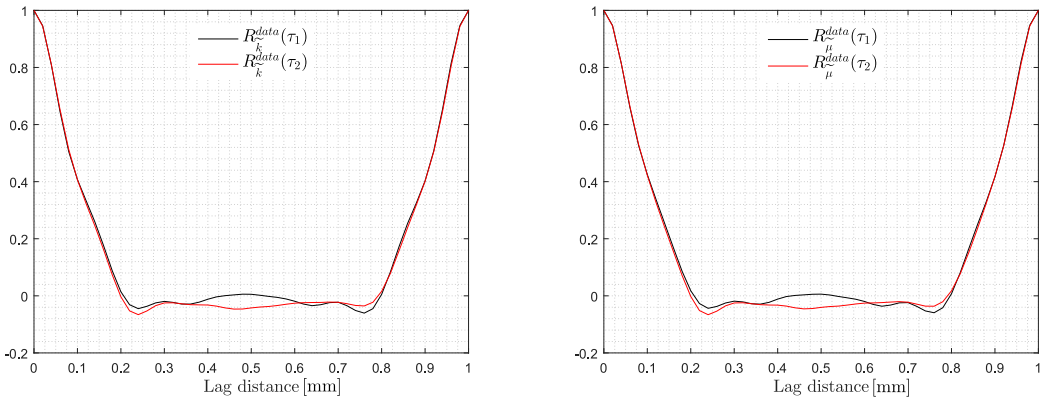

Figure 2.11 – Graph of the correlation function along $\boldsymbol{e}^{(1)}$ and $\boldsymbol{e}^{(2)}$, estimated from the simulated data, for the random fields of bulk (left) and shear (right) moduli.

2.3.3.1 Inverse problem strategy

Let us now turn to the identification of the fracture and phase-field parameters $\widetilde{g_c}$ and $\widetilde{\ell}$ at the mesoscale (see Section 2.3.1). In this work, the characteristic length $\widetilde{\ell}$ of the mesoscopic medium is set to be equal to the characteristic length at the microscale, previously denoted by ℓ, and $\widetilde{g_c}$ is assumed constant. These choices are supported by a set of parametric studies, unreported hereinafter for the sake of conciseness, and by the numerical results presented in [Nguyen et al., 2019] for similar propagation regimes. It is worth noticing that while the length scales are taken similar in both the microscopic and mesoscopic phase field equations (given by Eq. (2.7)), the mesh involved in the mesoscale description only needs to be refined in the vicinity of the crack. An adaptive meshing strategy can then be deployed to substantially reduce the computational cost (as opposed to the microscopic description in which the mesh must be uniformly fine over the entire microstructure). The mesoscopic toughness parameter $\widetilde{g_c}$ is next identified by solving an inverse problem involving the peak force $F_{max} = \max_{u_D} F(u_D)$. More precisely, $\widetilde{g_c}$ is calibrated by imposing a match between the mean value $\underline{F}_{max}$ of F_{max}, estimated with 500 independent microstructural samples and the fine-scale elasticity-phase-field simulations (detailed in Section 2.2.2), and the mean value determined with the mesoscopic description introduced in Section 2.3.1, denoted by $\underline{\widetilde{F}}_{max}$. In the latter description, samples of the elasticity random field are estimated through the mowing-window homogenization procedure, and the mesoscopic toughness then appears as the unique unknown parameter. Let $\underline{\widetilde{F}}_{max}(\widetilde{g_c^*})$ be the mean peak force associated with the candidate value $\widetilde{g_c^*}$ for the mesoscopic toughness (that is, by substituting $\widetilde{g_c^*}$ for $\widetilde{g_c}$ in Eq. (2.7)). An optimal value can thus be defined by minimizing the relative error function

$$\mathscr{J}(\widetilde{g_c^*}) = \frac{|\underline{F}_{max} - \underline{\widetilde{F}}_{max}(\widetilde{g_c^*})|}{\underline{F}_{max}} \tag{2.20}$$

over the admissible set $[g_{c,m}, g_{c,i}]$:

$$\widetilde{g_c} = \underset{\widetilde{g_c^*} \in [g_{c,m}, g_{c,i}]}{\operatorname{argmin}} \quad \mathscr{J}(\widetilde{g_c^*}) \ . \tag{2.21}$$

2.3.4 Identification results and validation study

Since the mesoscopic elasticity field depends on the boundary conditions applied, the optimization problem defined in the previous section must be solved independently for KUBC and SUBC. The

graph of the cost function obtained for a resolution parameter $\widetilde{R}/R = 3$ is shown in the left panel in Fig. 2.12.

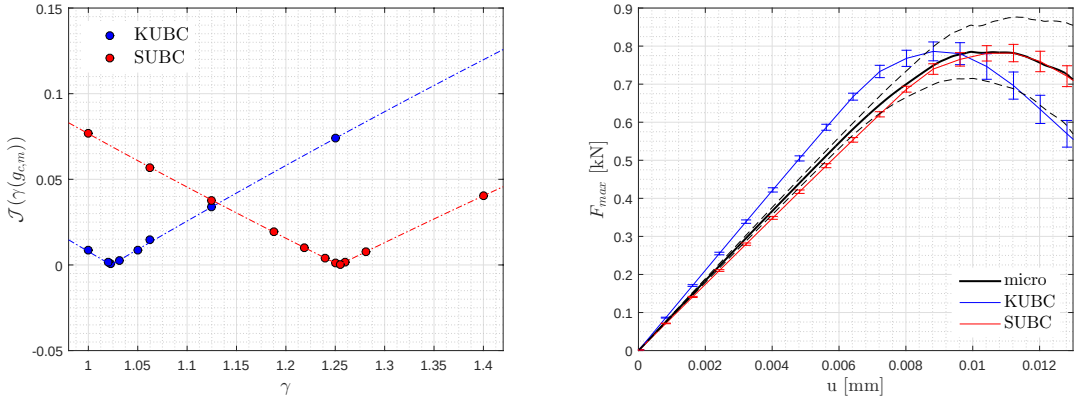

Figure 2.12 – Graphs of the cost function for KUBC and SUBC (left), and envelopes of the macroscopic response for the reference microscale model and the mesoscopic formulations (right).

The optimal values are obtained as

$$\widetilde{g_c} = 1.022 \times g_{c,m} \approx 2.75 \times 10^{-3} \text{ [kN.mm}^{-1}\text{]} \tag{2.22}$$

for KUBC and

$$\widetilde{g_c} = 1.255 \times g_{c,m} \approx 3.375 \times 10^{-3} \text{ [kN.mm}^{-1}\text{]} \tag{2.23}$$

for SUBC. A comparison of the macroscopic responses obtained with the mesoscopic formulations (for KUBC and SUBC), parametrized with the identified values, and the reference computations is shown in the right panel in Fig. 2.12; see also Fig. 2.13 for a comparison on crack path (for a given microstructural samples). This figure shows that the mesoscale formulation identified under

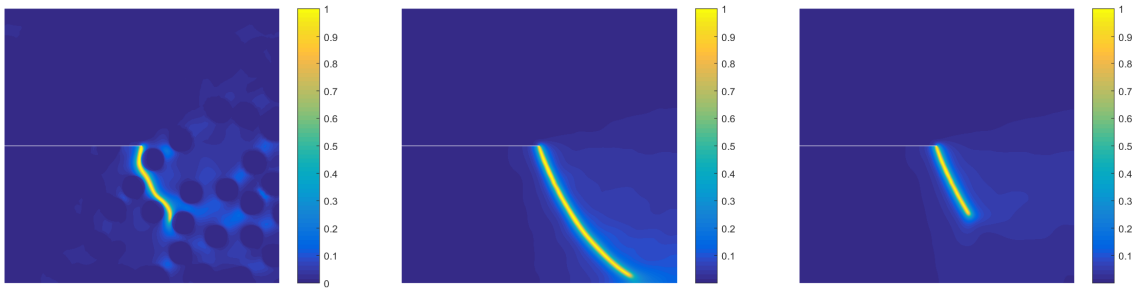

Figure 2.13 – Illustration of different crack path for the same microstructure: microscale description (left), KUBC-based description (middle), SUBC-based description (right).

SUBC provides a fairly accurate estimate of the *mean* macroscopic response. This conclusion similarly holds for KUBC, although this type of boundary conditions leads to a stiffening of the response, in accordance with the fact that apparent tensors obtained under KUBC constitute upper bounds for the mesoscopic elasticity (it becomes surrealistic in particular when $\widetilde{R}/R \mapsto 1$).

In both cases, the variability is underestimated due to filtered elasticity fluctuations. These effects can clearly observed in Fig. 2.14, where the mean and standard deviation on crack paths are reported for the two types of boundary conditions. It is seen that the cracks paths obtained with the mesoscopic formulations are localized near the mean crack path at microscale, for both KUBC and SUBC. Not surprisingly, the mesoscopic-based crack paths exhibit a variability that is much smaller than the one obtained at microscale (where the crack trajectory is constrained by the radius of the inclusions). While these results support the relevance of the formulation,

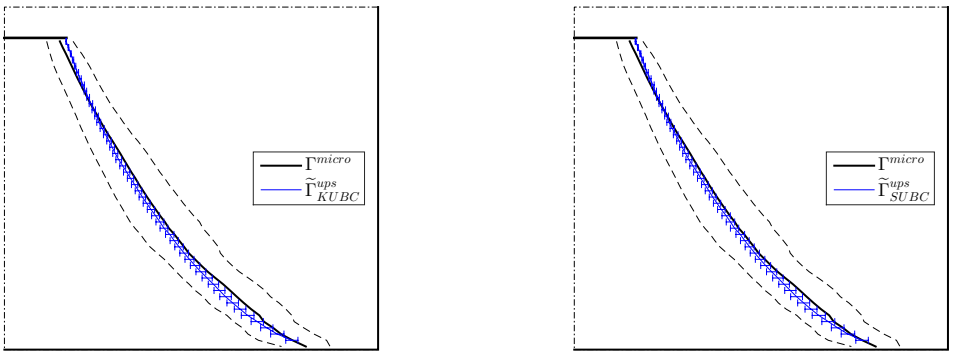

Figure 2.14 – Comparison of crack paths obtained with the microscopic description (black dashed/solid lines) and the mesoscopic formulation. Left panel: case of KUBC. Right panel: case of SUBC.

the latter necessitates solving a very large number of homogenization problems to represent the fluctuations of the elasticity field at the mesoscopic scale. In the next section, we address the construction of a stochastic model that enables the elasticity tensor random field to be sampled in a robust manner.

2.4 Stochastic Modeling of Mesoscopic Crack Propagation

In this section, we first address the construction and identification of a stochastic representation for the mesoscopic elasticity tensor random field. We subsequently discuss the validation of the proposed model using direct and indirect data.

2.4.1 Stochastic modeling

The construction of stochastic models for random fields of elasticity tensors exhibiting arbitrary material symmetries has been investigated in [Guilleminot and Soize, 2013b, Guilleminot and Soize, 2013a, Staber and Guilleminot, 2017] using an information-theoretic formulation [Soize, 2006] (see [Guilleminot and Soize, 2017] for a survey), and in [Malyarenko and Ostoja-Starzewski, 2017] using a spectral expansion. In what follows, we seek to define a representation that is consistent, on the one hand, with the observations drawn from the analysis of the samples obtained through the moving-window upscaling and, on the other hand, with the theoretical results derived in the aforementioned references.

2.4.1.1 Construction of random field models

For a given type of boundary conditions, let $\{\widetilde{k}_{BC}(\boldsymbol{x}), \boldsymbol{x} \in \Omega\}$ and $\{\widetilde{\mu}_{BC}(\boldsymbol{x}), \boldsymbol{x} \in \Omega\}$ be the random fields of three-dimensional bulk and shear moduli as defined in Eq. (2.14).

Let $\{\boldsymbol{\Xi}(\boldsymbol{x}) = (\Xi_1(\boldsymbol{x}), \Xi_2(\boldsymbol{x})), \boldsymbol{x} \in \Omega\}$ be a bivariate Gaussian field with statistically independent, normalized components. These components are defined by the correlation functions $(\boldsymbol{x}, \boldsymbol{y}) \mapsto R_{\Xi_1}(\boldsymbol{x}, \boldsymbol{y}; \boldsymbol{\alpha}^{(1)})$ and $(\boldsymbol{x}, \boldsymbol{y}) \mapsto R_{\Xi_2}(\boldsymbol{x}, \boldsymbol{y}; \boldsymbol{\alpha}^{(2)})$ ($\alpha^{(i)}$ is a model parameter defined for $\boldsymbol{\Xi}_i$). The non-Gaussian random fields of elastic moduli are then defined through the nonlinear transformations

$$\widetilde{k}_{BC}(\boldsymbol{x}) = F^{-1}_{G(p_{\widetilde{k}}, q_{\widetilde{k}})}\left(F_{N(0,1)}(\Xi_1(\boldsymbol{x}))\right) \tag{2.24}$$

and

$$\widetilde{\mu}_{BC}(\boldsymbol{x}) = F^{-1}_{G(p_{\widetilde{\mu}}, q_{\widetilde{\mu}})}\left(F_{N(0,1)}(\rho\,\Xi_1(\boldsymbol{x}) + \sqrt{1-\rho^2}\,\Xi_2(\boldsymbol{x}))\right) \ , \tag{2.25}$$

where $F^{-1}_{G(p,q)}$ is the inverse cumulative distribution function of the Gamma law, ensuring the positivity of the modulus and with (shape and scale) parameters p and q (note that the dependence of these parameters on the KUBC and SUBC boundary conditions of homogenization procedure is not reported for notational convenience), $F_{N(0,1)}$ is the cumulative distribution function of the standard Gaussian law and ρ controls the dependance between $\widetilde{k}_{BC}(\boldsymbol{x})$ and $\widetilde{\mu}_{BC}(\boldsymbol{x})$.

Given the stationarity and the form of the correlation functions estimated for the random fields of elastic moduli (see Fig. 2.11), the following separable form is retained:

$$R_{\Xi_i}(\boldsymbol{x}, \boldsymbol{y}; \boldsymbol{\alpha}^{(i)}) = r(\tau_1; \alpha_1^{(i)}) \times r(\tau_2; \alpha_2^{(i)}) \ , \quad \forall\, \boldsymbol{\tau} \in ([0, L])^2 \ , \quad i \in \{1, 2\} \ , \tag{2.26}$$

where $\tau_j = |x_j - y_j|$ is the lag distance along $\boldsymbol{e}^{(j)}$, $j \in \{1, 2\}$, and the one-dimensional normalized correlation function $\tau \mapsto r(\tau; \alpha)$ is defined as

$$r(\tau; \alpha) = \exp\left(-\frac{2}{\alpha^2}\sin^2\left(\frac{\pi\tau}{L}\right)\right) \ . \tag{2.27}$$

In Eq. (2.27), α is a model parameter related to the internal length

$$\mathscr{L} = \int_0^{L/2} |r(\tau; \alpha)|\, d\tau \ , \tag{2.28}$$

which is interpreted, in the periodic setting under consideration, as the spatial correlation length of the Gaussian random field along the associated basis vector (*e.g.*, along $\boldsymbol{e}^{(1)}$ if the function $\tau_1 \mapsto r(\tau_1; \alpha_1^{(i)})$ is considered). It can be shown that the correlation length $\mathscr{L} < L/2$ reads as

$$\mathscr{L} = \frac{L}{2}\exp\{-\alpha^{-2}\}\mathscr{I}_0(\alpha^{-2}) \ , \tag{2.29}$$

where $\mathscr{I}_0$ denotes the zero-order modified Bessel function. It should be noted that by construction, one has $\ell < L/2$. The graph of $\tau \mapsto r(\tau; \alpha)$ is shown in Fig. 2.15 for different values of α.

The following properties can easily be deduced.

- The first-order marginal probability measure is a bivariate Gamma law [Moran, 1969, Arnst and Ponthot, 2014], which is consistent with previous results derived within the framework of information theory (see [Guilleminot and Soize, 2017] and the references therein).

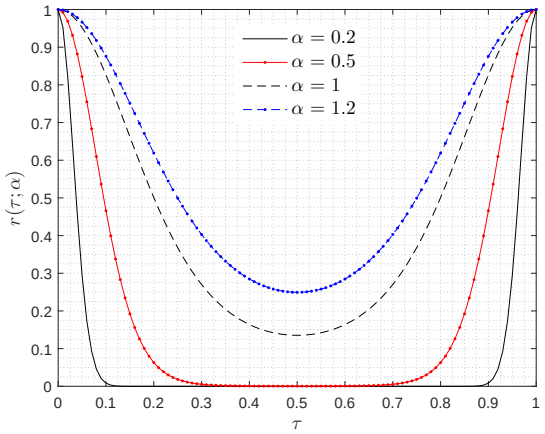

Figure 2.15 – Plot of the correlation function $\tau \mapsto r(\tau;\alpha)$ for different values of α.

- The mean values $\underline{\widetilde{k}}_{BC} = E\{\widetilde{k}_{BC}(\boldsymbol{x})\}$ and $\underline{\widetilde{\mu}}_{BC} = E\{\widetilde{\mu}_{BC}(\boldsymbol{x})\}$ read as

$$\underline{\widetilde{k}}_{BC} = p_{\widetilde{k}} \times q_{\widetilde{k}} \ , \quad \underline{\widetilde{\mu}}_{BC} = p_{\widetilde{\mu}} \times q_{\widetilde{\mu}} \ , \tag{2.30}$$

  and the coefficients of variation are given as

$$\delta_{\widetilde{k}_{BC}} = \frac{1}{\sqrt{p_{\widetilde{k}}}} \ , \quad \delta_{\widetilde{\mu}_{BC}} = \frac{1}{\sqrt{p_{\widetilde{\mu}}}} \ . \tag{2.31}$$

  These properties are chosen independent of location $\boldsymbol{x}$, owing to the stationarity of the random fields.

- The fields of stiffness and compliance tensors are of second-order:

$$E\{\|[\widetilde{\mathbb{C}}^{iso}_{BC}(\boldsymbol{x})]\|_F^2\} < +\infty \ , \quad E\{\|[\widetilde{\mathbb{C}}^{iso}_{BC}(\boldsymbol{x})]^{-1}\|_F^2\} < +\infty \ , \quad \forall\, \boldsymbol{x} \in \Omega \ . \tag{2.32}$$

  hence ensuring that the stochastic linear elastic boundary value problem is well posed [Soize, 2006].

- The random fields $\{\widetilde{k}_{BC}(\boldsymbol{x}), \boldsymbol{x} \in \Omega\}$ and $\{\widetilde{\mu}_{BC}(\boldsymbol{x}), \boldsymbol{x} \in \Omega\}$ are mean-square continuous and mean-square differentiable.

From a computational standpoint, the underlying Gaussian fields are sampled using a truncated Karhunen-Loève expansion. In order to reduce the associated computation time, the random fields are sampled on a grid that is coarser than the one used to solve the elasticity-phase-field problem at the mesoscale. Realizations of fields are then obtained by interpolating on the fine mesoscopic grid. To that end, the coarse mesoscopic grid is specifically defined so that the correlation structure is properly discretized. In the results presented hereinafter, the coarse mesh includes six Gauss points per correlation length, along each direction.

2.4.1.2 Identification of the elasticity random field

The probabilistic model involves two sets of parameters controlling (i) the joint probability density function of the elastic moduli at a given location, and (ii) the correlation structure of the underlying Gaussian fields. The first set of parameters gathers $(p_{\widetilde{k}}, q_{\widetilde{k}})$ and $(p_{\widetilde{\mu}}, q_{\widetilde{\mu}})$ (or equivalently $(\underline{\widetilde{k}}_{BC}, \delta_{\widetilde{k}_{BC}})$ and $(\underline{\widetilde{\mu}}_{BC}, \delta_{\widetilde{\mu}_{BC}})$, in view of Eq. (2.30) and (2.31)), as well as the the

coefficient of correlation ρ. These hyperparameters can be estimated from the database using standard statistical estimators, here with 500 sample realizations (which ensures the convergence of the estimators) and for the same resolution $\widetilde{R}/R = 3$:

- For KUBC, we found $\rho = 0.9775$, with

$$\underline{\widetilde{k}}_{KUBC} = 258.7 \text{ [GPa]} , \quad \delta_{\widetilde{k}_{KUBC}} = 10.25\% , \tag{2.33}$$

and

$$\underline{\widetilde{\mu}}_{KUBC} = 137.7 \text{ [GPa]} , \quad \delta_{\widetilde{\mu}_{KUBC}} = 13.30\% . \tag{2.34}$$

- For SUBC, $\rho = 0.995$, with

$$\underline{\widetilde{k}}_{SUBC} = 238.6 \text{ [GPa]} , \quad \delta_{\widetilde{k}_{SUBC}} = 9.3\% , \tag{2.35}$$

and

$$\underline{\widetilde{\mu}}_{SUBC} = 112.2 \text{ [GPa]} , \quad \delta_{\widetilde{\mu}_{SUBC}} = 10\% . \tag{2.36}$$

The kernel density estimations of the first-order marginal and joint distribution for the bulk and shear moduli obtained with the data and the model-based samples are shown in Figs. 2.16 and 2.17 (recall that the resolution is fixed by $\widetilde{R}/R$ =3 here). A very good agreement is observed

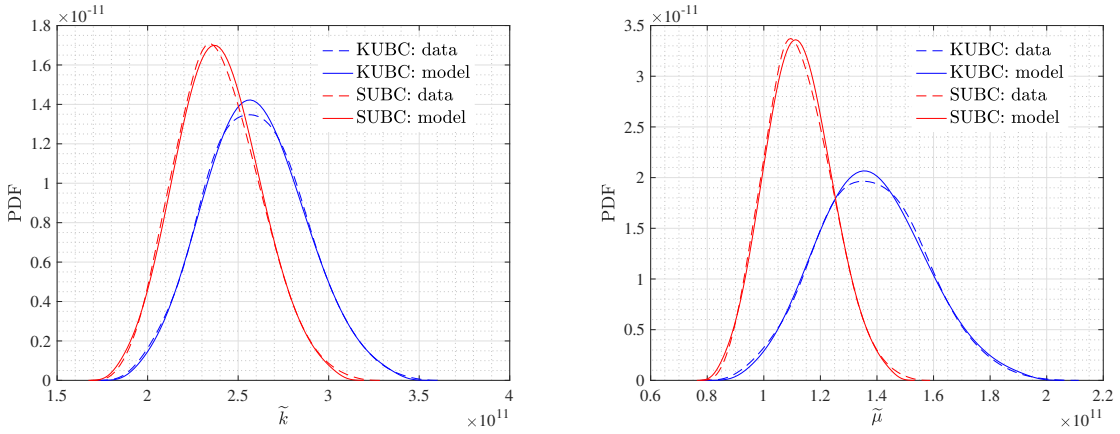

Figure 2.16 – Kernel density estimates for the probability density function of the bulk (left) and shear (right) moduli, for the two types of boundary conditions KUBC (blue) and SUBC (red).

between the probability density functions corresponding to the homogenization-based data and those estimated with model-based samples.

Since the transformations given by Eqs. (2.24) and (2.25) are nonlinear, the correlation functions associated with the random fields of elastic moduli cannot be inferred explicitly. In this case, the identification of the vector-valued hyperparameters $\boldsymbol{\alpha}^{(1)}$ and $\boldsymbol{\alpha}^{(2)}$ is performed through the following two-step procedure. Let the correlation functions of $\{\widetilde{k}_{BC}(\boldsymbol{x}), \boldsymbol{x} \in \Omega\}$ and $\{\widetilde{\mu}_{BC}(\boldsymbol{x}), \boldsymbol{x} \in \Omega\}$ be written as $\boldsymbol{\tau} \mapsto R^{model}_{\widetilde{k}}(\boldsymbol{\tau}; \boldsymbol{\alpha}^{(1)})$ and $\boldsymbol{\tau} \mapsto R^{model}_{\widetilde{\mu}}(\boldsymbol{\tau}; (\boldsymbol{\alpha}^{(1)}, \boldsymbol{\alpha}^{(2)}))$, respectively: this notation emphasizes the underlying dependence on the parameters of the Gaussian fields (see Eqs. (2.24) and (2.25)). By a slight abuse of notation, these correlation functions will also be denoted as $\tau_j \mapsto R^{model}_{\widetilde{k}}(\tau_j; \alpha^{(1)}_j)$ and $\tau_j \mapsto R^{model}_{\widetilde{\mu}}(\tau_j; (\alpha^{(1)}_j, \alpha^{(2)}_j))$ when evaluated along

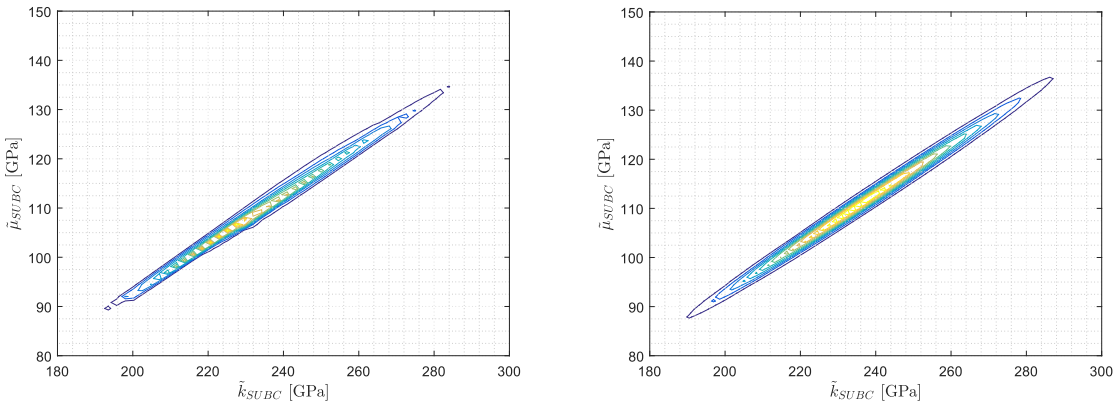

Figure 2.17 – Kernel density estimates for the joint probability density function of the bulk and shear moduli, for homogenization-based (left) and model-based (right) samples (for SUBC).

$\boldsymbol{e}^{(j)}$, $j \in \{1,2\}$. In a first step, the components of $\boldsymbol{\alpha}^{(1)}$ are identified, for a given type of boundary conditions, as

$$\alpha_1^{(1)} = \underset{\alpha>0}{\operatorname{argmin}}\ \mathscr{J}_1^{(1)}(\alpha)\ , \quad \alpha_2^{(1)} = \underset{\alpha>0}{\operatorname{argmin}}\ \mathscr{J}_2^{(1)}(\alpha)\ , \tag{2.37}$$

where the cost functions are given by

$$\mathscr{J}_1^{(1)}(\alpha) = \left(\int_0^{L/2} (R_{\tilde{k}}^{data}(\tau_1) - R_{\tilde{k}}^{model}(\tau_1;\alpha))^2 d\tau_1 \right)^{1/2} \tag{2.38}$$

and

$$\mathscr{J}_2^{(1)}(\alpha) = \left(\int_0^{L/2} (R_{\tilde{k}}^{data}(\tau_2) - R_{\tilde{k}}^{model}(\tau_2;\alpha))^2 d\tau_2 \right)^{1/2} . \tag{2.39}$$

In a second step, the hyperparameters controlling the correlation structure of the Gaussian random field $\{\Xi_2(\boldsymbol{x}), \boldsymbol{x} \in \Omega\}$ are identified as

$$\alpha_1^{(2)} = \underset{\alpha>0}{\operatorname{argmin}}\ \mathscr{J}_1^{(2)}(\alpha)\ , \quad \alpha_2^{(2)} = \underset{\alpha>0}{\operatorname{argmin}}\ \mathscr{J}_2^{(2)}(\alpha)\ , \tag{2.40}$$

in which

$$\mathscr{J}_1^{(2)}(\alpha) = \left(\int_0^{L/2} (R_{\tilde{\mu}}^{data}(\tau_1) - R_{\tilde{\mu}}^{model}(\tau_1;(\alpha_1^{(1)},\alpha))^2 d\tau_1 \right)^{1/2} \tag{2.41}$$

and

$$\mathscr{J}_2^{(2)}(\alpha) = \left(\int_0^{L/2} (R_{\tilde{\mu}}^{data}(\tau_2) - R_{\tilde{\mu}}^{model}(\tau_2;(\alpha_2^{(1)},\alpha))^2 d\tau_2 \right)^{1/2} . \tag{2.42}$$

In Eqs. (2.41) and (2.42), the values of $\alpha_1^{(1)}$ and $\alpha_2^{(1)}$ are those obtained within the first step of the methodology (see Eq. (2.37)). Above, the estimations of the correlation functions associated with the stochastic model are obtained as follows. For given values of the hyperparameters, a set of 500 independent realizations of the random fields is first generated on a coarse grid with equidistant points. Usual statistical estimators are then used to estimate a set of correlation functions, indexed by the reference point (which is the point with respect to which the lag

vector $\boldsymbol{\tau}$ is defined). Spatial averaging over properly selected reference points is finally applied to improve the quality of the estimations. The optimal values are found as

$$\boldsymbol{\alpha}^{(1)} = (0.4624, 0.4574) \ , \quad \boldsymbol{\alpha}^{(2)} = (0.4043, 0.4014) \tag{2.43}$$

for the elasticity random fields identified under KUBC, and

$$\boldsymbol{\alpha}^{(1)} = (0.4654, 0.4604) \ , \quad \boldsymbol{\alpha}^{(2)} = (0.4694, 0.4654) \tag{2.44}$$

for the case of SUBC. The graphs of the normalized correlation functions estimated with the data and with the stochastic model thus identified (under SUBC) are shown in Figs. 2.18 and 2.19 for the bulk and shear moduli random fields, respectively.

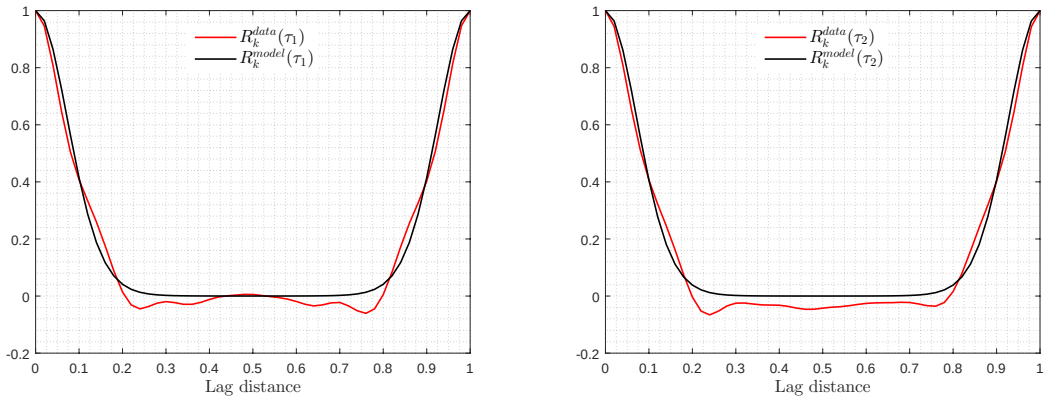

Figure 2.18 – Normalized correlation function of the bulk modulus random field along $\boldsymbol{e}^{(1)}$ (left) and $\boldsymbol{e}^{(2)}$ (right), estimated from the multiscale data (red line) and the calibrated stochastic model (black line).

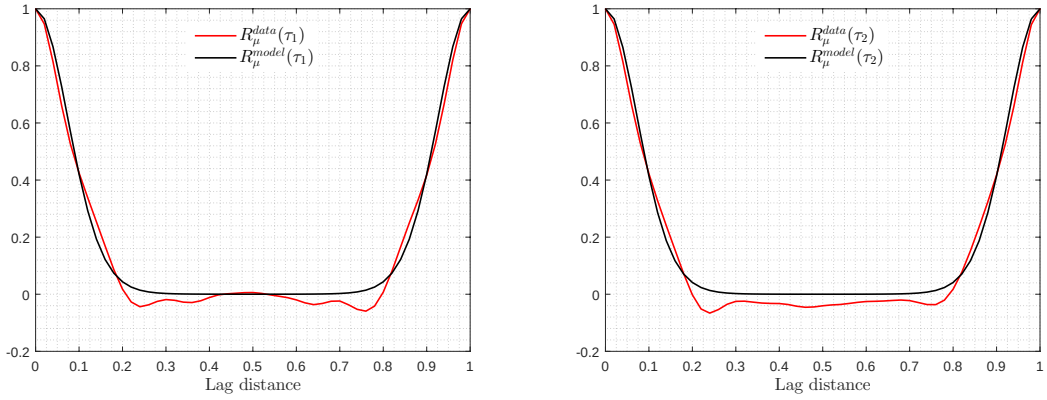

Figure 2.19 – Normalized correlation function of the shear modulus random field along $\boldsymbol{e}^{(1)}$ (left) and $\boldsymbol{e}^{(2)}$ (right), estimated from the multiscale data (red line) and the calibrated stochastic model (black line).

It is seen that the calibrated model allows the decays of the correlation functions to be accurately reproduced, which is key to mimicking the mesoscopic elasticity (and in particular, the frequency of sample path oscillations that has a substantial impact on the crack paths in the phase-field formulation at mesoscale).

2.4.2 Comparison of stochastic microscopic and mesoscopic modeling

The comparison is then carried out regarding the crack path and the force response, to determine whether the statistical structure of the fracture model and generated elasticity fields is sufficient to represent the crack test.

2.4.2.1 Results on the crack propagation

The variability in crack paths can be observed in Fig. 2.20 for the reference microscale-based computations and the mesoscopic formulation defined with either locally-homogenized microstructural samples (following the approach detailed in Section 2.3.2.1) or the elasticity field stochastic model. It can be observed that the crack paths corresponding to a description at microscale

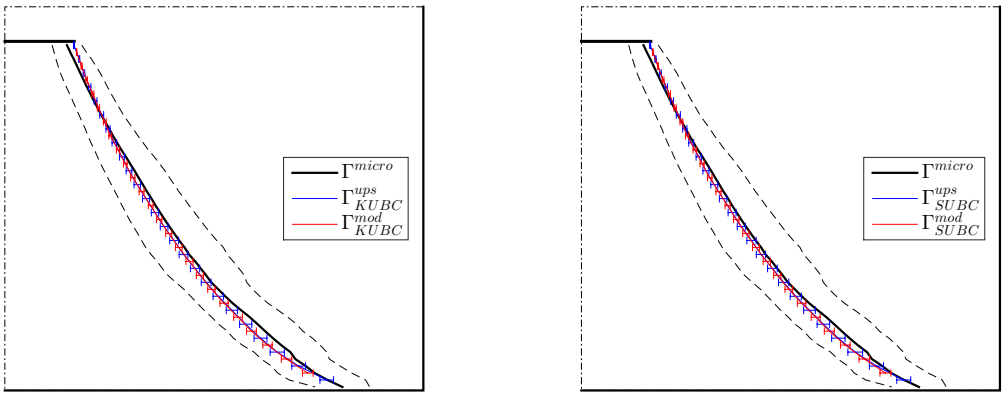

Figure 2.20 – Comparison of crack paths obtained with the microscopic description (black dashed/solid lines), the mesoscopic formulation where the elasticity is obtained from microstructural samples (blue lines), and the mesoscopic formulation involving the stochastic model for elasticity tensors (red lines). Left panel: case of KUBC. Right panel: case of SUBC.

present larger statistical fluctuations. As previously indicated, this result is indeed expected, since the propagation only occurs in the matrix phase then (hence forcing the crack to get around inclusions). In contrast, the mesoscopic formulations exhibit much smaller variability but capture quite accurately the mean crack path. Interestingly, it is seen that the stochastic model for the elasticity tensor random field performs well in delivering crack paths that are consistent those computed with homogenization-based fields.

The predictions of the macroscopic force-displacement curve are shown in Fig. 2.21. In accordance with the results presented in Section 2.3.3 (see the right panel in Fig. 2.12), where microscopic and homogenization-based mesoscopic formulations were compared, it is observed that the mesoscopic elasticity-phase-field formulation defined under SUBC delivers predictions in better agreement with the reference solution, in terms of both the mean elastic response and mean peak force. In contrast, the use of KUBC at the mesoscale generates a stiffer response in the elastic regime, while still allowing for a good prediction of the mean peak force. In addition, the use of the stochastic model in lieu of homogenization-based samples does not introduce any significant bias in the predictions, regardless of the type of boundary conditions. Upon interpreting the macroscopic force as a stochastic process indexed by the prescribed displacement,

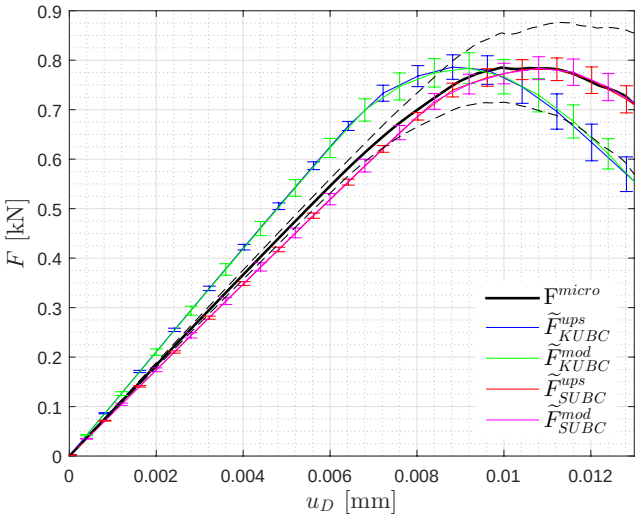

Figure 2.21 – Envelopes of the macroscopic response for the reference microscale model (F) and the mesoscopic formulations parametrized either by upscaled coefficients ($\widetilde{F}^{ups}_{KUBC}$, $\widetilde{F}^{ups}_{SUBC}$) or model-based coefficients ($\widetilde{F}^{mod}_{KUBC}$, $\widetilde{F}^{mod}_{SUBC}$).

the error generated by the proposed model-based, mesoscopic formulation can be characterized as

$$\varepsilon = \frac{|E\{\int_0^{\overline{u}_D} F(u_D)^2\, du_D\}^{1/2} - E\{\int_0^{\overline{u}_D} \widetilde{F}(u_D)^2\, du_D\}^{1/2}|}{E\{\int_0^{\overline{u}_D} F(u_D)^2\, du_D\}^{1/2}} \,, \tag{2.45}$$

where the stochastic process $\{\widetilde{F}(u_D), u_D \in [0, \overline{u}_D]\}$ implicitly depends on the boundary conditions applied at mesoscale. The right-hand side term in Eq. 2.45 can be estimated through Monte Carlo simulations, and the relative error remains small for the two types of boundary conditions, with $\varepsilon \approx 1.6\%$ for KUBC and $\varepsilon \approx 2.2\%$ for SUBC. The error for the prediction of the mean peak force can be characterized by

$$\varepsilon_{max} = |\underline{F}_{max} - \underline{\widetilde{F}}_{max}|/\underline{F}_{max} \,. \tag{2.46}$$

The error measure is given by $\varepsilon_{max} \approx 0.084\%$ for KUBC and $\varepsilon_{max} \approx 0.037\%$ for SUBC, showing that an accurate prediction of the mean peak force can be obtained with the two types of boundary conditions. Finally, the fact that the mesoscopic approach underestimates the variability in the macroscopic response is expected, given the nature of the propagation at microscale. In this context, the deviation from the mean crack path is more contained than in the microscopic simulations where the crack essentially propagates around the heterogeneities. Depending on the application of interest, one possible way to compensate for this intrinsic effect could be to adopt a goal-oriented strategy where (fictitious) anisotropic fluctuations are incorporated into the mesoscopic elasticity field (by means of a generalized stochastic model; see [Guilleminot and Soize, 2012a, Guilleminot and Soize, 2013b]), and where the hyperparameters of the stochastic model are calibrated by solving a statistical inverse problem on the macroscopic response (using an appropriate identification metric that is sensitive to both the mean and variance along the macroscopic loading path).

2.5 Conclusion

A stochastic approach to model crack propagation in random media has been proposed in this chapter. The formulation relies on a phase-field formulation where material coefficients are defined and identified through multiscale computations. Monte-Carlo simulations were first performed using a description at the microscopic scale. These computations enable the characterization of subscale-induced randomness on the macroscopic response of the domain and were subsequently used as reference results to assess the relevance of the framework. The definition of the mesoscopic parameters was then addressed. The elasticity field at mesoscale was specifically defined as the isotropic approximation of spatially dependent homogenized tensors, obtained by means of a moving-window upscaling approach (under kinematically and statically uniform boundary conditions). The (deterministic) mesoscopic toughness was identified by solving an inverse problem related to the mean peak force. It is shown that the formulation under statically uniform boundary conditions allows for an accurate prediction of the mean elastic response and mean peak force. In contrast, kinematically uniform boundary conditions generate a stiffening of mesoscale elasticity, in accordance with theoretical results derived elsewhere. An information-theoretical probabilistic model for the elasticity random field was then constructed and allows for a fast, robust sampling of mesoscopic elasticity. The results obtained by feeding this stochastic surrogate model into the phase-field formulation were finally compared with those corresponding to the full-scale, microscopic model. It is shown, in particular, that the model-based, mesoscopic elasticity-phase-field formulation associated with statically uniform boundary conditions allows for an accurate prediction of both the mean elastic response and mean peak force. Extensions of the present framework are further discussed in the perspective chapter of this thesis (see Chapter 5.5) .

Chapter 3

Phase-field formulation for finite strains and shrinkage

Contents

3.1 Introduction

In this chapter, a phase-field model for finite strains is presented. This formulation is motivated by the large deformations that are experimentally observed during drying tests on clay samples, as discussed in chapter 4. Several works have been devoted to the extension of the phase-field method (PFM) to nonlinear behaviors or finite strains in the literature. In [Miehe and Schänzel, 2014, Miehe et al., 2015], the PFM has been adapted to model polymers with thermoplastic properties. The energy was specifically described through a Neo-Hookean model coupled with a damage term. In [Ambati et al., 2016], the authors also used a Neo-Hookean model which differs

from the aforementioned one by decomposing the potential into deviatoric and volumetric parts. The damage affects this energy according to the decomposition model proposed by [Amor et al., 2009] in the case of small deformations. Theirs works was carried out on the quasi-static ductile fracture model and compared with experimental data, from the literature, for steel and aluminum samples. Good predictions on the force response in the plastic regime, and also on the crack path, have been presented. In [Raina and Miehe, 2016, Gültekin et al., 2018], another model was developed for soft tissue materials by incorporating in the energy an additional potential taking into account the preferential fibrous orientation in the material.

In this chapter, we present our phase-field formulation for finite strains, reviewing both the formulation and its numerical implementation. These aspects are mostly borrowed from the literature. In addition, an extension to drying shrinkage is proposed, together with an analysis on parameter sensitivity, solving strategies, and a comparison with the linear case. For convenience, the finite strains and the shrinkage extension are studied independently. The chapter 5 will deal with the two models together.

3.2 Finite strain kinematics and mechanical modeling

3.2.1 Background in finite elasticity

Let $\mathbf{X}$ be the position of a material point in the reference configuration Ω, and let $\mathbf{x} = \phi(\boldsymbol{X})$ denote the position of this material point in the actual configuration Ω_t, with ϕ is the deformation map. The second-order deformation gradient tensor $\mathbf{F}$ is defined by:

$$\boldsymbol{F} = \nabla_X(\phi(\boldsymbol{X})) \ , \tag{3.1}$$

where $\nabla_X(.)$ denotes the gradient operator with respect to the reference configuration Ω. The right Cauchy-Green deformation tensor is defined as

$$\boldsymbol{C} = \boldsymbol{F}^T\boldsymbol{F} \ , \tag{3.2}$$

and the Green-Lagrange strain tensor is given by

$$\boldsymbol{E} = \frac{1}{2}(\boldsymbol{C} - \boldsymbol{I}) \ , \tag{3.3}$$

where $\boldsymbol{I}$ is the second-order identity tensor. In the present work, we adopt the linear Saint-Venant-Kirchhoff material constitutive law defined by the strain density function:

$$\Psi(\boldsymbol{E}) = \frac{1}{2}\boldsymbol{E} : \mathbb{C} : \boldsymbol{E} \ . \tag{3.4}$$

For this choice of strain density function, the associated second Piola-Kirchhoff stress tensor reads as

$$\boldsymbol{S} = \frac{\partial\Psi(\boldsymbol{E})}{\partial\mathbf{E}} = \mathbb{C} : \boldsymbol{E} \ . \tag{3.5}$$

3.2.2 Phase-field formulation for finite strains

Consider the body Ω, subjected to mixed boundary conditions

$$\boldsymbol{P} \cdot \boldsymbol{N} = \bar{\boldsymbol{t}} \text{ on } \partial\Omega_N \tag{3.6}$$

and

$$\boldsymbol{u} = \overline{\boldsymbol{u}} \text{ on } \partial\Omega_D \ , \tag{3.7}$$

where $\boldsymbol{P} = \boldsymbol{F}\boldsymbol{S}$ is the first Piola-Kirchhoff stress, and $\boldsymbol{N}$ is the outward-pointing unit vector on boundary $\partial\Omega_N$ in reference configuration. The total energy of the system is then given by:

$$\mathscr{E}(\boldsymbol{u}, d) = \int_\Omega \widetilde{\Psi}(\boldsymbol{E}(\boldsymbol{u}), d)\, d\Omega + g_c \int_\Omega \gamma(d, \nabla(d))\, d\Omega - \int_{\partial\Omega_N} \bar{\boldsymbol{t}} \cdot \boldsymbol{u}\, d\Gamma \ , \tag{3.8}$$

where $\widetilde{\Psi}$ is the degraded strain energy function and γ denotes the crack density function. In what follows, we only consider the case of local traction strain fields and do not take into account closure of cracks, for the sake of simplicity. Formulations considering the asymmetry of fracture (by spectrally decomposing in this context the local deformation operator $\boldsymbol{F}$) can be found elsewhere in the literature; see, e.g., [Hesch and Weinberg, 2014]. We thus define

$$\widetilde{\Psi}(\boldsymbol{E}, d) = g(d)\Psi(\boldsymbol{E}) \ , \tag{3.9}$$

where $g(d)$ is the degradation function described in section 1.3.4.2 (see [Bourdin et al., 2000]). The second Piola-Kirchhoff stress tensor is then given by

$$\boldsymbol{S}(\boldsymbol{E}, d) = \frac{\partial \tilde{\Psi}(\boldsymbol{E}, d)}{\partial \boldsymbol{E}} = g(d)\frac{\partial \Psi(\boldsymbol{E})}{\partial \boldsymbol{E}} = g(d)(\mathbb{C} : \boldsymbol{E}) \ .$$

The function γ takes the form

$$\gamma(d, \nabla d) = \frac{1}{2}\left(\frac{1}{\ell} d^2 + \ell \nabla(d) \cdot \nabla(d)\right) \ . \tag{3.10}$$

The coupled problem is nonlinear due to geometric nonlinearities. In this work, the solution is obtained by using a standard staggered scheme recalled in section 3.3.1.

3.3 Computational aspects

3.3.1 Staggered resolution strategy

As previously mentioned, a staggered solution strategy is adopted in which the damage and mechanical problems are alternatively solved for each quasi-static load increment. For a given state of damage, the mechanical problem

$$\boldsymbol{u} = \underset{\boldsymbol{u}^* \in \mathcal{S}_{\boldsymbol{u}}}{\operatorname{argmin}}\ \mathscr{E}(\boldsymbol{u}^*, d)) \ , \tag{3.11}$$

where $\mathcal{S}_{\boldsymbol{u}}$ is a set of kinematically admissible fields, is solved by using the Newton-Raphson method. The associated weak form can be expressed as :

$$\int_\Omega (\boldsymbol{P}(\boldsymbol{u}), \nabla\delta\boldsymbol{u}) d\Omega = \int_{\partial\Omega_N} (\bar{\boldsymbol{t}}(\boldsymbol{u}), \delta\boldsymbol{u}) dS \ , \tag{3.12}$$

with $\boldsymbol{P}$ the first Piola-Kirchhoff stress. It can also be written as :

$$\int_\Omega \Big(\boldsymbol{S}(\boldsymbol{E}(\boldsymbol{u})), \delta\boldsymbol{E}(\delta\boldsymbol{u}, \boldsymbol{u})\Big) d\Omega = \int_{\partial\Omega_N} (\bar{\boldsymbol{t}}(\boldsymbol{u}^*), \delta\boldsymbol{u}) dS \ , \tag{3.13}$$

with $\boldsymbol{S}$ the second Piola-Kirchhoff stress express in Eq. (3.64) and $\boldsymbol{E}$ the Green-Lagrange strain tensor. Regarding the phase-field problem, a weak form similar to the one obtained at small strains is derived :

$$\int_\Omega \left[\left(\frac{g_c}{\ell} + 2\mathscr{H} \right) (d, \delta d) + g_c \ell (\nabla d, \nabla \delta d) \right] d\Omega = \int_\Omega (2\mathscr{H}, \delta d) d\Omega \ , \tag{3.14}$$

where the history function is given by

$$\mathscr{H}(\boldsymbol{x}, t) = \max_{\tau \in [0,t]} \{ \Psi (\boldsymbol{E}(\boldsymbol{x}, \tau)) \} \ , \tag{3.15}$$

describing the irreversible process of damage in time and Ψ is defined in (3.4).

The algorithmic structure for this procedure is described in Fig 3.1.

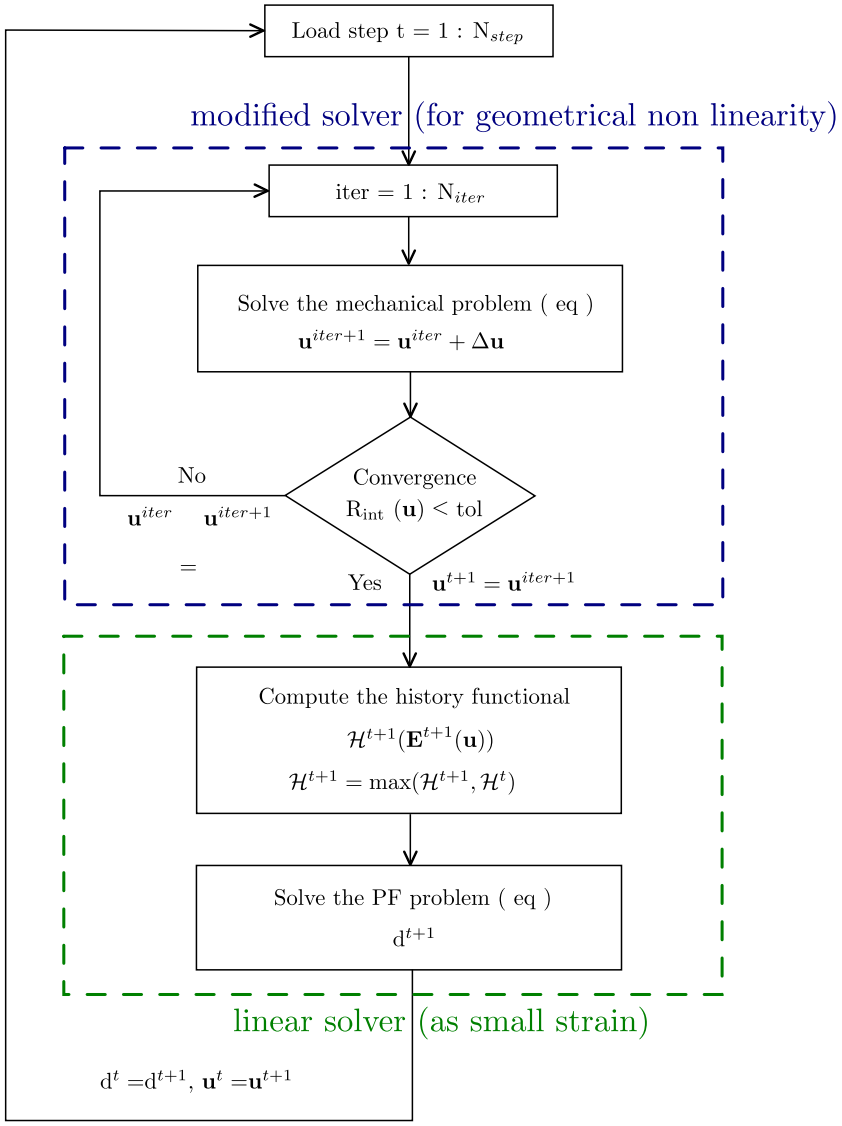

Figure 3.1 – Algorithm used to solve the phase-field formulation at finite strains.

3.3.2 Linearization of the mechanical problem

The residual associated with the weak form of the mechanical problem in the initial configuration is defined as :

$$R(\boldsymbol{u},\delta\boldsymbol{u}) = \int_\Omega \boldsymbol{S}(\boldsymbol{E}(\boldsymbol{u}),d) : \delta\boldsymbol{E}(\boldsymbol{u},\delta\boldsymbol{u})\, d\Omega - \int_{\partial\Omega_N} \bar{\boldsymbol{t}}(\boldsymbol{u})\cdot\delta\boldsymbol{u}\, d\Gamma \ , \tag{3.16}$$

where d is temporarily frozen (staggered scheme) and $\delta\boldsymbol{E}$ is the variation of $\boldsymbol{E}$ obtained through the directional derivative. Let

$$R(\boldsymbol{u},\delta\boldsymbol{u}) = R_{\text{int}}(\boldsymbol{u},\delta\boldsymbol{u}) - R_{\text{ext}}(\boldsymbol{u},\delta\boldsymbol{u}) = 0 \ , \tag{3.17}$$

where R_{int} and R_{ext} are defined as

$$R_{\text{int}}(\boldsymbol{u},\delta\boldsymbol{u}) = \int_\Omega \boldsymbol{S}(\boldsymbol{E}(\boldsymbol{u}),d) : \delta\boldsymbol{E}(\boldsymbol{u},\delta\boldsymbol{u})\, d\Omega, \quad R_{\text{ext}}(\boldsymbol{u},\delta\boldsymbol{u}) = \int_{\partial\Omega_N} \bar{\boldsymbol{t}}\cdot\delta\boldsymbol{u}\, d\Gamma \ . \tag{3.18}$$

Here an implicit assumption is made on R_{ext} that there is no tracking force, such as pressure. By applying the Newton-Raphson method, the linearization of the residual is written

$$R(\boldsymbol{u}^{k+1},\delta\boldsymbol{u}) \approx R(\boldsymbol{u}^{k},\delta\boldsymbol{u}) + D_{\Delta\boldsymbol{u}}R(\boldsymbol{u}^{k},\delta\boldsymbol{u}) \ , \tag{3.19}$$

must be evaluated, where $D_{\Delta\boldsymbol{u}}R(\boldsymbol{u}^k,\delta\boldsymbol{u}) = D_{\Delta\boldsymbol{u}}R_{\text{int}}(\boldsymbol{u}^k,\delta\boldsymbol{u})$ is the directional derivative of the residual at $\boldsymbol{u}^k$ in the direction of $\Delta\boldsymbol{u}$, with $\boldsymbol{u}^{k+1} = \boldsymbol{u}^k + \Delta\boldsymbol{u}$. This derivative reads

$$D_{\Delta\boldsymbol{u}}R(\boldsymbol{u},\delta\boldsymbol{u}) = D_{\Delta\boldsymbol{u}}\bigg(\int_\Omega \boldsymbol{S}(\boldsymbol{E}(\boldsymbol{u}),d) : \delta\mathbf{E}(\boldsymbol{u},\delta\boldsymbol{u})\bigg) d\Omega \ , \tag{3.20}$$

where the superscript indicating the iteration is omitted for notational convenience. Proceeding with calculus leads to

$$\begin{aligned}
D_{\Delta\boldsymbol{u}}R(\boldsymbol{u},\delta\boldsymbol{u}) &= \int_\Omega D_{\Delta\boldsymbol{u}}\Big(\boldsymbol{S}(\boldsymbol{E}(\boldsymbol{u}),d)\Big) : \delta\boldsymbol{E}(\boldsymbol{u},\delta\boldsymbol{u})\, d\Omega \\
&\qquad + \int_\Omega \boldsymbol{S}(\boldsymbol{E}(\boldsymbol{u},d)) : D_{\Delta\boldsymbol{u}}\Big(\delta\boldsymbol{E}(\boldsymbol{u},\delta\boldsymbol{u})\Big) d\Omega \\
&= \int_\Omega \Delta\mathbf{E}(\boldsymbol{u},\Delta\boldsymbol{u}) : \frac{\partial}{\partial\boldsymbol{E}}\Big(\boldsymbol{S}(\boldsymbol{E}(\boldsymbol{u}),d)\Big) : \delta\boldsymbol{E}(\boldsymbol{u},\delta\boldsymbol{u})\, d\Omega \\
&\qquad + \int_\Omega \boldsymbol{S}(\boldsymbol{E}(\boldsymbol{u}),d) : \Delta\delta\boldsymbol{E}(\Delta\boldsymbol{u},\delta\boldsymbol{u})\, d\Omega \\
&= \int_\Omega \Delta\mathbf{E}(\boldsymbol{u},\Delta\boldsymbol{u}) : \mathbb{C}^t_M(\boldsymbol{E}(\boldsymbol{u}),d) : \delta\boldsymbol{E}(\boldsymbol{u},\delta\boldsymbol{u})\, d\Omega \\
&\qquad + \int_\Omega \boldsymbol{S}(\boldsymbol{E}(\boldsymbol{u}),d) : \Delta\delta\boldsymbol{E}(\Delta\boldsymbol{u},\delta\boldsymbol{u})\, d\Omega,
\end{aligned}$$

where $\Delta\delta\boldsymbol{E} = \delta\boldsymbol{F}^T\Delta\boldsymbol{F} + \Delta\boldsymbol{F}\delta\boldsymbol{F}^T$, with $\Delta\boldsymbol{F} = \nabla(\Delta\boldsymbol{u})$, and $\mathbb{C}^t_M$ is the fourth-order tensor for isotropic material and defined by

$$\mathbb{C}^t_M(\boldsymbol{E}(\boldsymbol{u}),d) = \frac{\partial}{\partial\boldsymbol{E}}\Big(g(d)[\lambda\,\mathrm{tr}(\boldsymbol{E})\boldsymbol{I} + 2\mu\boldsymbol{E}]\Big) \ . \tag{3.21}$$

By using the relationships:

$$\frac{\partial\boldsymbol{E}}{\partial\boldsymbol{E}} = \mathbb{I} \ \text{ and } \ \frac{\partial\mathrm{tr}(\boldsymbol{E})\boldsymbol{I}}{\partial\boldsymbol{E}} = \boldsymbol{I}\otimes\boldsymbol{I} \ , \tag{3.22}$$

or in indicial notation

$$\frac{\partial E_{ij}}{\partial E_{kl}} = \frac{1}{2}(\delta_{ik}\delta_{jl} + \delta_{il}\delta_{jk}) \quad \text{and} \quad \frac{\partial E_{pp}\delta_{ij}}{\partial E_{kl}} = \delta_{ij}\delta_{pk}\delta_{pl} = \delta_{ij}\delta_{kl} \ , \tag{3.23}$$

where $\mathbb{I}$ is the fourth-order (symmetric) identity tensor and $\otimes$ denotes the tensor product, the tangent material tensor $\mathbb{C}_M^t$ can be defined as:

$$\mathbb{C}_M^t(\boldsymbol{E}(\boldsymbol{u}), d) = g(d)[\lambda \boldsymbol{I} \otimes \boldsymbol{I} + 2\mu\mathbb{I}] \ . \tag{3.24}$$

Combining

$$D_{\Delta \boldsymbol{u}} R(\boldsymbol{u}^k, \delta\boldsymbol{u}) = -R(\boldsymbol{u}^k, \delta\boldsymbol{u}) \ , \tag{3.25}$$

the finite element discretization then leads to a linear system

$$[\boldsymbol{K}_u(\boldsymbol{u})]\{\Delta\boldsymbol{u}\} = \{\boldsymbol{F}_u(\boldsymbol{u})\} \tag{3.26}$$

to be solved for the increment $\Delta\boldsymbol{u}$. The finite element discretization is presented in the next section.

3.3.3 Finite element discretization

This section is devoted to the finite element discretization of the linearized problem.

Mechanical problem

La solution en déplacement $\boldsymbol{u}$, la fonction de test $\delta\boldsymbol{u}$ et le déplacement incrémental $\Delta\boldsymbol{u}$ sont interpolés sur chaque élément comme :

$$\boldsymbol{u}(\boldsymbol{x}) = [\boldsymbol{N}_u(\boldsymbol{x})]\{\boldsymbol{u}_e^i\} \ , \tag{3.27}$$

$$\delta\boldsymbol{u}(\boldsymbol{x}) = [\boldsymbol{N}_u(\boldsymbol{x})]\{\delta\boldsymbol{u}_e^i\} \ , \tag{3.28}$$

$$\Delta\boldsymbol{u}(\boldsymbol{x}) = [\boldsymbol{N}_u(\boldsymbol{x})]\{\Delta\boldsymbol{u}_e^i\} \ , \tag{3.29}$$

where $[\boldsymbol{N}_u(\boldsymbol{x})]$ is the matrix of shape functions and the subscript e indicates vectors of i-nodal values. The gradient $\nabla_X \boldsymbol{u}$ is defined according to the convention

$$\nabla_X \boldsymbol{u} = (u_{1,1}, u_{1,2}, u_{2,1}, u_{2,2})^T \tag{3.30}$$

in 2D and

$$\nabla_X \boldsymbol{u} = (u_{1,1}, u_{1,2}, u_{1,3}, u_{2,1}, u_{2,2}, u_{2,3}, u_{3,1}, u_{3,2}, u_{3,3})^T \tag{3.31}$$

in 3D, and is computed through

$$\nabla_X \boldsymbol{u}(\boldsymbol{x}) = [\boldsymbol{G}(\boldsymbol{x})]\{\boldsymbol{u}_e^i\} \ , \tag{3.32}$$

where the matrix $[\boldsymbol{G}(\boldsymbol{x})]$ gathers spatial derivatives of the shape functions; see Appendix. (A.2.1) for examples in 2D (T3 element) and 3D (T4 element). A Kelvin notation (or convention) is adopted to define the vector forms of the second Piola-Kirchhoff stress tensor and Green-Lagrange tensor, that is

$$\{\boldsymbol{S}\} \overset{2D}{:=} \{S_{11}, S_{22}, \sqrt{2}S_{12}\}^T \ , \quad \{\boldsymbol{S}\} \overset{3D}{:=} (S_{11}, S_{22}, S_{33}, \sqrt{2}S_{23}, \sqrt{2}S_{13}, \sqrt{2}S_{12})^T \ , \tag{3.33}$$

and

$$\{\boldsymbol{E}\} \overset{2D}{:=} \{E_{11}, E_{22}, \sqrt{2}E_{12}\}^T, \quad \{\boldsymbol{E}\} \overset{3D}{:=} (E_{11}, E_{22}, E_{33}, \sqrt{2}E_{23}, \sqrt{2}E_{13}, \sqrt{2}E_{12})^T \ . \tag{3.34}$$

Furthermore, we let

$$\{\delta \boldsymbol{E}\} = [\boldsymbol{B_t}(\boldsymbol{x}, \boldsymbol{u})]\{\delta \boldsymbol{u}_e^i\} \tag{3.35}$$

and

$$\{\Delta \boldsymbol{E}\} = [\boldsymbol{B_t}(\boldsymbol{x}, \boldsymbol{u})]\{\Delta \boldsymbol{u}_e^i\} \ , \tag{3.36}$$

with

$$[\boldsymbol{B_t}(\boldsymbol{x}, \boldsymbol{u})] = [\boldsymbol{B_e}(\boldsymbol{x}) + \boldsymbol{B_u}(\boldsymbol{x}, \boldsymbol{u})] \ . \tag{3.37}$$

Expressions for these matrices can be found in Appendix. (A.2.2) for the 2D and 3D cases. The matrix form of the fourth-order elasticity tensor at small strains is written as

$$[\mathbb{C}] = \begin{bmatrix} \lambda + 2\mu & \lambda & 0 \\ \lambda & \lambda + 2\mu & 0 \\ 0 & 0 & 2\mu \end{bmatrix} \tag{3.38}$$

in 2D plane strain, and as

$$[\mathbb{C}] = \begin{bmatrix} \lambda + 2\mu & \lambda & \lambda & 0 & 0 & 0 \\ \lambda & \lambda + 2\mu & \lambda & 0 & 0 & 0 \\ \lambda & \lambda & \lambda + 2\mu & 0 & 0 & 0 \\ 0 & 0 & 0 & 2\mu & 0 & 0 \\ 0 & 0 & 0 & 0 & 2\mu & 0 \\ 0 & 0 & 0 & 0 & 0 & 2\mu \end{bmatrix} \tag{3.39}$$

in 3D.

Introducing the above discretization in Eq. (3.25), the problem can be written in each element Ω_e as

$$\forall \Omega_e, \quad [\boldsymbol{k}_u(\boldsymbol{u}; e)]\{\Delta \boldsymbol{u}_e^i\} = \{\boldsymbol{f}_u(\boldsymbol{u}; e)\} \ , \tag{3.40}$$

where damage variable d is omitted to simplify notation, and the stiffness matrix $[\boldsymbol{k}_u(\boldsymbol{u}, e)]$ is decomposed as

$$[\boldsymbol{k}_u(\boldsymbol{u}; e)] = [\boldsymbol{k}_u^1(\boldsymbol{u}; e)] + [\boldsymbol{k}_u^2(\boldsymbol{u}; e)] \ , \tag{3.41}$$

$\boldsymbol{k}_u^1$, $\boldsymbol{k}_u^2$ are interpreted here as the elementary elastic stiffness and the geometric stiffness, defined as

$$[\boldsymbol{k}_u^1(\boldsymbol{u}; e)] = \int_{\Omega_e} g(d) \Big\{ [\boldsymbol{B}_t(\boldsymbol{x}, \boldsymbol{u}; e)]^T \Big(\lambda(e)[\boldsymbol{I} \otimes \boldsymbol{I}] + 2\mu(e)[\mathbb{I}] \Big) [\boldsymbol{B}_t(\boldsymbol{x}, \boldsymbol{u}; e)] \Big\} d\Omega \tag{3.42}$$

and

$$[\boldsymbol{k}_u^2(\boldsymbol{u}; e)] = \int_{\Omega_e} [\boldsymbol{G}(\boldsymbol{x}; e)]^T [\boldsymbol{B_p}(\boldsymbol{S}(\boldsymbol{u}), \boldsymbol{x}; e)] d\Omega \ . \tag{3.43}$$

correspond to the first and second members in the left-hand side in Eq. (3.25). In the equations above, brackets indicate matrix forms of tensor-valued quantities, and $[\boldsymbol{B_p}]$ is defined in Appendix. A.2.3. Concerning the force vector in Eq. (3.40), we write

$$\{\boldsymbol{f}_u(\boldsymbol{x}, \boldsymbol{u}; e)\} = \{\boldsymbol{f}_u^{ext}(\boldsymbol{x}, \boldsymbol{u}; e)\} - \{\boldsymbol{f}_u^{int}(\boldsymbol{x}, \boldsymbol{u}; e)\} \ , \tag{3.44}$$

where the first term, associated with the external force contribution, is expressed as

$$\{\boldsymbol{f}_u^{ext}(\boldsymbol{x},\boldsymbol{u};e)\} = \int_{\Omega_e} [\boldsymbol{N}_u(\boldsymbol{x},\boldsymbol{u};e)]^T \{\bar{\boldsymbol{t}}(e)\} d\Omega \ , \tag{3.45}$$

with $\{\bar{\boldsymbol{t}}(e)\}$ the force vector defined by the Neumann boundary condition and applied on element Ω_e. The assumption of a well known force (without tracking force) has been made. The second term related to the internal force is defined as:

$$\{\boldsymbol{f}_u^{int}(\boldsymbol{u};e)\} = \int_{\Omega_e} [\boldsymbol{B}_t(\boldsymbol{x},\boldsymbol{u};e)]^T \{\boldsymbol{S}(\boldsymbol{u};e)\} d\Omega \ . \tag{3.46}$$

The displacement increment $\boldsymbol{\Delta u}$ is thus obtained by solving the linear problem

$$[\boldsymbol{K}_u(\boldsymbol{u})]\{\boldsymbol{\Delta u}\} = \{\boldsymbol{F}_u(\boldsymbol{u})\} \ , \tag{3.47}$$

where $[\boldsymbol{K}_u(\boldsymbol{u})]$ and $\{\boldsymbol{F}_u(\boldsymbol{u})\}$ are obtained by assembling elementary matrices:

$$[\boldsymbol{K}_u(\boldsymbol{u})] = \mathop{\mathrm{A}}_{e=1}^{N_e} [\boldsymbol{k}_u(\boldsymbol{u};e)], \quad [\boldsymbol{F}_u(\boldsymbol{u})] = \mathop{\mathrm{A}}_{e=1}^{N_e} [\boldsymbol{f}_u(\boldsymbol{u};e)] \ , \tag{3.48}$$

where A symbolically denotes here the assembly operator for displacement field problem. Note that the construction of all operators is based on the notation presented in [Bonnet and Frangi, 2007].

History functional

The computation of the history functional (see Eq. (3.68)) requires the Green-Lagrange matrix evaluated with displacement $\boldsymbol{u}$:

$$\boldsymbol{E} = \frac{1}{2}(\nabla_X \boldsymbol{u} + \nabla_X \boldsymbol{u}^T + \nabla_X \boldsymbol{u}^T \nabla_X \boldsymbol{u}) \ . \tag{3.49}$$

The function is then computed on the integration points according to:

$$\mathscr{H}(\boldsymbol{x},t) = \max_{\tau \in [0,t]} \left\{ \frac{\lambda}{2} \left(\mathrm{tr}\left(\boldsymbol{E}(\boldsymbol{x},\tau)\right)\right)^2 + \mu \mathrm{tr}\left\{ \left(\boldsymbol{E}(\boldsymbol{x},\tau)\right)^2 \right\} \right\} \ . \tag{3.50}$$

Damage problem

We proceed similarly for the damage problem defined identically as in small strain. So we recall the damage scalar field d and the associated test function δd are interpolated as

$$d(\boldsymbol{x}) = [\boldsymbol{N}_d(\boldsymbol{x})]\{\boldsymbol{d}_e^i\} \tag{3.51}$$

and

$$\delta d(\boldsymbol{x}) = [\boldsymbol{N}_d(\boldsymbol{x})]\{\delta \boldsymbol{d}_e^i\} \ . \tag{3.52}$$

Gradients are written as

$$\nabla_X d(\boldsymbol{x}) = [\boldsymbol{B}_d(\boldsymbol{x})]\{\boldsymbol{d}_e^i\} \tag{3.53}$$

and

$$\nabla_X \delta d(\boldsymbol{x}) = [\boldsymbol{B}_d(\boldsymbol{x})]\{\delta \boldsymbol{d}_e^i\} \ . \tag{3.54}$$

Above, $[\boldsymbol{N}_d(\boldsymbol{x})]$ and $[\boldsymbol{B}_d(\boldsymbol{x})]$ are the matrix of shape functions and their derivatives, respectively. The damage stiffness matrix $[\boldsymbol{k}_d(e)]$ in element Ω_e is defined as

$$[\boldsymbol{k}_d(e)] = \int_{\Omega_e} \left(\left(\frac{g_c}{\ell} + 2\mathscr{H} \right) [\boldsymbol{N}_d(\boldsymbol{x})]^T [\boldsymbol{N}_d(\boldsymbol{x})] + g_c \ell [\boldsymbol{B}_d(\boldsymbol{x})]^T [\boldsymbol{B}_d(\boldsymbol{x})] \right) d\Omega \ , \tag{3.55}$$

while the force vector $\{\boldsymbol{f}_d(\boldsymbol{x})\}$ reads as

$$\{\boldsymbol{f}_d(e)\} = \int_{\Omega_e} 2[\boldsymbol{N}_d(\boldsymbol{x})]^T \mathscr{H} d\Omega \ . \tag{3.56}$$

The above integrals are computed using a standard quadrature rule (see Eq. (A.9)).
Finally, the unknown damage field vector d is obtained by solving the global problem:

$$[\boldsymbol{K}_d]\{\boldsymbol{d}\} = \{\boldsymbol{F}_d\} \ , \tag{3.57}$$

where $[\boldsymbol{K}_d]$ and $\{\boldsymbol{F}_d\}$ are the assembled matrix and assembled force vector of the global damage problem

$$[\boldsymbol{K}_d] = \mathop{\mathrm{A}}_{e=1}^{N_e} [\boldsymbol{k}_d(e)] \ , \quad [\boldsymbol{F}_d] = \mathop{\mathrm{A}}_{e=1}^{N_e} [\boldsymbol{f}_d(e)] \ , \tag{3.58}$$

and where A symbolically denotes here the assembly operator for damage scalar problem relating the elementary operator ($[\boldsymbol{k}_d(e)]$, $\{\boldsymbol{f}_d(e)\}$) to the global system matrix ($[\boldsymbol{K}_d]$, $\{\boldsymbol{F}_d\}$).

3.4 Modeling of hydric shrinkage

In this section, we introduce the large deformation shrinkage model applied to 2D plane strain and 3D cases in order to model the experiments that will be presented in chapter 4, assuming either uniform strain in the thickness of clay the samples, as a first modeling attempt, or taking into account the full 3D complexity of the experiments and in particular heterogeneous shinkages along the thickness of the samples. Note here that the coupling with the phase field has been formulated in the retraction model to gather all the equations to deal with the complete problem: finite strain and shrinkage.

3.4.1 Phase-field formulation including hydric strains

Models coupling finite strains with thermal expansions can be found in, e.g., [Lu and Pister, 1975, Erbts and DüSter, 2012]. Here, we pursue a similar approach, substituting hydric parameters for thermal coefficients. The total deformation gradient is thus defined through the multiplicative decomposition:

$$\boldsymbol{F} = \boldsymbol{F}_e \boldsymbol{F}_\hbar \ , \tag{3.59}$$

where $\boldsymbol{F}_e$ and $\boldsymbol{F}_\hbar$ are associated with the elastic and hydric parts of the strain; see Fig. 3.2.
In the present work, the hydric strain is modeled as a purely volumetric contribution and is defined as

$$\boldsymbol{F}_\hbar = \mathscr{F}(\hbar)\boldsymbol{I} \ , \tag{3.60}$$

where $\mathscr{F}$ is a nonlinear function of the hydric evolution parameter, denoted by h. This function can be identified based on an experimental study; see chapter 5. Below, we simply exemplify the procedure and choose

$$\boldsymbol{F}_\hbar = \hbar \boldsymbol{I} \ , \tag{3.61}$$

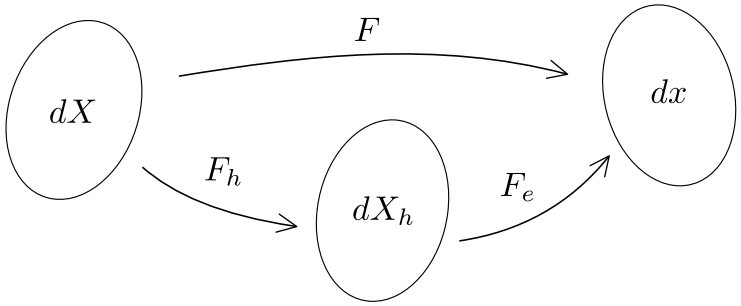

Figure 3.2 – Decomposition of the total deformation gradient.

for the sake of illustration. It is known that the Lagrangian strain $\boldsymbol{E}$ corresponding to $\boldsymbol{F}$ is given by

$$\boldsymbol{E} = \boldsymbol{E}_{\hbar} + \boldsymbol{F}_{\hbar}^{T} \boldsymbol{E}_e \boldsymbol{F}_{\hbar} \ , \tag{3.62}$$

where $\boldsymbol{E}_{\hbar}$ and $\boldsymbol{E}_e$ are the Green-Lagrange strain tensors associated with $\boldsymbol{F}_{\hbar}$ and $\boldsymbol{F}_e$, respectively. By combining Eq. (3.61) and Eq. (3.62), it follows that

$$\boldsymbol{E} = \boldsymbol{E}_{\hbar} + h^2 \boldsymbol{E}_e \ , \tag{3.63}$$

where $\boldsymbol{E}_{\hbar} = \alpha_{\hbar} \mathbf{1}$ with $\alpha_{\hbar} = \frac{1}{2}(h^2 - 1)$. Using the constitutive relationship defined in Eq. (3.5), we deduce

$$\boldsymbol{S}(\boldsymbol{E}(\boldsymbol{u}), \boldsymbol{E}_{\hbar}, d) = \frac{g(d)}{h^2} \Big([\lambda \mathrm{tr}(\boldsymbol{E}) + 2\mu \boldsymbol{E}] - [\lambda \mathrm{tr}(\boldsymbol{E}_{\hbar}) + 2\mu \boldsymbol{E}_{\hbar}] \Big) \ . \tag{3.64}$$

History functional

To take into account the damage only within traction, the strain density function is modified according to

$$\Psi(\boldsymbol{E}, \boldsymbol{E}_{\hbar}) = \Psi^{+}(\boldsymbol{E}, \boldsymbol{E}_{\hbar}) + \Psi^{-}(\boldsymbol{E}, \boldsymbol{E}_{\hbar}) \ , \tag{3.65}$$

with

$$\Psi^{\pm}(\boldsymbol{E_e}) = \frac{\lambda}{2} \left(\langle \mathrm{tr}\,(\boldsymbol{E_e}) \rangle^{\pm} \right)^2 + \mu \mathrm{tr} \left\{ \left(\boldsymbol{E_e^{\pm}} \right)^2 \right\} \ . \tag{3.66}$$

The spectral decomposition is applied in this case to $\boldsymbol{E}_e$ tensor as:

$$\boldsymbol{E}_e^{\pm} = \sum_{i=1}^{m} < \kappa_i >^{\pm} \boldsymbol{\varphi}^{(i)} \otimes \boldsymbol{\varphi}^{(i)} \ , \tag{3.67}$$

in which $\{(\kappa_i, \boldsymbol{\varphi}^{(i)})\}_{i=1}^{m}$ are the pairs of associated eigenvalues and eigenvectors of the strain tensor $\boldsymbol{E}_e$, and $< \cdot >^{\pm}$ is the same operator defined in (1.48).

The history function $\mathscr{H}$ is actualized in finite strain, on the positive part(see e.g. [Areias et al., 2016]) and caused only by the total strain tensor $\boldsymbol{E}$ according to

$$\mathscr{H}(\mathbf{x}, t) = \max_{\tau \in [0,t]} \left\{ \Psi^{+}(\boldsymbol{E}\,(\boldsymbol{x}, \tau)) \right\} \ . \tag{3.68}$$

The equations of the model with hydric shrinkage are summarized as follows.

Strong forms

The cracking problem is defined as two incremental problems (mechanical and damage) solved with a history function updated at each time step $\tau \in [0,t]$; the strong forms associated are defined as:
Mechanical problem:

$$\begin{cases} \mathrm{Div}_X(\boldsymbol{P}) = 0 \text{ on } \Omega \\ \boldsymbol{S}(\boldsymbol{E}(\boldsymbol{u}), \boldsymbol{E}_\hbar, d) = \frac{g(d)}{h^2}\mathbb{C}(\boldsymbol{E} - \boldsymbol{E}_\hbar) \\ \boldsymbol{E}_\hbar = \alpha_\hbar \boldsymbol{I} \\ \boldsymbol{u} = \boldsymbol{u}^D \text{ on } \partial\Omega_D \\ \boldsymbol{P}\cdot\boldsymbol{N} = (\bar{\boldsymbol{t}}) \text{ on } \partial\Omega_N \end{cases} \tag{3.69}$$

where $\mathrm{Div}_X(.)$ denotes divergence operator with respect to the reference configuration and assuming $\bar{\boldsymbol{t}}$ well known (no tracking forces).

Damage problem:

$$\begin{cases} 2(1-d)\mathscr{H}(\tau) - \frac{g_c}{l}\{d - \Delta_X d\} = 0 \text{ on } \Omega \\ d(\boldsymbol{x}) = 1 \text{ on } \Gamma \\ \nabla_X d(\boldsymbol{x})\cdot n = 0 \text{ on } \partial\Omega \end{cases} \tag{3.70}$$

where $\Delta_X(.)$ denotes the Laplacian operator with respect to the reference configuration.

Weak forms

Mechanical problem:

$$\int_\Omega \boldsymbol{S}(\boldsymbol{E}(\boldsymbol{u}), \boldsymbol{E}_\hbar, d) : \delta\boldsymbol{E}(\boldsymbol{u}, \delta\boldsymbol{u})\, d\Omega = \int_{\partial\Omega_N} \bar{\boldsymbol{t}}\cdot\delta\boldsymbol{u}\, d\Gamma \ , \tag{3.71}$$

Damage problem:

$$\int_\Omega \left[\left(\frac{g_c}{\ell} + 2\mathscr{H}\right)(d, \delta d) + g_c\ell(\nabla d, \nabla\delta d)\right] d\Omega = \int_\Omega (2\mathscr{H}, \delta d) d\Omega \ . \tag{3.72}$$

Discretization

Using Eqs. (3.71) and (3.64), problem (3.69) can be written as:

$$\int_\Omega \frac{g(d)}{h^2}(\mathbb{C} : (\boldsymbol{E}(\boldsymbol{u}) - \boldsymbol{E}_\hbar)) : \delta\boldsymbol{E}(\boldsymbol{u}, \delta\boldsymbol{u})\, d\Omega = \int_{\partial\Omega_N} \bar{\boldsymbol{t}}\cdot\delta\boldsymbol{u}\, d\Gamma \ . \tag{3.73}$$

Using the same linearization procedure described in Eq (3.3.2) the problem can be formulated as

$$\forall\Omega_e, \quad [\boldsymbol{k}_u(\boldsymbol{u}; e)]\{\Delta\boldsymbol{u}_e^i\} = \{\boldsymbol{f}_u(\boldsymbol{u}; e)\} \ . \tag{3.74}$$

The stiffness matrix $[\boldsymbol{k}_u(\boldsymbol{u}, e)]$ is decomposed according to:

$$[\boldsymbol{k}_u(\boldsymbol{u}; e)] = [\boldsymbol{k}_u^1(\boldsymbol{u}; e)] + [\boldsymbol{k}_u^2(\boldsymbol{u}; e)] \ , \tag{3.75}$$

where

$$[\boldsymbol{k}_u^1(\boldsymbol{u}; e)] = \int_{\Omega_e} \frac{g(d)}{h^2}\left\{[\boldsymbol{B}_t(\boldsymbol{x}, \boldsymbol{u}; e)]^T\left(\lambda(e)[\boldsymbol{I}\otimes\boldsymbol{I}] + 2\mu(e)[\mathbb{I}]\right)[\boldsymbol{B}_t(\boldsymbol{x}, \boldsymbol{u}; e)]\right\} d\Omega \ . \tag{3.76}$$

The modified operator is described in Appendix A.2.4.

$$[\boldsymbol{k}_u^2(\boldsymbol{u};e)] = \int_{\Omega_e} \frac{g(d)}{h^2}[\boldsymbol{G}(\boldsymbol{x};e)]^T[\boldsymbol{B}_{\boldsymbol{p}}(\boldsymbol{S}(\boldsymbol{E}(\boldsymbol{u}) - \boldsymbol{E}_{\hbar}), \boldsymbol{x};e)]d\Omega \ . \tag{3.77}$$

The force vector in Eq. (3.74) becomes:

$$\{\boldsymbol{f}_u(\boldsymbol{x},\boldsymbol{u};e)\} = \{\boldsymbol{f}_u^{ext}(\boldsymbol{x},\boldsymbol{u};e)\} - \{\boldsymbol{f}_u^{int}(\boldsymbol{x},\boldsymbol{u};e)\} \ , \tag{3.78}$$

where the first term, associated with the external force contribution, is still expressed as

$$\{\boldsymbol{f}_u^{ext}(\boldsymbol{x},\boldsymbol{u};e)\} = \int_{\Omega_e} [\boldsymbol{N}_u(\boldsymbol{x},\boldsymbol{u};e)]^T\{\bar{\boldsymbol{t}}(e)\}d\Omega \ . \tag{3.79}$$

where $\{\bar{\boldsymbol{t}}(e)\}$ is the force vector defined by the assumed fixed Neumann boundary condition and applied on element Ω_e. The second term related to the internal force is defined as:

$$\{\boldsymbol{f}_u^{int}(\boldsymbol{u};e)\} = \int_{\Omega_e} [\boldsymbol{B}_t(\boldsymbol{x},\boldsymbol{u};e)]^T\{\boldsymbol{S}(\boldsymbol{E}(\boldsymbol{u}) - \boldsymbol{E}_{\hbar};e)\}d\Omega \ . \tag{3.80}$$

or explicitly written as:

$$\{\boldsymbol{f}_u^{int}(\boldsymbol{u};e)\} = \int_{\Omega_e} \frac{g(d)}{h^2}[\boldsymbol{B}_t(\boldsymbol{x},\boldsymbol{u};e)]^T(\mathbb{C} : (\boldsymbol{E} - \boldsymbol{E}_{\hbar}))\}d\Omega \ . \tag{3.81}$$

The displacement increment $\boldsymbol{\Delta u}$ is thus obtained with shrinkage contribution by solving the linear problem

$$[\boldsymbol{K}_u(\boldsymbol{u})]\{\boldsymbol{\Delta u}\} = \{\boldsymbol{F}_u(\boldsymbol{u})\} \ , \tag{3.82}$$

where $[\boldsymbol{K}_u(\boldsymbol{u})]$ and $\{\boldsymbol{F}_u(\boldsymbol{u})\}$ are obtained by assembling elementary matrices:

$$[\boldsymbol{K}_u(\boldsymbol{u})] = \mathop{\mathrm{A}}_{e=1}^{N_e}[\boldsymbol{k}_u(\boldsymbol{u};e)] \ , \quad [\boldsymbol{F}_u(\boldsymbol{u})] = \mathop{\mathrm{A}}_{e=1}^{N_e}[\boldsymbol{f}_u(\boldsymbol{u};e)] \ , \tag{3.83}$$

where A symbolically denotes the assembly operator for displacement problem. The phase field discretization does not change and is formulated in section 3.3.3.

3.5 Numerical applications

Some computational tests will be presented, including a sensitivity analysis of the mesh, load increment, followed by a comparison test between linear and nonlinear modeling of the cracking model on sandard tests such as traction and pure shear. Finally, the last tests using the drying model will be presented.

3.5.1 Convergence with respect to mesh size

We firstly investigate a $S = 1 \times 1$ mm^2 square plate with a half notch placed on the left side of the specimen. The setup of the problem is shown in Fig. 3.3 for two boundary conditions. The first problem is denoted by "M$_I$" and is used to study the full traction problem attached to the mode-I fracture. The second example, referred to as "M$_{II}$" is related to a mode-II fracture (see the crack paths on Fig. 3.4).

Parameters of the system and boundary conditions are summarized in Table 3.1.

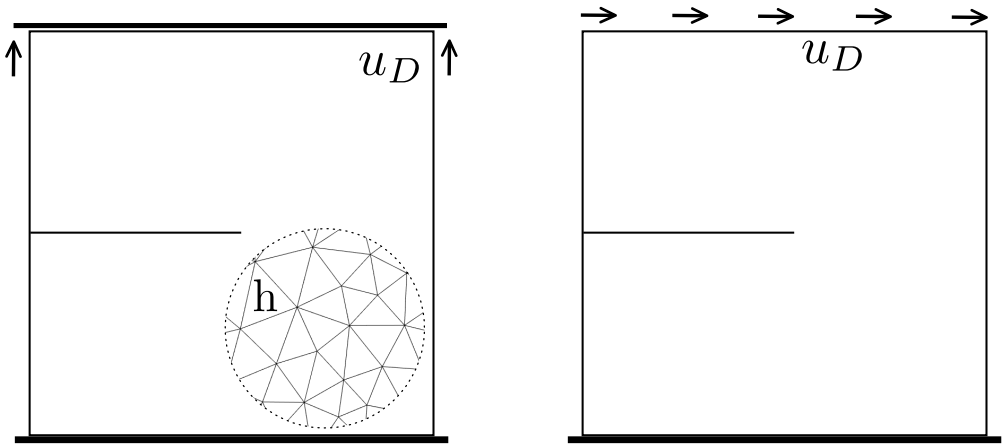

Figure 3.3 – Definition of boundary conditions for M_I (left) and M_{II} (right) tests.

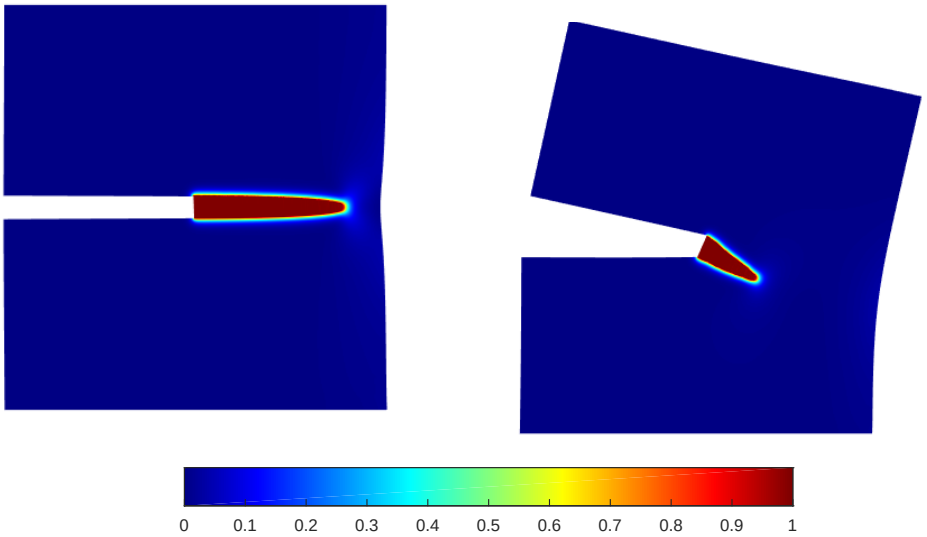

Figure 3.4 – Crack path illustration for: M_I (left) and M_{II} (right) tests.

	M_I (traction test)	M_{II} (shear test)
λ [GPa]	121.15	121.15
μ [GPa]	80.77	80.77
g_c [kN/mm]	$2.7e^{-3}$	$2.7e^{-3}$
ℓ [mm]	7.5^{-3}	7.5^{-3}
Δu [mm]	$1.0e^{-5}$	$1.0e^{-5}$
h [mm]	$1.0e^{-3}$ - $3.0e^{-2}$	$1.0e^{-3}$ - $3.0e^{-2}$

Table 3.1 – M_I and M_{II} problem parameters for mesh convergence.

We use here 6 different mesh sizes to study the mesh convergence $h \in [1.0e^{-3} : 3.0e^{-2}]$ mm, refined within the areas where the crack propagates. We can observe in Fig. 3.5 the force response of the system for the M_I and M_{II} problems for the different mesh sizes h, which allows verifying the convergence with respect to the mesh discretization.

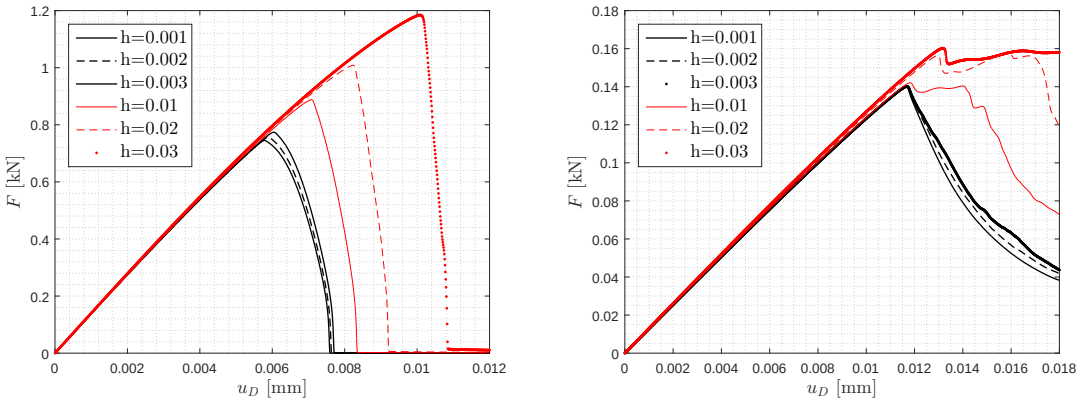

Figure 3.5 – Material response for M_I (left) and M_{II} (right) tests for different mesh size h.

The convergence of the maximum force response is analyzed with respect to the mesh size through M_I and M_{II} tests (see Fig. 3.6).

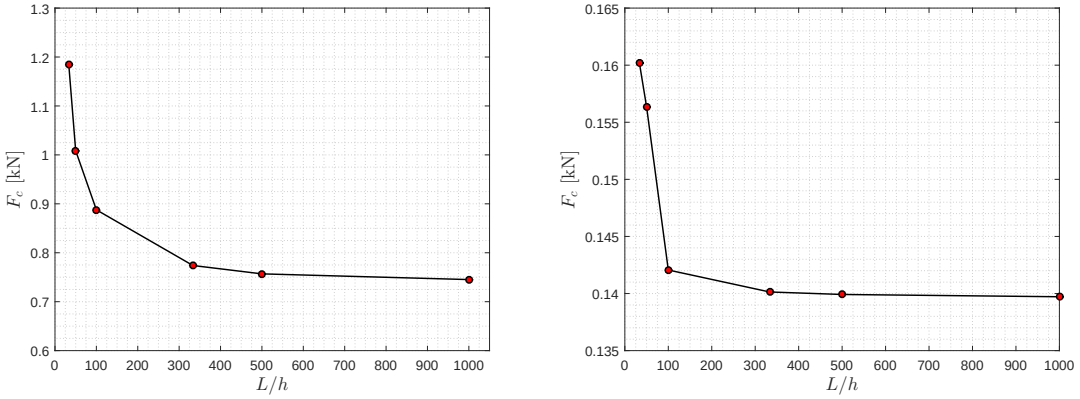

Figure 3.6 – Mesh convergence on critical energy F_c for M_I (left) and M_{II} (right) tests.

These results show the convergence with respect to the mesh size. It has been noticed in the literature [Nguyen et al., 2016a] that the convergence of the phase-field simulation is achieved when the relation between mesh size and the length of regularization respect: $h \leq 2\ell$. In the studied examples, convergence according to the regularization criterion is estimated at $L/h \geq 300$. For the next following study, we have chosen the mesh size $h = 2 \times 10^{-3}$ corresponding to $L/h = 500$.

3.5.2 Sensitivity with respect to load increments

In the previous tests, a constant load step $\Delta u = 1.0e^{-5}$ has been used (see Table 3.1). In the present example, (see Fig. 3.7), different load steps have been used. We can observe the influence of the load step on the mechanical response in the nonlinear phase after the maximal force F_c has been reached, as well as on the speed of crack propagation.

	M_I (traction test)	M_{II} (shear test)
λ [GPa]	121.15	121.15
μ [GPa]	80.77	80.77
g_c [kN/mm]	$2.7e^{-3}$	$2.7e^{-3}$
ℓ [mm]	7.5^{-3}	7.5^{-3}
$\Delta u_{(d<0.4))}$ [mm]	$1.0e^{-4}$	$1.0e^{-4}$
$\Delta u_{(d\geq 0.4))}$ [mm]	$1.0e^{-5}$ - $1.0e^{-6}$	$1.0e^{-5}$ - $1.0e^{-6}$
h [mm]	$2.0e^{-3}$	$2.0e^{-3}$

Table 3.2 – M_I and M_{II} problem parameters.

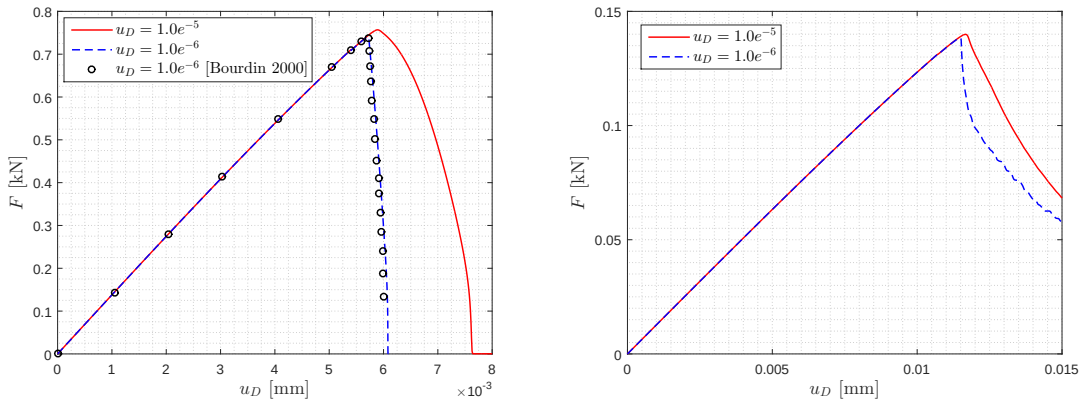

Figure 3.7 – Influence of loading step with respect to the mechanical response.

In Table 3.2 a coarse first step $\Delta u_{(d<\bar{d})} = 1.0e^{-4}$ is chosen until the system reaches a threshold of damage state $\bar{d}$ (here $\bar{d} = 0.4$). Then, the load displacement step is changed to $\Delta u_{(d\geq 0.4))}$ (here $\Delta u_{(d\geq 0.4))} = 1.0e^{-5}$ or $1.0e^{-6}$). In the present case of nonlinear solving procedure, the load step has been observed to yield instabilities with divergences of the Newton-Raphson for large loading steps and especially when d locally reaches 1. In the next numerical test, the fine load displacement step will be fixed for $\Delta u_{(d\geq 0.4))} = 1.0e^{-6}$.

3.5.3 Comparison between the linear and nonlinear formulations

The aim of this section is to qualitatively compare the responses obtained with the linear (Lin) and nonlinear (NL) phase-field formulations. For this first comparative study, we use the same definitions for problems M_I and M_{II} tests as previously. The crack propagation and the mechanical response are observed. The idea of the test is to change synthetically the g_c parameter controlling the crack apparition and to estimate the error between the classical linear mechanical problem and this non-linear formulation. Then, a parameter is defined as :

$$r_{gc} = \frac{g_c}{\bar{g}_c} \ , \tag{3.84}$$

where $\bar{g}_c$ is the Griffith energy parameter defined in Table 3.1 and commonly used in the literature as concrete property.

We first compare the critical force response (see Fig. 3.8). We can observe that for different values of r_{gc}, the difference of the maximal force value between Lin and NL formulation is important when increasing the critical displacement u_c controlled by an increase of the g_c parameter. Physically, we can interpret this as follows: when the crack nucleates for a prescribed displacement, the linear formulation underestimates the force response and overestimates the critical displacement as compared to the geometrical non-linear formulation.

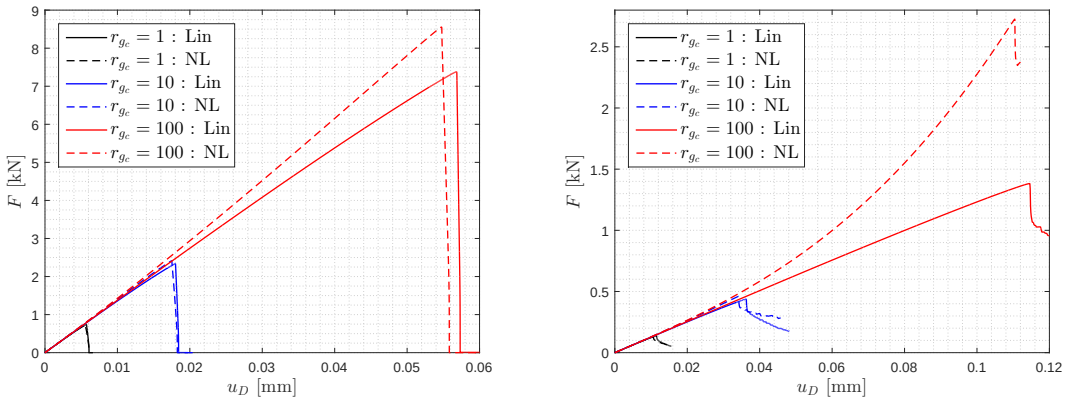

Figure 3.8 – Mechanical response for linear (Lin) and non-linear (NL) models for different values of fracture energy r_{gc} for (left) M_I and (right) M_{II} tests.

More specifically, by using the two comparison parameters (related to the critical force F_c or critical displacement u_c), we define the error between the linear and non-linear responses as:

$$\mathrm{err}(X) = 100 \times \left(1 - \frac{(X)_{\mathrm{Lin}}}{(X)_{\mathrm{NL}}}\right) \ . \tag{3.85}$$

Based on the previous tests, we can note that a significant difference between the Lin and NL formulation is achieved:

- For the M_I test :
  - The error $err(F_c)$ reaches $\approx 16\%$ when the crack starts to propagate around $u_c < 6\%L$ ($r_{gc} = 100$).
  - The error on the critical displacement is stable and around $err(u_c) = 3 - 4\%$.

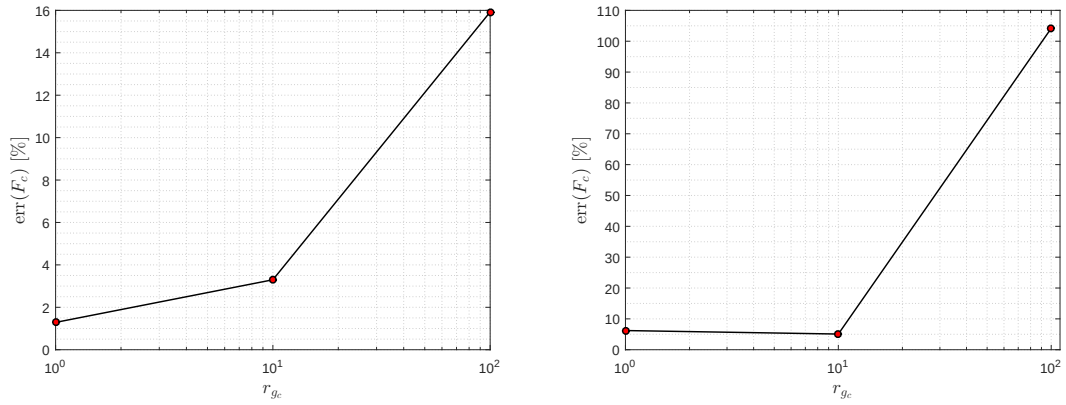

Figure 3.9 – Error on the maximum force response for several fracture energies r_{gc} for (left) M_I and (right) M_{II} tests.

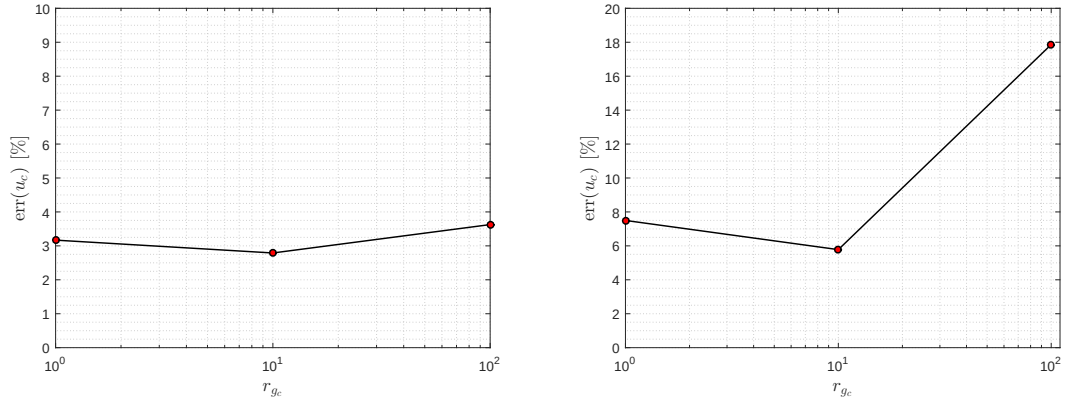

Figure 3.10 – Error on the critical displacement u_c for several fracture energies r_{gc} for (left) M_I and (right) M_{II} tests.

- For the M_{II} test :
  - The error $err(F_c)$ reaches $\approx 100\%$ when the crack starts to propagate around $u_c = 12\%L$ ($r_{gc} = 100$)
  - The error on the critical displacement is significally larger than for tension (always above 6

These errors have a consequence on the crack initiation, as observed in Fig. 3.11 for the M_I test and in Fig. 3.12 for the M_{II} test. We observe that the crack propagation in the NL context appears before the classical Lin formulation.

Based on these first results we conclude that even considering moderate amplitudes of loads, taking into account the geometrical nonlinear behavior has a significant influence on both the overall response of the sample as well as on the crack path.

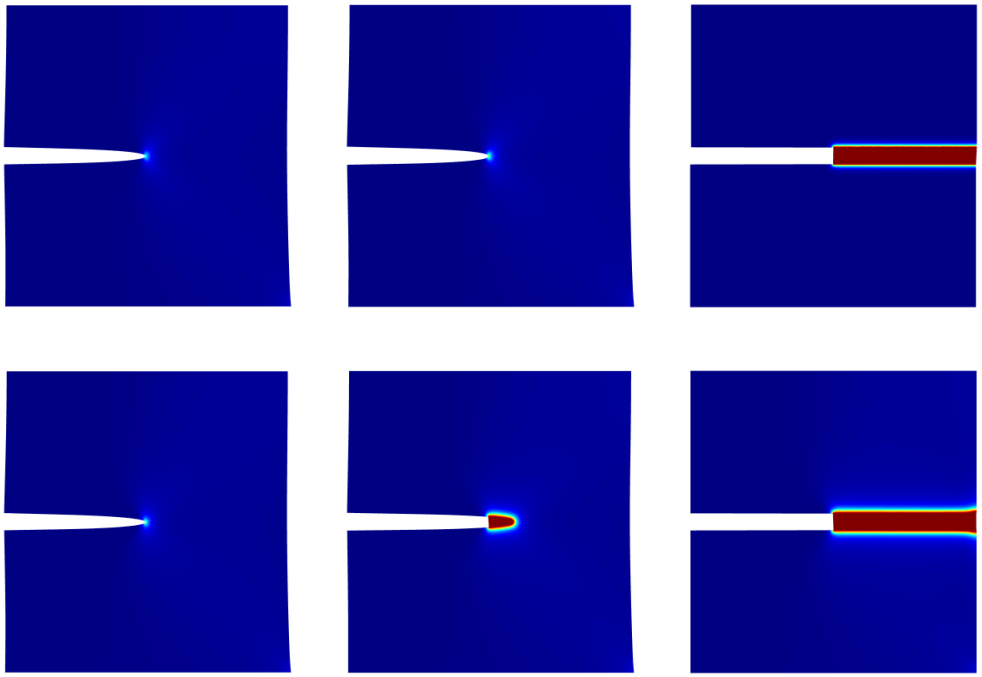

Figure 3.11 – Damage evolution M_I test (from left to right) for $u_D = \{1.10e^{-1}, 1.14e^{-1}, 1.18e^{-1}\}$ mm, with (top) linear formulation and (bottom) non-linear formulation.

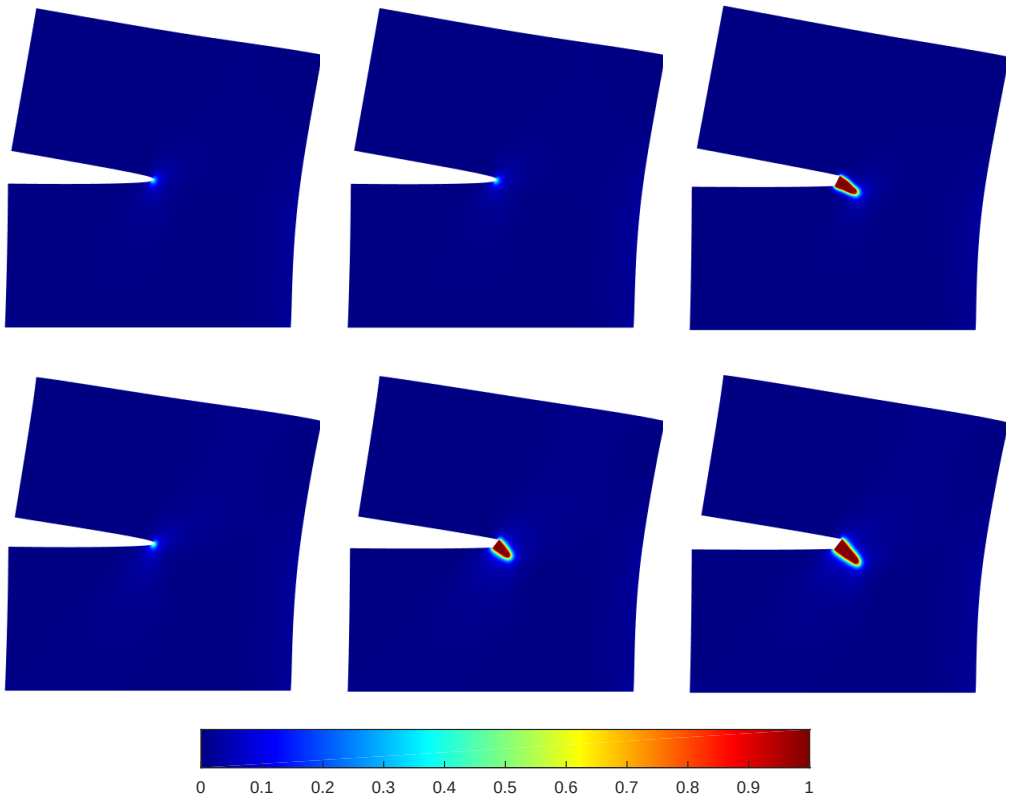

Figure 3.12 – Damage evolution M_{II} test (from left to right) for $u_D = \{5.5e^{-2}, 5.7e^{-2}, 6.0e^{-2}\}$ mm, with (top) linear formulation and (bottom) non-linear formulation.

3.5.4 3-point bending test

The three-point bending (3-PB) test is now investigated. The boundary conditions allow to reach the nonlinear regime quickly. The interest is therefore to observe with this formulation in large displacement how the structure behaves as compared to the small strain formulation, without changing the damage model. The geometry of the system is defined in Fig. 3.13 and the parameters are defined in Table 3.3.

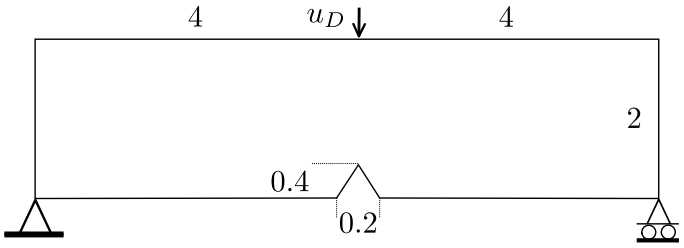

Figure 3.13 – 3-PB geometry and boundary conditions.

In the 3-PB test, the stress concentration at the point of application of the u_d displacement induces premature damage at this point. In order to avoid this, the evolution of the history function is deliberately locked at zero, over the entire (e = 0.2) top thickness of the sample.

As in the previous tests the mechanical responses are summarized in Fig. 3.14. Linear and non-linear formulations are compared directly with the elasticity without damage ($\forall t \in [0, t^n[$ $d = 0$). We notice once again that there is a significant difference between the Lin and NL responses. However, it is shown here that the Lin model overestimates the mechanical response as compared to the NL model.

Parameter [Unit]	Value
λ [GPa]	12.00
μ [GPa]	8.00
g_c [kN/mm]	$2.5e^{-4}$
ℓ [mm]	$3.0e^{-3}$
$\Delta u_{(d<0.40))}$ [mm]	$1.0e^{-4}$
$\Delta u_{(d\geq 0.40))}$ [mm]	$1.0e^{-6}$
h [mm]	$1.0e^{-3}$

Table 3.3 – 3-PB problem parameters.

These different tests (M_I, M_{II}, and 3-PB) allow to highlight, both quantitatively and qualitatively, the differences observed on the maximum force response and crack initiation between the models derived at small and large strains. It is noted that significant, problem-dependent differences are observed.

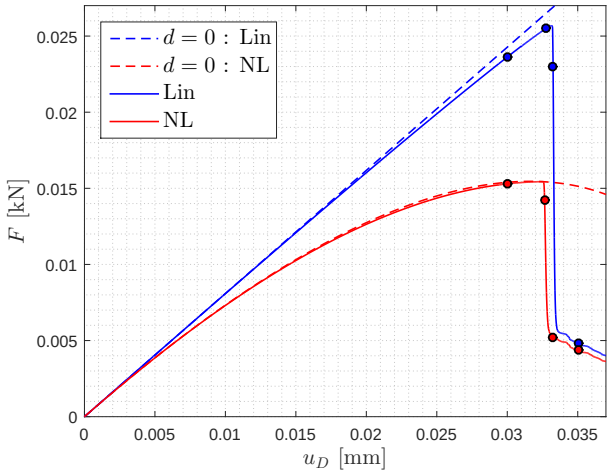

Figure 3.14 – Comparison between linear and non-linear 3-PB response with and without damage. The points on the curves relates to the crack path corresponding to the same displacement $\bar{u}_D = \{3.00e^{-2}, 3.27e^{-2}, 3.33e^{-2}, 3.50e^{-2}\}$ mm (see Fig. 3.15).

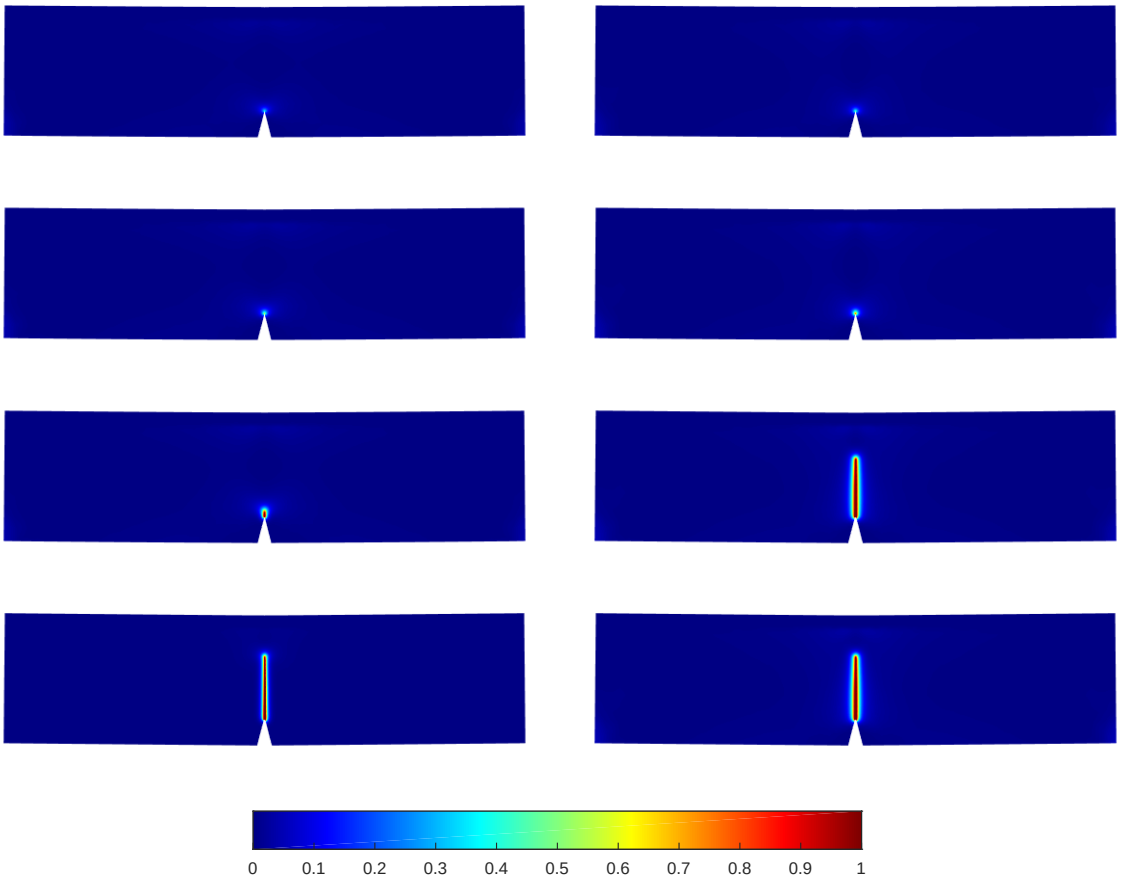

Figure 3.15 – 3-PB damage field with the linear (left) and nonlinear (right) formulation for $\bar{u}_D = \{3.00e^{-2}, 3.27e^{-2}, 3.33e^{-2}, 3.50e^{-2}\}$ mm (from top to bottom).

3.5.5 Hydric shrinkage of a homogeneous sample

In this numerical test, we consider a cylindrical sample as described in Figs. 3.17 and 3.18. The parameter $\hbar$ of retraction is related to the hydric strain through:

$$\boldsymbol{E}_{\hbar} = \alpha_{\hbar} \boldsymbol{I} \ , \tag{3.86}$$

with $\alpha_{\hbar} = \frac{1}{2}(\hbar^2 - 1)$. The hydric shrinkage is modeled as a compressive strain that increases linearly with time, according to :

$$\alpha_{\hbar}(t) = \alpha_{\hbar 0} t \ , \quad \forall t \in [0, 1] \ , \tag{3.87}$$

where the strain coefficient $\alpha_{\hbar 0}$ is arbitrarily set to $(0, 0.3)$.

The parameters for the simulations are defined in Table 3.4). The geometries for the 2D and 3D cases are as follows: in 2D, the sample is defined in an initial circular domain of r_0 and the shrinkage parameter $\alpha_{\hbar}$ acts on plan. In 3D we use the same radius and a height $h_0 = 0.1$ (see Fig. 3.18), $\alpha_{\hbar}$ affects also the height.

Parameter [Unit]	Value
E [MPa]	1.00
ν [–]	0.30
r_0 [mm]	1.0
h [mm]	4.0e^{-2}

Table 3.4 – Shrinkage problem parameters.

Note that no cracking parameters are used because we study in this part only the hydric shrinkage.
The evolution of the radius with respect to the retraction coefficient $\alpha_{\hbar}$ is shown in Fig. 3.16, for both the small strain and finite strain formulations.

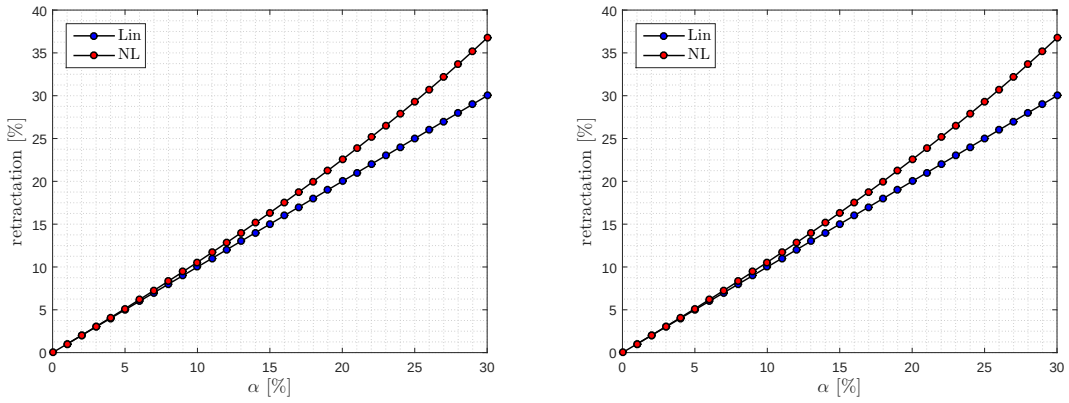

Figure 3.16 – Radius evolution with respect to hydric parameter $\alpha_{\hbar}$ for the linear and nonlinear formulations for 2D and 3D.

As expected, we can note from Fig. 3.16 that the two models significantly differ from one another for large values of the retraction coefficient.

From a qualitative standpoint, the difference becomes noticeable at $\alpha_{\hbar} = 30\%$, as seen in Fig. 3.17 for 2D plane strain and in Fig. 3.18 fo 3D, where contours of deformed configurations are displayed.

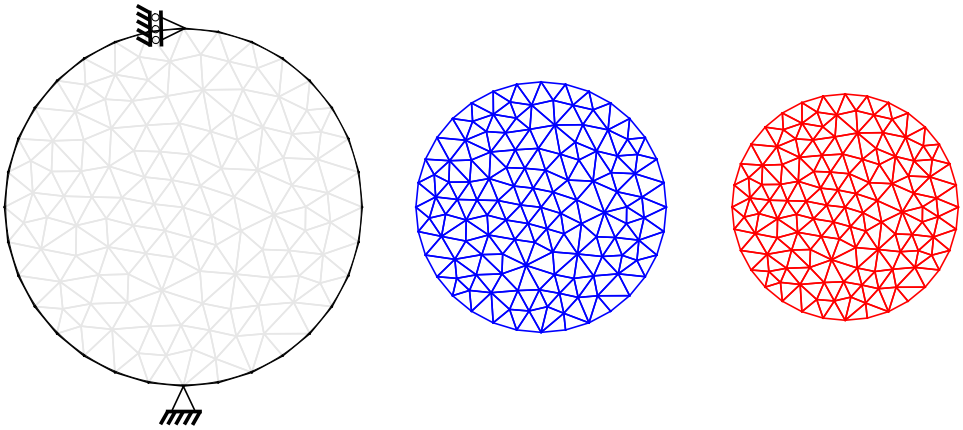

Figure 3.17 – Different shrinkage radius in 2D for initial (black) and after drying process with linear (blue) and non-linear (red) formulation.

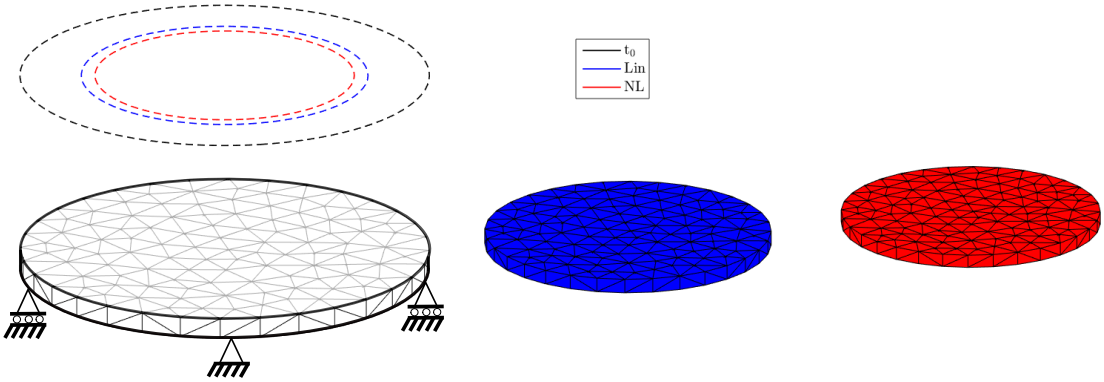

Figure 3.18 – Different shrinkage sample and the projection of their radius in 3D for initial (black) and after drying process with linear (blue) and non-linear (red) formulation.

The purpose of this test is to evaluate the evolution of the radius with the function of the water retraction parameter $\alpha_{\hbar}$ and then identify it experimentally.

3.5.6 Hydric shrinkage induced crack propagation

In this next example, we apply the above framework including finite strains, shrinkage strains and crack propagation. We consider a 2D circular domain as described in Fig. 3.19 (a)) containing a square stiff inclusion in its center. The radius is $r_0 = 50$ mm and the length of the square is $L_i = 30$ mm. The geometry was inspired from an experimental result of clay desiccation with such a geometry provided in [Barnier, 2015]. An illustration of the cracks induced in such test are provided in Fig. 3.20). The boundary conditions are as follows: the displacements on the external boundary $\partial\Omega$ (see Fig.3.19 (a)) are set to zero in the beginning of the simulation and the boundary of the square inclusion are stress-free. When cracks reach the external boundary, the boundary conditions are changed to stress free conditions. This choice is *a priori* opposed to experience. It is rather the contrary for an ideal drying experience, i.e. without friction, the displacement would be blocked around the rigid square and free edges at the outer contour. Thus the clay would want to shrink, but the square prevents it from moving. Finally, the conditions adopted here are closer to a sticking of the sample on the edges of the cup. However, the experiment is probably imperfect and would contain surface forces (below and/or around) that would change the loading conditions. The sample would contract but outwardly, possibly due to increased friction (such as contact surfaces) from the middle, which would cause a crack near the centre. These conditions, which we are going to use all the same, represent an advantage in terms of simplicity of numerical implementation.

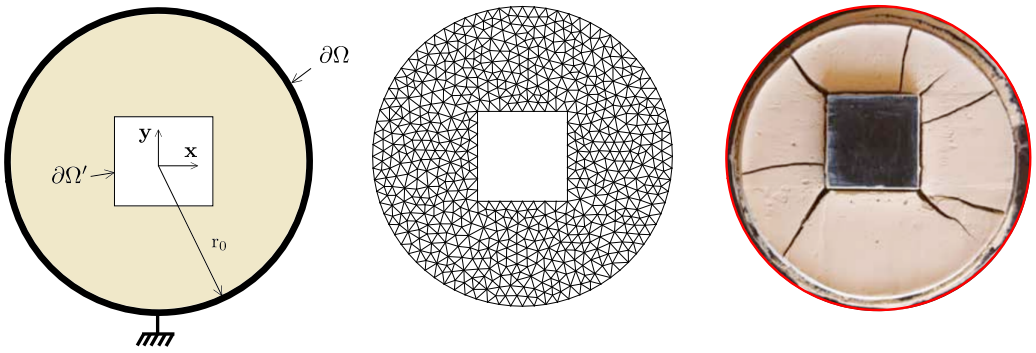

(a) (b) (c)

Figure 3.19 – (a) Geometry and boundaries conditions, (b) Mesh, (c) experimental result [Barnier, 2015].

Parameter [Unit]	Value
E [MPa]	1.00
ν [–]	0.30
g_c [N/m]	1.15
ℓ [mm]	2
r_0 [mm]	50.0
L_i [mm]	30.0
$\Delta t(d < 0.1))$ [–]	$1.0e^{-2}$
$\Delta t_{(d \geq 0.1))}$ [–]	$1.0e^{-4}$
h [mm]	0.8

Table 3.5 – Shrinkage induced crack problem parameters.

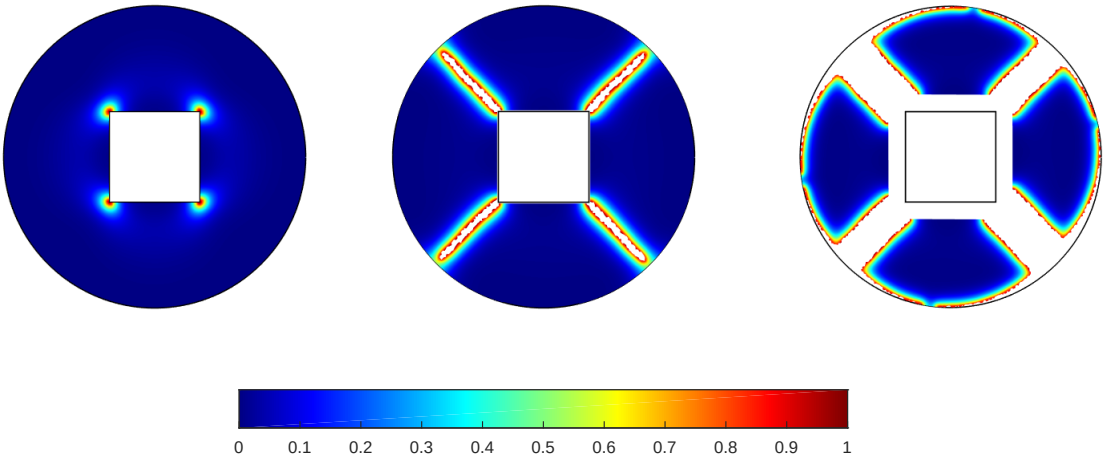

Figure 3.20 – Different shrinkage states $\alpha_{\hbar} = 0.01\% - 1\% - 10\%$.

We use a linear evolution of $\alpha_{\hbar}(t)$ with respect to time in Eq. (3.86) in the form

$$\alpha_{\hbar}(t) = A.t \ , \tag{3.88}$$

with A a constant $A = -0.1$, for a range time of $t \in [0,]$, using first, a time step $\Delta t = 10^{-2}$ s and then $\Delta t = 10^{-4}$ s when $d(\boldsymbol{x}) > 0.1$. All parameters of the simulation are listed in Table 3.5

Even though this example is used for illustration only of the theoretical model framework and does not intend to reproduce the experiments, we can appreciate that qualitatively, the cracks start from the boundaries of the inclusion and then propagate to the external boundary. After the propagation, the remaining parts continue to shrink as in the experiments.

3.6 Conclusion

In this chapter, we have presented a phase-field formulation for finite strains that accounts for compressive shrinkage strains. Borrowing most of the formulation from the literature, we first focused on parametric analyses, with the aim of characterizing the sensitivity to model parameters. In particular, we have investigated the effects of geometrical nonlinearities, even at moderate loading, and quantified the effects of the parameters on the convergence and stability for the macroscopic response. We then introduced a simple formulation where shrinkage is taken into account. A simple application example has been presented involving a heterogeneous sample, where both shrinkage and cracking were involved. In Chapter 5, the proposed model will be used for comparisons with the experimental results presented in the next chapter.

Chapter 4

Experimental clay desiccation

Contents

4.1 Introduction

This chapter presents an experimental study of the desiccation processes of a model heterogenous clayey medium. First, the clay material properties, the setup and the experimental conditions are presented. This allows observing and quantifying the shrinkage, the initiation and the propagation of cracks in the clay. The other objective is to identify the mechanisms involved during the shrinkage. An image correlation analysis on the deformation kinematics is also presented and adds valuable additional information to the observation. The presented experiments have been conducted at laboratoire Navier in the context of the post-doctoral project of Abdellali Dadda, also funded by Labex MMCD. The experimental program and the associated numerical simulations presented in chapter 5 were regularly discussed within the context of this collaborative project.

4.2 Experimental setup

4.2.1 Material

The material used in this experimental study is Romainville clay, found in the East Paris Basin. Its ability to shrink, swell and crack causes a lot of damage to buildings, especially in periods of severe drought. That is why several study campaigns have been conducted [Audiguier et al., 2007, Zemenu et al., 2009], to understand and analyze these phenomena. Geologically this clay is a composition of different sediments: Illite and Scmectite, carbonate, quartz and feldspath. The physical properties of this clay are referenced in Tab. 4.1.

Soil properties	Values
Density of solid phase [Mg.m^{-3}]	2.79
Liquid limit$^{(1)}$ [%]	77
Plastic limit$^{(2)}$ [%]	40
Plasticity index$^{(3)}$ [%]	37
USUC classification	CH
Clay (<2 μm) [%]	79
Clay composition	Illite and smectite
Specific surface area (methylene blue absorption) [m^2.g^{-1}]	340

Table 4.1 – Physical properties of Romainville clay [Tang et al., 2011].

(1) Liquid Limit is the water content at which soil changes from a plastic to a liquid state, the indication is related to the mass proportion of water in the mixture.
(2) Plastic Limit is the water content at the change from a plastic to a semisolid state.
(3) The plasticity index of a soil is the difference between its liquid and plastic limits.

4.2.2 Experimental method

For the preparation of the experiment, the clay paste was conditioned as in the studies of [Tang et al., 2011, Tang et al., 2012] and many others. In this work the same clay was used, and experimental investigations were carried out on cracking under hydro-mechanical effect, cyclic loading, for different temperatures, and other physical phenomena.

Figure 4.1 – Experimental sample : S_0, S_1, S_{1c}, S_3 and S_6.

For the sample preparation :

- the clay was taken directly from the site (Romainville, Paris-Est, France) by block;
- the material was cut into small 2 cm pieces and immersed in distilled water to liquify it for a period of $t = 24$ hours;
- then the whole set was passed through a $s = 2$ mm sieve, allowing us to filter out the larger particles;
- the resulting mixed sludge contains a water content of about $wc = 170\%$ at this stage, and was poured into $D = 116$ mm diameter petri dishes. Rigid inclusions (cylinders with circular cross section made of PMMA) were randomly placed in number ($n = 0, 1, 3$ or 6) as illustrated in Fig. 4.1. Note that the Petri dishes in which the clay is poured, is covered with a Teflon film in order to limit the effects of friction on the surface (both on the lateral walls and the bottom) as much as possible. A diagram of the preparation is shown in Fig. 4.2;

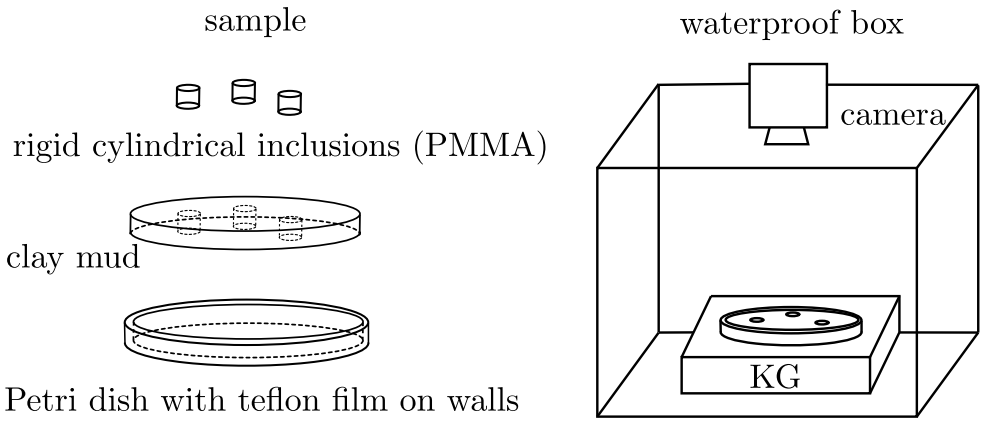

Figure 4.2 – Experimental setup sketch.

- the last step is the removal of air bubbles from the clay slurry: the samples are placed under vacuum for a period of 2 hours and left covered for sedimentation for 72 hours;
- before starting the analysis, the clay mud has evacuated the supernatant water film on the surface; the water content at t= 0 s of the test is $wr \sim 115\%$ and the thickness is $H = 8$ mm.

The clay sample is ready to be analyzed, and is placed in a wooden box of dimension $V = 50 \times 50 \times 50$ cm, preserves the sample from rapid variations of thermal or humidity variations or the surrounding the ambiant air. This box is however not tight, and its internal hygrothermal,conditions evolve with current laboratory conditions. Several measuring tools are placed in this box, namely: a scale, a thermometer and an ambient humidity probe, giving access to the water loss of the sample (and thus after processing of the full data the water content), the temperature and the humidity of the environment throughout the drying test.

After 72 hours, the sample has sufficiently stiffened and has been painted with black speckles on its surface, allowing to follow the retraction kinematics and to access the local deformations using a digital camera (Canon EOS TTL camera, equipped with a 18-55mm zoom lens, providing 8bit color images with 5184x3456 pixels). The image acquisition is done at time intervals of $\Delta t = 10$ min for different samples with different numbers of inclusions, as schematized in Fig. 4.2 and illustrated in Fig. 4.3.

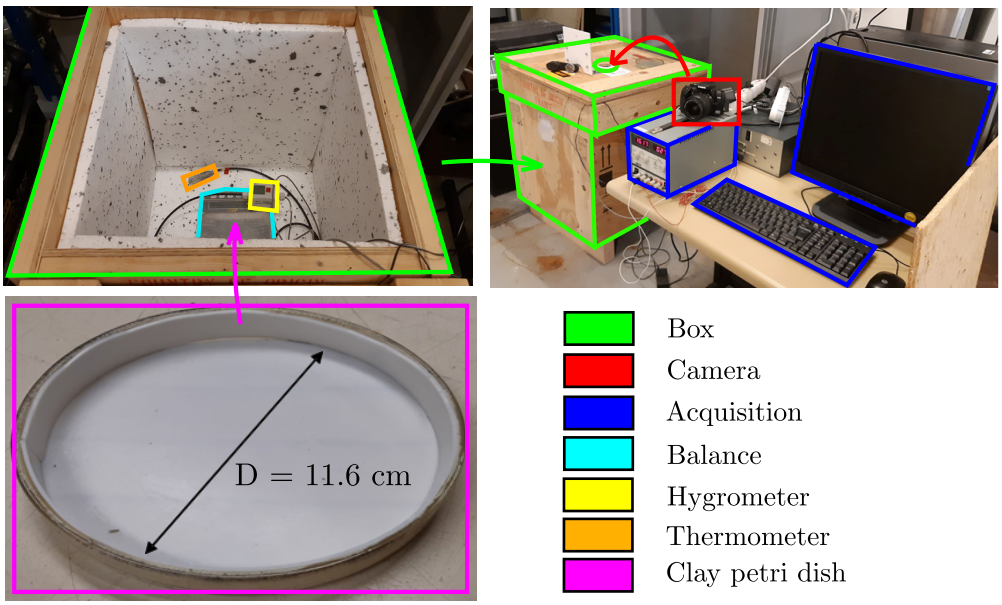

Figure 4.3 – Experimental setup photos.

These images are then analyzed using the digital image correlation technique (DIC) [Bornert et al., 2011, Wang et al., 2018], and provide access to the 2D deformation field at the upper surface of the sample. The experiment thus provides many information during the drying process such as: temperature, humidity, water volume fraction, crack evolutions, and also the deformation field. It is noted that many simulation models in literature only provide crack pattern images. Here the DIC provides a new, more accurate and relevant level of understanding of drying kinematics and crack dynamics, which will help enrich our model.

The collection of images, is then analyzed by DIC, using an image correlation software developed (CMV) at Ecole des ponts ParisTech, France. The complete description of the calculation of the local deformations is described in the work of [Wang et al., 2018] using the same software. The processed images provide the local displacement field and finally a map of the local deformations including two quantities of interest that will be exploited: the spherical (or hydrostatic) strain ϵ_S part and the deviatoric part ϵ_D defined as

$$\epsilon_S = \frac{1}{2}\mathrm{tr}(\boldsymbol{\epsilon}) \text{ , and } \epsilon_D = \frac{2}{3}(\bar{\epsilon}_2 - \bar{\epsilon}_1) \text{ ,} \tag{4.1}$$

$\bar{\epsilon}_1$ and $\bar{\epsilon}_2$ are the eigenvalues of the 2D Green-Lagrange strain tensor, and $\mathrm{tr}(\epsilon) = \epsilon_1 + \epsilon_2$ measures the variation of surface. It is emphasized that ϵ_s is different from a volume variation which cannot be measured locally by purely surface investigations. These quantities are evaluated for a gauge length limited by the typical length scale of the speckle painting and the (adapted) optical magnification of the camera. With about 2700 pixels along the diameter of the Petri dish, there are about 50 independent local evaluations of the 2D strain tensor along such a distance, so that the spatial resolution is of the order of 2mm. Accuracy of the measurement is limited by image quality and noise and other artifacts not detailed here, but is better than 1%, and thus sufficient to quantify the heterogeneity of the investigated strain field.

4.3 Results

4.4 Experimental conditions

The global study has been performed on different samples :

- S_0: a clay sample without inclusion,
- S_1, S_3, S_6: clay samples containing $n = 1, 3, 6$ randomly-distributed rigid inclusions,
- S_{1c}: sample with a unique inclusion placed at the center of the circular geometry.

The first results, shown in Fig. 4.4 first indicate the conditions of the experiment, with an ambient relative humidity of $RH = 48\% \pm 6$, a temperature of $T = 20 \pm 2^o$C, and the water content (ratio of weight of water and clay) of $wc = 115 - 10\%$. Then the relatively small variations of these parameters from one sample to another show that the experiment was carried out under similar measured conditions and shows the repeatability of the environment for a drying study. Even if the conditions might be slightly different form one sample to the other, it turns out the drying rate is very slow (tests last about one week) with respect to the typical time of the moisture transfer within the clay matrix, so that the water content in the clay material can be considered uniform and is directly given by the overall mass loss quantified by the scale. The latter is almost linear with time, as observed in the last graph of Fig. 4.4. Moreover, as viscous effects are likely to be negligeable in such experiments, the current loading state of a sample is directly provided by this water content which apperas thus as the main loading parameter, to be used in particular for comparisons with numerical simulations.

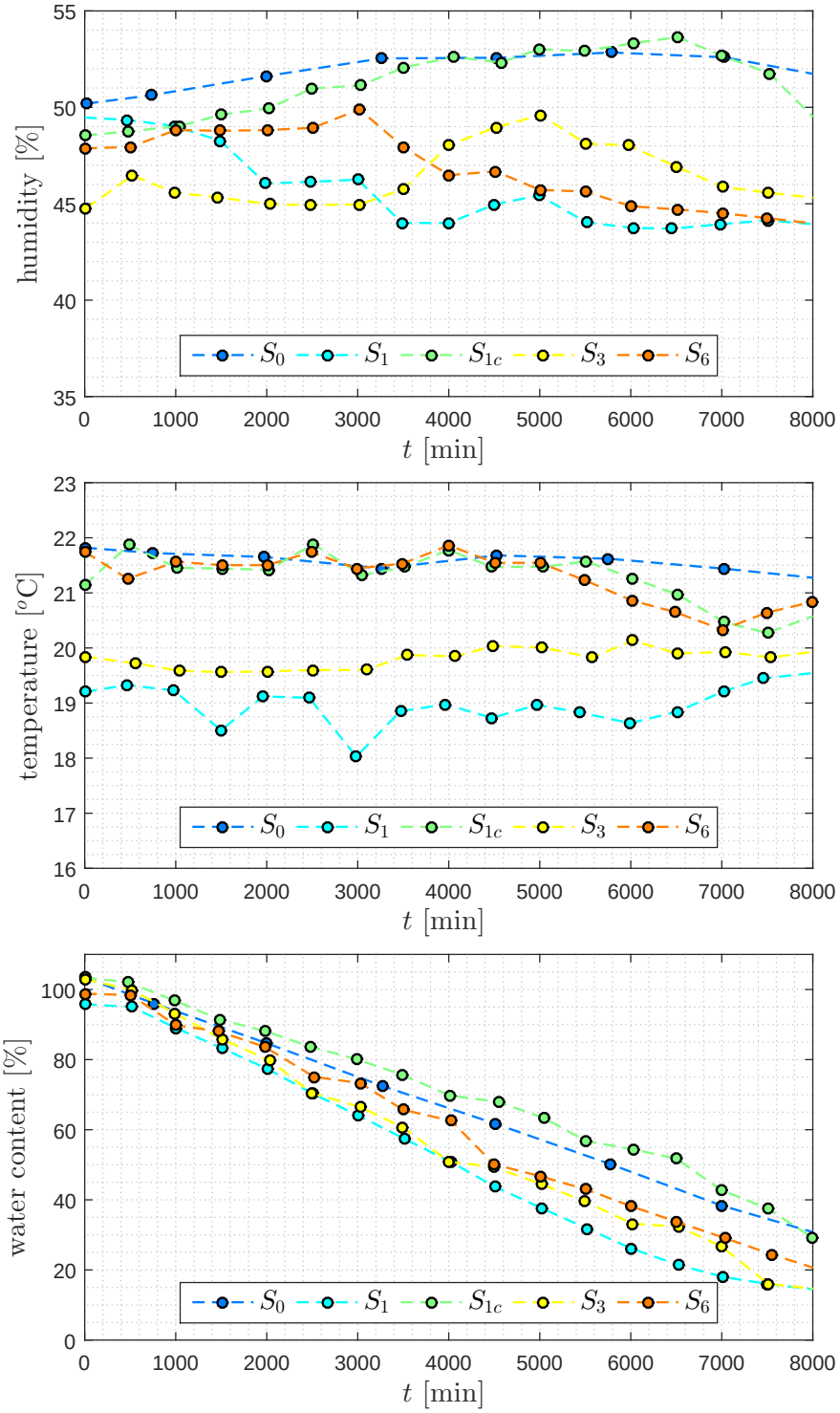

Figure 4.4 – humidity, temperature and water content experimental conditions.

4.5 Crack process

Figs. 4.6,4.8,4.7,4.9 and 4.10 show the states of the material at different times $t = 4000, 6000, 8000$ min each representing an initial state without cracks, the first propagations, and the final state. The crack paths obtained on each specimen show some similar features of the propagation pattern. The cracks initiate near the rigid inclusions and propagate towards to the outer edge of the specimen. Once all cracks have propagated, the material shrinks over its entire range, dividing the material into small independent subassemblies. It should be noted that the crack paths over the entire test set consists of 3 or 4 branches with angles betwen these branches θ_c such that: $\pi/2 \leqslant \theta_c \leqslant \pi/3$.

4.6 Strain analysis

In this part the deformation maps from the DIC technique are presented for the three steps in the cracking process: shrinkage without cracking (t =4000), crack initiation (t =6000), then propagation (t =8000). These maps are defined on the set of samples ($S_0, S_1, S_{1c}, S_3, S_6$), and show the spherical and deviatoric deformation of the samples. The spherical and deviatoric deformations are defined by the Eq.4.1 in percentage. The intensity of these strains are indicated by a color, giving an indication of the kinematics of the drying cracking process in a qualitative and quantitative way.

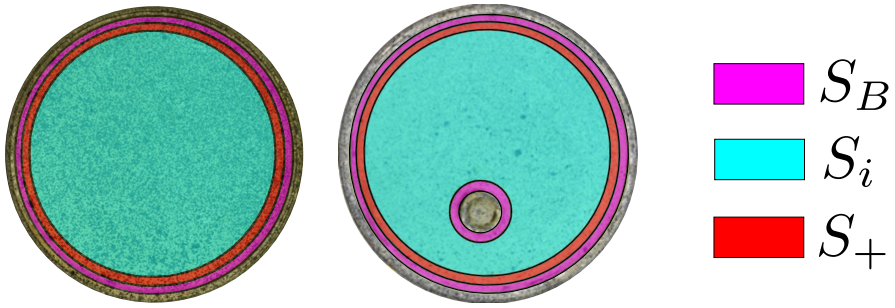

Figure 4.5 – Definition of certain areas of interest.

Before commenting on these maps, a delimitation of the sample into several zones is introduced and illustrated in Fig. 4.5.

- S_B is a ring surface defined as near-edge surface ring ,
- S_+ is another ring surface, the closest to S_B,
- S_i is the rest of the surface introduced as an interior surface.

4.6.1 S_0 test

The spherical and deviatoric deformation show a quite remarkable radial deformation pattern (see Fig. 4.6):

- First, at $t = 4000$ min, the intensity of the spherical deformation is first negative (as expected) on S_i, of low intensity $\epsilon_S \sim -2\%$, homogeneous on the surface except on the surface close to the edge $S_B \cup S_+$ where another regime settles. We observe a surface in a positive deformation crown (S_+) then another negative deformation crown (S_B) more intense than in the center of the sample. Concerning the deviatoric strain, it appears to be almost zero in the central area S_i, indicating a purely isotropic surface deformation as expected from a homogeneous shrinkage. However the deviatoric strain exhibits a small value $\epsilon_D \sim 2\%$ in the surrounding area $S_B \cup S^+$ where the surface strain was heterogeneous. It appears thus that the sample shrinks almost homogeneously and isotropically (in 2D) in its central part, as expected, but that it also undergoes some more complex deformation at its outer edge, due to some boundary effect. A possible explanation might be associtated with some adherence of the sample on the walls of the dish.

- Secondly at $t = 6000$ min, a wall debonding appears at the top left of the sample. The spherical and deviatoric strain maps are modified in consequence. On the first crown (S_i) the spherical strain remains at $\epsilon_S \sim -2\%$, while the second S_+ crown splits into two distinct parts: a first part which is not affected by the wall detachment as seen at $t = t_1$, then the second part close to the detachment where there is no longer an extension but now a strong compression $\epsilon_S \sim -14\%$. These observations confirm the adhesion of the sample to the external walls. The last crown on the periphery of the border, which remains negative, is of strong intensity. Concerning the deviatoric strain, the obverall features observed for the previous step are still present. But the debonding induces a more intense deviatoric strain in its vicinity. In addition, some heterogeneities in the central part S_i are now much more visible.

- In the last step at $t = 8000$ min, the sample is fully detached form the dish walls and the strain field exhibits again an essentially axisymetric distribution. The contrasts in strains become more accentuated, with two distinct zones: the external zone (S_B) of strong intensity $\epsilon_S \sim -40\%$ and $\epsilon_S \sim 15\%$, and the central zone $S_+ \cup S_i$ with a less intense but nevertheless important shrinkage of $\epsilon_S \sim 15\%$ associated with a moderate deviatoric strain $\epsilon_D \sim 5\%$. Some heterogeneities are also observed in areas where they had already been seen in the earlier steps.

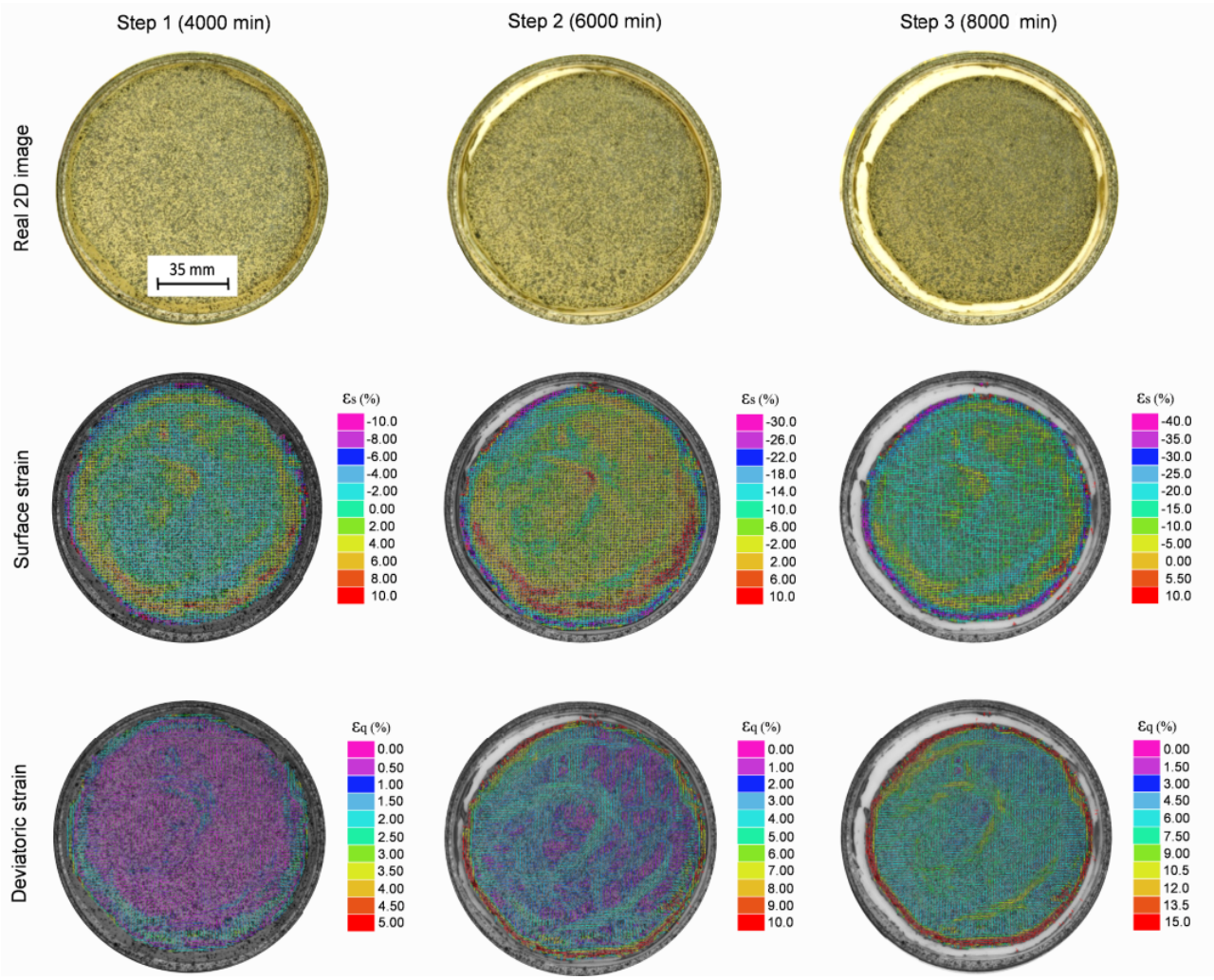

Figure 4.6 – S_0 test with shrinkage, spherical and deviatoric strain for t = 4000, 6000, and 8000 min.

4.6.2 S_{1c} test

The S_{1c} test is comparable to the test without inclusion (S_0 test), with additional features in the vicinity of the inclusion, see Fig. 4.7:

- At step $t = t_1$, an additional ring surface surrounds the inclusion (S_B). This area has a strong retraction $\epsilon_S = -10\%$, equal to the deformation on the outer edge. Moving away from the crown close to the inclusion, we have, as in the previous case (S_0 test), a zone S_i of negative strain of weak intensity $\epsilon_S \sim -2\%$. Then a last zone (S_+), in weak extension ($\epsilon_D \sim +4\%$). For the deviatoric part, the intensity is strong ($\epsilon_D \sim 5\%$) near the edges S_B, then weak elsewhere $S_+ \cup S_i$ (with $\epsilon_D \sim 0\%$). These observations show that the perturbations induced by the presence of the inclusion are concentrated in area with a diameter of the order of three times the diameter of the inclusion. Because of the central position of the inclusion, these perturbation do no interact with the phenomena observed at the periphery of the sample. There is an intermediate zone which behaves almost as in the S_0 test.

- At $t = t_2$ a debounding of the clay on the wall appears at the bottom of the sample. The strain maps are modified as in the case without inclusion. The first crown S_B linked to the inclusion is still in maximum shrinkage as well as the outer edge ($\epsilon_S \sim -14\%$). Then the surface S_i keeps a weak retraction ($\epsilon_S \sim -2\%$). Then the last crown S_+ splits into two distinct parts: a first part which is not affected by the wall detachment, identically to the previous observation ($t = 4000$ min). For the deviatoric part, the overall intensity increases with a greater concentration on the outer edges S_B and the inclusion ($\epsilon_D \sim 10\%$) for a relatively low intensity ($\epsilon_D < 4\%$) on the remaining surfaces $S_+ \cup S_i$. The debonding at the lower part induces also a local increase of the deviatoric strain.

- Finally, at $t = t_3$, the clay separates from the edge over 40% of the outer edge. In contrast to the previous case (S_0 test), the upper half of the crown S_+ remains in extension ($\epsilon_S \sim +5\%$). For the other part, as in the previous commentary, there is a strong shrinking zone ($\epsilon_S \sim -20\%$) on the borders S_B and a lower one ($\epsilon_S \sim -5\%$) on the last remaining area S_i. for the deviatoric part, intense strains are again observed in the edges S_B (outer part and near the inclusion). It is almost null in areas far away from the borders, the inclusion, especially on the non-debonded half part of the sample.

Note also that the very intens value of the deviatoric strains at the borders of the cracks is a post-processing artefact and should not be interpreted as the local deformation of the clay. Indeed the displacement jump over the crack is integrated in the local evaluation of the strain which is based on some finite differences (see [Allais et al., 1994] for the details about the calculation of the strain).

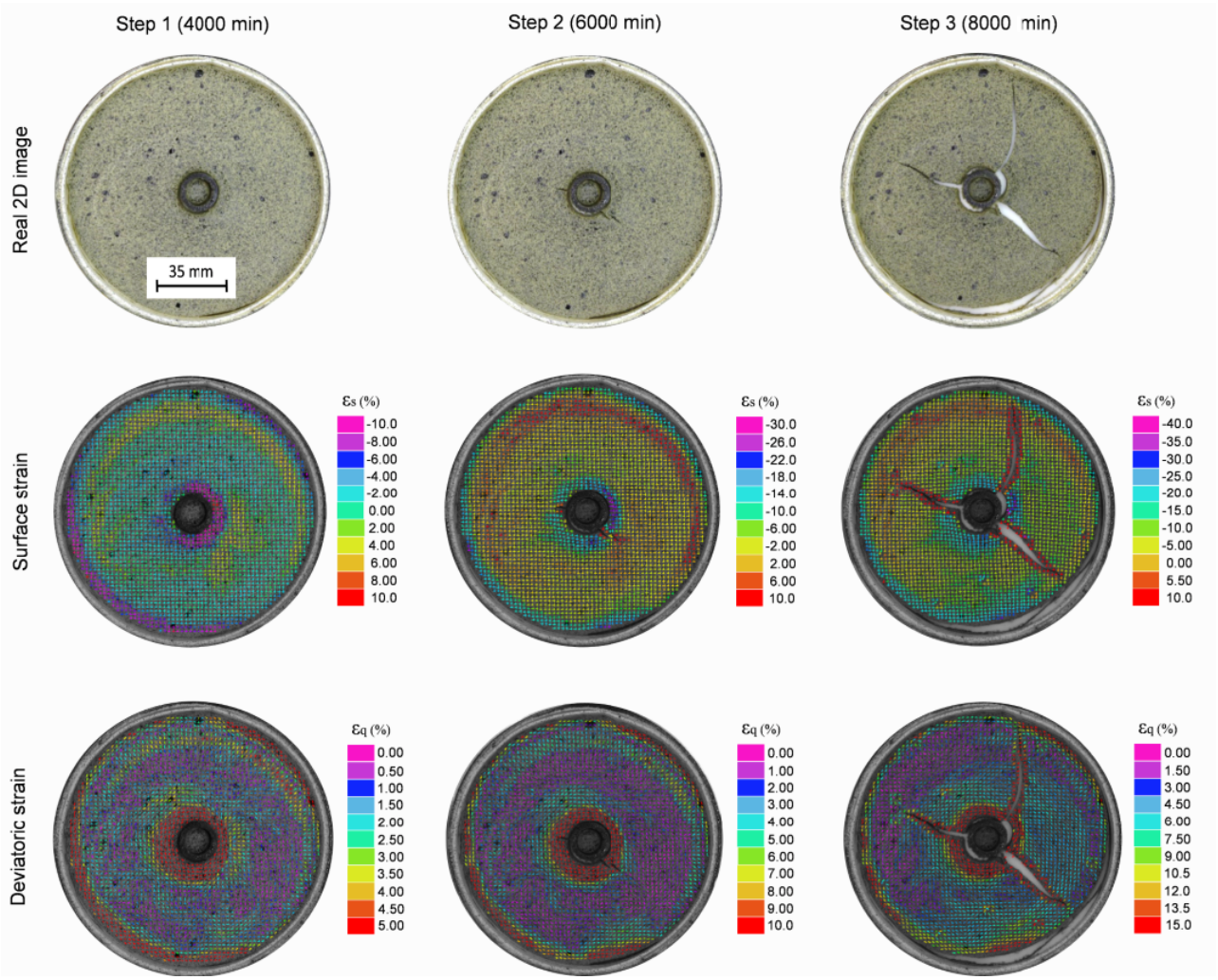

Figure 4.7 – S_{1c} test with shrinkage, spherical and deviatoric strain for t = 4000, 6000, and 8000 min.

4.6.3 S_1 test

In this test, a single rigid inclusion is inserted within the sample, but is here off-centered to break the symmetry of revolution.

- At $t = t_1$, as in the previous cases, the high intensity areas are located on the edges S_B of the sample exhibiting a large contraction, of intensity $\epsilon_S \sim -10\%$. One may also notice that the field surrounding the inclusion is also more heterogeneous than in the S_1c sample. In this test the crown S_+ is not apparent, the remaining surface S_i being a mixture of low intensity positive and negative surface stress $|\epsilon_S| < 5\%$. For the deviatoric part, the intensity is relatively, as in the previous samples, strong $\epsilon_D \sim 5\%$, on the outer areas S_B, and then weaker in the inner area $S_+ \cup S_i$, but with some noticeable heterogeneities.

- At $t = t_2$, the intensities on the outer edges of S_B increase with $\epsilon_S \sim -14\%$. The S_+ zone does not seem to develop in this case. The inner zone S_i remains of relatively weak intensity $\epsilon_S \sim 2\%$ with nevertheless some scattered zones with a stronger intensity up to $\epsilon_S \sim +10\%$. Regarding the deviatoric part, the intensity continues to increase on the edges S_B and remains small on the interior surface $S_+ \cup S_i$.

- At the last step $t = t_3$, the specimen maintains and confirms a trend of strong retraction $\epsilon_S \sim 20\%$ on the outer edges S_B. The inner zone S_i has extensional strains $\epsilon_S \sim [5\%, 10\%]$, larger than in the previous S_0 and S_{1c} tests but remaining relatively low. For the deviatoric part, the trend seems to be confirmed with an intensification $\epsilon_D \sim [7\%, 15\%]$ on the outer edges S_B and weaker values in the inner areas S_i.

In this sample with an excentred inclusion, debonding at the outer edge was limited. Adhesion induces very strong contractive strains in areas very close to these edges, together with extensive strains of lower intensity in larger zones and far away from the edges. So that the average surface change is zero, as required from the absence of debonding. Some fluctuations are observed in these area in extension but are not associated with strong deviatoric strains. The presence of the inclusion in the lower part generates first local deviatoric strains and then cracks. This allows the surrounding clay to shrink, first in the near-neighborhood of the inclusion and then in the larger areas around the cracks.

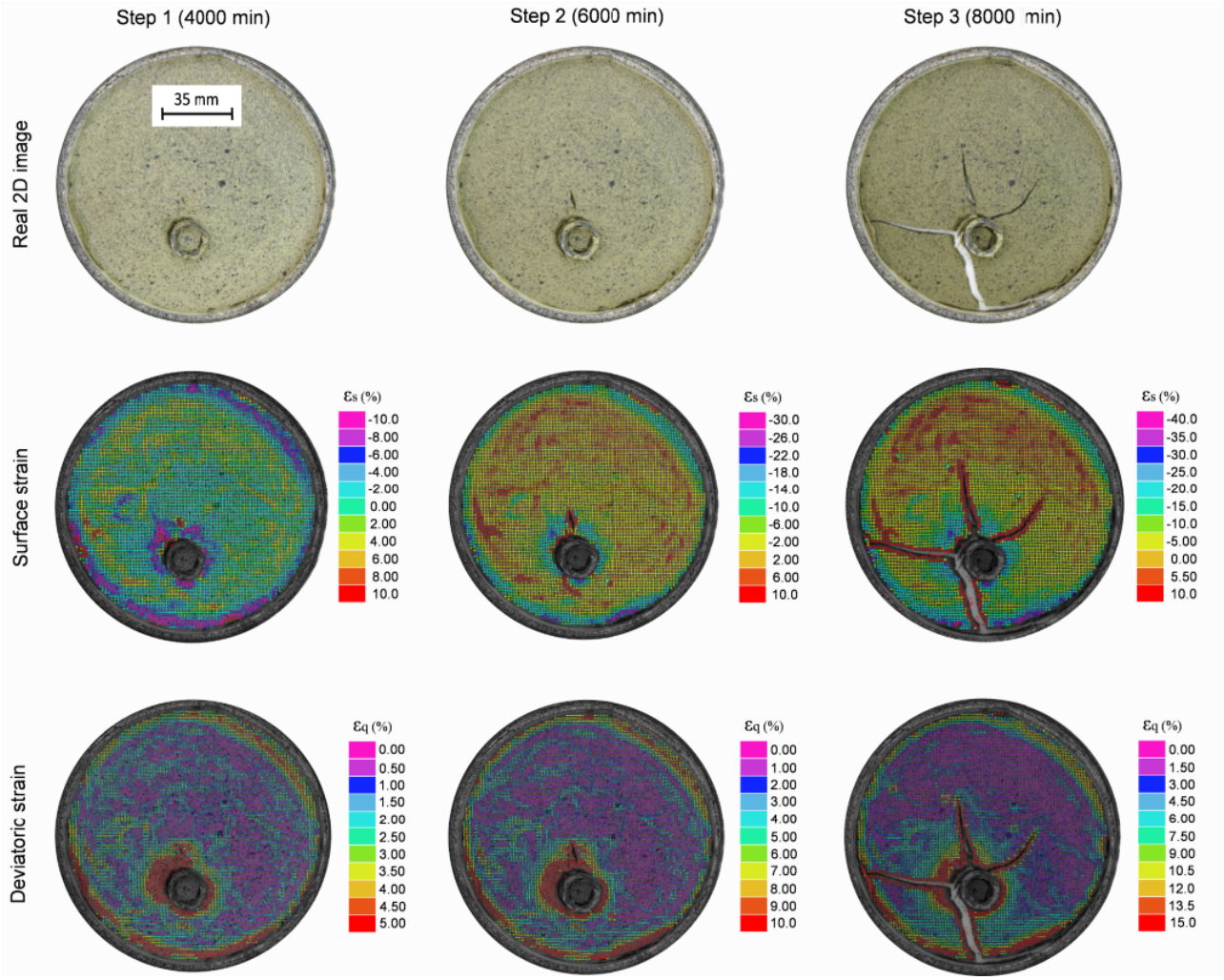

Figure 4.8 – S_1 test with shrinkage, spherical and deviatoric strain for t = 4000, 6000, and 8000 min.

4.6.4 S_3 and S_6 tests

These final tests were carried out to explore the interactions between inclusions during the drying process (see Fig. 4.9 and Fig. 4.10).

- At $t = t_1$, for both samples, a localization of strain is observed on the surface near the inclusions and on the outer edges S_B with $\epsilon_S \sim -10\%$ and $\epsilon_D \sim 2\%$, These values progressively decrease and ultimately vanish far away from the sample and inclusion edges. One may however notice the symmetry of revolution of this expansive strain field around the inclusions is broken in the sample S_6, while it is essentially preserved in S_3 where inclusions are farer away from each other. In the inner surface S_i, we notice the presence of the S_+ zone, with a surface strain of intensity $\epsilon_S \sim +4\%$ a limited debonding at the upper right sample edge. surface, relatively far from the inclusions.

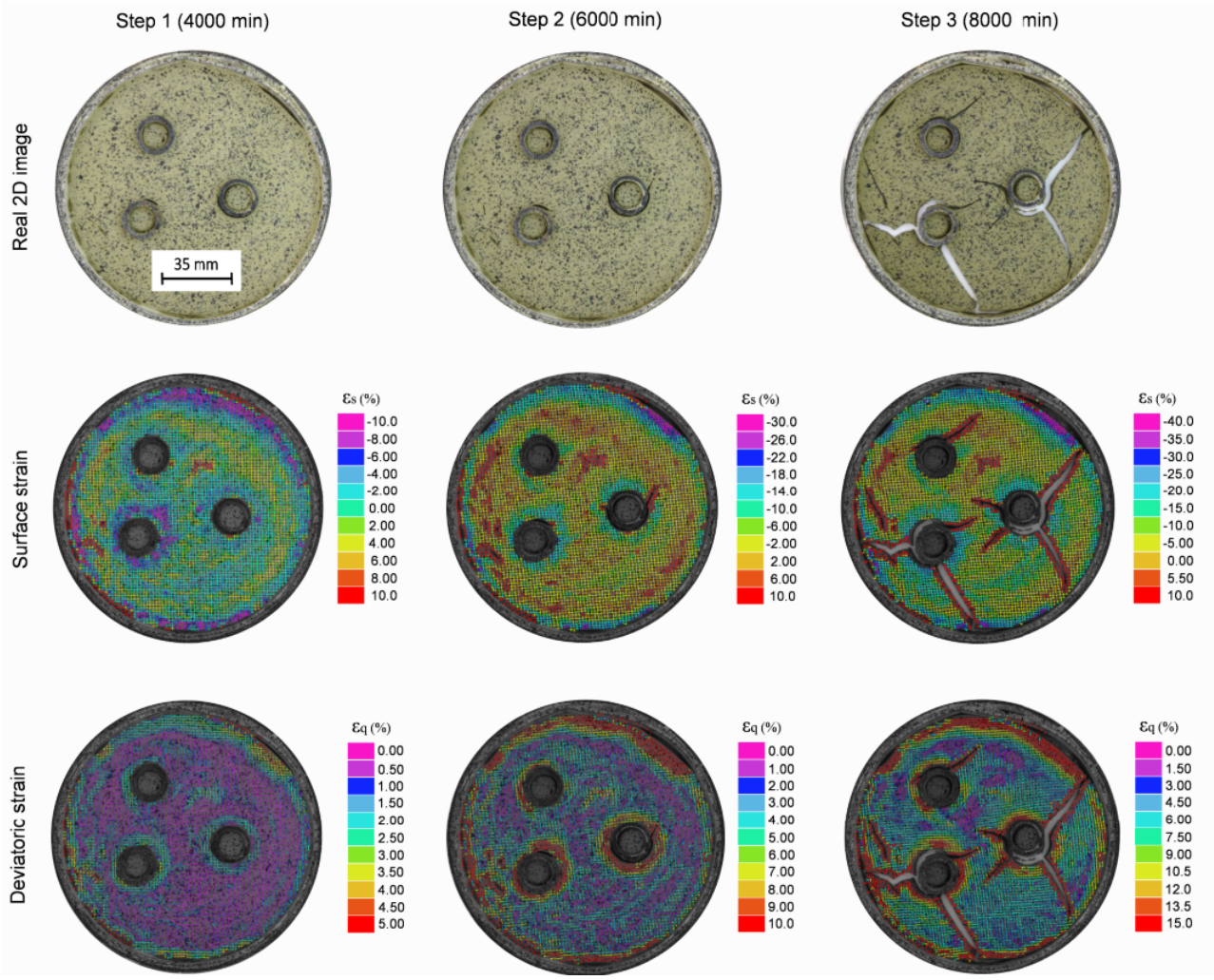

Figure 4.9 – S_3 test with shrinkage, spherical and deviatoric strain for t = 4000, 6000, and 8000 min.

- In the following state $t = t_2$, as in all previous tests, the contrasts noted at $t = t_1$ are globally preserved in terms of spatial distribution but are emphasized in terms of amplitudes of strains, at least for the most strained areas. The intermediate areas with ϵ_S close to 2%

essentially keep the same value. It can also be noticed that there is no significant additional debonding at the outer edge of the sample, unlike in samples S_0 or S_{1c}.

- At the final stage $t = t_3$, the contrasts intensify again. It can be noted that on the sample S_3 the extension zones $S+$ have almost all disappeared, and are transformed into a contraction zone or cracking. A few expansive zones a preserved inbetween the two upper inclusions and between the upper inclusion and the left sample border. For the sample S_6, this extension zone S_+ has globally been kept. Some of them turn out to be the location of secondary cracks.

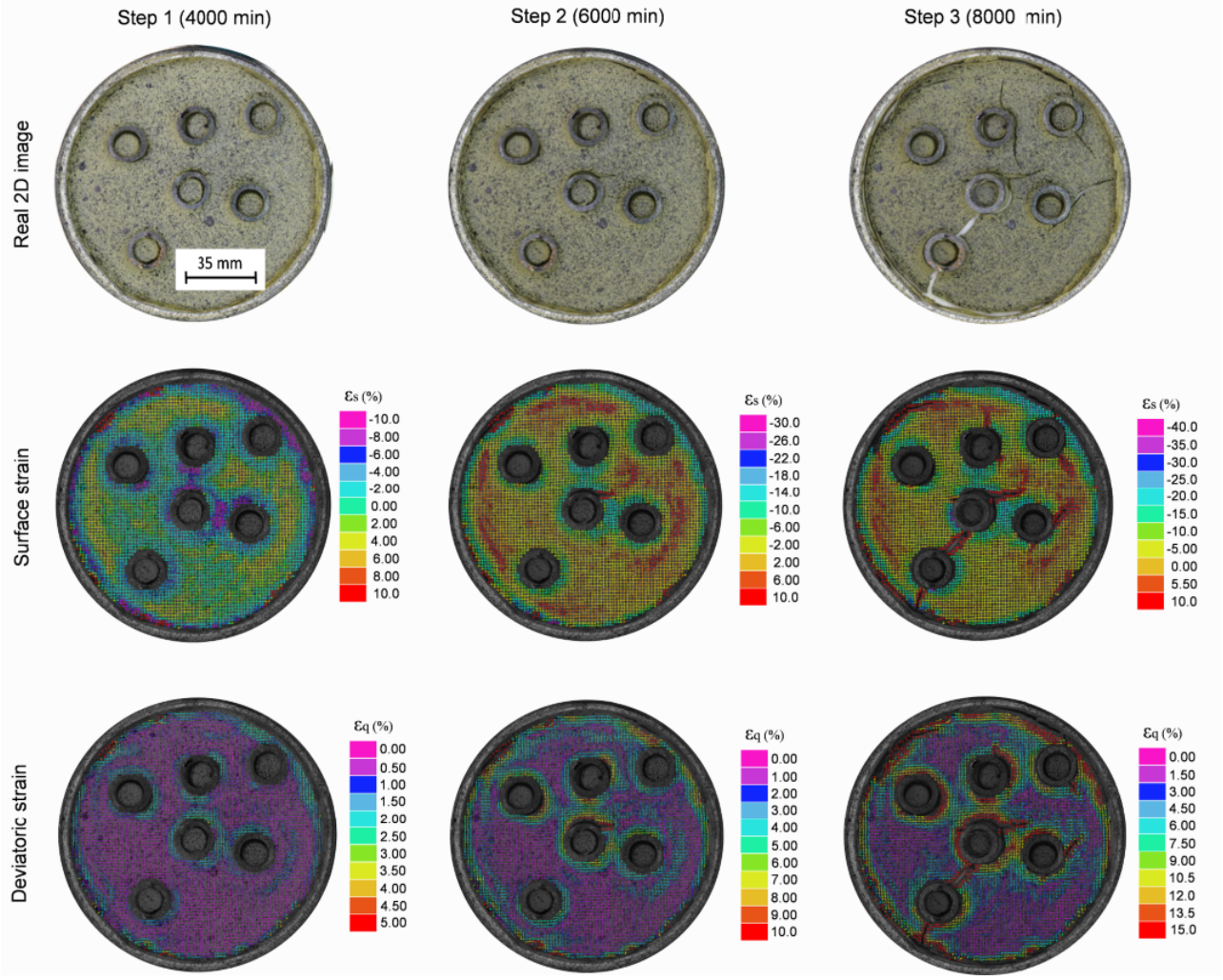

Figure 4.10 – S_6 test with shrinkage, spherical and deviatoric strain for t = 4000, 6000, and 8000 min.

A general observation is that the overall features of the strain field around the inclusions in S_3 are similar as those observed in S_1 and S_1c. This is also true for the crack geometries:cracks emitted from an inclusion do not interact with the others. This is no longer true for the S_6 sample in which positive ϵ_S strains are no longer observed between the closer inclusions. In addition cracks have different features: some are generated in areas with positive ϵ_S, and one clearly connects two inclusions (the lower left ones).

4.7 Discussion

4.7.1 Main mechanisms

A clear pattern of deformation and cracks is observed for all the tests carried out. At the beginning of the desiccation process, the material generates a high-intensity shrinkage deformation close to all edges and defined by the surface S_B. The rest of the surface is shared by (i) a low intensity, and overall shrinking portion, (ii) or possibly an extensional portion defined as the higher intensity S_+ surface. This extended area appears relatively far from the edges, and may partially disappear as the material debounds from the wall, or as a crack passes through it. Eventually, a large number of cracks have been generated, and the sample globally shrinks, facilitating and enlarging the cracks.

4.7.2 Stochastic aspects

The deformation and cracking processes share some common deterministic features as discussed above. But their are also characterised by some strong stochastic aspects, regarding in particular the detailed geometry of the cracks. This is in particular illustrated in Fig. 4.11, showing three tests with similar positions of the inclusions but very different crack geometries. These stochastic behaviours are of course related to the detailed position of the inclusions, but also to some other features of the experiments which are much more difficult to control. In particular, the friction betwwen the lower surface of the sample and the teflon substrate involves local fluctuations, whichare hard to control. The same holds for the adhesion or debonding of the lateral edge of the sample to the teflon wall. The three examples of Fig. 4.11 illustrate the potentiel influence of this interfacial behaviour on the cracking perocess: for the test at the left, the debonding was total, as in S_0; in the central text, it was partial as for most other earlier examples; it the right example, there was almost no debonding as in S_6.

We provide here some observations which might be taken into account for future stochastic modeling studies of the shrinkage process:

1. The ground friction has been limited by the application of a non-stick Teflon layer. However a quantification of this surface interaction remains to be identified. Numerical studies on an experimental basis [Sima et al., 2014, Amarasiri et al., 2011] have studied the influence of this interaction on the cracking process.

2. The detachment at the outer walls influences the overall kinematics of retraction and has been found in many similar experimental works. The construction of a model specifically accounting for this phenomenon could be proposed and inferred.

3. This debonding could be modeled through interface models, possible accounting for the variability. Interface models using the phase field modeling has been carried out in [Verhoosel and de Borst, 2013, Nguyen et al., 2016c].

4. Elastic and fracture properties are spatially-varying, time-dependent model parameters, due to the heterogeneous nature of the mixture, as well as to the possible complexity of the drying process, when such heterogeneity is taken into consideration.In particular, the local fluctuations observed in the central part of sample S_1 might be linked to such constitutive heterogeneities.

Figure 4.11 – Different crack patterns are observed on similar configurations.

4.8 Conclusion

In this chapter, we have presented an experimental campaign focusing on the characterization of crack propagation in clay samples filled with rigid inclusions. The analysis relies on the use of a digital image correlation technique, which is used to monitor displacement and deformation fields and crack patterns during the drying process.

The observations made on the different samples showed several interesting mechanisms. The first concerns the initiation and propagation of cracks in the presence of heterogeneities. Indeed, a clear pattern was observed for all samples in which damage first initiates near the inclusions and crack propagation (driven by shrinkage) then occurs. The deformation maps thus obtained also give us additional information about local deformations. In particular, a concentration of hydrostatic and deviatoric strains close to the inclusions is observed, leading to the initiation of damage. Potential sources of uncertainties are finally listed with the aim of explaining the variability observed in the experiments. In particular the adhesion or debonding the the clay at the outer boundary of the sample, and possibly also the friction properties at the interface of sample and substrate might have a prominent role of the deformation and cracking patterns.

Chapter 5

Model identification and validation using drying experiments

Contents

5.1 Introduction

In this chapter, the numerical modeling tools developed in chapter 3 are used to simulate crack initiation and propagation during hydric shrinkage of clay samples. The experimental results presented in chapter 4 are then used to identify and carry out comparisons with the numerical simulations. This work and results has been presented in [Hun et al., 2019b,Hun et al., 2019a] and adapted from the scientific paper [Hun et al., 2020].

5.2 Description of the problem

We consider the numerical model schematically described in Fig. 5.1. For a given test (that is, for one sample and a given number and distribution of obstacles), a digital replica is defined using the experimental data described in Chapter 4. Based on measurements, the initial radius of the cylindrical cup is set to $r_0 = 58$ mm, the radius of inclusions to $r_{inc} = 8$ mm, and the

height to $h_0 = 8$ mm. The clay material is contained within the domain Ω (see Fig. 5.1 (a) for an example with 3 inclusions).

In order to account for the damage mechanisms observed experimentally, boundary conditions are defined as follows:

- Zero-displacement Dirichlet boundary conditions are initially applied on $\partial\Omega$, while stress-free conditions are considered at the boundaries of the inclusions, denoted collectively as $\partial\Omega'$. Shrinkage is then induced by increasing the eigenstrain $\boldsymbol{E}_h = \alpha_{\hbar}\boldsymbol{I}$ (see Eq. $(3.69)_3$), where the parameter $\alpha_{\hbar}$ is to be defined. The problem (3.69) is then solved at each time step, and fracture is observed if localized traction area are created within the sample.

- When the condition $d = 1$ is met on a subset $\partial\Omega_{deb}$ of $\partial\Omega$ (note that $\partial\Omega_{deb}$ is not connected in general), boundary conditions on $\partial\Omega_{deb}$ are switched to free tractions, with the aim of modeling the sudden debounding observed during the experiments.

- Concerning the bottom of the sample, denoted by $\partial\Omega_{z=0}$, the boundary conditions are vertically fixed to 0.

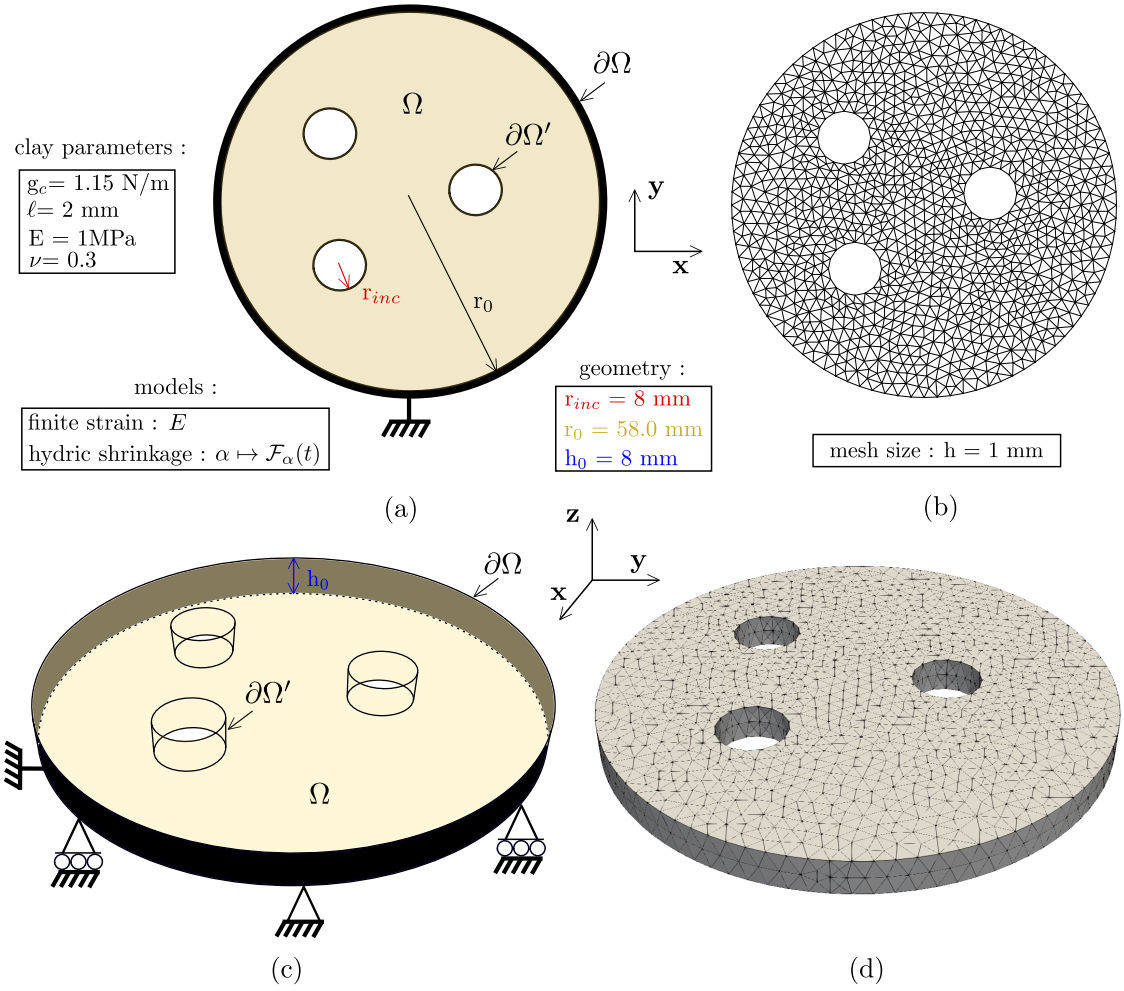

Figure 5.1 – Problem definition for a specific configuration: (a) geometry and boundary conditions for the 2D model; (b) 2D mesh; (c) geometry and boundary conditions for the 3D model; (d) 3D mesh.

5.3 Identification of model parameters

5.3.1 Mechanical parameters

The mechanical parameters used in the model described in section 3.3.3 are extracted from the literature. The Young's modulus for the clay material is taken as $E = 1$ MPa, according to the study in [Vo et al., 2017], where the simulation of crack propagation in the 2D plane with a cohesive zone model on clayey materials was conducted. This modulus was defined experimentally in [El Mountassir et al., 2014] where a variable Young's modulus was defined as a function of the compaction of the material. In our clayey material, we assume to be in a similar situation when the material solidifies according to the decrease of the water content. In [Vo et al., 2017], this modulus was averaged over the range of compaction. This hypothesis will be retained for the numerical study. In other works, [Cajuhi et al., 2018] proposed a variation of this modulus according to the water content in the experimental work of [Lakshmikantha, 2009] on the Barcelona soil, and in [Peron et al., 2009] where Bioley clayey silt was investigated. The Poisson's ratio will be chosen as $\nu = 0.3$ [Vo et al., 2017].

5.3.2 Fracture parameters

The damage parameters used in the following simulations require the estimation of the toughness g_c and of the regularization length ℓ, as this parameter is here interpreted as a material parameter (see a discussion in [Nguyen et al., 2016b]). In the literature, many authors have studied the impact of water content on crack resistance. [Kodikara and Costa, 2013] has provided a comprehensive review of environmental factors in the cracking process through multiple experiments. More specifically, numerous studies have allowed identifying parameters of linear mechanical fracture models through experiments (see [Wang et al., 2007,Lakshmikantha et al., 2009,Peron et al., 2009]). The parameters used are often the stress intensity factor K_I or the tensile limit stress σ_t, which can then be theoretically related to the pair of parameters (g_c, ℓ) of the phase field method (see [Nguyen et al., 2016b]). Following these works, a numerical study on clay desiccation using the phase field method was reported in [Cajuhi et al., 2018]. The parameters used are a cracking energy depending on the water content ($g_c = 1.12(wr = 0\%) - 1.71(wr = 100\%)$ N/m) and a constant regularization length $\ell = 2e^{-3}$m. For our study, we will consider the toughness as a constant, with $g_c = 1.15$ N/m, and set the regularization length to $\ell = 2$ mm.

5.3.3 Hydric model

In this section, we describe the procedure to identify the function $\alpha_{\hbar}(t)$ of the coupled hydric shrinkage model (see Eq. (3.69)) from the experiments. The experimental test S_0 described in section 4.6.1 has been used, where a homogeneous circular sample is considered. In this test, the sample shrinks without cracks and remains circular during the drying process. Denoting the experimental radius by $R^{\text{exp}}(t)$, it is possible to record the evolution of this radius as a function of time. This evolution is depicted in Fig. 4.6 and the radius is reported in Fig. 5.2 (Left).

The experimental evolution of the radius (red dots) has been fitter by the R^T function defined as:

$$R^T(t) = A(1 + \tanh(B(t - \phi)) + R_\infty \ , \tag{5.1}$$

where A is the amplitude defined by

$$A = \frac{1}{2}(R_\infty - R_0) \ , \tag{5.2}$$

with R_0 and R_∞ denote the initial and final radius, B defines the transition time between radius R_0 and R_∞ according to

$$B = \frac{1}{\Delta T} \ , \tag{5.3}$$

with ΔT the transition time, and ϕ represents the shift of the hyperbolic tangent function. The other parameters are obtained for $\phi = 10750$ and $B = 7.0.10^{-4}$ corresponding to $\Delta T = 1.4.10^3$. The Fig. 5.2 shows both experimental and fitted radius function (in black line).

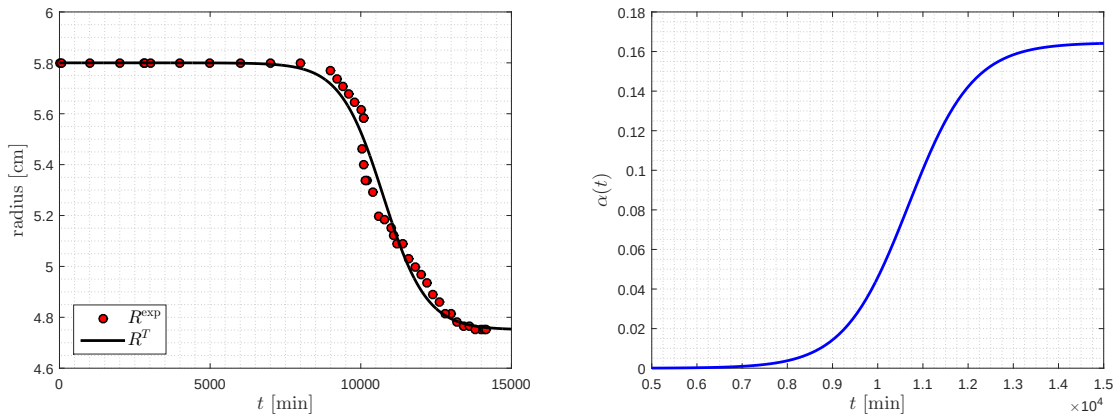

Figure 5.2 – (Left) Identified R^T function, (right) the identified shrinkage parameter $\alpha_{\hbar}$.

Then, the parameter $\alpha_{\hbar}$ was identified using the numerical application in section 3.5.5, and is directly related to the radius retraction measurement. Thus we obtain the time function of $\alpha_{\hbar}$, illustrated in Fig. 5.2 (right). In the next simulations, the identified function $\alpha_{\hbar}(t)$ is used, even the ones involving cracks, keeping in mind and being aware that this is a strong simplification of the model. The others parameters are summarized in Table 5.1.

E	ν	g_c	ℓ	h
1 MPa	0.3	1.15 N/m	2 mm	1 mm

Table 5.1 – Identified parameters for the shrinkage model.

From a computational standpoint, both 2D plane strain and 3D simulations have been carried out. The geometry was discretized with

- T3 elements in the 2D case, resulting in a mesh with $N^d_{dof} = 15 \times 10^3$ degrees of freedom for the damage problem, and $N^e_{dof} = 2N^d_{dof}$ degrees of freedom for the elastic problem;
- T4 elements for the 3D case. The mesh contains $N_e = 400 \times 10^3$ elements, corresponding to $N^d_{dof} = 80 \times 10^3$ degrees of freedom for the damage problem, and to $N^e_{dof} = 3 \times N^d_{dof}$ for the elastic problem.

An in-house implementation combining C++ and Matlab algorithms was used. Computational times per time step on a computer equipped with an Intel(R) Xeon (R) platinum 8168 CPU (with 1TB of RAM and 2×24 cores rated at 2.7 GHz) ranged from 0.7 to 3 seconds for the 2D case, and from 55 to 150 seconds in the 3D case. Total computational times based on 1000 time steps were 2.5 hours and 42 hours for each 2D or 3D case, respectively.

5.4 Simulation results

5.4.1 Crack patterns

In order to obtain a meaningful comparison between the experimental tests and the numerical simulations, we define the following characteristic times:

- $t = t_1$ is associated with damage initiation within the (solid) sample;
- $t = t_2$ corresponds to the time at which the first crack starts propagating;
- $t = t_3$ is the time at which all cracks have propagated and do not evolve anymore.

The above times were estimated for all experiments, and are given by: $t_1 = 4000$ min, $t_2 = 6000$ min, and $t_3 = 8000$ min. In what follows, we compare the crack patterns observed experimentally with the profiles predicted by the numerical model.

S_{1C} configuration

First, we consider the specimen S_{1c}, which contains a single, centered inclusion; see Fig. 5.3.

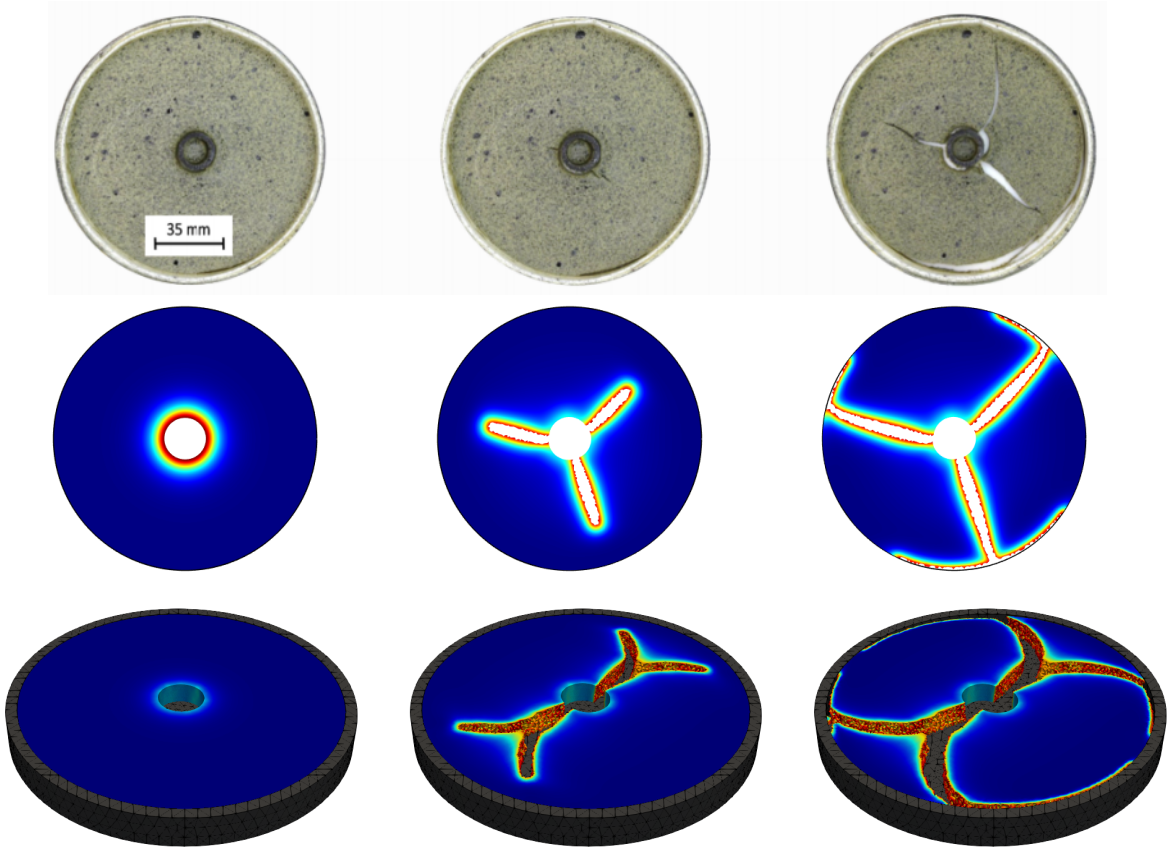

Figure 5.3 – Crack pattern in S_{1c} : experimental results (top), numerical results in 2D (middle), and numerical results in 3D (bottom) at times t_1, t_2, and t_3 (from left to right).

It is observed that the specimen exhibits 3 crack branches in the physical experiment. The 2D simulation also gives rise to 3 branches, whereas only 2 primary branches (that subsequently split into 2 secondary branches each) are obtained in the 3D case. However, it should be noted that the solution is not unique, and that the propagation only depends on the numerical perturbations related to mesh construction in the present case. The discrepancy between the 2D and 3D cases may also be explained by the fact that the 3D simulation includes through-thickness shrinkage that the 2D model does not.

S_1 configuration

We now consider a second example (specimen S_1) where a non-centered inclusion breaks the symmetry of revolution; see Fig. 5.4. In this case, 4 cracks are observed experimentally, while both 2D and 3D simulation results only present 3 cracks. It is noticed that despite the loss of symmetry, the angle between the directions of propagation for two adjacent cracks remains almost constant over crack pairs and is roughly equal to $2\pi/3$.

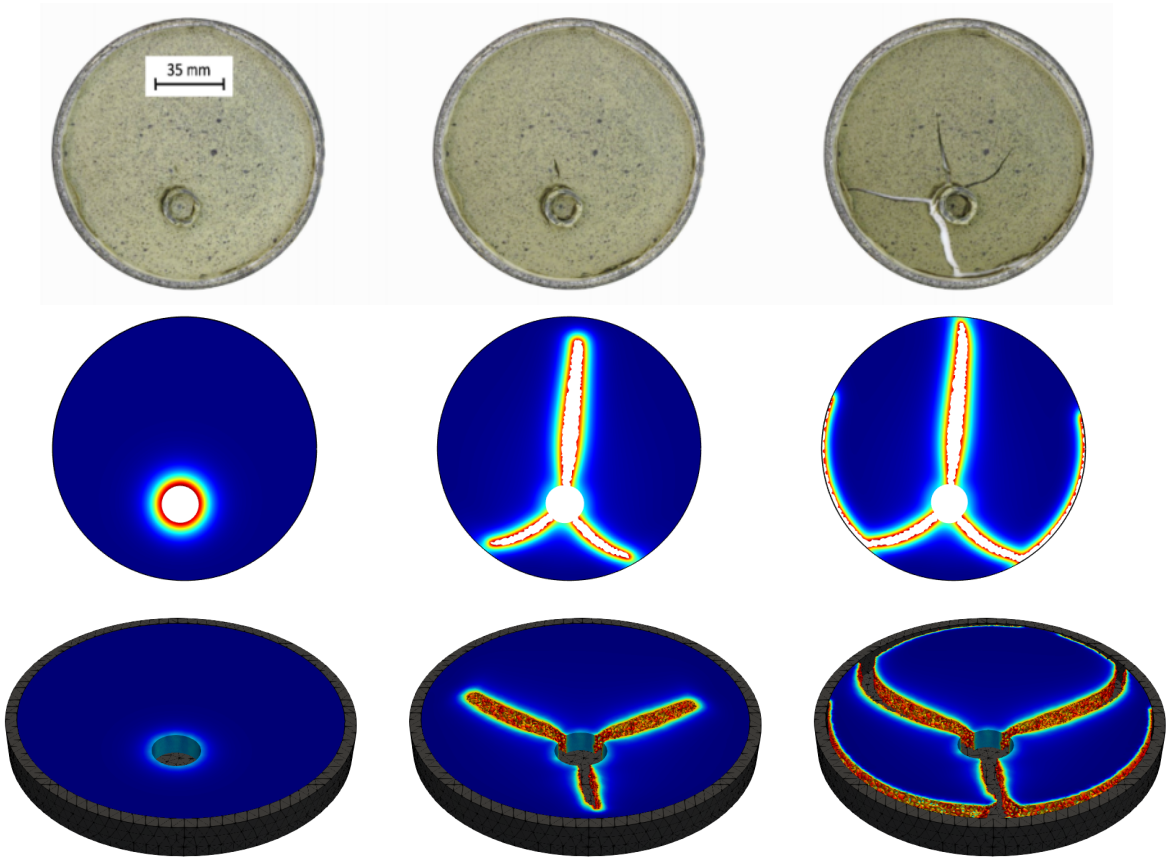

Figure 5.4 – Crack pattern in S_1 : experimental results (top), numerical results in 2D (middle), and numerical results in 3D (bottom) at times t_1, t_2, and t_3 (from left to right).

S_3 configuration

In the configuration S_3 shown in Fig. 5.5, 3 stiff inclusions are inserted with the goal of inducing potential interactions between cracks.

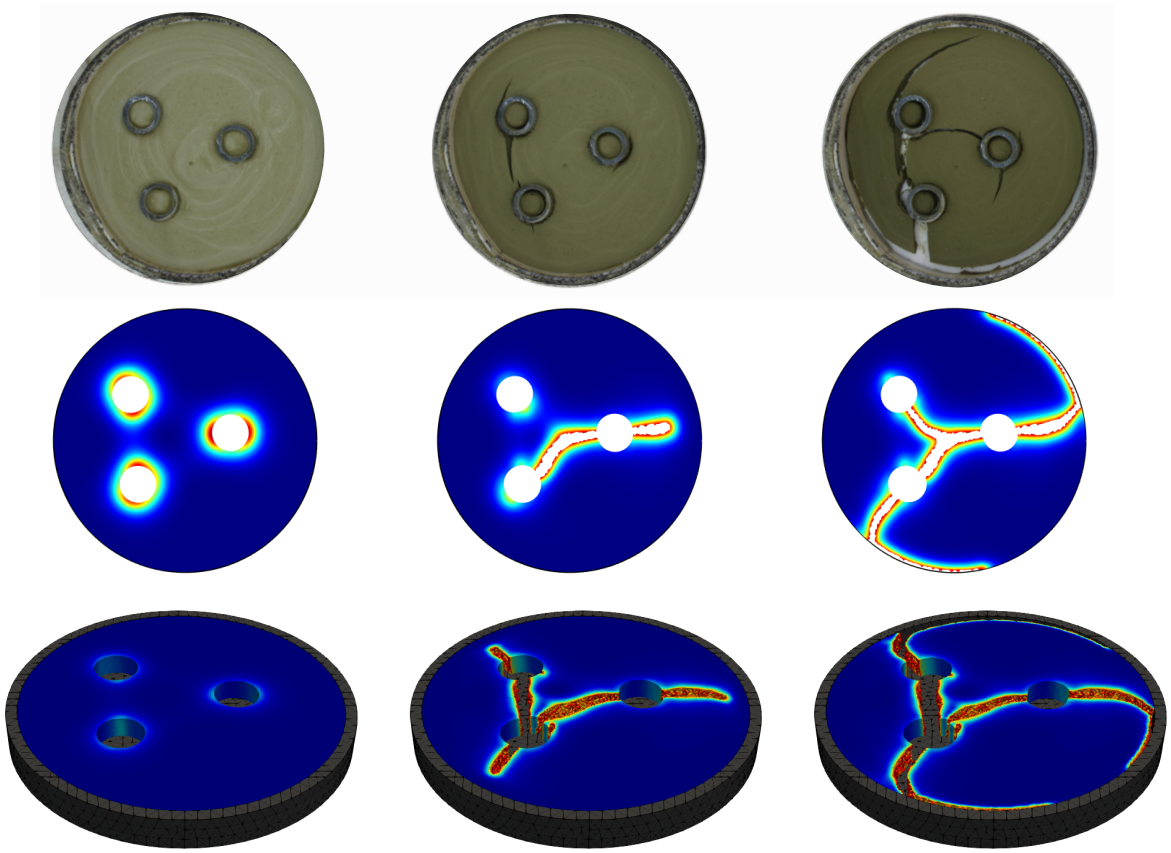

Figure 5.5 – Crack pattern in S_3 : experimental results (top), numerical results in 2D (middle), and numerical results in 3D (bottom) at times t_1, t_2, and t_3 (from left to right).

At the initiation stage (see the left panel in Fig. 5.5), we observe that the damage field is strongly localized in the vicinity of the inclusions (with crack initiation taking place simultaneously at diametrically opposed locations, for each inclusion). Crack growth occurs through these zones of higher strain localization in the early stage of propagation—until the cracks reach the boundary $\partial\Omega$ and generate partial debounding.

S_6 configuration

Similar conclusions can be drawn from the last example (specimen S_6), for which 6 inclusions are considered; see Fig. 5.6.

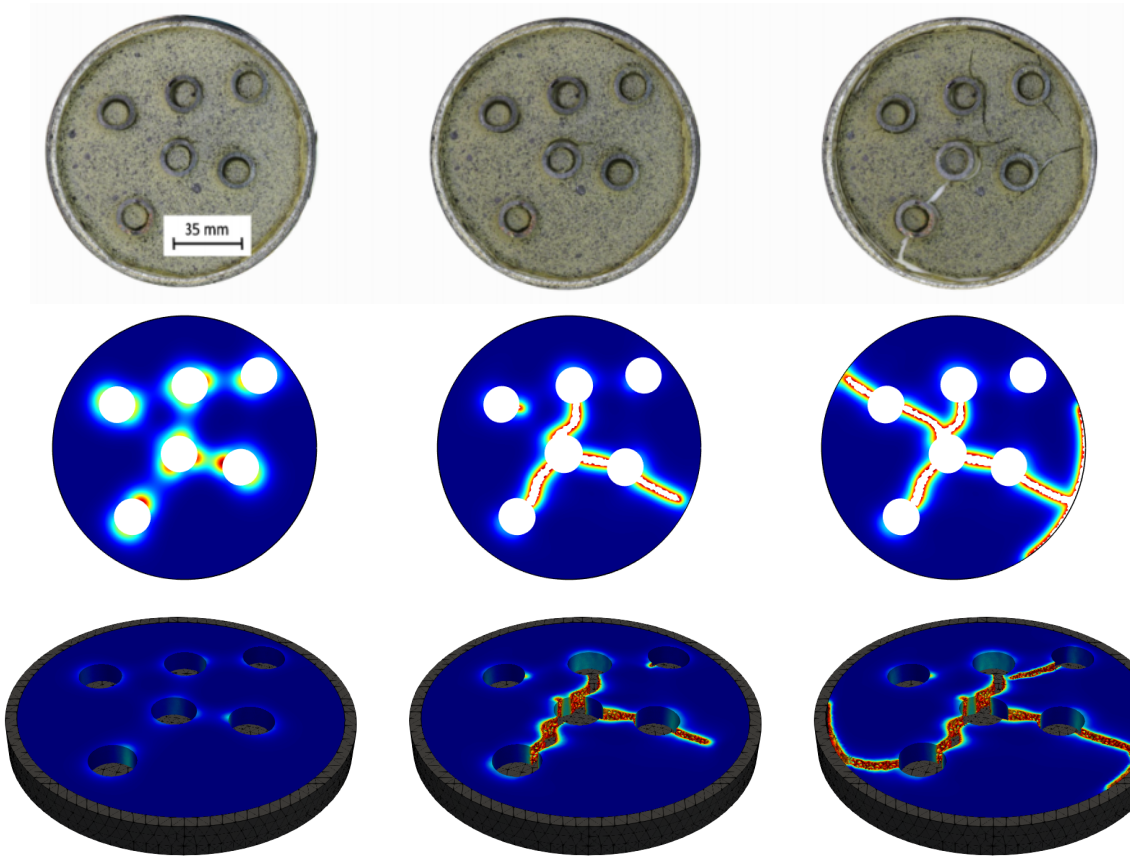

Figure 5.6 – Crack pattern S_6: experimental results (top), numerical results in 2D (middle), and numerical results in 3D (bottom) at times t_1, t_2, and t_3 (from left to right).

Based on these results, we note that the crack patterns predicted by the 2D and 3D computational models present good qualitative agreement with the experimental observations. In particular, it is noticed that crack propagation always initiates in the vicinity of an inclusion and remains mostly radial (until the boundary of the sample is reached, at which point debounding occurs). Coalescence between cracks having initiated at adjacent inclusions is also observed in the simulations and on certain experiments (as S_6).

5.4.2 Spherical (hydrostatic) strain distribution

S_{1C} configuration

In the case of the centered inclusion (see Fig. 5.7), we compare the distribution of the hydrostatic field ϵ_s between the experiment and the 2D/3D simulations.

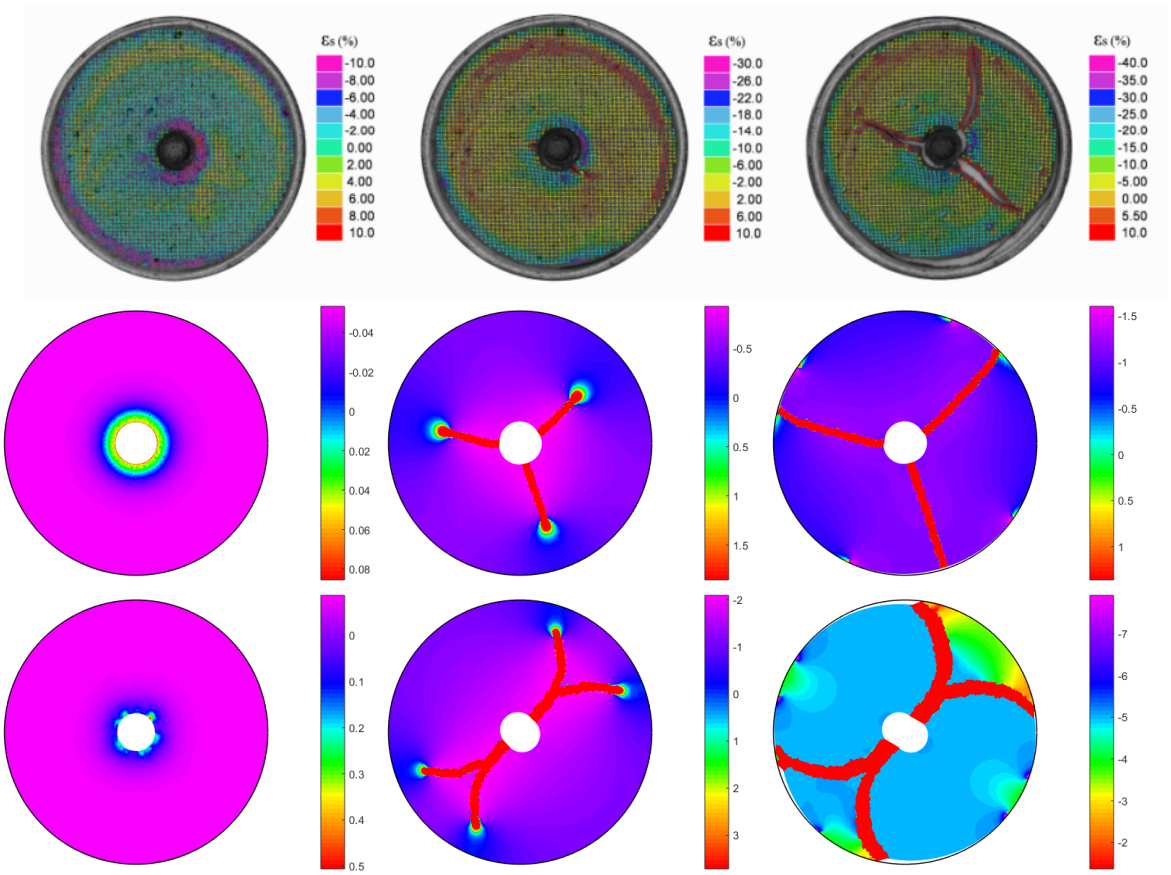

Figure 5.7 – Spherical strain map in S_{1C}: experimental results (top), numerical results in 2D (middle), and numerical results in 3D (bottom) at times t_1, t_2, and t_3 (from left to right).

While a negative shrinkage is globally observed in the experiment, some quantitative differences can be noticed with the 2D and 3D simulation. More specifically, we observe a region of compressive strain localization in the experiments (near the external boundary and inclusion edges) that is not captured by the chosen model (which, on the contrary, predicts a positive strain in both 2D and 3D). From the point of view of deformation far from the edges, the deformation is almost uniformly negative in the 2D case, as in the experiment. In this 2D simulation, the clay grips the outer edge, causing a uniform pull around the central hole of the inclusion, which results in a positive deformation, despite the imposed negative shrinkage water deformation. In the 3D case, the surface deformation is zero, as a consequence of the boundary condition of the problem. All the water volume variation occurs in the vertical direction. Except near the inclusion where a gradient develops, and which is caused by the free surface. The deformation is then locally positive on this upper surface as in the 2D case.

S_1 configuration

Similar results are shown in Fig. 5.8 for the configuration with the off-centered inclusion.

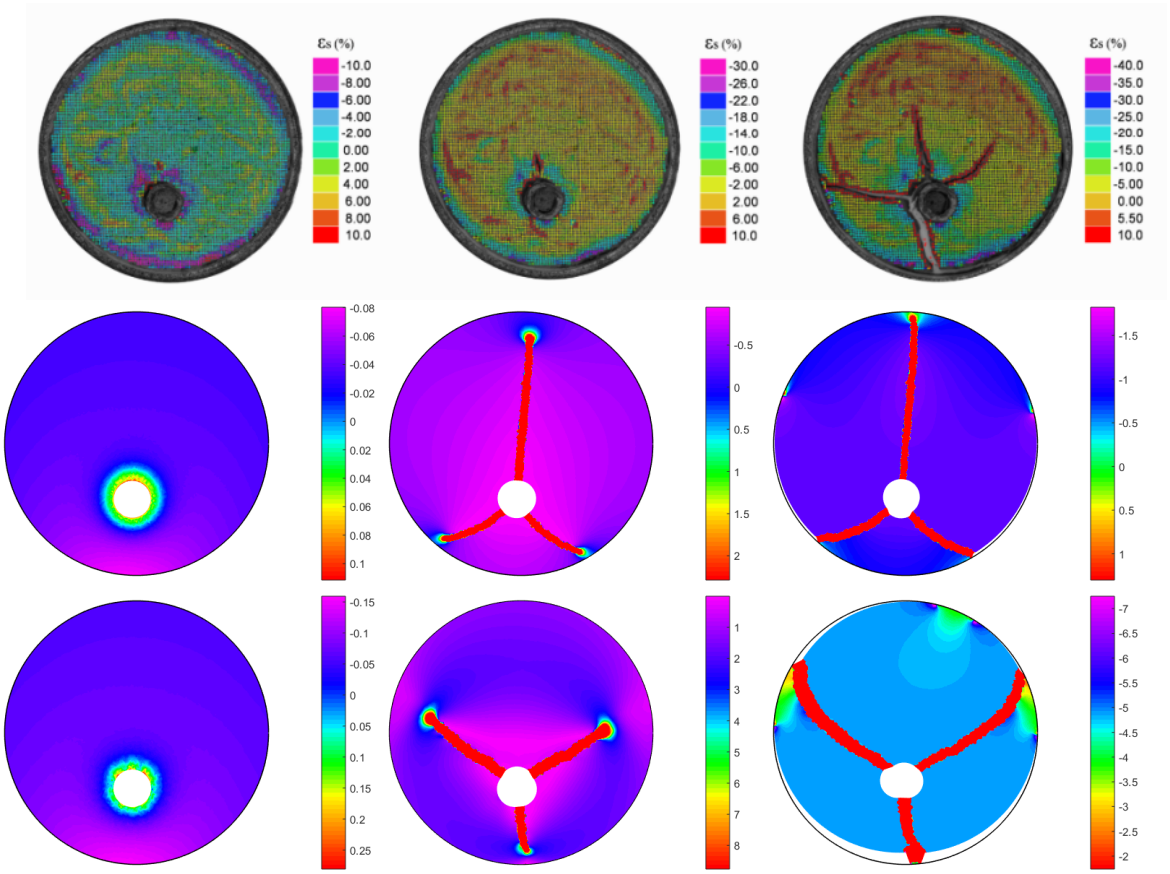

Figure 5.8 – Spherical strain map in S_1: experimental results (top), numerical results in 2D (middle), and numerical results in 3D (bottom) at times t_1, t_2, and t_3 (from left to right).

Here, we observe the same characteristics regarding the amplitudes as in the previous case, both globally and at the edges, with some local differences due to the lack of the geometry of revolution though. Indeed, we notice that the zone at the edges of the inclusion and the nearest outer edge zone are associated with localized extensive strains when damage initiates ($t = t_1$). This zone does not seem to affect or to predetermine a path, moreover with this geometry, the 3D case is quantitatively closer to 2D, regarding t=t1.

S_3 configuration

For the 3-inclusion geometry presented in Fig. 5.9, interaction effects are observed in both 2D and 3D simulations at $t = t_1$, with specific high-intensity areas located at the edges of the inclusions and facing each other. The crack paths follow these zones at t_2 and t_3. Branching seems to occur at the center of the sample for $t = t_2$ in the 2D case, with the creation of a positive deformation zone (rouge). these areas of strong extension occurs exactly in the damaged areas ($d \geq 0.8$) which stretches at $t = (t_2, t_3)$.

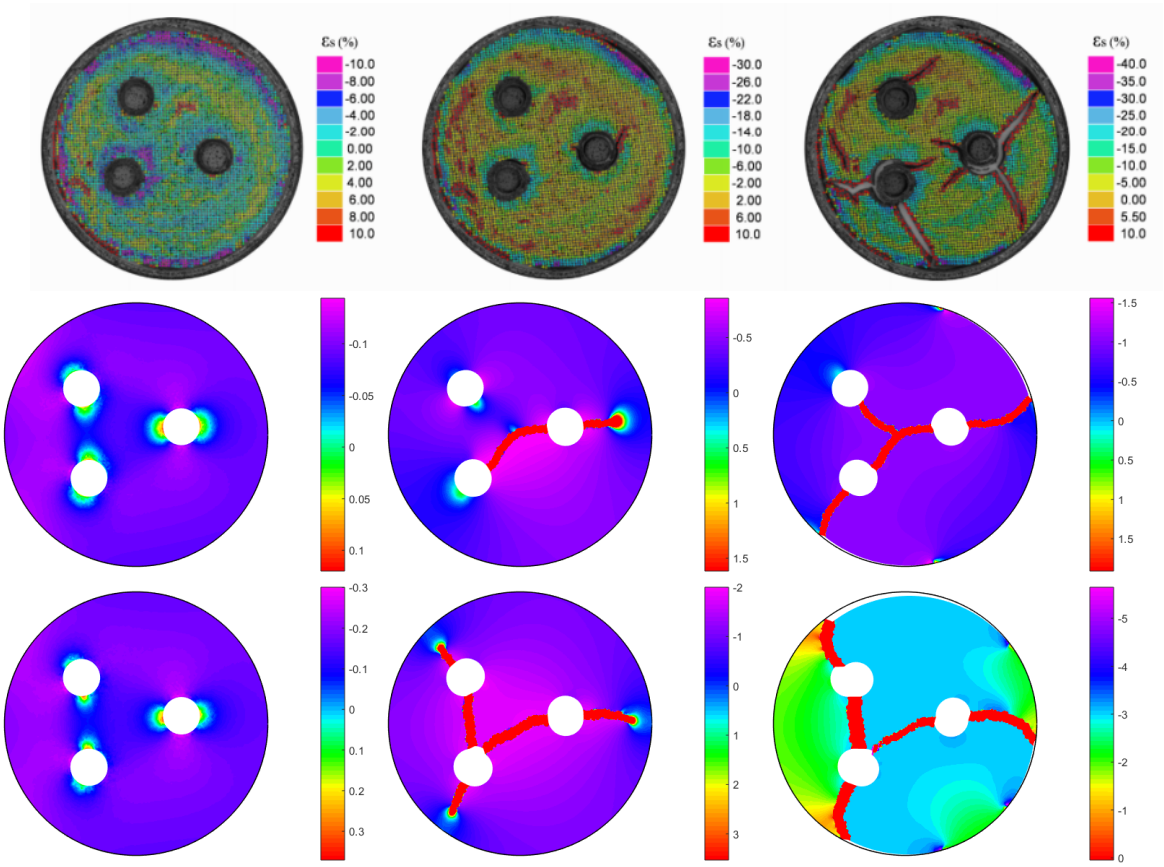

Figure 5.9 – Spherical strain map S_3: experimental results (top), numerical results in 2D (middle), and numerical results in 3D (bottom) at times t_1, t_2, and t_3 (from left to right).

It should be highligted that the positive deformations are here concentrated around the inclusions, with a loss of symmetry of revolution, whereas they are distributed in the experiment and preserve this symmetry locally around the inclusions. A complex phenomenon in the experiment causes a mechanical deformations distributed and which is opposed to the simulation. An explanation could come from a non-linear elastic behaviour law that would disadvantage high deformations (as in elastomer materials) or from an unknown complex friction effect.

S_6 configuration

As expected, interaction effects become more noticeable with a larger number of inclusions; see Fig. 5.10.

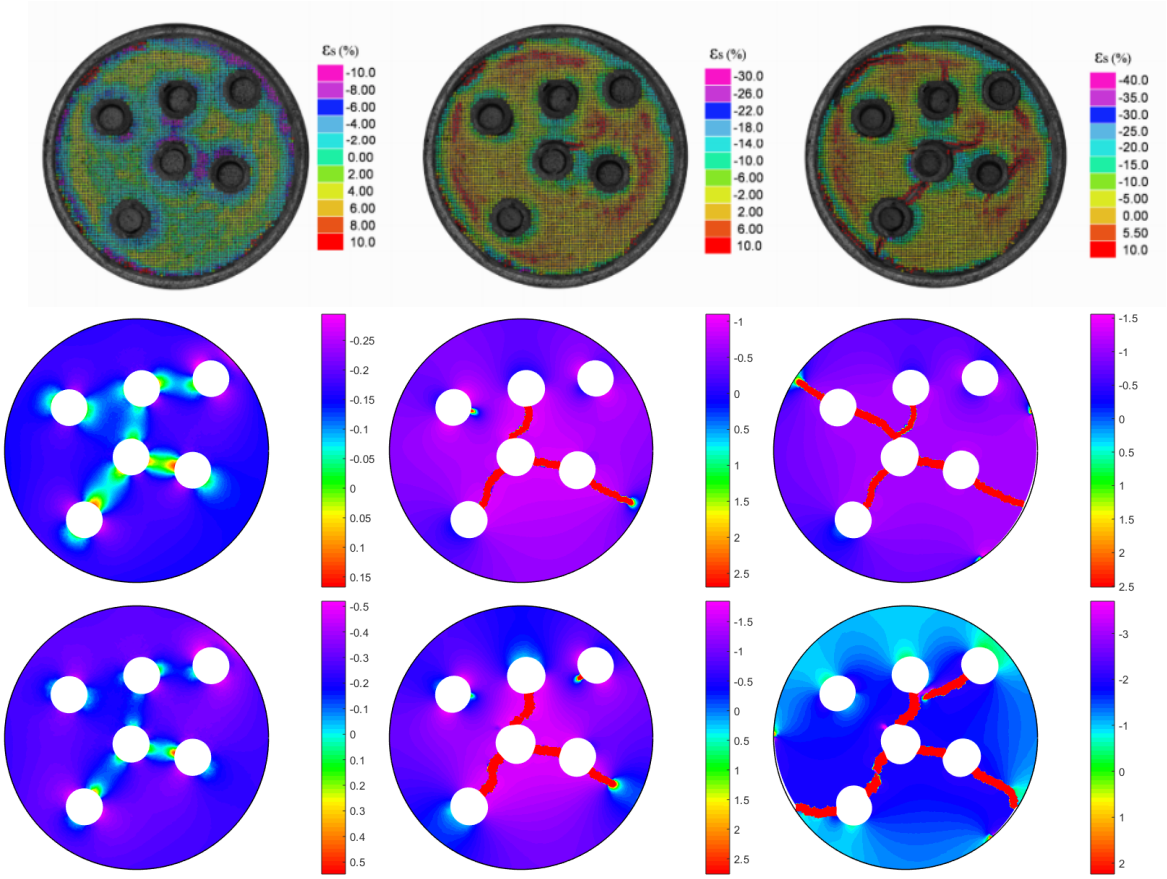

Figure 5.10 – Spherical strain map in S_6: experimental results (top), numerical results in 2D (middle), and numerical results in 3D (bottom) at times t_1, t_2, and t_3 (from left to right).

Based on the observations made on all the geometries, we can now highlight several qualitative disagreement points between the simulations and the experiments. From a general perspective, the results of the experiment show a compressive strain localization near the boundaries and homogeneous deformation intensity in accordance with the boundary conditions of retraction specific to the modeling. However, it has been noted that these areas of strong compression accumulate and are not well reproduced in the simulations at this stage, moreover the origin has not yet been clearly identified. On the opposite, we have an expansion regime at the edges of the inclusions. Once the crack propagates, the simulation generates a dilatation deformation of high intensity along its path, as in the experiment.

5.4.3 Deviatoric strain map

S_{1C} and S_{1C} configurations

For deviatoric deformation maps, qualitatively similar experimental and numerical fields are observed (see Fig. 5.6 for instance). It is seen, in particular, that the intensity substantially decreases far away from the edges. There remains, however, a zone of high intensity on the external boundary of the experimental sample that is not reproduced in the simulation.

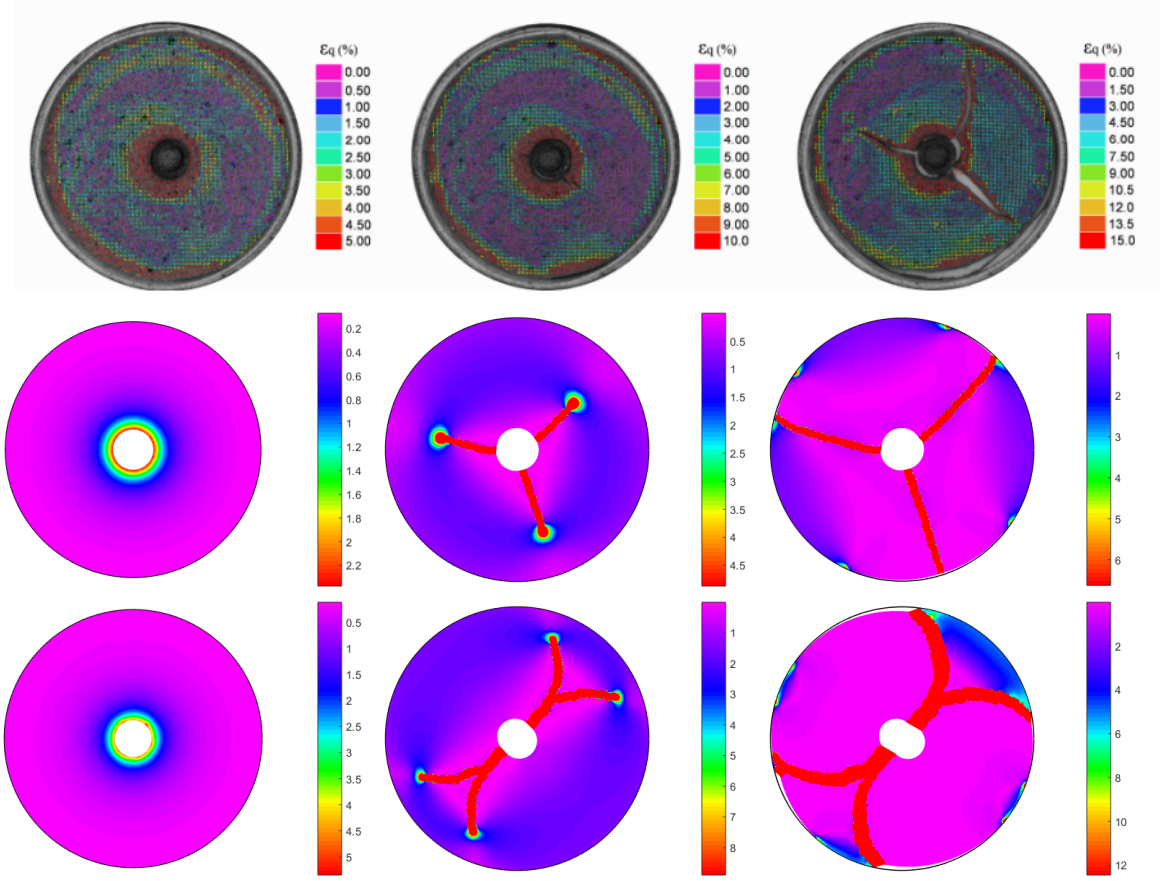

Figure 5.11 – Deviatoric strain map in S_{1C}: experimental results (top), numerical results in 2D (middle), and numerical results in 3D (bottom) at times t_1, t_2, and t_3 (from left to right).

We notice that the deviatoric strain concentrates in the totally damaged zone ($d = 1$) in both the experiments and the simulations. The graphic representations are adapted by clipping (set by a damage threshold $d = 0.8$). In order to observe the spatial fluctuation of the deformation fields, excluding the highly damaged areas (d>=0.8) concentrating high intensity deformation.

The same conclusions can be drawn for the configuration with a single centered inclusion; see Fig. 5.12.

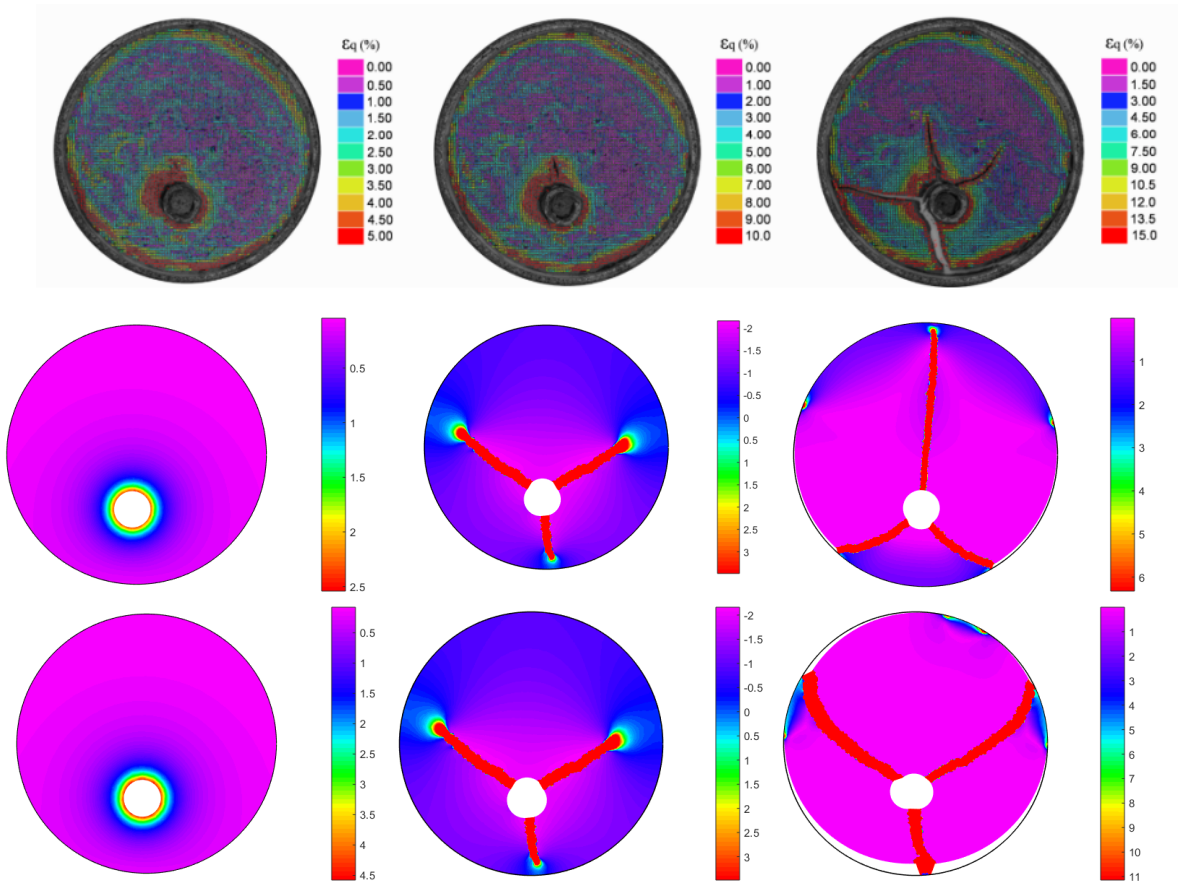

Figure 5.12 – Deviatoric strain map in S_1: experimental results (top), numerical results in 2D (middle), and numerical results in 3D (bottom) at times t_1, t_2, and t_3 (from left to right).

S_3 and S_6 configurations

Interaction effects are more pronounced for the configurations with three and six inclusions, illustrated in Fig. 5.13 and Fig. 5.14 respectively. Here, cracks initiate near the inclusions and merge in between, in both the experiments and the simulations.

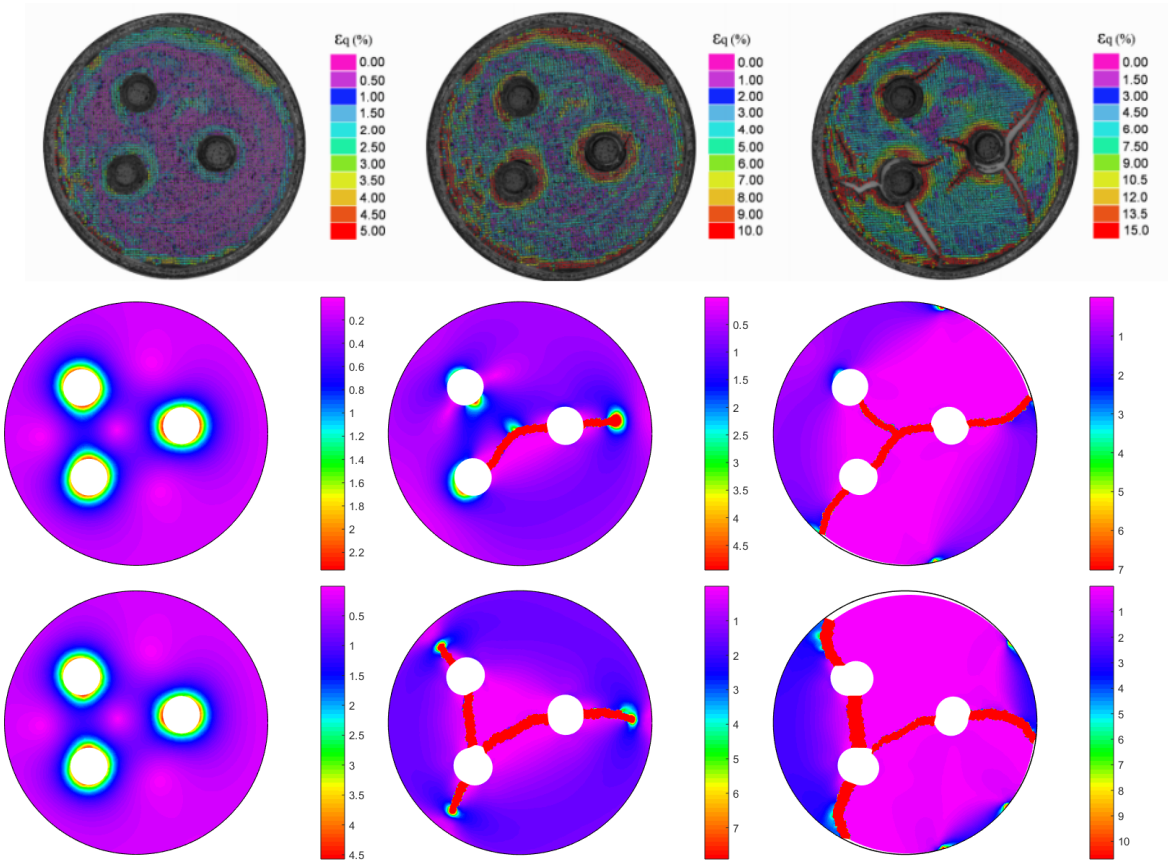

Figure 5.13 – Deviatoric strain map in S_3: experimental results (top), numerical results in 2D (middle), and numerical results in 3D (bottom) at times t_1, t_2, and t_3 (from left to right).

Here, a better agreement on the strain fields is obtained. In the experiments, areas of higher intensity around the inclusions and the outer edges appear during the damage initiation. These effects are well captured in the simulation, but in the vicinity of the inclusions only. In the rest of the sample, the deformation values remain quite low and in agreement with the experiment overall. Finally, the locations of inclusions seem to play a more predominant role in the simulations where interaction effects may give rise to privileged crack paths.

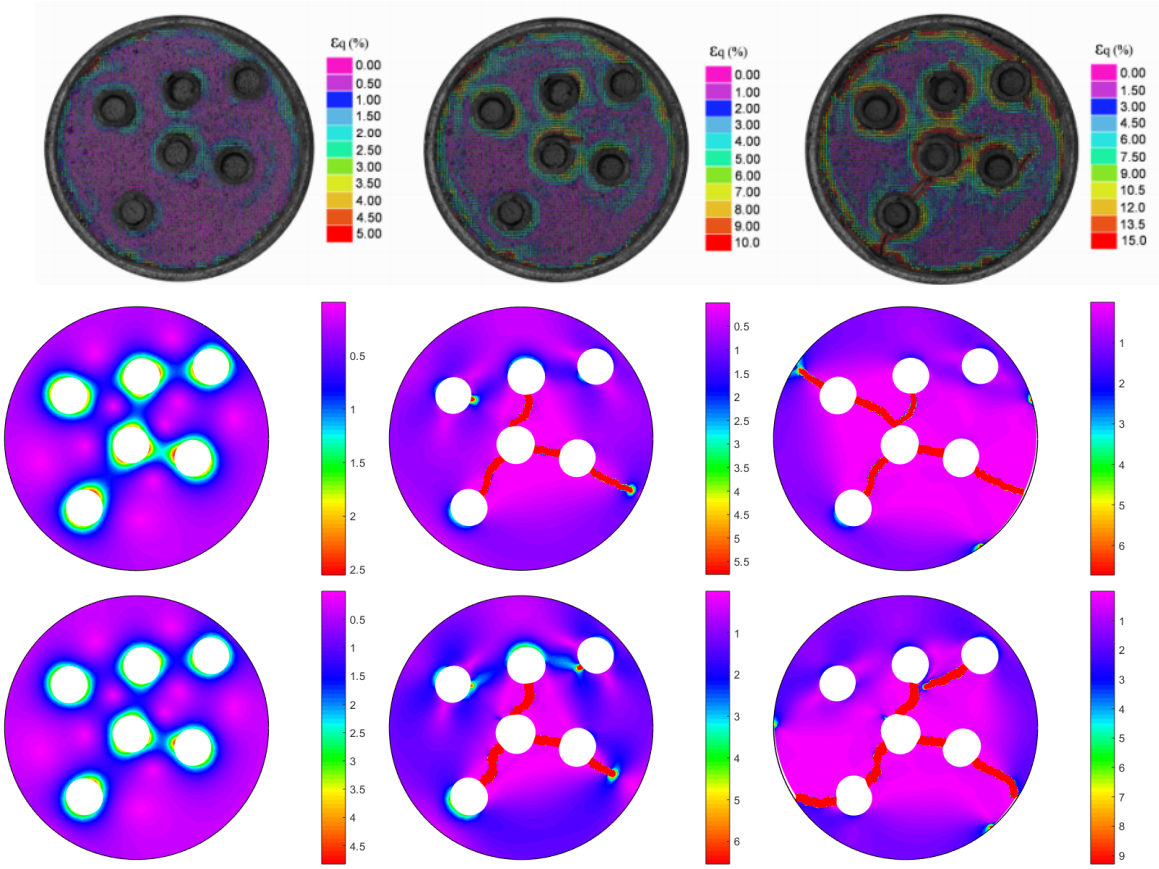

Figure 5.14 – Deviatoric strain map in S_6: experimental results (top), numerical results in 2D (middle), and numerical results in 3D (bottom) at times t_1, t_2, and t_3 (from left to right).

5.5 Discussion

In the above comparisons, we have observed some encouraging qualitative agreement on some points between experiments and simulations, while some others remaining to be clarified. These points can be summarized as follows.

1. The zero-displacement boundary condition applied at the outer edge is a first approximation of the frictional forces that prevent the clay matrix from retracting freely, hence creating the conditions for cracking. However, it has been observed that the clay matrix slightly lifts off the bottom at the edges, and that the amplitude of this phenomenon increases with time. This results in a soil-clay interaction zone offset. The modeling of frictional forces is therefore a natural extension to the present model. To illustrate this point, results are presented in Fig. 5.15 where the sample is not retained on its outer edges, but in a zone of small thickness close to the edges and in the clay. In this case, the edge effects observed experimentally are qualitatively recovered.

2. A localized, compressive strain zone is experimentally observed close to the outer edge and at the interface between the inclusions and the matrix. This complex interface phenomenon requires further studies and is presently not captured by our model.

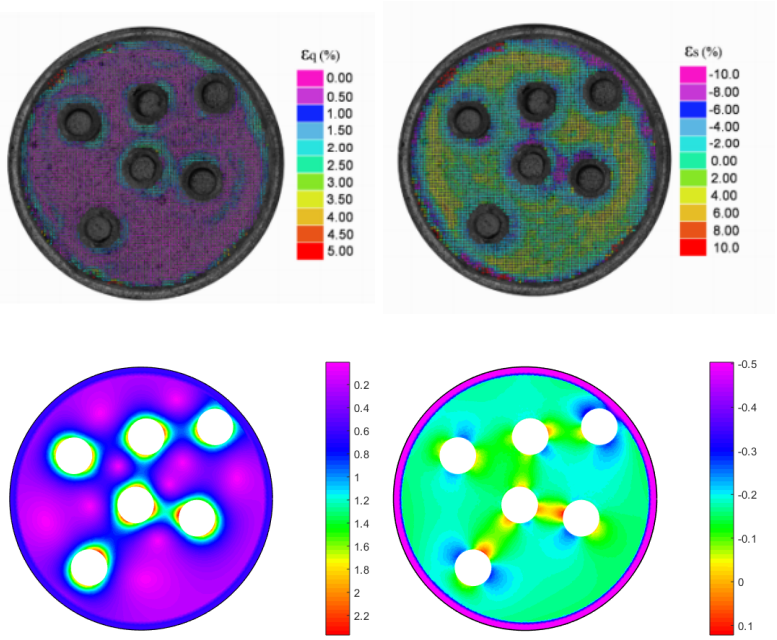

Figure 5.15 – Deviatoric (left) and spherical (right) strain maps in S_6: experimental (top) and simulation results (bottom).

3. The parameters which have been used in the simulations have been chosen as constant. However, some experimental results available in the literature show that these parameters may be spatially varying and depend on the state of water content. In this context, a more advanced experimental campaign involving variable water content could enhance the predictive capability of the computational model.

4. A large discrepancy is also observed in terms of crack propagation velocity (quantified by crack extension in a quasi-static regime). While crack propagation is typically observed over long time ranges in the experiments (about 3000 to 4000 min), crack propagation is about 10 to 20 times faster in the corresponding simulations.

5. Due to time constraints, it was not possible to include and model stochastic aspects such as those developed in Chapter 2. It is however reasonable to assume that random subscale details within the clay induce substantial variability in the elastic and fracture properties. Other sources of uncertainties related to the experiments have also been listed at the end of Chapter 4. One priority for future works will be to include all these uncertainties within the modeling framework.

5.6 Conclusion

In this chapter, we have compared results obtained through the drying experiments detailed in Chapter 4 with predictions delivered by 2D and 3D numerical models. The experimental results were notably used to identify an appropriate form for the hydric shrinkage strain. An extensive simulation campaign was then carried out to investigate the impact of inclusions on crack propagation, for various configurations.

From a qualitative standpoint, predictions were shown to be in reasonable agreement with the experimental results. The strain fields and the hydrostatic strain are mostly negative, and localize on the edges of the inclusions. As expected, localized strain fields are also observed in the vicinity of crack paths.

Many issues remain, however, to obtain better quantitative agreement. The present model lacks in representing some features observed during the experiments, such as local compressive strain at the matrix-inclusion interface and near the external boundary. This strain induces a large discrepancy in the numerical values of local strains and crack paths.

We have suggested several improvements to enhance the present models, including a deeper analysis of the cohesion at the boundaries and at the matrix-inclusion interface, the introduction of friction at the bottom surface, a more realistic phase change model for the clay (which passes from liquid to solid state), and the introduction of uncertainties within the model.

Conclusion and Perspectives

General conclusion

In this thesis, we have investigated the fracture of heterogeneous quasi-brittle materials through both computational analysis and physical experiments, putting emphasis on random media and fracture induced by desiccation. The contributions of the present work are summarized as follows.

First, a stochastic approach to model crack propagation in random media was proposed in Chapter 2. The formulation relies on a phase-field model involving mesoscopic material coefficients. Monte-Carlo simulations were first performed at microscale to characterize stochasticity in the macroscopic response. The definition of the mesoscopic parameters was then addressed. The elasticity field at mesoscale was defined as the isotropic approximation of spatially varying apparent tensors, obtained under kinematically and statically uniform boundary conditions. The mesoscopic toughness was identified solving an inverse problem related to the mean peak force. A probabilistic model for the elasticity random field was then constructed and allows for a fast, robust sampling of mesoscopic elasticity. The results obtained by combining this surrogate with the phase-field model were finally compared with the reference, microscopic model. It was shown, in particular, that the model-based, mesoscopic phase-field formulation associated with statically uniform boundary conditions allows for an accurate prediction of both the mean elastic response and mean peak force.

In Chapter 3, we reviewed a finite-strain phase-field formulation, with the aim of capturing the effects of the large deformations occurring during the drying of clay samples. A parametric analysis was then conducted in order to quantify the impact of the numerical parameters in terms of convergence and accuracy of the solution. We then extended the model to account for the hydric effects arising during the drying tests. A generic, low-dimensional representation was retained to parameterize the driving term, hence allowing the choice of a calibration from the available experimental data.

Chapter 4 is concerned with the description of the physical experiments (conducted by Dr. A. Dadda, Navier Laboratory, Ecole des Ponts ParisTech). In these experiments, cylindrical clay samples are dried and cracks start propagating due to shrinkage. In order to introduce and characterize the impact of potential interaction effects in a controlled manner, fixed cylindrical obstacles were inserted within the samples. In addition to crack patterns, strain fields were also obtained as a function of time, using a digital image correlation technique. The combination of these results constitutes an original contribution enabling us to discuss some correlation effects between the nature (and evolution) of the strain fields and the creation of crack paths.

The experimental results were finally compared with numerical predictions in Chapter 5. The

identification of the hydric strain function based on the variation of the sample geometry during the shrinkage has been carried out. We then addressed validation with different configurations of obstacles, using both 2D and 3D numerical models. This validation step constitutes a first step towards the construction of such models, and while some qualitative agreement was found overall, some major discrepancies were also identified. This suggests that the present model could be enhanced in many ways and possible strategies to improve predictions, reported as perspectives for future work below, were proposed.

Perspectives

There are many perspectives for this work, which are listed below.

- The stochastic model presented in Chapter 2 could be extended by generating random fields of damage parameters. In the present work, we have used a random elastic medium, but the effective stochastic medium was limited to the elastic aspects and the effective fracture was considered as constant. Extension to random fields of fracture models constitutes a direct perspective for this work.

- This stochastic fracture model could be applied to a large class of other materials such as porous media, lattice models or polycrystalline materials. A study using this identification model applied to other geometries or stresses would be another perspective.

- As mentioned above, the constructed phase field model for the drying-induced model still requires improvement to provide satisfactory agreement with the experiments. The possible improvements of the model include: (a) a better description of the experimental boundary conditions, like the friction at the bottom of the specimen and the role of decohesion on the external boundaries; (b) a better description of interfacial conditions around the obstacles within the sample; (c) elucidating the localization of compressive strain near the matrix/interface inclusions; (d) a nonlinear model for model parameters, including a dependence on the water content, and a full phase change description of the clay through its liquid-solid state during the drying.

- Finally, a complete description of uncertainties of the process and its introduction of the model will be an important improvement. A first class of uncertainties are related to the experimental conditions (decohesion of the boundaries, friction on the bottom, etc). Another class of uncertainties are related to the material, where the heterogeneities at the microscale induce random effects during the drying and influence the crack paths. This is obvious in homogeneous samples, where the crack patterns are highly random, and more deterministic when obstacles induce predetermined localization paths during the process. An analysis on how these macro heterogeneities (obstacles) change the stochastic nature of the crack path will be a challenging and exciting perspective for this work.

Appendix A

Discretization and FE operators

A.1 Isoparametric formulation

In this formulation each element of the domain Ω_E is defined on the physical space E and is associated to a reference element $\Omega_{\bar{E}}$ defined also in it reference space $\bar{E}$ (see Fig. A.1). The

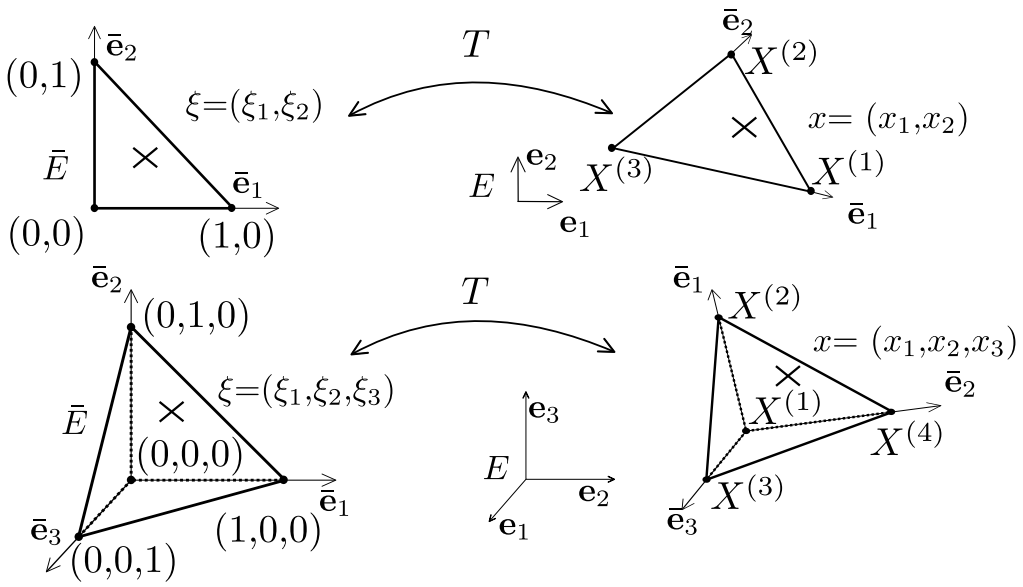

Figure A.1 – Geometrical transformation T : isoparametric $\bar{E}$ to physical E space).

bijective geometrical transformation from the reference element to physical element have some properties as :

- local coordinate form:

$$\boldsymbol{x} = [x_1(\boldsymbol{\xi}), x_2(\boldsymbol{\xi})]^T = [x_1(\boldsymbol{X}), x_2(\boldsymbol{X})]^T, \text{ in 2D case,} \tag{A.1}$$

$$\boldsymbol{x} = [x_1(\boldsymbol{\xi}), x_2(\boldsymbol{\xi}), x_3(\boldsymbol{\xi})]^T = [x_1(\boldsymbol{X}), x_2(\boldsymbol{X}), x_3(\boldsymbol{X})]^T, \text{ in 3D case.} \tag{A.2}$$

  which

  – the following interpolation:

$$x_p(\boldsymbol{\xi}) = \sum_{i=1}^{n} N_i(\boldsymbol{\xi}) X_p^{(i)}, \tag{A.3}$$

- n : the number of nodes in one element Ω_E,
- p : the dimension of the space,
- $x_p(\boldsymbol{\xi})$: the p-coordinates of $\boldsymbol{x}$,
- ξ_p : the p-coordinates of $\boldsymbol{\xi}$ define on the isoparametric basis $\bar{E}$,
- X_p : the p-coordinates of $\boldsymbol{X}$ define on the physical basis $\bar{E}$,
- $X_p^{(i)}$: the p-coordinates of the (i)-node,
- $N_i(\boldsymbol{\xi})$ the shape functions define on isoparametric basis.

- Jacobian matrix of the transformation T:

$$[J]_{ij}(\boldsymbol{\xi}) := \frac{\partial x_j(\boldsymbol{\xi})}{\partial \xi_i} = x_{j,\xi_i}, \tag{A.4}$$

$$[J(\boldsymbol{\xi})]_{(pxp)} \overset{p=2}{:=} \underbrace{\begin{bmatrix} x_{1,\xi_1} & x_{2,\xi_1} \\ x_{1,\xi_2} & x_{2,\xi_2} \end{bmatrix}}_{(2x2)} \text{(2D case)} \overset{p=3}{:=} \underbrace{\begin{bmatrix} x_1(\boldsymbol{\xi})_{,\xi_1} & x_2(\boldsymbol{\xi})_{,\xi_1} & x_3(\boldsymbol{\xi})_{,\xi_1} \\ x_1(\boldsymbol{\xi})_{,\xi_2} & x_2(\boldsymbol{\xi})_{,\xi_2} & x_3(\boldsymbol{\xi})_{,\xi_2} \\ x_1(\boldsymbol{\xi})_{,\xi_3} & x_2(\boldsymbol{\xi})_{,\xi_3} & x_3(\boldsymbol{\xi})_{,\xi_3} \end{bmatrix}}_{(3x3)} \text{(for 3D case)},$$

using the Eq. A.3 interpolation the jacobian can be written as :

$$[J]_{(pxp)} = \underbrace{\begin{bmatrix} N_1(\boldsymbol{\xi})_{,\xi_1} & \dots & N_i(\boldsymbol{\xi})_{,\xi_1} & \dots & N_n(\boldsymbol{\xi})_{,\xi_1} \\ \vdots & \dots & \vdots & \dots & \vdots \\ N_1(\boldsymbol{\xi})_{,\xi_p} & \dots & N_i(\boldsymbol{\xi})_{,\xi_p} & \dots & N_n(\boldsymbol{\xi})_{,\xi_p} \end{bmatrix}}_{(pxn)} \underbrace{\begin{bmatrix} x_1 & y_1 \\ \vdots & \vdots \\ x_i & y_i \\ \vdots & \vdots \\ x_n & y_n \end{bmatrix}}_{(nxp)}. \tag{A.5}$$

- derivative transformation : the gradient of $f(\boldsymbol{x})$ function with respect to $\boldsymbol{\xi}$

$$\nabla_{\boldsymbol{\xi}}(f(\boldsymbol{x})) := \begin{bmatrix} f(\boldsymbol{x})_{,\xi_1} \\ f(\boldsymbol{x})_{,\xi_2} \end{bmatrix} = \begin{bmatrix} \frac{\partial f(\boldsymbol{x})}{\partial x_1}\frac{\partial x_1}{\partial \xi_1} & \frac{\partial f(\boldsymbol{x})}{\partial x_2}\frac{\partial x_2}{\partial \xi_1} \\ \frac{\partial f(\boldsymbol{x})}{\partial x_1}\frac{\partial x_1}{\partial \xi_2} & \frac{\partial f(\boldsymbol{x})}{\partial x_2}\frac{\partial x_2}{\partial \xi_2} \end{bmatrix} = [J] \begin{bmatrix} f(\boldsymbol{x})_{,x_1} \\ f(\boldsymbol{x})_{,x_2} \end{bmatrix}. \tag{A.6}$$

it can be deduced that :

$$\nabla_{\boldsymbol{x}}(f(\boldsymbol{x})) = [J]^{-1}\nabla_{\boldsymbol{\xi}}(f(\boldsymbol{x})), \tag{A.7}$$

in particular f can be interpolated using in the same way the Eq. A.3 :

$$f(\boldsymbol{x}) = \sum_{i=1}^{n} N_i(\boldsymbol{\xi}) f^{(i)}, \tag{A.8}$$

Here $f^{(i)}$ is the nodal value of f function estimated on the $i \in 1, ..., n$ node .

- computational evaluation of integral : The integral is estimated by the classical Gauss quadrature for example here :

$$\int_{\Omega_E} f(\boldsymbol{x}) d\Omega_E = \int_{\Omega_{\bar{E}}} f(\boldsymbol{\xi}) det([J(\boldsymbol{\xi})]) d\Omega_{\bar{E}} \simeq \sum_{p=1}^{Ng} \omega_p f(\boldsymbol{\xi}_p) det(J(\boldsymbol{\xi}_p)), \tag{A.9}$$

$p = \{1, 2, ..., Ng\}$ is the Gauss quadrature points, Ng the maximal number of Gauss quadrature, and ω_p the gauss weight associated to the Ng quadrature chosen.

A.2 Finite element operators

A.2.1 [G(x)] operator

The operator $[\boldsymbol{G}(\boldsymbol{x})]$ is defined as :

$$\nabla \boldsymbol{u}(\boldsymbol{x}) = [\boldsymbol{G}(\boldsymbol{x})]\{\boldsymbol{u}_e^i\}, \tag{A.10}$$

and the explicite form for 2D (T3 element) can be written as :

$$\{\nabla u\} \overset{(2D)}{:=} \begin{bmatrix} N_{u1,1}(\boldsymbol{x}) & 0 & N_{u2,1}(\boldsymbol{x}) & 0 & N_{u3,1}(\boldsymbol{x}) & 0 \\ N_{u1,2}(\boldsymbol{x}) & 0 & N_{u2,2}(\boldsymbol{x}) & 0 & N_{u3,2}(\boldsymbol{x}) & 0 \\ 0 & N_{u1,1}(\boldsymbol{x}) & 0 & N_{u2,1}(\boldsymbol{x}) & 0 & N_{u3,1}(\boldsymbol{x}) \\ 0 & N_{u1,2}(\boldsymbol{x}) & 0 & N_{u2,2}(\boldsymbol{x}) & 0 & N_{u3,2}(\boldsymbol{x}) \end{bmatrix} \{\boldsymbol{u}_e^i\},$$

or for 3D (T4 element) as :

$$\{\nabla u\} \overset{(3D)}{:=} \begin{bmatrix} N_{u1,1} & 0 & 0 & N_{u2,1} & 0 & 0 & N_{u3,1} & 0 & 0 & N_{u4,1} & 0 & 0 \\ N_{u1,2} & 0 & 0 & N_{u2,2} & 0 & 0 & N_{u3,2} & 0 & 0 & N_{u4,2} & 0 & 0 \\ N_{u1,3} & 0 & 0 & N_{u2,3} & 0 & 0 & N_{u3,3} & 0 & 0 & N_{u4,3} & 0 & 0 \\ 0 & N_{u1,1} & 0 & 0 & N_{u2,1} & 0 & 0 & N_{u3,1} & 0 & 0 & N_{u4,1} & 0 \\ 0 & N_{u1,2} & 0 & 0 & N_{u2,2} & 0 & 0 & N_{u3,2} & 0 & 0 & N_{u4,2} & 0 \\ 0 & N_{u1,3} & 0 & 0 & N_{u2,3} & 0 & 0 & N_{u3,3} & 0 & 0 & N_{u4,3} & 0 \\ 0 & 0 & N_{u1,1} & 0 & 0 & N_{u2,1} & 0 & 0 & N_{u3,1} & 0 & 0 & N_{u4,1} \\ 0 & 0 & N_{u1,2} & 0 & 0 & N_{u2,2} & 0 & 0 & N_{u3,2} & 0 & 0 & N_{u4,2} \\ 0 & 0 & N_{u1,3} & 0 & 0 & N_{u2,3} & 0 & 0 & N_{u3,3} & 0 & 0 & N_{u4,3} \end{bmatrix}$$

A.2.2 $[B_e]$ and $[B_u]$ operators

Those operators can be explicitly describe for 2D (T3 element) as :

$$[\boldsymbol{B_e}] \overset{(2D)}{:=} \begin{bmatrix} G(1,:) \\ G(3,:) \\ (1/\sqrt{2})(G(2,:) + G(4,:)) \end{bmatrix},$$

$$[\boldsymbol{B_u}] \overset{(2D)}{:=} \begin{bmatrix} \{\nabla u(1)\}G(1,:) + \{\nabla u(3)\}G(3,:) \\ \{\nabla u(2)\}G(2,:) + \{\nabla u(4)\}G(4,:) \\ (1/\sqrt{2})(\{\nabla u(1)\}G(2,:) + \{\nabla u(3)\}G(4,:)\{\nabla u(2)\}G(1,:) + \{\nabla u(4)\}G(3,:)) \end{bmatrix}$$

and for 3D (T4 element) :

$$[\boldsymbol{B_e}] \overset{(3D)}{:=} \begin{bmatrix} G(1,:) \\ G(5,:) \\ G(9,:) \\ (1/\sqrt{2})(G(6,:) + G(8,:)) \\ (1/\sqrt{2})(G(3,:) + G(7,:)) \\ (1/\sqrt{2})(G(2,:) + G(4,:)) \end{bmatrix}.$$

$$[\boldsymbol{B_u}] \overset{(3D)}{:=} ...$$

$$\begin{bmatrix} \{\nabla u(1)\}G(1,:) + \{\nabla u(4)\}G(4,:) + \{\nabla u(7)\}G(7,:) \\ \{\nabla u(2)\}G(2,:) + \{\nabla u(5)\}G(5,:) + \{\nabla u(8)\}G(8,:) \\ \{\nabla u(3)\}G(3,:) + \{\nabla u(6)\}G(6,:) + \{\nabla u(9)\}G(9,:) \\ (1/\sqrt{2})(\{\nabla u(3)\}G(2,:) + \{\nabla u(6)\}G(5,:) + \{\nabla u(9)\}G(8,:) + \{\nabla u(2)\}G(3,:) + \{\nabla u(5)\}G(6,:) + \{\nabla u(8)\}G(9,:)) \\ (1/\sqrt{2})(\{\nabla u(3)\}G(1,:) + \{\nabla u(6)\}G(4,:) + \{\nabla u(9)\}G(7,:) + \{\nabla u(1)\}G(3,:) + \{\nabla u(4)\}G(6,:) + \{\nabla u(7)\}G(9,:)) \\ (1/\sqrt{2})(\{\nabla u(2)\}G(1,:) + \{\nabla u(5)\}G(4,:) + \{\nabla u(8)\}G(7,:) + \{\nabla u(1)\}G(2,:) + \{\nabla u(4)\}G(5,:) + \{\nabla u(7)\}G(8,:)) \end{bmatrix}$$

A.2.3 $[B_p]$ operator

$[\boldsymbol{B_p}]$ operator is defined for 2D case (T3 element) as:

$$[\boldsymbol{B_p}] \overset{(2D)}{:=} \begin{bmatrix} S(1)G(1,:) + (1/\sqrt{2})S(3)G(2,:) \\ S(2)G(2,:) + (1/\sqrt{2})S(2)G(2,:) \\ S(1)G(2,:) + (1/\sqrt{2})S(3)G(4,:) \\ S(2)G(4,:) + (1/\sqrt{2})S(3)G(1,:) \end{bmatrix}.$$

and for 3D (T4 element) as :

$$[\boldsymbol{B_p}] \overset{(2D)}{:=} \begin{bmatrix} S(1)G(1,:) + (1/\sqrt{2})[S(5)G(3,:) + S(6)G(2,:)] \\ S(2)G(2,:) + (1/\sqrt{2})[S(4)G(2,:) + S(6)G(1,:)] \\ S(3)G(3,:) + (1/\sqrt{2})[S(4)G(2,:) + S(5)G(1,:)] \\ S(1)G(4,:) + (1/\sqrt{2})[S(5)G(6,:) + S(6)G(5,:)] \\ S(2)G(5,:) + (1/\sqrt{2})[S(4)G(6,:) + S(6)G(4,:)] \\ S(3)G(6,:) + (1/\sqrt{2})[S(4)G(5,:) + S(5)G(4,:)] \\ S(1)G(7,:) + (1/\sqrt{2})[S(5)G(9,:) + S(6)G(8,:)] \\ S(2)G(8,:) + (1/\sqrt{2})[S(4)G(9,:) + S(6)G(7,:)] \\ S(3)G(9,:) + (1/\sqrt{2})[S(4)G(8,:) + S(5)G(7,:)] \end{bmatrix}.$$

A.2.4 $[B_p]$ operator with shrinkage

$[\boldsymbol{B_p}]$ operator is defined for 2D case (T3 element) with :

$$S = \mathbb{C}(\boldsymbol{E} - \boldsymbol{E}_h)$$

where $E_h = \alpha[1,1,0]'$ as :

$$[\boldsymbol{B_p}] \overset{(2D)}{:=} \begin{bmatrix} \overline{S}(1)G(1,:) + (1/\sqrt{2})\overline{S}(3)G(2,:) \\ \overline{S}(2)G(2,:) + (1/\sqrt{2})\overline{S}(2)G(2,:) \\ \overline{S}(1)G(2,:) + (1/\sqrt{2})\overline{S}(3)G(4,:) \\ \overline{S}(2)G(4,:) + (1/\sqrt{2})\overline{S}(3)G(1,:) \end{bmatrix}.$$

and for 3D (T4 element) with the same way and where $E_h = \alpha[1,1,1,0,0,0]'$

$$[\boldsymbol{B_p}] \overset{(2D)}{:=} \begin{bmatrix} \overline{S}(1)G(1,:) + (1/\sqrt{2})[\overline{S}(5)G(3,:) + \overline{S}(6)G(2,:)] \\ \overline{S}(2)G(2,:) + (1/\sqrt{2})[\overline{S}(4)G(2,:) + \overline{S}(6)G(1,:)] \\ \overline{S}(3)G(3,:) + (1/\sqrt{2})[\overline{S}(4)G(2,:) + \overline{S}(5)G(1,:)] \\ \overline{S}(1)G(4,:) + (1/\sqrt{2})[\overline{S}(5)G(6,:) + \overline{S}(6)G(5,:)] \\ \overline{S}(2)G(5,:) + (1/\sqrt{2})[\overline{S}(4)G(6,:) + \overline{S}(6)G(4,:)] \\ \overline{S}(3)G(6,:) + (1/\sqrt{2})[\overline{S}(4)G(5,:) + \overline{S}(5)G(4,:)] \\ \overline{S}(1)G(7,:) + (1/\sqrt{2})[\overline{S}(5)G(9,:) + \overline{S}(6)G(8,:)] \\ \overline{S}(2)G(8,:) + (1/\sqrt{2})[\overline{S}(4)G(9,:) + \overline{S}(6)G(7,:)] \\ \overline{S}(3)G(9,:) + (1/\sqrt{2})[\overline{S}(4)G(8,:) + \overline{S}(5)G(7,:)] \end{bmatrix}.$$

Bibliography

[Abraham et al., 1994] Abraham, F. F., Brodbeck, D., Rafey, R., and Rudge, W. (1994). Instability dynamics of fracture: a computer simulation investigation. *Physical Review Letters*, 73(2):272.

[Acton et al., 2018] Acton, K. A., Baxter, S. C., Bahmani, B., Clarke, P. L., and Abedi, R. (2018). Voronoi tessellation based statistical volume element characterization for use in fracture modeling. *Computer Methods in Applied Mechanics and Engineering*, 336:135 – 155.

[Allais et al., 1994] Allais, L., Bornert, M., Bretheau, T., and Caldemaison, D. (1994). Experimental characterization of the local strain field in a heterogeneous elastoplastic material. *Acta Metallurgica et materialia*, 42(11):3865–3880.

[Amarasiri et al., 2011] Amarasiri, A. L., Kodikara, J. K., and Costa, S. (2011). Numerical modelling of desiccation cracking. *International Journal for Numerical and Analytical Methods in Geomechanics*, 35(1):82–96.

[Ambati et al., 2015] Ambati, M., Gerasimov, T., and de Lorenzis, L. (2015). A review on phase-field models of brittle fracture and a new fast hybrid formulation. *Computational Mechanics*, 55(2):383–405.

[Ambati et al., 2016] Ambati, M., Kruse, R., and De Lorenzis, L. (2016). A phase-field model for ductile fracture at finite strains and its experimental verification. *Computational Mechanics*, 57(1):149–167.

[Ambrosio and Tortorelli, 1990] Ambrosio, L. and Tortorelli, V. M. (1990). Approximation of functional depending on jumps by elliptic functional via t-convergence. *Communications on Pure and Applied Mathematics*, 43(8):999–1036.

[Amor et al., 2009] Amor, H., Marigo, J.-J., and Maurini, C. (2009). Regularized formulation of the variational brittle fracture with unilateral contact: Numerical experiments. *Journal of the Mechanics and Physics of Solids*, 57(8):1209–1229.

[Aranson et al., 2000] Aranson, I., Kalatsky, V., and Vinokur, V. (2000). Continuum field description of crack propagation. *Physical review letters*, 85(1):118.

[Areias et al., 2016] Areias, P., Rabczuk, T., and Msekh, M. (2016). Phase-field analysis of finite-strain plates and shells including element subdivision. *Computer Methods in Applied Mechanics and Engineering*, 312:322–350.

[Arnst and Ponthot, 2014] Arnst, M. and Ponthot, J.-P. (2014). An overview of nonintrusive characterization, propagation, and sensitivity analysis of uncertainties in computational mechanics. *International Journal for Uncertainty Quantification*, 4(5).

[Audiguier et al., 2007] Audiguier, M., Geremew, Z., Laribi, S., and Cojean, R. (2007). Caractérisation au laboratoire de la sensibilité au retrait-gonflement des sols argileux. *Revue française de Géotechnique*, (120-121):67–82.

[Babuška and Melenk, 1997] Babuška, I. and Melenk, J. M. (1997). The partition of unity method. *International journal for numerical methods in engineering*, 40(4):727–758.

[Barenblatt, 1961] Barenblatt, G. (1961). Mathematical theory of equilibrium cracks formed in brittle fracture. *Zh. Prikl. Mekh. Tekh. Fiz*, (4):3–56.

[Barnier, 2015] Barnier, F. (2015). Fissuration et déformation des mortiers de terre crue au séchage. *Compte rendu de stage Amàco-INSA Lyon*, pages 1–45.

[Bažant and Novák, 2000] Bažant, Z. P. and Novák, D. (2000). Probabilistic nonlocal theory for quasibrittle fracture initiation and size effect. i: Theory. *Journal of Engineering Mechanics*, 126(2):166–174.

[Bažant and Oh, 1983] Bažant, Z. and Oh, B. (1983). Crack band theory for fracture of concrete. *Matériaux et construction*, 16(3):155–177.

[Bažant and Pijaudier-Cabot, 1988] Bažant, Z. and Pijaudier-Cabot, G. (1988). Nonlocal continuum damage, localization instability and convergence. *J. Appl. Mech.*, 55:521–539.

[Bazant and Planas, 1997] Bazant, Z. P. and Planas, J. (1997). *Fracture and size effect in concrete and other quasibrittle materials*, volume 16. CRC press.

[Belytschko and Black, 1999] Belytschko, T. and Black, T. (1999). Elastic crack growth in finite elements with minimal remeshing. *International journal for numerical methods in engineering*, 45(5):601–620.

[Bignonnet et al., 2014] Bignonnet, F., Sab, K., Dormieux, L., Brisard, S., and Bisson, A. (2014). Macroscopically consistent non-local modeling of heterogeneous media. *Computer Methods in Applied Mechanics and Engineering*, 278:218 – 238.

[Bonnet and Frangi, 2007] Bonnet, d. M. and Frangi, A. (2007). Analyse des solides déformables par la méthode des éléments finis. *European Journal of Computational Mechanics/Revue Européenne de Mécanique Numérique*, 16(5):667–668.

[Borden et al., 2014] Borden, M., Hughes, T. J., Landis, C. M., and Verhoosel, C. V. (2014). A higher-order phase-field model for brittle fracture: Formulation and analysis within the isogeometric analysis framework. *Computer Methods in Applied Mechanics and Engineering*, 273:100–118.

[Borden et al., 2016] Borden, M. J., Hughes, T. J., Landis, C. M., Anvari, A., and Lee, I. J. (2016). A phase-field formulation for fracture in ductile materials: Finite deformation balance law derivation, plastic degradation, and stress triaxiality effects. *Computer Methods in Applied Mechanics and Engineering*, 312:130–166.

[Bornert et al., 2011] Bornert, M., Orteu, J., and Roux, S. (2011). Mesures de champs et identification en mécanique des solides, chapter corrélation d'images. *Hermes, Lavoisier*.

[Borst, 1991] Borst, R. D. (1991). Simulation of strain localization: a reappraisal of the cosserat continuum. *Engineering computations*, 8(4):317–332.

[Borst et al., 1993] Borst, R. D., l.J. Sluys, and Pamin, H. M. J. (1993). Fundamental issues in finite element analysis of localization of deformation. *Eng. Comput.*, 10:99–121.

[Borst and Verhoosel, 2016] Borst, R. D. and Verhoosel, C. (2016). Gradient damage vs phase-field approaches for fracture: Similarities and differences. *Computer Methods in Applied Mechanics and Engineering*, 312:78–94.

[Bourdin et al., 2000] Bourdin, B., Francfort, G. A., and Marigo, J.-J. (2000). Numerical experiments in revisited brittle fracture. *Journal of the Mechanics and Physics of Solids*, 48(4):797–826.

[Bourdin et al., 2008] Bourdin, B., Francfort, G. A., and Marigo, J.-J. (2008). The variational approach to fracture. *Journal of elasticity*, 91(1-3):5–148.

[Cajuhi et al., 2018] Cajuhi, T., Sanavia, L., and De Lorenzis, L. (2018). Phase-field modeling of fracture in variably saturated porous media. *Computational Mechanics*, 61(3):299–318.

[Chaboche, 1988] Chaboche, J.-L. (1988). Continuum damage mechanics: Part ii—damage growth, crack initiation, and crack growth. *Journal of applied mechanics*, 55(1):65–72.

[Cundall and Strack, 1979] Cundall, P. A. and Strack, O. D. (1979). A discrete numerical model for granular assemblies. *geotechnique*, 29(1):47–65.

[Daphalapurkar et al., 2011] Daphalapurkar, N. P., Ramesh, K., Graham-Brady, L., and Molinari, J.-F. (2011). Predicting variability in the dynamic failure strength of brittle materials considering pre-existing flaws. *Journal of the Mechanics and Physics of Solids*, 59(2):297 – 319.

[Donev et al., 2005] Donev, A., Torquato, S., and Stillinger, F. H. (2005). Neighbor list collision-driven molecular dynamics simulation for nonspherical hard particles. i. algorithmic details. *Journal of computational physics*, 202(2):737–764.

[Dugdale, 1960] Dugdale, D. S. (1960). Yielding of steel sheets containing slits. *Journal of the Mechanics and Physics of Solids*, 8(2):100–104.

[El Mountassir et al., 2014] El Mountassir, G., Sánchez, M., and Romero, E. (2014). An experimental study on the compaction and collapsible behaviour of a flood defence embankment fill. *Engineering geology*, 179:132–145.

[Elices et al., 2002] Elices, M., Guinea, G., Gomez, J., and Planas, J. (2002). The cohesive zone model: advantages, limitations and challenges. *Engineering fracture mechanics*, 69(2):137–163.

[Erbts and DüSter, 2012] Erbts, P. and DüSter, A. (2012). Accelerated staggered coupling schemes for problems of thermoelasticity at finite strains. *Computers & Mathematics with Applications*, 64(8):2408–2430.

[Etse and Willam, 1999] Etse, G. and Willam, K. (1999). Failure analysis of elastoviscoplastic material models. *Journal of Engineering Mechanics*, 125(1):60–69.

[Francfort and Marigo, 1998] Francfort, G. A. and Marigo, J.-J. (1998). Revisiting brittle fracture as an energy minimization problem. *Journal of the Mechanics and Physics of Solids*, 46(8):1319–1342.

[Geelen et al., 2019] Geelen, R. J., Liu, Y., Hu, T., Tupek, M. R., and Dolbow, J. E. (2019). A phase-field formulation for dynamic cohesive fracture. *Computer Methods in Applied Mechanics and Engineering*, 348:680–711.

[Genet et al., 2014] Genet, M., Couégnat, G., Tomsia, A. P., and Ritchie, R. O. (2014). Scaling strength distributions in quasi-brittle materials from micro- to macro-scales: A computational approach to modeling nature-inspired structural ceramics. *Journal of the Mechanics and Physics of Solids*, 68:93 – 106.

[Graham et al., 2003] Graham, L., Gurley, K., and Masters, F. (2003). Non-gaussian simulation of local material properties based on a moving-window technique. *Probabilistic Engineering Mechanics*, 18(3):223 – 234.

[Guilleminot and Soize, 2012a] Guilleminot, J. and Soize, C. (2012a). Generalized stochastic approach for constitutive equation in linear elasticity: a random matrix model. *International Journal for Numerical Methods in Engineering*, 90(5):613–635.

[Guilleminot and Soize, 2012b] Guilleminot, J. and Soize, C. (2012b). Stochastic modeling of anisotropy in multiscale analysis of heterogeneous materials: A comprehensive overview on random matrix approaches. *Mechanics of Materials*, 44:35–46.

[Guilleminot and Soize, 2013a] Guilleminot, J. and Soize, C. (2013a). On the statistical dependence for the components of random elasticity tensors exhibiting material symmetry properties. *Journal of Elasticity*, 111:109–130.

[Guilleminot and Soize, 2013b] Guilleminot, J. and Soize, C. (2013b). Stochastic model and generator for random fields with symmetry properties: Application to the mesoscopic modeling of elastic random media. *SIAM Multiscale Modeling & Simulation*, 11:840–870.

[Guilleminot and Soize, 2017] Guilleminot, J. and Soize, C. (2017). *Non-Gaussian Random Fields in Multiscale Mechanics of Heterogeneous Materials*, pages 1–9. Springer Berlin Heidelberg, Berlin, Heidelberg.

[Gültekin et al., 2018] Gültekin, O., Dal, H., and Holzapfel, G. A. (2018). Numerical aspects of anisotropic failure in soft biological tissues favor energy-based criteria: a rate-dependent anisotropic crack phase-field model. *Computer Methods in Applied Mechanics and Engineering*, 331:23–52.

[Hansbo and Hansbo, 2004] Hansbo, A. and Hansbo, P. (2004). A finite element method for the simulation of strong and weak discontinuities in solid mechanics. *Computer methods in applied mechanics and engineering*, 193(33-35):3523–3540.

[Hazanov and Huet, 1994] Hazanov, S. and Huet, C. (1994). Order relationships for boundary condition effect in heterogeneous bodies smaller than the representative volume. *Journal of the Mechanics and Physics of Solids*, 42(12):1995–2011.

[He and Shao, 2019] He, Q.-C. and Shao, Q. (2019). Closed-form coordinate-free decompositions of the two-dimensional strain and stress for modeling tension–compression dissymmetry. *Journal of Applied Mechanics*, 86(3):031007.

[Hedjazi et al., 2012] Hedjazi, L., Martin, C., Guessasma, S., Della Valle, G., and Dendievel, R. (2012). Application of the discrete element method to crack propagation and crack branching in a vitreous dense biopolymer material. *International Journal of Solids and Structures*, 49(13):1893–1899.

[Henry and Levine, 2004] Henry, H. and Levine, H. (2004). Dynamic instabilities of fracture under biaxial strain using a phase field model. *Physical review letters*, 93(10):105504.

[Hesch and Weinberg, 2014] Hesch, C. and Weinberg, K. (2014). Thermodynamically consistent algorithms for a finite-deformation phase-field approach to fracture. *International Journal for Numerical Methods in Engineering*, 99(12):906–924.

[Huet, 1990] Huet, C. (1990). Application of variational concepts to size effects in elastic heterogeneous bodies. *Journal of the Mechanics and Physics of Solids*, 38(6):813–841.

[Hun et al., 2018] Hun, D.-A., Guilleminot, J., Yvonnet, J., and Bornert, M. (2018). Construction of simplified models for crack propagation in random heterogeneous media. *The 13th World Congress in Computational Mechanics, New York, USA*.

[Hun et al., 2019a] Hun, D.-A., Guilleminot, J., Yvonnet, J., and Bornert, M. (2019a). Approche stochastique multi-échelles de la propagation de fissures dans les matériaux hétérogènes. *Computational Structural Mechanics Association, Var, France*.

[Hun et al., 2019b] Hun, D.-A., Guilleminot, J., Yvonnet, J., and Bornert, M. (2019b). Computational modeling of crack propagation in a heterogeneous medium under drying conditions. *Engineering Mechanics Institute Conference, Caltech, Pasadena, California, USA*.

[Hun et al., 2019c] Hun, D.-A., Guilleminot, J., Yvonnet, J., and Bornert, M. (2019c). Stochastic multiscale modeling of crack propagation in random heterogeneous media. *International Journal for Numerical Methods in Engineering*, 119(13):1325–1344.

[Hun et al., 2020] Hun, D.-A., Guilleminot, J., Yvonnet, J., and Bornert, M. (2020). Crack propagation in a heterogeneous clay material under drying conditions, experimental study and numerical simulation. *In preparation*.

[Irwin, 1957] Irwin, G. R. (1957). Analysis of stresses and strains near the end of a crack transversing a plate. *Trans. ASME, Ser. E, J. Appl. Mech.*, 24:361–364.

[Jirásek, 2004] Jirásek, M. (2004). Non-local damage mechanics with application to concrete. *Revue française de génie civil*, 8(5-6):683–707.

[JiráSek, 2007] JiráSek, M. (2007). Nonlocal damage mechanics. *Revue européenne de génie civil*, 11(7-8):993–1021.

[JiráSek and Bauer, 2012] JiráSek, M. and Bauer, M. (2012). Numerical aspects of the crack band approach. *Computers & Structures*, 110:60–78.

[Kachanov, 1958] Kachanov, L. (1958). Rupture time under creep conditions. *Izv. Akad. Nauk SSSR*, 8:26–31.

[Karma, 2001] Karma, A. (2001). Phase-field formulation for quantitative modeling of alloy solidification. *Physical Review Letters*, 87(11):115701.

[Karma et al., 2001] Karma, A., Kessler, D., and H., L. (2001). Phase-field model of mode iii dynamic fracture. *Physical Review Letters*, 87(4):045501.

[Kodikara and Costa, 2013] Kodikara, J. and Costa, S. (2013). Desiccation cracking in clayey soils: mechanisms and modelling. In *Multiphysical testing of soils and shales*, pages 21–32. Springer.

[Krajcinovic, 1983] Krajcinovic, D. (1983). Constitutive equations for damaging materials. *Journal of applied Mechanics*, 50(2):355–360.

[Kuhn and Müller, 2008] Kuhn, C. and Müller, R. (2008). A phase field model for fracture. *PAMM*, 8(1):10223–10224.

[Kuhn et al., 2015] Kuhn, C., Schlüter, A., and Müller, R. (2015). On degradation functions in phase field fracture models. *Computational Materials Science*, 108:374–384.

[Lakes et al., 1990] Lakes, R., Nakamura, S., Behiri, J., and Bonfield, W. (1990). Fracture mechanics of bone with short cracks. *Journal of biomechanics*, 23(10):967–975.

[Lakshmikantha et al., 2009] Lakshmikantha, M., Prat, P., and Ledesma, A. (2009). Image analysis for the quantification of a developing crack network on a drying soil. *Geotechnical Testing Journal*, 32(6):505–515.

[Lakshmikantha, 2009] Lakshmikantha, M. R. (2009). Experimental and theoretical analysis of cracking in drying soils.

[Lemaitre and Chaboche, 1994] Lemaitre, J. and Chaboche, J.-L. (1994). *Mechanics of solid materials*. Cambridge university press.

[Ling et al., 2009] Ling, D., Yang, Q., and Cox, B. (2009). An augmented finite element method for modeling arbitrary discontinuities in composite materials. *International journal of fracture*, 156(1):53–73.

[Littlewood et al., 2015] Littlewood, D. J., Silling, S. A., Mitchell, J. A., Seleson, P. D., Bond, S. D., Parks, M. L., Turner, D. Z., Burnett, D. J., Ostien, J., and Gunzburger, M. (2015). Strong local-nonlocal coupling for integrated fracture modeling. *Sandia Report SAND2015-7998, Sandia National Laboratories*, 3.

[Lorentz, 2017] Lorentz, E. (2017). A nonlocal damage model for plain concrete consistent with cohesive fracture. *International Journal of Fracture*, 207(2):123–159.

[Lu and Pister, 1975] Lu, S. and Pister, K. (1975). Decomposition of deformation and representation of the free energy function for isotropic thermoelastic solids. *International Journal of Solids and Structures*, 11(7-8):927–934.

[Malthe-Sørenssen et al., 1998] Malthe-Sørenssen, A., Walmann, T., Feder, J., Jøssang, T., Meakin, P., and Hardy, H. (1998). Simulation of extensional clay fractures. *Physical Review E*, 58(5):5548.

[Malyarenko and Ostoja-Starzewski, 2017] Malyarenko, A. and Ostoja-Starzewski, M. (2017). A random field formulation of hooke's law in all elasticity classes. *Journal of Elasticity*, 127(2):269–302.

[Mazars, 1984] Mazars, J. (1984). *Application of Continuous Damage Mechanic to Non-Linear Behavior of Concrete Structures*. PhD thesis, PhD Thesis, Paris 6 University, Paris. (in French).

[Mergheim et al., 2005] Mergheim, J., Kuhl, E., and Steinmann, P. (2005). A finite element method for the computational modelling of cohesive cracks. *International Journal for Numerical Methods in Engineering*, 63(2):276–289.

[Miehe, 1998] Miehe, C. (1998). Comparison of two algorithms for the computation of fourth-order isotropic tensor functions. *Computers & structures*, 66(1):37–43.

[Miehe et al., 2015] Miehe, C., Hofacker, M., Schänzel, L.-M., and Aldakheel, F. (2015). Phase field modeling of fracture in multi-physics problems. part ii. coupled brittle-to-ductile failure criteria and crack propagation in thermo-elastic–plastic solids. *Computer Methods in Applied Mechanics and Engineering*, 294:486–522.

[Miehe et al., 2010a] Miehe, C., Hofacker, M., and Welschinger, F. (2010a). A phase field model for rate-independent crack propagation: Robust algorithmic implementation based on operator splits. *Computer Methods in Applied Mechanics and Engineering*, 199:2765–2778.

[Miehe and Schänzel, 2014] Miehe, C. and Schänzel, L.-M. (2014). Phase field modeling of fracture in rubbery polymers. part i: Finite elasticity coupled with brittle failure. *Journal of the Mechanics and Physics of Solids*, 65:93–113.

[Miehe et al., 2010b] Miehe, C., Welschinger, F., and Hofacker, M. (2010b). Thermodynamically consistent phase-field models of fracture: Variational principles and multi-field fe implementations. *International Journal for Numerical Methods in Engineering*, 83(10):1273–1311.

[Moës et al., 1999] Moës, N., Dolbow, J., and Belytschko, T. (1999). A finite element method for crack growth without remeshing. *International journal for numerical methods in engineering*, 46(1):131–150.

[Moran, 1969] Moran, P. (1969). Statistical inference with bivariate gamma distributions. *BiometrikaTrust*, 56:627–634.

[Munjiza et al., 1999] Munjiza, A., Andrews, K., and White, J. (1999). Combined single and smeared crack model in combined finite-discrete element analysis. *International Journal for Numerical Methods in Engineering*, 44(1):41–57.

[Needleman, 1988] Needleman, A. (1988). Material rate dependence and mesh sensitivity in localization problems. *Computer methods in applied mechanics and engineering*, 67(1):69–85.

[Needleman, 1990] Needleman, A. (1990). An analysis of tensile decohesion along an interface. *Journal of the Mechanics and Physics of Solids*, 38(3):289–324.

[Nguyen et al., 2019] Nguyen, N., Yvonnet, J., Réthoré, J., and Tran, A. (2019). Identification of fracture models based on phase field for crack propagation in heterogeneous lattices in a context of non-separated scales. *Computational Mechanics*, 63(5):1047–1068.

[Nguyen et al., 2016a] Nguyen, T., Yvonnet, J., Zhu, Q.-Z., Bornert, M., and Chateau, C. (2016a). A phase-field method for computational modeling of interfacial damage interacting with crack propagation in realistic microstructures obtained by microtomography. *Computer Methods in Applied Mechanics and Engineering*, (312):567–595.

[Nguyen et al., 2016b] Nguyen, T. T., Yvonnet, J., Bornert, M., Chateau, C., Sab, K., Romani, R., and Le Roy, R. (2016b). On the choice of parameters in the phase field method for simulating crack initiation with experimental validation. *International Journal of Fracture*, 197(2):213–226.

[Nguyen et al., 2016c] Nguyen, T. T., Yvonnet, J., Zhu, Q.-Z., Bornert, M., and Chateau, C. (2016c). A phase-field method for computational modeling of interfacial damage interacting with crack propagation in realistic microstructures obtained by microtomography. *Computer Methods in Applied Mechanics and Engineering*, 312:567–595.

[Ostoja-Starzewski, 1998] Ostoja-Starzewski, M. (1998). Random field models of heterogeneous materials. *International Journal of Solids and Structures*, 35(19):2429–2455.

[Ostoja-Starzewski, 2008] Ostoja-Starzewski, M. (2008). *Microstructural Randomness and Scaling in Mechanics of Materials*. Chapman and Hall-CRC.

[Ostoja-Starzewski et al., 1996] Ostoja-Starzewski, M., Sheng, P., and Alzebdeh, K. (1996). Spring network models in elasticity and fracture of composites and polycrystals. *Computational Materials Science*, 7(1-2):82–93.

[Peerlings et al., 1998] Peerlings, R., De Borst, R., Brekelmans, W., and Geers, M. (1998). Gradient-enhanced damage modelling of concrete fracture. *Mechanics of Cohesive-frictional Materials: An International Journal on Experiments, Modelling and Computation of Materials and Structures*, 3(4):323–342.

[Peerlings et al., 1996] Peerlings, R. H., de Borst, R., Brekelmans, W. M., and De Vree, J. (1996). Gradient enhanced damage for quasi-brittle materials. *International Journal for numerical methods in engineering*, 39(19):3391–3403.

[Peron et al., 2009] Peron, H., Laloui, L., Hueckel, T., and Hu, L. B. (2009). Desiccation cracking of soils. *European journal of environmental and civil engineering*, 13(7-8):869–888.

[Pham et al., 2011] Pham, K., Marigo, J.-J., and Maurini, C. (2011). The issues of the uniqueness and the stability of the homogeneous response in uniaxial tests with gradient damage models. *Journal of the Mechanics and Physics of Solids*, 59(6):1163–1190.

[Rahman and Chakraborty, 2011] Rahman, S. and Chakraborty, A. (2011). Stochastic multiscale fracture analysis of three-dimensional functionally graded composites. *Engineering Fracture Mechanics*, 78(1):27 – 46.

[Raina and Miehe, 2016] Raina, A. and Miehe, C. (2016). A phase-field model for fracture in biological tissues. *Biomechanics and modeling in mechanobiology*, 15(3):479–496.

[Rapaport, 2004] Rapaport, D. (2004). *The art of molecular dynamics simulation*. Cambridge university press.

[Rice, 1968] Rice, J. R. (1968). A path independent integral and the approximate analysis of strain concentration by notches and cracks. *Journal of applied mechanics*, 35(2):379–386.

[Salmi et al., 2012] Salmi, M., Auslender, F., Bornert, M., and Fogli, M. (2012). Apparent and effective mechanical properties of linear matrix-inclusion random composites: Improved bounds for the effective behavior. *International Journal of Solids and Structures*, 49(10):1195–1211.

[Silling, 2000] Silling, S. A. (2000). Reformulation of elasticity theory for discontinuities and long-range forces. *Journal of the Mechanics and Physics of Solids*, 48(1):175–209.

[Sima et al., 2014] Sima, J., Jiang, M., and Zhou, C. (2014). Numerical simulation of desiccation cracking in a thin clay layer using 3d discrete element modeling. *Computers and Geotechnics*, 56:168–180.

[Skoge et al., 2006] Skoge, M., Donev, A., Stillinger, F. H., and Torquato, S. (2006). Packing hyperspheres in high-dimensional euclidean spaces. *Physical Review E*, 74(4):041127.

[Soize, 2006] Soize, C. (2006). Non-gaussian positive-definite matrix-valued random fields for elliptic stochastic partial derivative operators. *Computer Methods in Applied Mechanics and Engineering*, 195:26–64.

[Souguir, 2018] Souguir, S. (2018). Simulation numérique de l'initiation de la rupture à l'échelle atomique.

[Staber and Guilleminot, 2017] Staber, B. and Guilleminot, J. (2017). Stochastic modeling and generation of random fields of elasticity tensors: A unified information-theoretic approach. *Comptes Rendus Mécanique*, 345(6):399–416.

[Stolarska et al., 2001] Stolarska, M., Chopp, D. L., Moës, N., and Belytschko, T. (2001). Modelling crack growth by level sets in the extended finite element method. *International journal for numerical methods in Engineering*, 51(8):943–960.

[Tadmor et al., 1996] Tadmor, E. B., Ortiz, M., and Phillips, R. (1996). Quasicontinuum analysis of defects in solids. *Philosophical magazine A*, 73(6):1529–1563.

[Tang et al., 2012] Tang, C.-S., Shi, B., Cui, Y.-J., Liu, C., and Gu, K. (2012). Desiccation cracking behavior of polypropylene fiber–reinforced clayey soil. *Canadian Geotechnical Journal*, 49(9):1088–1101.

[Tang et al., 2011] Tang, C.-S., Shi, B., Liu, C., Suo, W.-B., and Gao, L. (2011). Experimental characterization of shrinkage and desiccation cracking in thin clay layer. *Applied Clay Science*, 52(1-2):69–77.

[Tran et al., 2016] Tran, V. P., Guilleminot, J., Brisard, S., and Sab, K. (2016). Stochastic modeling of mesoscopic elasticity random field. *Mechanics of Materials*, 93:1–12.

[Tregger et al., 2006] Tregger, N., Corr, D., Graham-Brady, L., and Shah, S. (2006). Modeling the effect of mesoscale randomness on concrete fracture. *Probabilistic Engineering Mechanics*, 21(3):217 – 225.

[van Vliet and van Mier, 2000] van Vliet, M. R. and van Mier, J. G. (2000). Experimental investigation of size effect in concrete and sandstone under uniaxial tension. *Engineering Fracture Mechanics*, 65(2):165 – 188.

[Vanlerberghe, 2017] Vanlerberghe, C. (2017). Pourquoi la sécurité du stockage des déchets radioactifs de bure inquiète. *Le Figaro sciences*.

[Verhoosel and de Borst, 2013] Verhoosel, C. V. and de Borst, R. (2013). A phase-field model for cohesive fracture. *International Journal for numerical methods in Engineering*, 96(1):43–62.

[Vo et al., 2017] Vo, T. D., Pouya, A., Hemmati, S., and Tang, A. M. (2017). Numerical modelling of desiccation cracking of clayey soil using a cohesive fracture method. *Computers and Geotechnics*, 85:15–27.

[Vogel et al., 2005] Vogel, H.-J., Hoffmann, H., Leopold, A., and Roth, K. (2005). Studies of crack dynamics in clay soil: Ii. a physically based model for crack formation. *Geoderma*, 125(3-4):213–223.

[Wang et al., 2007] Wang, J.-J., Zhu, J.-G., Chiu, C., and Zhang, H. (2007). Experimental study on fracture toughness and tensile strength of a clay. *Engineering Geology*, 94(1-2):65–75.

[Wang, 2012] Wang, L. (2012). Micromechanical experimental investigation and modelling of strain and damage of argillaceous rocks under combined hydric and mechanical loads. *PhD Thesis*.

[Wang et al., 2018] Wang, L.-L., Tang, C.-S., Shi, B., Cui, Y.-J., Zhang, G.-Q., and Hilary, I. (2018). Nucleation and propagation mechanisms of soil desiccation cracks. *Engineering Geology*, 238:27–35.

[Wang et al., 2015] Wang, X., Fan, F., Wang, J., Wang, H., Tao, S., Yang, A., Liu, Y., Chew, H. B., Mao, S. X., Zhu, T., et al. (2015). High damage tolerance of electrochemically lithiated silicon. *Nature communications*, 6:8417.

[Wu, 2017] Wu, J.-Y. (2017). A unified phase-field theory for the mechanics of damage and quasi-brittle failure. *Journal of the Mechanics and Physics of Solids*, 103:72–99.

[Wu et al., 2018] Wu, J.-Y., Nguyen, V., Nguyen, C. T., Sutula, D., Bordas, S., and Sinaie, S. (2018). Phase field modeling of fracture. *Advances in Applied Mechancis: Multi-scale Theory and Computation*, 52.

[Xiao and Belytschko, 2004] Xiao, S. and Belytschko, T. (2004). A bridging domain method for coupling continua with molecular dynamics. *Computer methods in applied mechanics and engineering*, 193(17-20):1645–1669.

[Yvonnet and Bonnet, 2014] Yvonnet, J. and Bonnet, G. (2014). A consistent nonlocal scheme based on filters for the homogenization of heterogeneous linear materials with non-separated scales. *International Journal of Solids and Structures*, 51(1):196–209.

[Zemenu et al., 2009] Zemenu, G., Martine, A., and Roger, C. (2009). Analysis of the behaviour of a natural expansive soil under cyclic drying and wetting. *Bulletin of engineering geology and the environment*.

[Zhou et al., 1996] Zhou, S., Lomdahl, P., Thomson, R., and Holian, B. (1996). Dynamic crack processes via molecular dynamics. *Physical review letters*, 76(13):2318.